Spring 5-2016

High Resolution XRF Sediment Analysis of Late Season Precipitation Events in a High Arctic Glaciated Watershed: Svalbard, Norway

Christiane P. McCabe
Bates College, cmccabe@bates.edu

High Resolution XRF Sediment Analysis of Late Season Precipitation Events in a High Arctic Glaciated Watershed: *Svalbard, Norway.*

An Honors Thesis

Presented to the Faculty of the Department of Geology, Bates College,
in partial fulfillment of the requirements for the Degree of Bachelor of Science

by
Christiane McCabe

Lewiston, Maine
March 28th, 2016

Abstract

Sediment transport in High Arctic watersheds have historically been dominated by melt-induced processes (Woo and McCann, 1994). However, in Svalbard, the last decade has experienced increased discharge variability and late season precipitation events (Nowak and Hodson, 2013). This study provides a detailed description of sedimentation corresponding to these late season precipitation events in Linnevatnet, western Spitsbergen. Annual sediment traps of three consecutive years (‘11-‘12, ‘13-‘14, and ‘14-‘15) were examined through the coupling of high-resolution X-ray fluorescence (XRF) analysis with lower resolution grain size and magnetic susceptibility measurements. Geochemical signatures were compared temporally and geographically across the basin. Zirconium counts and Fe/Ti ratios (Cuven et al., 2010) were used to delineate events and seasonal boundaries.

All three years experienced heavy late season precipitation events, resulting in peaks of coarse sediment deposition coupled with variable Ca content. Principle Component Analysis was run on 10 elemental constituents (Al, Si, K, Ca, Ti, Mn, Fe, Rb, Sr, and Zr) in order to examine the relationship between them. The ‘13-‘14 year showed a strong relationship (PC1>0.5) between all 10 elements and the first principle component (PC1), suggesting the elements varied together. The ‘13-‘14 sediment budget was dominated (>40%) by a single late August precipitation event. Multiple late season precipitation events in ‘11-‘12 and ‘14-‘15, on the other hand, were characterized by increased variance in sediment geochemistry.

Acknowledgments

This project would not have been possible without the generous support from the Bates College, the Hoffman Fellowship, and the Bates Student Research Fund. I am very grateful to the University Center in Svalbard (UNIS) and the UNIS geology department, without whom I would not have had the opportunity to explore all the facets of the Arctic landscape, deepening my understanding of its dynamic systems first hand. Thanks are also given to UNIS Logistics, without whose support, this field work our field work would never have been possible... and our polar bear encounter (the quartzite boulder rolling up the hill) would have never been safe. I would also like to acknowledge Al Werner and Paul Philips for making this field season such an enjoyable time, as well as Steve Roof, for his help during the analysis process.

It should be noted that this thesis has been in its conception since before I ever entered under the Garnet Gates. When I sent an email to some random professor at a school in Maine, I had no idea I was taking such a big step towards my future. Mike, if you had not responded to my email inquiries about Bates Geology with such genuine interest in me, the unknown high schooler, I probably never would have ended up at Bates. You have been such an integral part of my journey from Lewiston to the Polar Regions and beyond. Thank you for always being my teacher, my advocate, and my friend.

To Bates Geology (on the rocks), after so many months spent in the frozen Arctic, I was dreading my reintegration into the society here... you have created a warm and welcoming environment that I am proud to be a part of. It has been a pleasure to have been a part of such a great group of people. May we all one day look fondly on our late nights that seamlessly morphed into early mornings wasted away in Coram.

To my father, I believe this is the part where I thank you for ‘sponsoring’ many of my polar adventures and university costs. We both know I would not be where I am today with our your never ending support, and cease-less nudges on the phone calls to just stay focused.

To my mother and sister, who both have accepted that I will just be MIA whenever thesis calls... Thank you for your love and understanding.

Hannah, I know you if I ever needed you, you would quite literally travel to the ends of the world for me... Thank you for lending your ear when I need to vent, your shoulder when I need to cry, and your car when I just need to get away from it all.

Julia, I am so glad that we have had the opportunity to live together not once, but twice. Start/end college with a bang?.. or just a soak in the hot-tube? Thank you for being my field partner, my confidant, and my friend. I don’t know if we would have made it through the year without our late night rants in kitchen about all things thesis, and the great sink or swim debate... I believe I am still treading water.

Sarah Cooley, I am not sure how I would have survived, spending every waking hour of every day in the library here, not knowing that my endless snaps about thesis struggles would be instantly replied with your vastly more research struggles at Cambridge and SPRI. It has kept me grounded and focused on what lies at the other end of this really long tunnel.

Finally, to the frozen lands at the ends of the earth that have taught me so much... you will always captivate me and draw me back into your icy grasp. I am so glad that you have grown to become such an intrinsic part of me. You have warmed my heart. I will be back soon.

Note to reader

Many geographic features mentioned in this study are referred to by their Norwegian names.Thus, Linnévatnet is Lake Linné, Linnédalen is the Linné Valley, Kapp Linné is Cape Linné, Linnébreen is the Linné Glacier, and Linnéelva is the Linné River.

Contents

Abstract ii
Acknowledgments iii
Note to reader iv

Chapter 1 11

Introduction 11
Purpose and Significance 12
Study Area 13
Location 13
Bedrock Geology 16
Geomorphology 16
Permafrost 17
Solifluction 17
Slope Processes 17
Climate 18
Glacial and Climatic History 18
Arctic Hydrology 20
Sediment distribution 22
Linnévatnet sedimentation: 22
Linnévatnet Provenance 23
Previous Work and Goals of this Study 23

Chapter 2 25

Methods 25
Field Methods 26
Moorings 26
Sediment traps 26
Intervalometer 28
Temperature loggers 29
TROLL CTD 29
Time-lapse photography 29
Weather data 30
Temperature and Precipitation: 30
Snowpack 31
Lab Methods 32
Grain size 32
Magnetic Susceptibility 33
Geochemical analysis 33
Analytical processing 34
Principle Component Analysis 34

Chapter 3 37

Results 37
Sediment Receiving Tube Stratigraphy 38

2014-2015 Sediment Budget Year 38
C4_15 38
Visual Stratigraphy 38
Grain Size and Geochemical Composition 38
D4_15 39
Visual Stratigraphy 39
Grain Size and Geochemical composition 39
Visual Stratigraphy 44
Grain Size and Geochemical Composition 44
G5_15 44
Visual Stratigraphy 44
Grain Size and Geochemical Composition 44
2013-2014 Sediment Budget Year 45
C3_14 45
Visual Stratigraphy 45
Grain Size and Geochemical Composition: 45
D3_14 46
Visual Stratigraphy 46
Grain Size and Geochemical Composition 46
H3_14 46
Visual Stratigraphy 46
Grain Size and Geochemical Composition 46
G3_14 47
Visual Stratigraphy 47
Grain Size and Geochemical composition 47
2011-2012 Sediment Budget Year 47
C3_12 47
Visual Stratigraphy 47
Grain Size and Geochemical composition 47
D3_12 52
Visual Stratigraphy 52
Grain Size and Geochemical composition 52
H4_12 52
Visual Stratigraphy 52
Grain Size and Geochemical composition 52
G4_12 56
Visual Stratigraphy: 56
Grain Size and Geochemical composition: 56
Weather Conditions 56
Lake Stage 58
Water Column 58
Meteorological conditions during summer/fall (2014) precipitation events 60
Late July storm 60
Late August storm 60
Mid-September storm: 60
Early October Storm 60

Principle Component Analysis 65
Chapter 4 67
Discussion 67
Differentiation of Sedimentary Layers. 68
Interpretation of Sedimentation Events 69
E2 70
E3 70
E4-E4a 70
Summer 2014/Event 1 71
Late-Summer 2014/Events 2 - Event 3 71
Event 3 71
7/24/14 72
7/26/14 72
7/27/14 72
Fall/Event 4 - Event 4a 73
8/28/14 74
8/29/14 74
9/12/14 75
9/13/14 75
9/14/14 76
9/16/14 76
9/29/14 78
10/5/14 78
9/30/14 78
10/4/14 78
Winter 79
Spring/ Event 5 79
Comparison to 2012 and 2014 sedimentation records 79
Influence of changing hydrology. 79
Geochemical Interpretation 81
Sediment Provenance 82
Sediment Provenance in ‘11-‘12 and ‘13-‘14 84
Conclusions 93
Works cited: 95
Appendix: A 100

List of Illustrations

Figure 1.1: The Svalbard Archipelago with an insert of the study area (npolar.no). 13

Figure 1.2: A bathymetric map of Linnévatnet showing the difference between the proximal subbasins and the deep basin to the north. Longterm monitoring sites are in marked C-I. This study is focused on a proximal to distal transect from C-G (from Nelson, 2010). 14

Figure 1.3: Bedrock geology of Linnédalen (Modified from Ohta et al, 1991 and Svendsen and Mangerud., 1997). 15

Figure 1.4: Examples of slope processes on the eastern side of Linnédalen seen from Kongress Pass; including debris flow (red), avalanche (orange), and rockfall (pink) deposits. It is apparent that avalanche deposits dominate the geomorphology of the area (Photo: Mike Retelle, 2014). 16

Figure 1.5: Relative sea level curves from Svalbard showing the variability in isostatic rebound around the archipelago. The highest marine limits are located in Eastern Svalbard. The study area, highlighted in red, had a marine limit of 65-75 m. (Modified from Forman et al., 2004). 19

Figure 1.6: Oblique 1936 aerial photo of Linnédalen. Linnébreen can still be seen against its LIA moraine. (Norwegian Polar Institute) 20

Figure 1.7: A comparison of the 30 year average (1961-1990) precipitation record at the Longyearbyen Airport and Isfjord Radio (Figure 1.1) demonstrates the precipitation gradient across Svalbard (modifed from Førland et al., 1997). 21

Figure 1.8: Sediment thickness isopach map of Linnévatnet (Adapted from Svendsen and Mangerud, 1997). 23

Figure 2.1: A 3D rendering of Linnédalen showing the position of the data sources. Weather Station encompasses both the main station and the two temperature loggers on the LIA moraines. Scale varies with perspective (toposvalbard.npolar.no). Moorings are retrieved and deployed, annually, at all sites during July. Additional springtime moorings are deployed at sites C, D, and H. 27

Figure 2.2: A diagram of the mooring setu[used in this study (adapted from Arnold, 2009). 28

Figure 2.3: H4 shows the construction of each sediment trap, which includes a funnel, a baffle, a support bracket, and a receiving tube - note the sediment in the receiving tube (Photo: Paul Phillips). 29

Figure 2.4: Receiving tubes were packaged for transport out of the field. Excess tubing was sawed off, and Zorbitrol was added. The receiving tubes were then capped, labeled, taped and packed out of the field. (Photo: Mike Retelle) 30

Figure 2.5: Schematic diagram of a snow tree. The light/temperature loggers face towards the ground. . .31

Figure 2.6: (a) The drumel-like apparatus used for scoring the plastic on the receiving tubes. (b) The scored side of a receiving tube. The tubes were not split open by the saw in order to minimize the impact of plastic fragments in later analyses. 32

Figure 2.7: An example of loading a sediment core into the ITRAX Core Scanner (BOSCOF, 2012). . .33

Figure 2.8: RGB image of the sediment trap retrieving tubes obtained with the ITRAX scanner. 33

Figure 2.9: Schematic diagram of the ITRAX core scanner. The first run of the ITRAX scanner obtains an optical image, an X-Ray Radiograph and a sediment surface profile by laser triangulation. The Si-drift detector moves up and down in accordance to the surface profile in order to maintain a consistent

distance of the detector and sample surface (Modified from Croudace et al., 2006). 35

Figure 3.1: Scatter plots of the elemental content (kcps) suggest a change in elemental composition between visual stratigraphic units. This is best exemplified in receiving tube D4_15. Points are grouped by the depths (in cm) of changes in the visual stratigraphy observed in D4_15. 39

Figure 3.2: Composite log of receiving tube C4_15. Units are divided based on grain size and Fe/Ti. . . .40

Figure 3.3: Composite log of receiving tube D4_15. Units are divided based on grain size and Fe/Ti. . . .41

Figure 3.4: Composite log of receiving tube H5_15. Units are divided based on grain size and Fe/Ti. . . .42

Figure 3.5: Composite log of receiving tube G5_15. Units are divided based on grain size and Fe/Ti. . . .43

Figure 3.6: Composite log of receiving tube C3_14. Units are divided based on grain size and Fe/Ti. . . .48

Figure 3.7: Composite log of receiving tube D3_14. Units are divided based on grain size and Fe/Ti. . . .49

Figure 3.8: Composite log of receiving tube H3_14. Units are divided based on grain size and Fe/Ti. . . .50

Figure 3.9: Composite log of sediment trap Composite log of receiving tube G3_14. Units are divided based on grain size and Fe/Ti. 51

Figure 3.10: Composite log of receiving tube C3_12 Units are divided based on grain size and Fe/Ti. . .53

Figure 3.11: Composite log of receiving tube D3_12. Units are divided based on grain size and Fe/Ti. . .54

Figure 3.12: Composite log of receiving tube H4_12. Units are divided based on grain size and Fe/Ti. .55

Figure 3.13: Composite log of receiving tube G4_12. Units are divided based on grain size and Fe/Ti. 57

Figure 3.16: Contoured plot of water temperatures measured during the July 2014-July 2015 period at Mooring C, the most proximal site. Annually (A), distinct phases of the water column can be observed. The water column is warm and mixed in the summer (B), stratified during the winter, and beginning to mix again in the spring (C). 59

Figure 3.17: Meteorological conditions during the late July 2014 precipitation event. Water temperatures show the conditions both in the shallow eastern sub-basin (Site D), and the distal basin (Site H). . . .61

Figure 3.18: Meteorological conditions surrounding the late August 2015 precipitation event. 62

Figure 3.19:Meteorological conditions during the mid September 2014 precipitation event. 63

Figure 3.20:Meteorological conditions surrounding the early October 2015 precipitation event. 64

Table 3.1: First and second resultant principle components, PC1 and PC2 respectively, for each receiving tube used in this study. PC values |>0.5| are bolded.. 66

Figure 4.1: Event interpretation of ‘14-‘15 sedimentation year, determined by peaks in Zr (black). Grain size (blue) is presented for visual comparison. 68

Figure 4.2: Seasonal interpretation of ‘14-‘15 sedimentation year, determined by peaks in grain size (blue). Zr content is presented for visual comparison (black). 69

Figure 4.3: The change in voltage of the intervalometer, showing the timing of sedimentation from July 2014 - February 2015. Three sedimentation events were recorded by the intervalometer across the basin. The thickest sediment deposition corresponds to the September storm (E4-E4a). Note: voltage values can decrease due to the settling of fine sediment within the receiving tube. 70

Figure 4.4: (A) Linnéelva swollen with discharge during the late July storm. The lake water is turbid and a reddish brown sediment plume can be seen hugging the western eastern shore. (B) A down lake view of the turbid lake water. The lake shore is blurry, possibly suggesting an interaction between the

sediment fans and the lake water. (C) Following the peak in precipitation, the lake appears less turbid. 72

Figure 4.5: The sediment dispersal in a narrow glacier-fed lake, dominated by overflow-interflow, results in a proximal-distal thinning (A) and a distally finning (B) distribution of sedimentation. (Modified from Smith and Ashley, 1985) 73

Figure 4.7: (A) The Linnéelva inflow the day before the 9/13/14 precipitation event. Note: the presence of snow on the hillside. (B) The Linnéelva inflow during peak precipitation. Note: the absence of snow, the flooding of Linnéelva, and the streams of water flowing over the 'twin fans' and from the western cirque glacier across the lake. 75

Figure 4.7: (C) Downlake view of the wind-driven transport of a sediment overflow. (D) Linnéelva, still flooding the delta, formed a visible sediment plume in the lake. Note: there is continued inflow of water from the western cirque glacier. 76

Figure 4.8: Interpretation of fall sedimentation events in relation to changes in lake stage. The precipitation events caused notable increases in surface level during an overall low lake stage. 77

Figure 4.9: Time lapse images of the glacier front (A,B) and the linneleva inlet (C,D). During this early October precipitation event, the snow disappeared from the highlands (B) and a sediment plume hugged the east coast of the lake (D). 78

Figure 4.10: The retreat of Linnébreen since 2004 in meters. The glacier has retreated over 330m over the last 12 years. (From Roof, 2014; Modified by Walther, 2015) 80

Figure 4.11: PCA Biplot of E2. The fit of each elementals to the resultant PC is presented by vectors related to the left and bottom axis. The relationship of each sampling point to the calculated PC is represented by the 'scores' or dots ploted against the top and right axis. No coordinate rotation has been applied to the data. This applies for all following Biplots. 83

Figure 4.12: PCA Biplot of E3. 85

Figure 4.13: PCA Biplot of E4. 86

Figure 4.14: PCA Biplot of E4a. 87

Figure 4.15: PCA Biplot of Winter sedimentation. 88

Figure 4.16: The seasonal interpretation of 2013-2014 receiving tubes determined by peaks in grain size (blue). Zr content is presented for visual comparison (black). 89

Figure 4.17: The seasonal interpretation of 2013-2014 receiving tubes determined by peaks in grain size (blue). Zr content is presented for visual comparison (black). 90

Figure 4.18: 2013-2014 seasonal elemental vector Biplots. There is a strong covariance between most elemental constituents throughout the year. 91

Figure 4.19: 2013-2014 seasonal elemental vector Biplots. 92

Chapter 1

Introduction

Purpose and Significance

The Arctic sits in a critical position for the global environment. Home to a complex array of earth-atmosphere interactions, Arctic climate conditions highly influences global circulation patterns, including sea ice extent, ocean salinity and ground surface albedo to name a few. These variables are all interconnected and form a series of feedback loops which have caused the highest projected climatic changes to impact the Arctic (Serreze et al., 2000) which in turn has a global reach. Svalbard stands as a "sensitive sentinel" to the Arctic climate (Humlum et al., 2005). Longyearbyen is home to the longest running high latitude weather record (Humlum, 2003) which provides the strong basis necessary to understand the context of the modern climate. In recent decades, changes in the observed record have been frequent and significant (Nowak and Hodson, 2013).

Knowledge of modern climatic and watershed processes combined with paleoclimate records provides insights into the climate system in the future. In order to develop an understanding of the relationship between earth systems and the paleoclimate, high resolution proxy records are needed for comparisons at measurable timescales. The annually varved sediment record of Linnévatnet, in western Spitsbergen, Svalbard, provides such a resolution. Therefore, the study area in Linnédalen offers an excellent case study for the impact of hydrometeorlogical changes on High Arctic proglacial lake sedimentation.

Study Area

Location

The Svalbard Archipelago is located in the northwestern Barents Sea approximately halfway between mainland Norway and the North Pole. The Archipelago encompasses all the islands between 74˚N to 81˚N latitude and 10˚E to 35˚E longitude. Spitsbergen (area = 37,673 km^2) is the largest island in the archipelago (Norskpolarinstitutte). Linnédalen, the field site for this study, is a glaciated catchment situated in western Nordenskiöldland near the conjuncture of the Isfjorden and the Greenland Sea (Figure 1.1).

Figure 1.1: The Svalbard Archipelago with an insert of the study area (npolar.no).

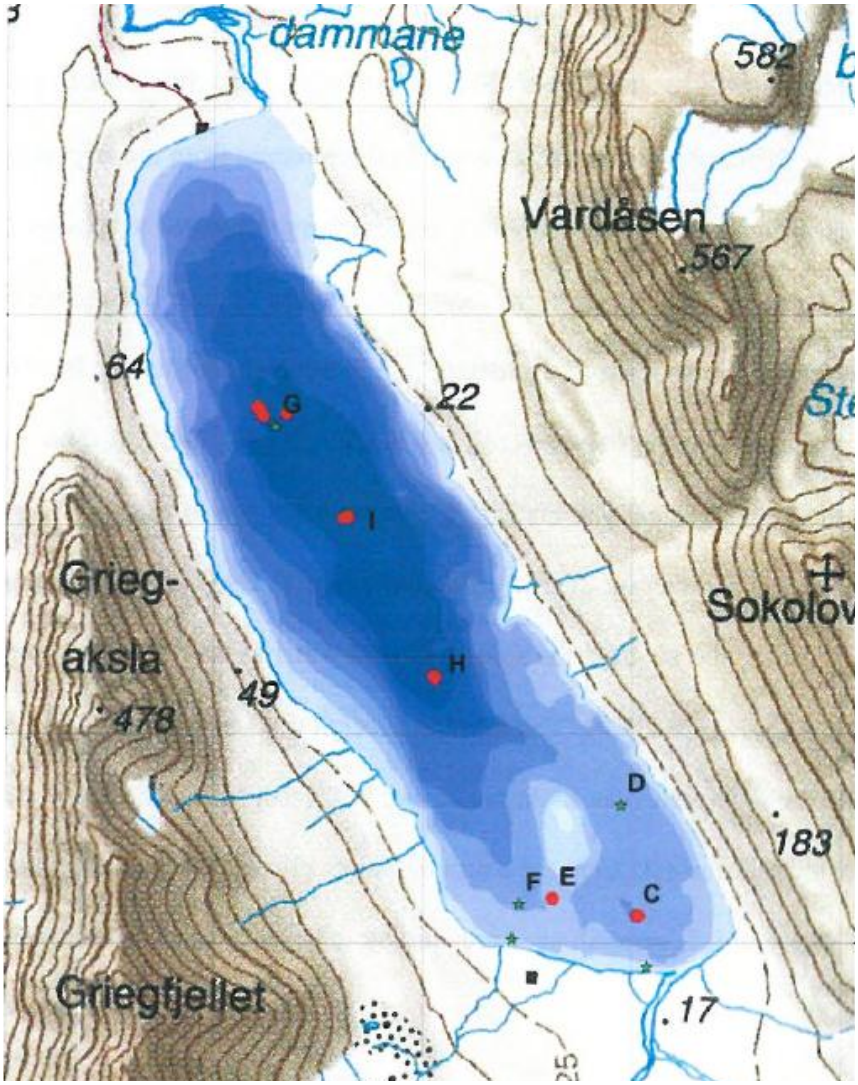

Figure 1.2: A bathymetric map of Linnévatnet showing the difference between the proximal subbasins and the deep basin to the north. Longterm monitoring sites are in marked C-I. This study is focused on a proximal to distal transect from C-G (from Nelson, 2010).

Linnnédalen

Linnédalen is a N-S oriented valley containing the polythermal* glacier, Linnébreen. Linnébreen is currently retreating, exposing an extensive glacial forefield with loose clastic material, bound by an ice-cored moraine. The moraine is incised by Linnéelva which flows across a sandur plain extending from the moraine to the edge of the lake. Linnévatnet is approximately 4.7 km long and 1.3 km wide. Located 12 m.a.s.l., Linnévatnet is a cold, monomictic lake. Due to exposure, it is subject to wind driven mixing of the water column, allowing the lake to maintain temperatures below 4^{o}C throughout the year (Boyum and Kjensmo, 1978). The bathymetry of Linnévatnet is divided into multiple sub-basins (Figure 1.2). The main basin is approximately 35 m deep (Snyder et al., 2000) while the southern half of the lake is split into two shallower sub-basins, separated by a bathymetric ridge. The east sub-basin is 1.5 km long by 0.5 km wide and 16 m deep, whereas, the west sub-basin is smaller and shallower at 11 m depth.

*It is possible that Linnébreen has thinned to a point where it now has a cold based glacial regime.

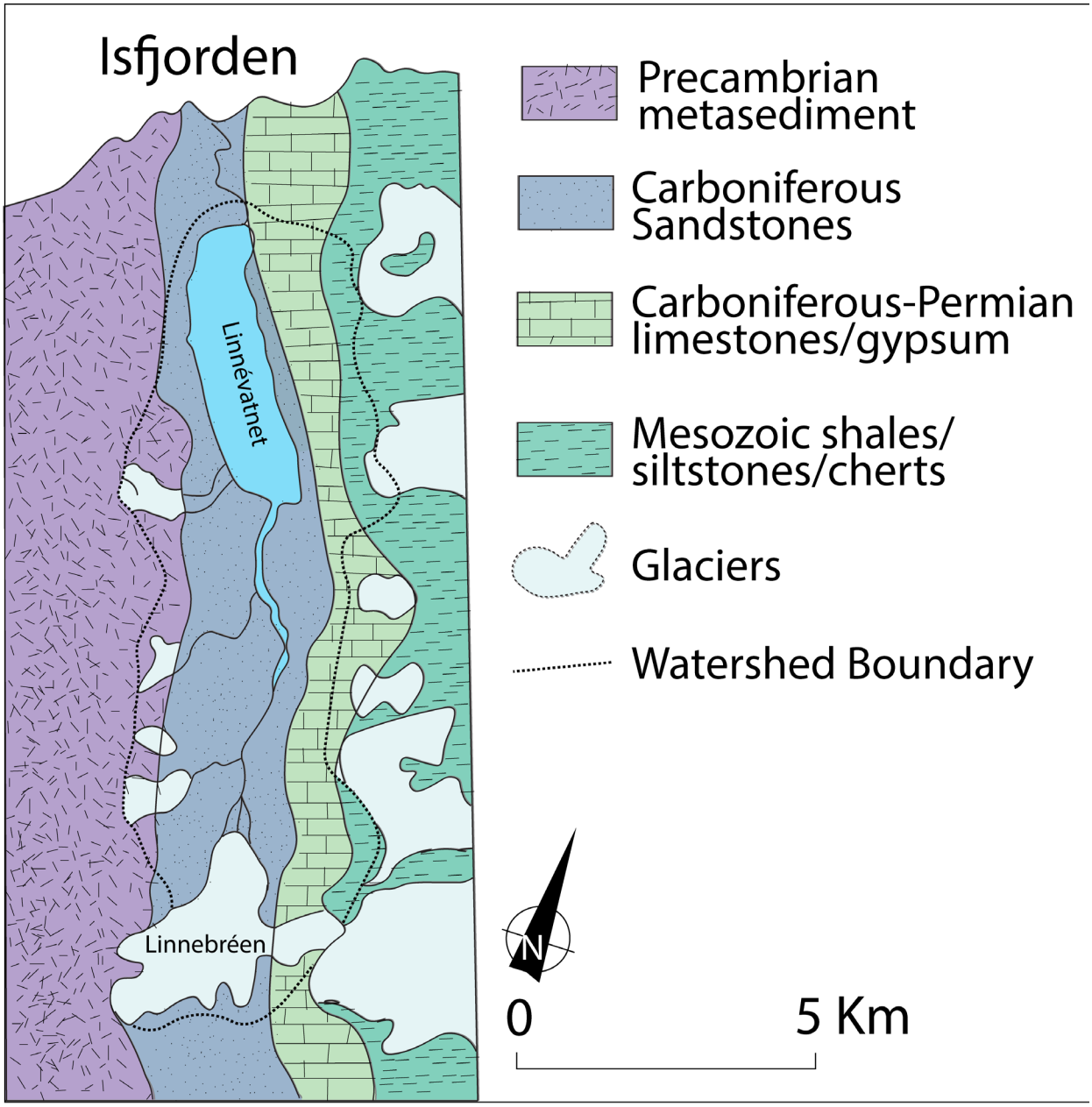

Figure 1.3: Bedrock geology of Linnédalen (Modified from Ohta et al, 1991 and Svendsen and Mangerud., 1997).

Bedrock Geology

Svalbard sits on the uplifted NW corner of the Barents Shelf. The opening of the Arctic Ocean during the Cretaceous resulted in regional uplift and the formation of the west Spitsbergen fold and thrust belt (Dallmann et al., 1992). In western Nordenskiöld land, this fold-belt exposes the entire geological history of Svalbard. Within Linnédalen, the north-south striking bedrock sequences from west to east, providing distinct local geologic sources for sediments in Linnévatnet (Figure 1.3). The westernmost exposure on Spitsbergen is the highly metamorphosed precambrian basement rocks of the Heckla Hoek formation diamictite which is exposed on the strandflats along the west coast. The west wall of Linnédalen is formed by the sharp ridge of Linnéfjella which is comprised of argillaceous phyllite (Dallman et al, 1992). Central Linnédalen is floored by the lower Carboniferous Orustdalen Formation, a quartzite with abundant plant and tree fossils. A sequence of Upper Carboniferous to Permian-age limestone, dolostone, and evaporates such as gypsum and anhydrite are exposed on the eastern wall of Linnédalen.

Geomorphology

The geomorphology of Linnédalen is dominated by glacial and periglacial features (Gogolek et al., 1980) representative of a High Arctic landscape. There are four major geomorphological elements in the valley: fan deposits, solifluction, permafrost, and ice-cored moraines. The geomorphic activity is controlled by both temperature and precipitation (Humlum, 2002).

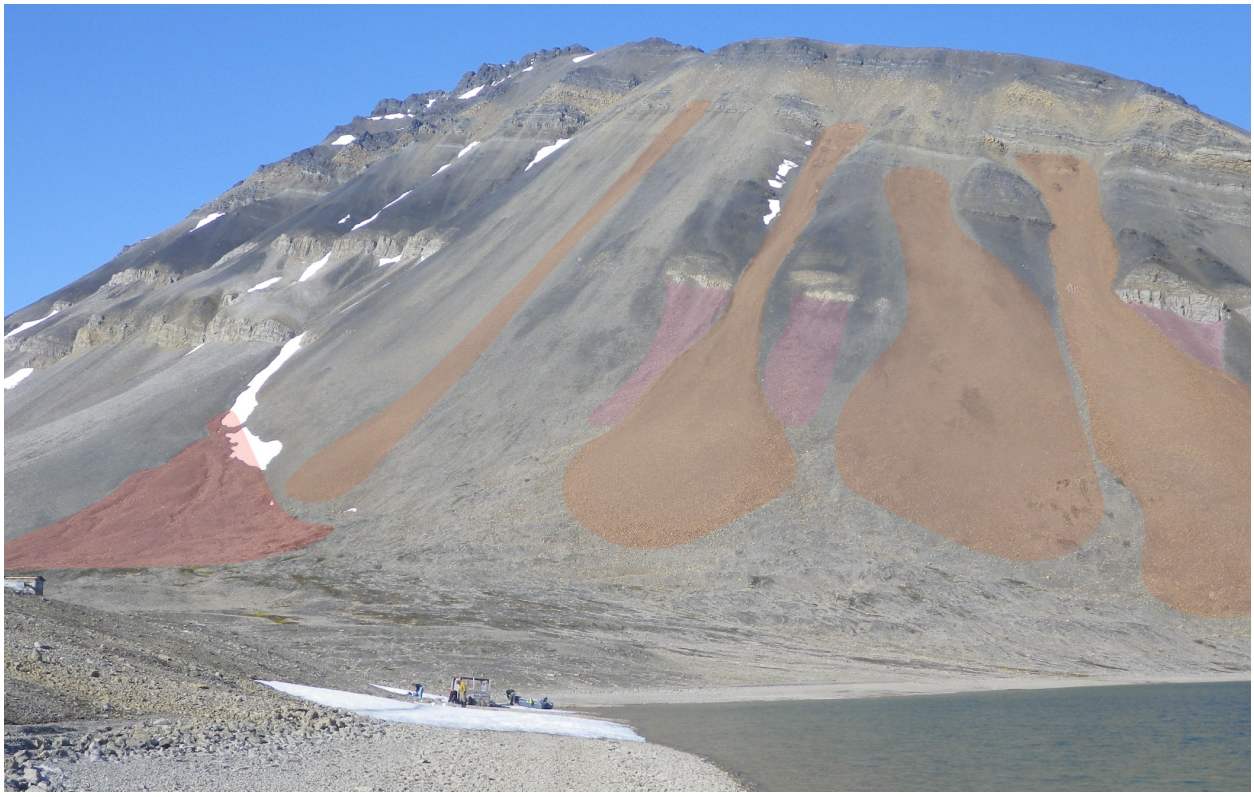

Figure 1.4: Examples of slope processes on the eastern side of Linnédalen seen from Kongress Pass; including debris flow (red), avalanche (orange), and rockfall (pink) deposits. It is apparent that avalanche deposits dominate the geomorphology of the area (Photo: Mike Retelle, 2014).

Permafrost

Permafrost is a prominent geomorphological feature in Linnédalen. Defined as ground that remains below 0˚C for at least two consecutive years (NRCC, 1988), the near surface zone of permafrost thaws during the summertime and is known as the active layer. While not being entirely impermeable, permafrost is considered an aquitard (Woo et al., 2008), thus influencing basin hydrology (Hodson, 1994). Svalbard is characterized by near-continuous permafrost cover (Humlum et al., 2003) in ice-free land areas ranging in thickness from 80-100 m near the coast to 400-500 m in the highlands (Humlum, 2005; Liestøl, 1977). The Svalbard permafrost is dynamic and the active layer thickness varies spatially. While the active layer is typically less than 1 m, it has shown signs of thickening (Christiansen et al., 2013). For example, the active layer atop a marine terrace in Linnédalen was measured to be 1.2 m deep (Gogolek et al., 1980). Given Svalbard's relatively mild climate for the high Arctic, the permafrost is subject to 'one-sided, top-down active layer freezing, thus increasing its sensitivity to meteorological variations (Christiansen et al., 2010).

Solifluction

Solifluction is the slow downslope creep of sediment within the active layer (Akerman, 2005). It smooths topographical relief and causes the down-slope transport of sedimentary material. Rates of solifluction vary based on summer air temperature, and winter snow cover (Christiansen et al., 2013). In Linnédalen, solifluction is prevalent along alluvial fans, on hillslopes comprised of marine mud, and on the ice cored moraines. The valley has been subject to intense solifluction, particularly during periods of increased ground moisture (Gogolek et la., 1980).

Slope Processes

Slope processes can result from either purely gravitational forces or a combination of gravity and water (Rubensdotter et al., 2015). Such processes form the fan-shaped deposits common in mountainous environments. Talus cones, scree slopes, fluvial and alluvial fans have been observed in different environments across the globe (Rubensdotter et al., 2015; Blair and McPherson, 2009). And while fan deposits have been studied extensively at lower latitudes it is suggested that there are similarities in the depositional processes of a fan in the high Arctic and the subtropics (de Haas et al., 2015).

Talus cones and scree slopes are built by rockfall deposits. They are characterized by a short run-out (Rubensdotter et al., 2015), and are an important agent in the denudation of a high Arctic landscape (Svendsen et al., 1989). In Linnédalen, rock fall is common along the steeper slopes of the valley walls (Figure 1.4). Sediment gravity flows, also known as debris flows, are formed by the rapid movement of a mixture of sediment, vegetation and water, producing a long run out (Rubensdotter et al., 2015). Associated with extreme precipitation or snowmelt events (Larsson, 1982), debris flows begin at inclinations >30˚, however this is dependent on the sediment saturation. Due to the prevalence of permafrost, Svalbard is susceptible to debris flows, as the active layer can become over-saturated (Larsson, 1982). When a debris flows reaches a shallow surface gradient, it spreads out and builds up an alluvial fan's shape. Alluvial fans form downslope of channelized mountainous catchments (Blair and McPherson, 2009), and their formation is dependent on topography, sediment production, and a triggering mechanism for the debris flows (de Haas et al., 2015; Blair and McPherson, 2009).

There is a relationship between permafrost and the formation of fan deposits. First, the impermeability of permafrost decreases the precipitation threshold needed to trigger a sediment-gravity flow (de Haas et al., 2015; Larsson, 1982). Second, the frost action weathering commonly associated with permafrost and periglacial environments increases the material available for downslope transport (Eckerstorfer et al., 2013).

In Svalbard, snow avalanching is the dominant force on the morphology of fan deposits (de Haas et al., 2015). Avalanches can carry large volumes of debris, which settles in-situ as the snow melts throughout the summer season (Humlum et al., 2007). The availability of these heterogeneous sized deposits increases the possibility of the mobilizing debris flows (Rubensdotter et al., 2015; de Haas et al., 2015).

Climate

Glacial and Climatic History

Svalbard has been subject to multiple glaciations throughout its history (Ingólfsson and Landvik, 2013). During the Last Glacial Maximum, glacial ice extended from the Barents Sea, across Spitsbergen and through the local valleys to the shelf edge west of Svalbard. Following this Late Weichselian glaciation, glacial retreat resulted in the inundation of the isostatically depressed landscape. The maximum elevation of this marine transgression is referred to as the marine limit (Forman et al., 1989). When Linnédalen was deglaciated ca. 12,500 BP, a thick succession of marine sediment was deposited in a fjord-like setting with a local marine limit of 65-75 m a.s.l. (Mangerud and Svendsen, 1990). However, decreasing isostatic pressure from the breakup of the Svalbard-Barents Sea ice-sheet allowed the land to rebound, outpacing the rising eustatic sea level (Ingólfsson, 2011), and by 10,300 cal. BP Linnévatnet was isolated from the marine environment (Svendsen and Mangerud, 1997). Above this lacustrine marine transition, Linnévatnet's sedimentation preserves a record of the area's climatic changes (Svendsen and Mangerud, 1997).

Following the deglaciation, there was a period of cool temperatures and glacial expansion across Europe (Bradley and England, 2008). This period, known as the Younger Dryas (YD), did not correspond to increased glacial extent in western Svalbard due to restricted precipitation (Mangerud and Landvik, 2007). The YD was followed by a period of warmer than present temperatures in Svalbard (Svendsen and Mangerud, 1997). During the Holocene thermal maximum it is believed that Linnébreen melted away entirely and the catchment remained non-glaciated until about 4400 BP. When Linnébreen reformed, sedimentation increased in Linnévatnet (Svendsen and Mangerud, 1997).

During the last 2,000 years there were two particularly notable climatic events, the Medieval Climate Anomaly (MCA) and the Little Ice Age (LIA). The MCA was characterized by warmer than present temperatures and a decreased glacial extent in Svalbard (Humlum et al., 2005). The MCA was followed by the LIA, which is distinguishable in the paleoclimate record by the 1400's (Mann et a., 2009). In western Spitsbergen, the LIA resulted in a regional advance of glaciers (Werner, 1993; Røthe et al., 2015; van der Bilt et al., 2015), including Linnébreen (Figure 1.6) (Svendsen and Mangerud, 1997), and lasted until the turn of the 20th century (D'Andrea et al., 2012).

Studies have shown there may be a link between these two climatic anomalies and persistent phases of the North Atlantic Oscillation (NAO) index (Lamb, 1985, Hanssen-Bauer, 2002). Changes in the NAO, a multidecadal oscillation of atmospheric air masses across the North Atlantic region, influence the storm track across Europe (Serreze et al., 1997). During its positive phase (NAO+), high atmospheric pressure gradients cause a northward shift in the storm track while the negative phase (NAO-) results in weaker pressure centers (Hurrell et al., 2001; Hurrell and van Loon,1997) and decreased storminess in

Northern Europe (Serreze et al., 1997). The short term effects of the NAO on Svalbard's climate are not well-pronounced (Marshall et al., 2001; Divine et al., 2011). However, long-term cooling trends which may have resulted in the LIA, are associated with a persistently NAO- and decreased oceanic heat fluxes (Trouet et al., 2009) as recorded in ice cores (Divine et al., 2011).

Present Arctic Climate

Much attention has been drawn to the current state of the Arctic climate. Sea ice extent is shrinking, temperatures are rising, precipitation patterns are changing, and there is an increase in ocean heat content (IPCC, 2014). The rate of these changes appears to be anomalous over past millennia, and is often referred to as Arctic Amplification (Serreze and Barry, 2011). The trends seen in the Svalbard climate are reflected throughout the northern hemisphere (Førland et al., 1997). There is a clear warming trend in Svalbard, seen both through the temperature record (Førland et al., 1997) and the net mass loss of glaciers since the turn of the 20th century (Nuth et al., 2009; Kohler et al., 2007; Svendsen and Mangerud, 1997).

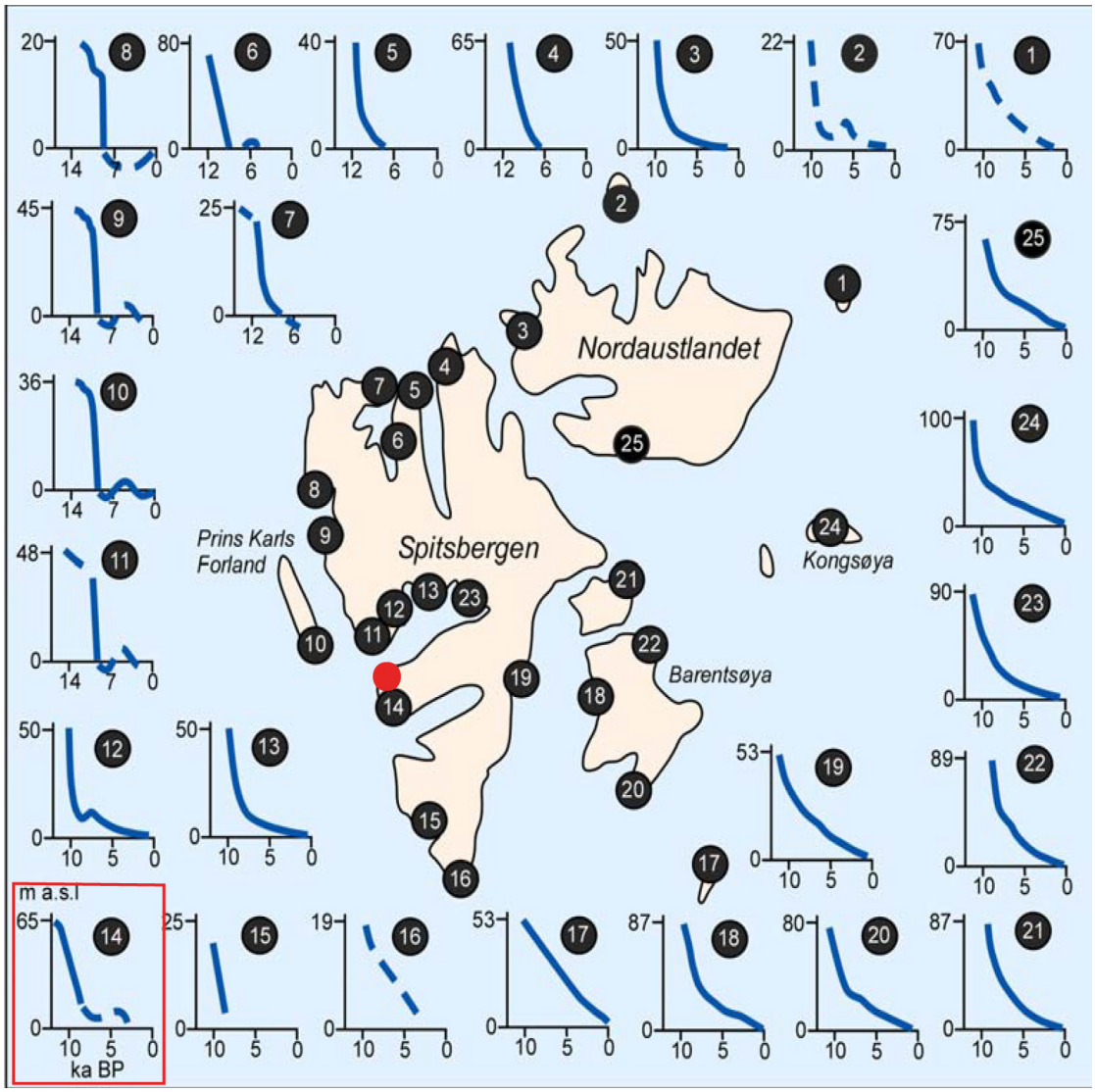

Figure 1.5: Relative sea level curves from Svalbard showing the variability in isostatic rebound around the archipelago. The highest marine limits are located in Eastern Svalbard. The study area, highlighted in red, had a marine limit of 65-75 m. (Modified from Forman et al., 2004).

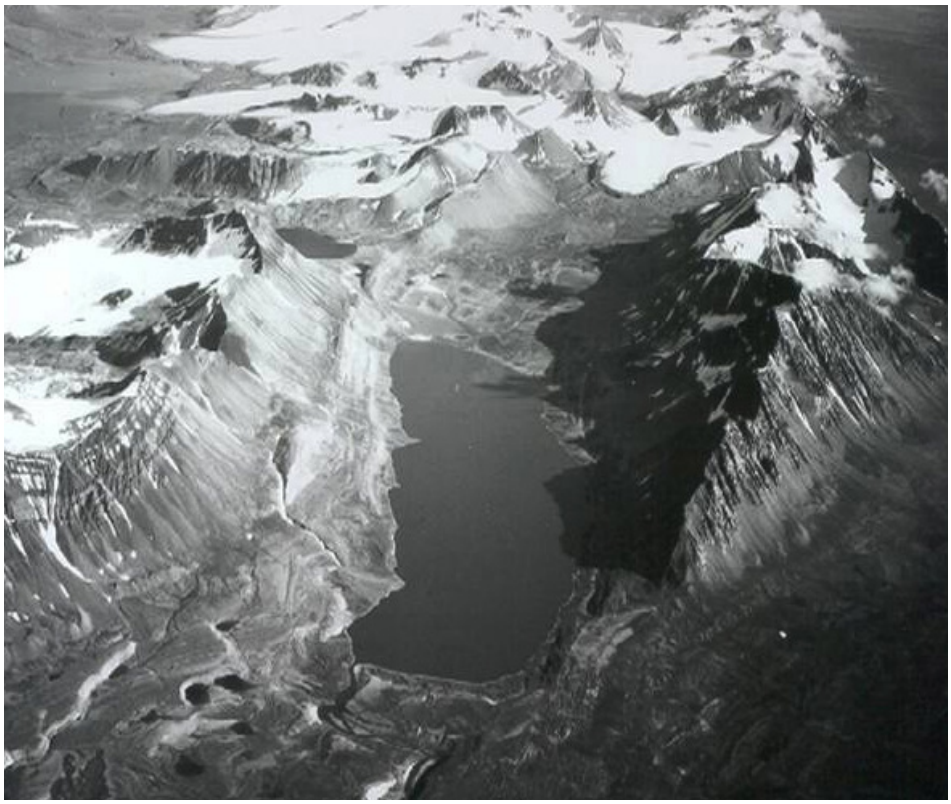

Figure 1.6: Oblique 1936 aerial photo of Linnédalen. Linnébreen can still be seen against its LIA moraine. (Norwegian Polar Institute)

Svalbard Climate

The Svalbard archipelago is situated at the boundary of distinct ocean currents and air masses (Spielhagen et al., 2011; Hald et al., 2007) producing a highly sensitive climate (Humlum et al., 2007). The interplay between these oceanic and the meteorological conditions have characterized Svalbard as a marine Arctic climate (Eckerstorfer and Christiansen, 2011). This marine influence provides Svalbard with a milder climate than other regions at similar latitudes. Both rain and snow can occur during any season across Svalbard (Førland et al., 1997). The maritime influence also causes greater degrees of inter-annual variability. Due to topography, the archipelago is subject to a strong precipitation gradient (Førland et al., 1997). The coastal mountains receive the highest amounts of precipitation, while the inner-fjords receive substantially less. For example, there is a large difference between Longyearbyen (LYR) and Isfjord Radio (Figure 1.7), where Isfjord Radio receives 435 mm water equivalents per annum while LYR receives just 200 mm (Humlum, 2002). Over the last century, MAAT (Hanssen-Bauer, 2002) and precipitation (Førland et al., 1997) have increased. Recent changes in Svalbard generally agree with climate change model predictions, such as increased precipitation events (Hanssen-Bauer, 2002).

Arctic Hydrology

Glaciated environments are hydrologically unique. The combination of permafrost, the potential for net snow accumulation, and cold winters cause precipitation to be stored within the system until the melt season. In northern Svalbard, the majority of melt-driven discharge occurs from June to August (Nowak and Hodson, 2013). There are two ‘shoulder seasons’ between summer and winter where discharge is present but variable. Additionally, due to the volatility of wintertime temperatures in Svalbard (Førland et

al., 1997; Humlum, 2002), there can be sporadic discharge from November to May.

Hydrology in a glacial environment is heavily influenced by the glacier thermal regime (Hodgkins, 1997). Svalbard is dominated by non-temperate ice, often referred to as sub-polar (Hagen et al., 1993). The ice in a cold based thermal regimes act as an aquaclude, restricting run-off drainage to incised surface channels. Additionally, if the glacier bed is near the pressure melting point, a subglacial talik (unfrozen area within permafrost) can form and connect the glacier to the groundwater (Hagen et al., 2003).

In permafrost environments, it has been common to assume that there is no change in the storage capacity of a catchment (Killingtveit et al., 2003). However, during the last decade a shift in Svalbard's hydrological systems (Nowak and Hodson, 2013; Rutter et al., 2011) suggests otherwise. There has been a noted increase in the water budget due to the melting of glaciers and ground ice, as well as a lengthened runoff season (Nowak and Hodson, 2013). Earlier runoff, warmer permafrost and a deepened active layer (Christiansen, et al., 2012) allow for increases in the water storage potential of these systems, altering the typical flow paths of runoff (Nowak and Hodson, 2013). Thus, the storage capacity now needs to be considered.

Most northern rivers exhibit a nival flow regime (Woo and McCann, 1994), with high inflow during the snow melt period, low flow during the summer and little or no flow during the winter. Sediment loading typically reflects the flow regime, with the highest sediment load during the nival melt period (Woo and McCann, 1994). In glaciated catchments it is expected that the available sediment supply would decrease throughout the runoff season (Hodgkins, 1997). But, due to the lack of subglacial drainage systems, cold-based glaciers do not typically exhaust their sediment supply during the melt season (Hodgkins, 1997). Thus, Svalbard watersheds have shown the potential for consistent sediment supply throughout the summer melt season. The non-erosive nature of a cold-based glacier bed (Benn and Evans, 2010) suggests another source of this sediment. These non-glacial sources can produce large but discontinuous contributions to the sediment supply (Hodson, 1994; Hodson et al., 1998).

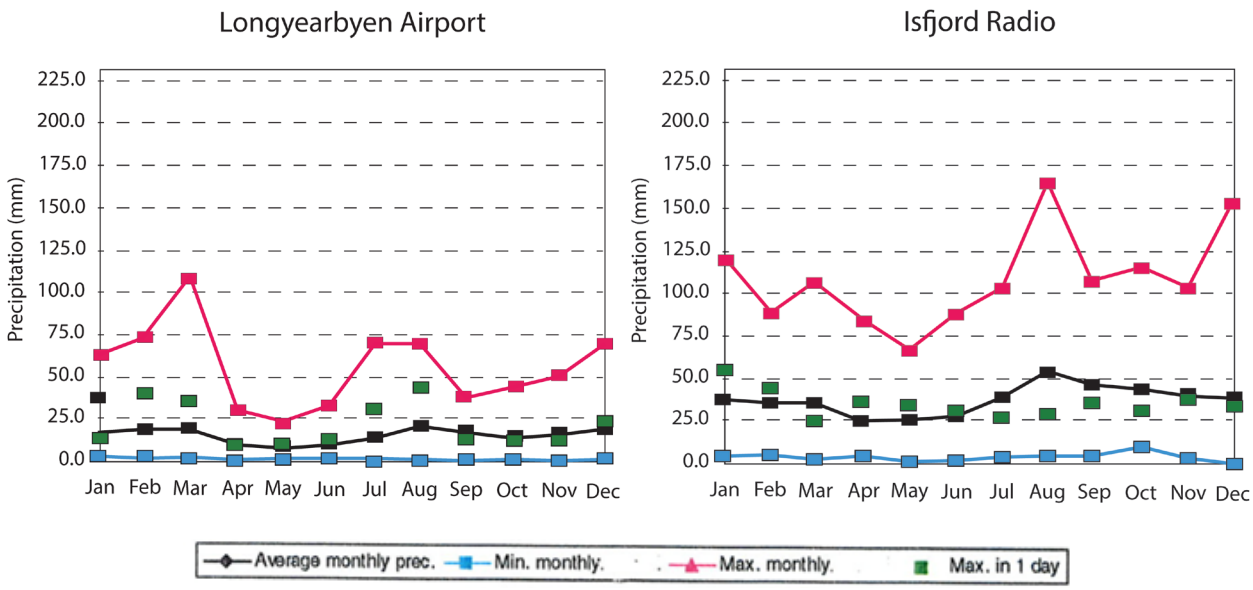

Figure 1.7: A comparison of the 30 year average (1961-1990) precipitation record at the Longyearbyen Airport and Isfjord Radio (Figure 1.1) demonstrates the precipitation gradient across Svalbard (modifed from Førland et al., 1997).

Lacustrine Sediment

Sediment distribution

Sedimentation in a proglacial lake is dependent on multiple factors (Smith and Ashley, 1985). Annual sediment transfer is closely related to the amount of snowmelt runoff in a basin, and the formation of subannual sedimentation features is controlled by both meteorology and geomorphology (Chutko and Lamoureux, 2008). Summer glaciofluvial sedimentation is commonly deposited as graded beds (Chutko and Lamoureux, 2008). And rainfall-induced discharge is associated with additional coarse grained sedimentation (Chutko and Lamoureux, 2008). During the winter, lake ice allows for the fine-grained sediments to settle through the water column, forming a fine clay cap above the summer layer (Chutko and Lamoureux, 2008).

Stratification of the water column is a dominant influence on sediment distribution in a lake. A lake can become stratified due to characteristics such as temperature, density or salinity. Typically during the summer months, the warm surface layer of a stratified lake is known as the epilimnion. The middle layer is referred to as the metalimnion or the thermocline and the cold bottom layer is the hypolimnion (Smith and Ashley, 1985). However, Linnévatnet is a cold monomictic lake, and thus is not normally subject to intense thermal stratification during the summer season.

Density stratification controls how sediment is transported (Carmack et al., 1979; Smith and Ashley, 1985). For example, if a sediment bedload reaches the lake it will either be more, equal or less dense than the ambient lake water. This will determine if the sediments will flow as a cap above the lake water in an overflow, along a density boundary within the water column as an interflow, or sink to the bottom as an underflow. If the inflowing water density is equal to that of an non-stratified lake the sediment will mix throughout the water column as a homopycnal flow (Smith and Ashley, 1985). There is a clear relationship between inflow proximity and grain size. For example, coarser sands and silts settle first, while finer mud will remain suspended in the water column and is subject to dispersal throughout the basin.

Linnévatnet sedimentation:

Linnévatnet is subject to a counter-clockwise distribution of sediment (Figure 1.8) because sediment plumes, entering via Linnéelva in the south, are deflected to the east (right-hand Coriolis deflection) resulting in the the thickest accumulation of sediment in the eastern sub-basin. The varved sedimentary record in Linnévatnet provides a paleorecord extending back over 3000 years (Svendsen and Mangerud, 1997). Each proximal sub-basin has a distinctive stratigraphy. The western sub-basin contains a record of the interplay between the two major sediment sources: the cirque glacier outflow and Linnéelva. When the cirque glacier dominates, there is a prominence of metamorphic lithic fragments in the laminae (Snyder et al., 2000). However, when Linnéelva is the dominant sediment source, there is an abundance of mono-mineralic grains (Snyder et al., 2000). Sediment deposits in the eastern basin are traceable across the deep basin as well (Snyder et al., 1994).

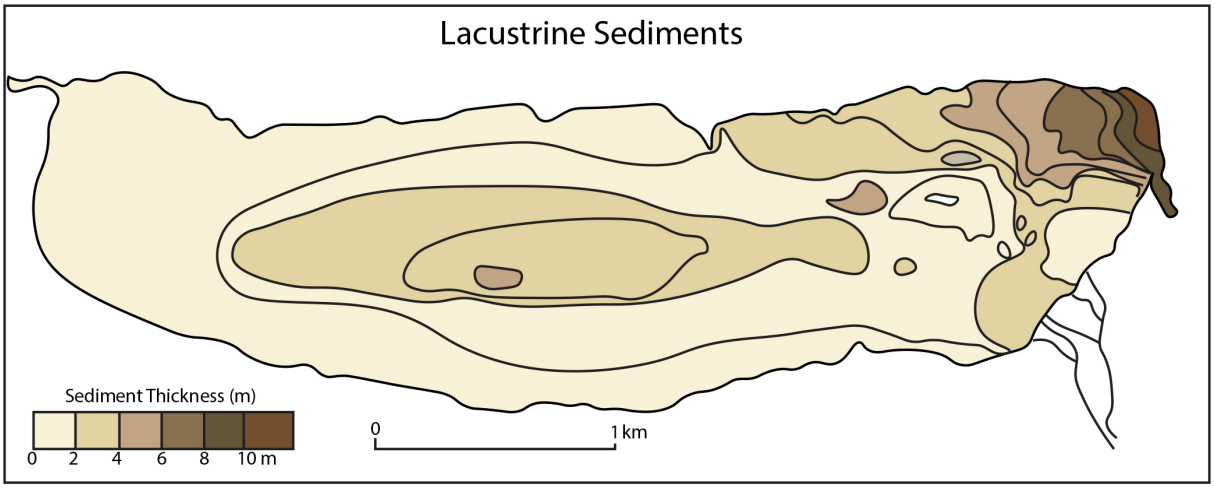

Figure 1.8: Sediment thickness isopach map of Linnévatnet (Adapted from Svendsen and Mangerud, 1997).

Linnévatnet Provenance

There are four main sources of sediment in Linnévatnet (Snyder et al., 2000). Because Linnébreen is underlain by coal-bearing sandstones (Hjelle et al., 1986), sediment in Linnéelva is characterized by low carbonate content [3-6%] (Snyder et al., 2000), and a high concentration of coal. Linnéelva drains the sandur plain from Linnébreen to Linnévatnet, mobilizing available sediment along the way. To the east of Linnéelva, is an alluvial fan which is subject to inflow from both groundwater and snow melt processes. Sediment from this fan is associated with high carbonate [10-40%] (Snyder et al., 2000) but low coal content. Additionally, the steep side channels and fans produce sediment with different carbonate content depending on its location. While the eastern valley wall is marked by a high carbonate content, the western side has a low carbonate content, and the remnant cirque glacier along the western valley wall contributes metamorphic lithic fragments to the lake (Snyder et al., 2000).

Previous Work and Goals of this Study

Linnédalen has been the site of a National Science Foundation (NSF) Research Experience for Undergraduates (REU) program over the past decade. Of particular significance to this current study, Perrault (2006) examined the provenance of lacustrine sediment in relationship to point sources around the lake using XRD analysis. Walther (2015) examined the relationship between sedimentation and late season hydrometeorological storm events using XRD analysis. Cuven et al. (2010) examined the relationship between grain-size and XRF data in varved lacustrine sediment. They found Zr and Si to be reliable proxies for coarse grained sedimentation and Fe/Ti to be a reliable proxy for clay sedimentation. This study furthers Walther's work by examining the physical characteristics associated of large late melt season events, particularly focusing on how sediment geochemistry varies spatially across the lake.

Chapter 2

Methods

Field Methods

The study site was selected, by the Svalbard REU, based on multiple parameters that make it unique. First, the proximity of Linnédalen to long weather records is rare among High Arctic locations. Second, the distinct difference in bedrock lithology between the valley walls allows for the analysis of lacustrine sediment provenance across the basin. Finally, the varved sedimentary record has facilitated the development of a more accurate long-term and high resolution paleoclimate record for this area.

Field-work was completed from July 16th-July 26th 2015. During the field campaign the weather was predominantly calm and clear, with one day of rain and fog.

Moorings

Moorings have been deployed annually in Linnévatnet since 2003. In late July 2014, moorings C, D, E, F, G and H were deployed for a full 12 month period (Figure 2.1). These 6 "annual" moorings contained both sediment traps (ranging from 1-6 traps) and temperature loggers (Figure 2.2).

In April 2015, a series of "spring" moorings were deployed through the lake ice at sites C, D and H. These moorings contained a series of Onset Water Temp Pro temperature loggers attached at equal intervals. Two Troll Conductivity Temperature and Depth (CTD) meters were also deployed to gather information about the bottom conditions in the lake at sites C and H.

The mooring sites were located in strategic positions throughout the lake. Site C is located in the eastern sub-basin near the main inlet, Linnéelva. Site D, also in the eastern sub-basin, is more distal and situated proximal to a carbonate alluvial fan. Site E is located on a bathymetric ridge between the eastern and western sub-basins. Site F is located in the western sub-basin, near the inflow from the LIA Cirque moraine. Site H is located in the deeper main basin, and is positioned off shore from a large alluvial fan. Finally, the most distal site in the main basin, site G ideally captures the overall lacustrine sedimentary record without too much influence from point sources, such as a fan or a delta.

Sediment traps

Sediment traps are one of the only ways to obtain a direct measurement of in situ sediment flux (Asper, 1987). Each sediment trap collects the sediment accumulated in one year. The sediment traps used in this study consisted of a 12.1 cm plastic funnel, a baffle, a bracket and a receiving tube (Figure 2.3). The funnel amplifies sample size (Asper, 1987), producing an approximately 8 fold increase in the observed sedimentation rate. The 1 cm^2 baffle prevented sedimentary resuspension and it disrupts laminar flow in the water column, thereby causing sediment to settle out of suspension. The L-shaped support bracket allowed the sediment traps to be attached to the mooring line. The traps were spaced evenly along a mooring line. This spacing ranged between 3 m (moorings C and D) and 6 m (moorings H, G, and F). And while sediment traps are 'admittedly an imperfect sampling tool' (Asper,1987) they have proven useful in studies of Linnévatnet, providing a relative sediment quantity per year and allowing for an estimate of annual sediment flux timing (e.g. Walther, 2015).

Mooring retrieval

In July 2015, all '14-'15 moorings were retrieved from the lake. The sediment traps were removed from the moorings, transported to land, and set to rest overnight allowing any sediment still suspended in the receiving tube to settle. The moorings were laid out on the beach and the position of each logger was recorded relative to the top of the rock anchor. The loggers were then downloaded and relaunched.

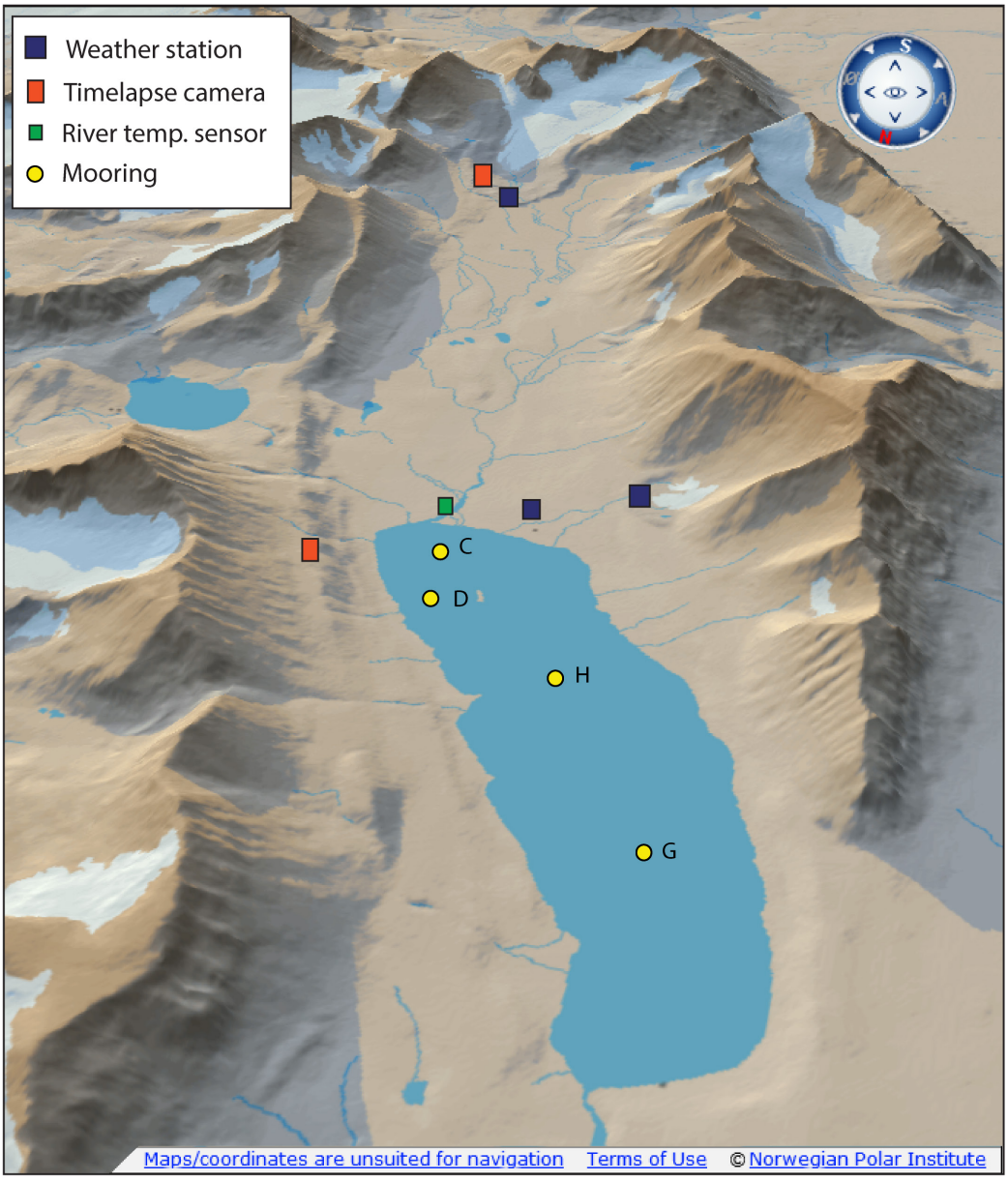

Figure 2.1: A 3D rendering of Linnédalen showing the position of the data sources. Weather Station encompasses both the main station and the two temperature loggers on the LIA moraines. Scale varies with perspective (toposvalbard.npolar.no). Moorings are retrieved and deployed, annually, at all sites during July. Additional springtime moorings are deployed at sites C, D, and H.

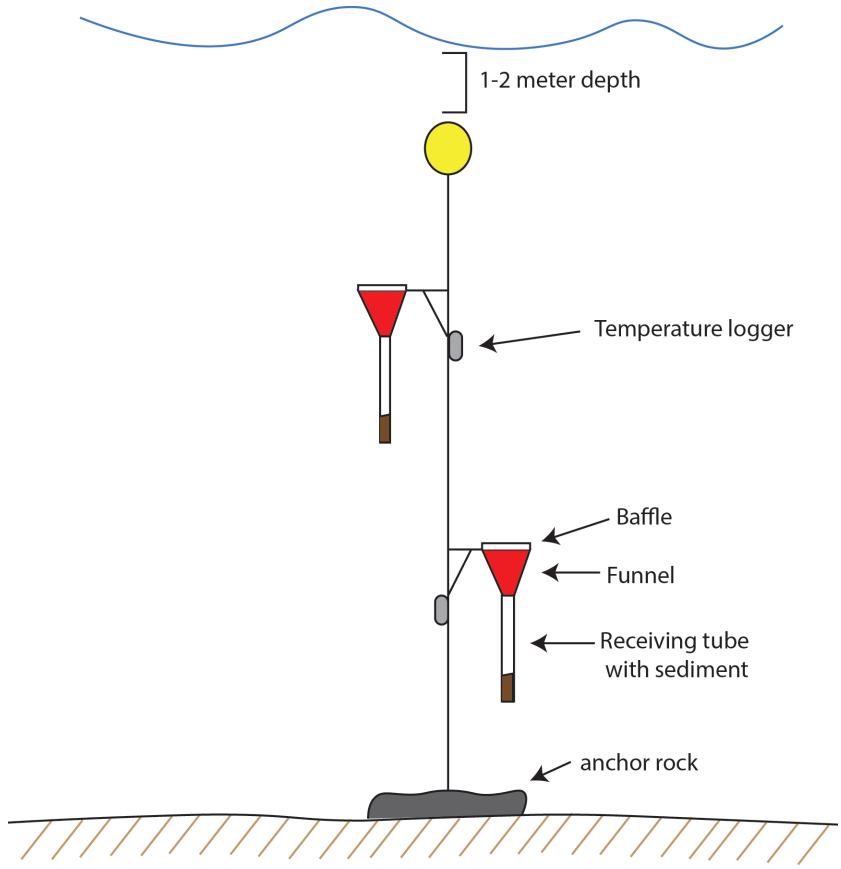

Figure 2.2: A diagram of the mooring setu[used in this study (adapted from Arnold, 2009).

After the samples settled, the receiving tubes were cut 3-5 cm above their sediment water interface, allowing the excess water to be drained and facilitating easier transport of the tubes (Figure 2.4). Zorbitrol Plus®, a highly absorbent acrylic acid polymer sodium salt, was added to each receiving tube in order to stabilize the sediment water interface. Zorbitrol Plus® was added until a white powder remained at the surface of the receiving tubes, and was not subsequently rehydrated. The samples were then capped, taped and carried out of the field. Before shipment to the USA, samples were uncapped, and if the Zorbitrol Plus® was fully saturated, more Zorbitrol Plus® was added, and the samples were recapped. Despite its origin as a powder for cleaning up spills in hospitals, Zorbitrol Plus® has been shown to preserve the sediment-water interface during transportation of sediment cores (Tomkins et al., 2008).

Intervalometer

In July 2014, an intervalometer was deployed near site C, approximately 1 m above the lake bottom. The intervalometer records the timing of sediment accumulation in 30 minute intervals. The intervalometer contains a receiving tube positioned in-between a series of LED lights and photo diodes. As the sediment is deposited in the tube, it obscures the LEDs. When the LED light is obscured, a change in voltage is recorded by a HOBO logger (Walther, 2015).

Unfortunately, the intervalometer stopped recording data in mid-February 2015. Therefore there is no data corresponding to the specific timing of spring and summer sedimentation events. Due to this realization, the sediment was removed from the receiving tube. However, the voltage record still provides information about the timing of late summer-fall 2014 sedimentation.

Figure 2.3: H4 shows the construction of each sediment trap, which includes a funnel, a baffle, a support bracket, and a receiving tube - note the sediment in the receiving tube (Photo: Paul Phillips).

Additional Sediment Samples

Sediment receiving tubes collected, as outlined above, in July 2012 and 2014 were also used for analysis in this study.

Temperature loggers

Characterizing water column temperature is important for the determination of the flow dynamics of sediment in the lake. Temperature loggers were attached to all of the moorings (Figure 2.1) and at two points along Linnéelva in 2014. Spring moorings were deployed with temperature loggers located at 3 m. intervals in order to better characterize water column densities during spring and early summer sedimentation events. In Linnéelva one logger was located at the midpoint and the other near the mouth of the river. These temperature loggers were retrieved in July 2015, downloaded in the field, and redeployed.

TROLL CTD

Two In-situ 9000 XP/e Troll instruments were deployed in April 2015. They were positioned 1 m above the lake bottom on the spring C and spring H moorings. From April 2015 until July 2015, the Troll CTD instruments were meant to recorded the water temperature, pressure, turbidity, dissolved oxygen and conductivity at one minute intervals, one meter above the lake bottom. However due to an issue with their deployment, this data is not available.

Time-lapse photography

Three automated time-lapse cameras were situated in Linnédalen (Figure 2.1). Two cameras were located on a ridge above the eastern shore of Linnévatnet. One faced up-valley towards Linnéelva, and the other camera faced down the lake. Each camera took two photos a day. These images allow for the visual inspection of conditions such as observing sediment plumes in the lake. A third camera is situated on the lateral LIA moraine of Linnébreen overlooking the glacial forefield.

Figure 2.4: Receiving tubes were packaged for transport out of the field. Excess tubing was sawed off, and Zorbitrol was added. The receiving tubes were then capped, labeled, taped and packed out of the field. (Photo: Mike Retelle)

Weather data

Temperature and Precipitation:

Svalbard is home to one of the longest observational weather records in the Arctic (Førland et al., 1997). The weather station at Longyearbyen Airport (LYR) has been recording temperature and precipitation data for over 100 years. LYR is located approximately 80 km in-fjord from the study site. A second weather record is available from Isfjord Radio near the mouth of Linnédalen. The Isfjord Radio record provides weather and precipitation data back to the 1930's. These data sets were downloaded from eklima.met.no (Norwegian Meteorological Institute).

Near the south shore of Linnévatnet, an ONSET HOBO U30 main weather station (Figure 2.1) is located near the southern shore of the lake. Its record extends back to the mid-2000's. The station logs air and ground temperature, precipitation, wind speed and direction, relative humidity and incoming and reflected radiation at a 30 minute sampling interval. During the fall, the station malfunctioned and stopped logging data (9/18/2014 2:00:00 AM). The station was not repaired until April 29th 2015. This 'gap' in the temperature and precipitation record was reconstructed using back-up loggers independent of the weather station. For example, an second Onset RG-3M rain gauge recorded the timing of "precipitation events". Each event corresponds to the deposition of 0.2 mm. of rainfall. The total rainfall associated with each storm precipitation event was calculated as follows: # of events X 0.2mm = precipitation (mm). The spacing of the timing of these events was used to establish a precipitation record between September 2014 until April 2015. A reconstruction of the wind data was not possible during the gap.

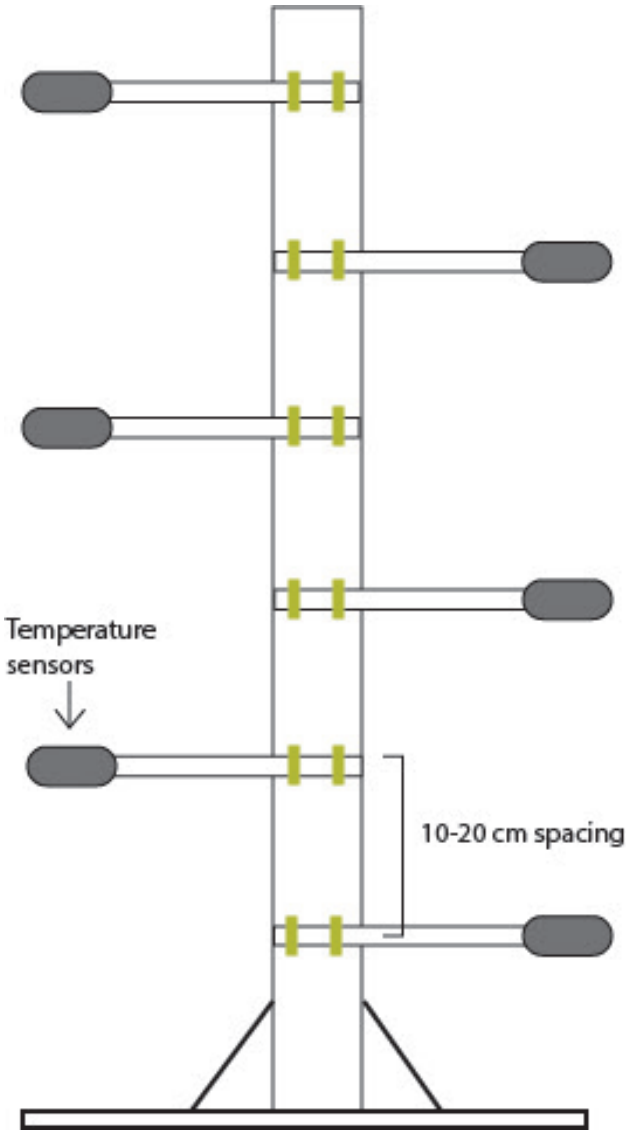

Figure 2.5: Schematic diagram of a snow tree. The light/temperature loggers face towards the ground.

Snowpack

Snow depth and snowpack temperature measurements were recorded using a snow tree designed by Prof. Steve Roof. The snow tree (Figure 2.5) is a 1.0 m tall post with a series of cross bars attached to downward facing HOBO pendant light sensor/temperature loggers. These cross bars were spaced at 10 cm. (lower valley) or 20 cm. intervals (mid-valley). When the loggers are buried in the snow, they were no longer exposed to the ambient light and air temperature. This change in the temperature allows snow events to be constrained. Additionally, the changes in the snowpack temperature are recorded at different depths. This allows for the determination of when the snowpack becomes isothermal and tracking its melt progress throughout the ablation season.

Lab Methods

The bottom-most available receiving tube from each mooring was analyzed for grain size, geochemical composition, and magnetic susceptibility. Peter Beach, the shop mechanic at Bates College built an apparatus for cutting the sediment receiving tubes (Figure 2.6). The tubes were scored on either side, without penetrating to the sediment layer. The scoring was to prevent the disruption or contamination of the sediment by the saw blade. Then using a flat head screwdriver, the cores tube separated into two halves. Finally a length of fishing-line was pulled lengthwise across the tube in order to split the sediment sample. The receiving tubes were logged and photographed. The better half of the sample was stored as an archive half and used for non-destructive analyses. The working half was used for grain size analysis.

Grain size

The working half of the receiving tubes were continuously sampled at 0.5 cm intervals. Continuous sediment samples were prepared following Dowey (2013). Each 0.5 cm thick slice of sediment was transferred to a 47 mL Oak Ridge centrifuge tube. Enough hydrogen peroxide (H_2O_2) was added to each centrifuge tube to cover the sediment. The samples were then partially capped, and allowed to sit overnight in order to disintegrate any organic matter (Dowey, 2013). At least 12 hours later, 20 mL of deionized water and 17 ml of dispersant (0.7 g/L sodium metaphosphate) were added to each sample. The samples were then shaken with a Vortex Genie 2 for 1 minute and sonicated with a Fisher Science Sonic Dismembrator 60 for 1 minute. Prepared samples were immediately loaded into a Coulter Laser Particle Size Analyzer. The Coulter LPSA uses diffracted laser light to calculate the grain size distribution of the

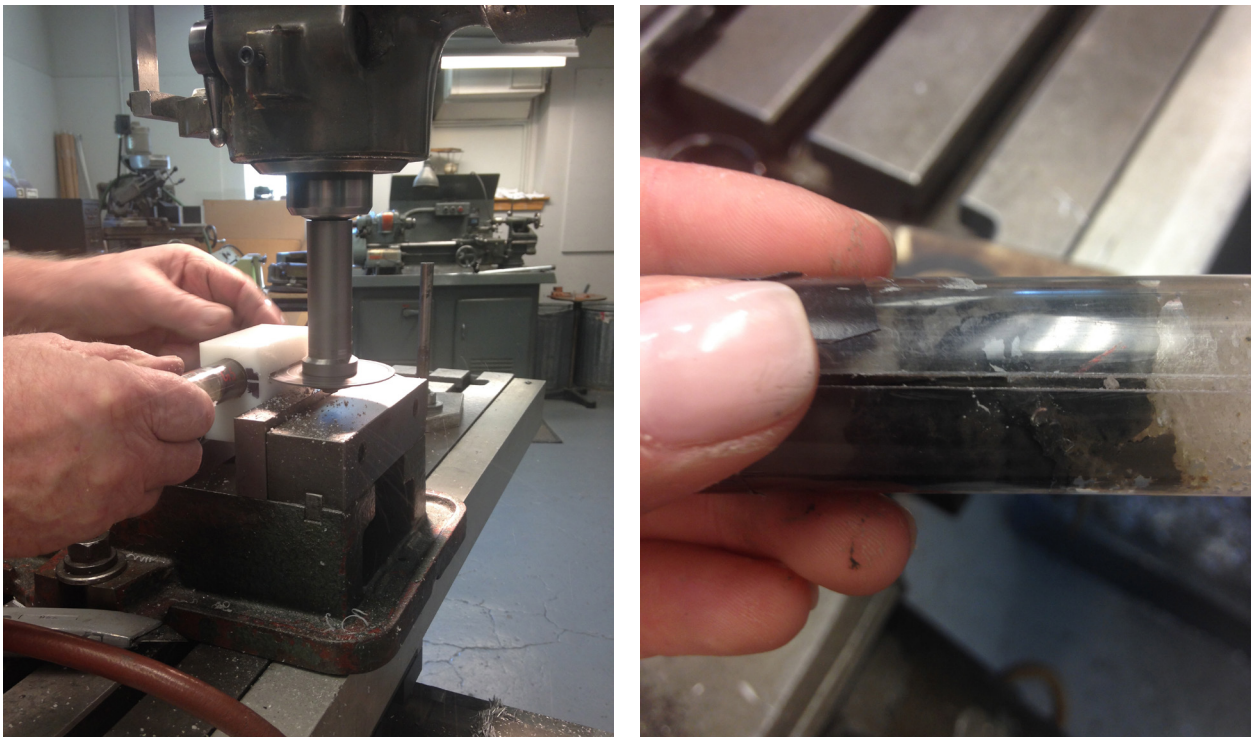

Figure 2.6: (a) The drumel-like apparatus used for scoring the plastic on the receiving tubes. (b) The scored side of a receiving tube. The tubes were not split open by the saw in order to minimize the impact of plastic fragments in later analyses.

entire sample. Each sample was run 3 times, and the mean grain size information was recorded for each run. Generally, the third run was used to characterize the sediment grain size due to increasing efficiency of the sonic dismembrator in breaking up particle aggregates or flocs. Mean, Median, 10th and 90th percentile values were determined in each analysis.

Magnetic Susceptibility

Magnetic susceptibility (MS) is a common analysis used to examine sediment cores (Røthe et al., 2015; van der Bilt et al., 2015; Rubensdotter and Rosqvist, 2009). It is a measurement of the ability of a material to become magnetized, and is a property related to a sediment lithology (Hall, 1998). The MS of the sediment traps was obtained using a Bartington MSE2 sensor. The sensor was set to 0.1 SI units, and the measurements were recorded in the Multisus software. Measurements were taken every 0.5 cm. These measurements were not corrected for drift, however the sensor was re-zeroed every 5 measurements. Each sample was measured twice and the resulting MS measurements were averaged.

Geochemical analysis

The geochemical structure of each sediment trap was examined through X-ray Fluorescence (XRF) analysis. XRF analysis has been used for high temporal paleohydrological and paleoclimatological interpretations in varved lacustrine sediment cores (Cuven et al., 2015; Van der Bilt et al., 2015; Bakke et al., 2009). The Cox ITRAX XRF Core scanner (Figure 2.7) located at the Ronald B. Gilmore XRF Laboratory, University of Massachusetts Amherst was used to carry out this analysis. The ability of an ITRAX scanner to obtain sub-millimeter precision non-destructive geochemical data has made it a good choice for lacustrine sediment provenance studies (Cuven et al., 2015).

Figure 2.7: An example of loading a sediment core into the ITRAX Core Scanner (BOSCOF, 2012).

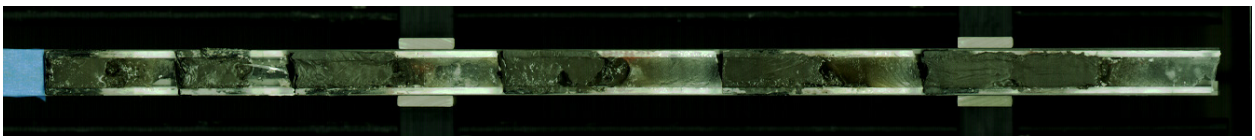

Figure 2.8: RGB image of the sediment trap retrieving tubes obtained with the ITRAX scanner.

All receiving tubes were loaded with the top of the sediment facing towards the machine. The machine required two scans to process a sample (Croudace et al., 2006). The first scan obtained an RGB image (Figure 2.8), a radiograph, and a laser triangulated surface topographic profile. The radiograph was obtained with a voltage of 50 kV, a current of 45 mA and an exposure time of 500 ms. Once the first scan was completed, the core was returned it its original loading position. A thin plastic film is then placed over the sample inorder to prevent the samples from drying during the slower secondary run. The ITRAX was then programed to perform an XRF scan of each sample by selecting start and end points from the RGB image corresponding to the top and bottom of each sediment trap. The system then ran a second scan and obtained the XRF data. XRF measurements were obtained with 10 second exposures in 500 micron steps. The X-Ray excitation parameters were selected based on the radiographic image. A molybdenum (Mo) tube was used to produce X-rays with a voltage of 30 kW and a current of 55 mA. The topographical profile created during the first scan of the sediment traps was used by the ITRAX XRF detector (Figure 2.9) to maintain a consistent height above the sediment (Croudace et al., 2006).

XRF data needs to be normalized or treated with care. The resultant geochemical data is semi-quantitative because the results can vary with changes in bulk density and water content (Rothwell and Croudace, 2015). Raw XRF profiles can be compared within a singular core however across core comparisons were qualitative (Cuven et al., 2015). 52 different elements were examined for each trap. Elements at the low end of the Mo tube's sensitivity range (Al-U) produced noisy profiles. Data can be normalized by dividing the intensity counts of the element in question by those of a conservative element. For example, the counts of Ca were divided by the counts of Ti.

Analytical processing

Principle Component Analysis

Principle component analysis (PCA) is useful for examining multidimentional relationships in 2D. PCA searches for a few uncorrelated linear combinations of the original variables that capture most of the information (Dunteman, 1989). The goal of PCA is to try to explain the deviation in a set of observed variables from the total variance. Thus, the principle component (PC) is a derived variable which maximizes the variance in the original observed variables (Dunteman, 1989). The first PC (PC1) is a new coordinate axis in the variable space which is oriented such that it maximizes the deviation of the projections of the points along the new coordinate axis, making it approximately equivalent to a line of best fit. The second PC (PC2) is orthogonal to PC1 and best describes the remaining variation. The analysis produces the same number of PCs as input variables; i.e. examining 5 variables will result in 5 PCs. However, the first few PC typically describe the majority of the variance and thus are the focus of analysis (Dunteman, 1989). Accordingly, the first two PCs have the highest possible sum of squared multiple correlations (where p = number of variables and R = a correlation matrix) as described by the equation:

$$\sum_{i=1}^{p} {R^2}_{xi} \times y_1, y_2 \qquad \text{(Dunteman, 1989)}$$

PCA was run on 10 original variables (Al, Si, K, Ca, Ti, Mn, Fe, Rb, Sr, Zr) in SigmaPlot 13. The data was log transformed prior to PCA in order to minimize the variation between the units of each variable. Only the resultant PC1 and PC2 component loadings were used for further examination.

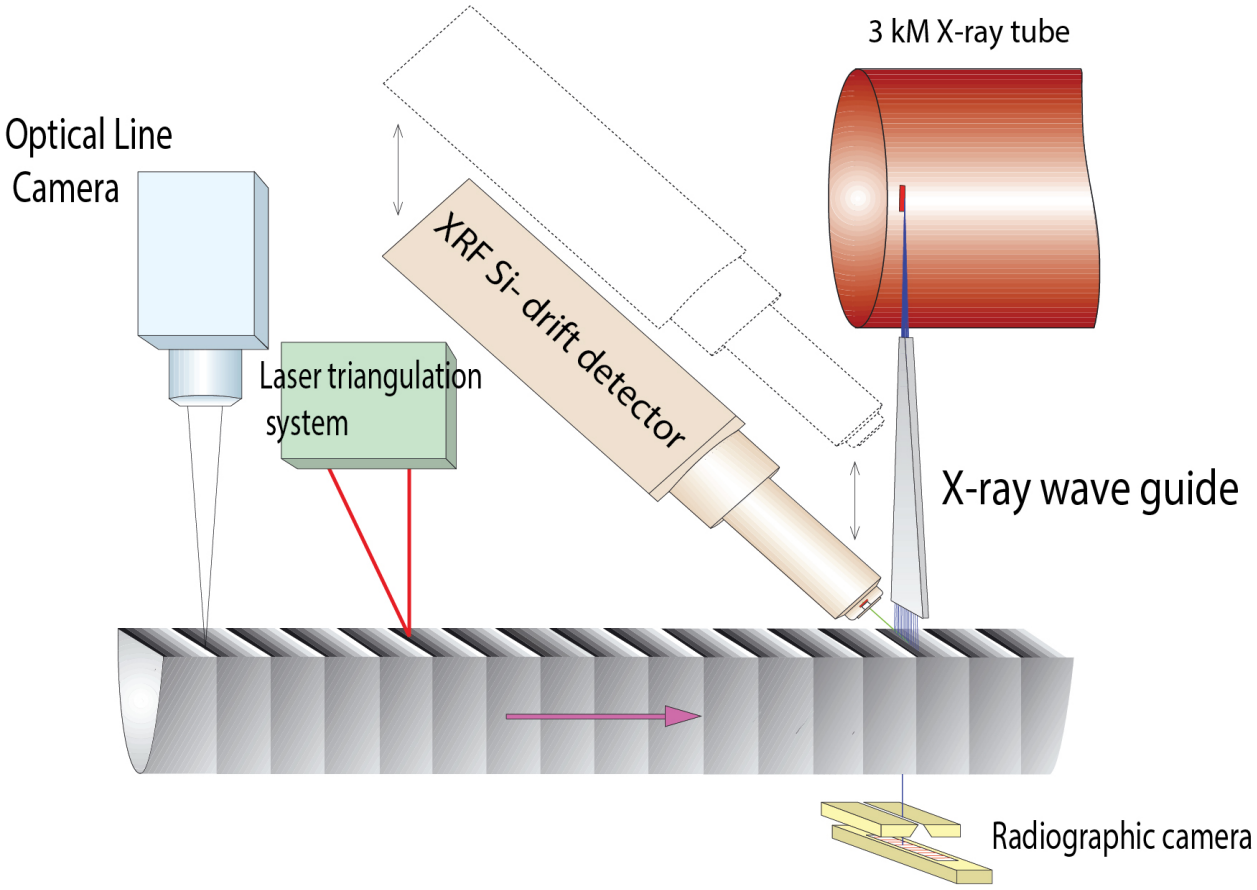

Figure 2.9: Schematic diagram of the ITRAX core scanner. The first run of the ITRAX scanner obtains an optical image, an X-Ray Radiograph and a sediment surface profile by laser triangulation. The Si-drift detector moves up and down in accordance to the surface profile in order to maintain a consistent distance of the detector and sample surface (Modified from Croudace et al., 2006).

Chapter 3

Results

Sediment Receiving Tube Stratigraphy

There is a distinctive vertical partitioning of the sediment texture and relative geochemical composition in each receiving tube (Figure 3.1). In the section below the sediments from each receiving tube are divided into units based on changes in grain size and general trends across the elemental profiles.

It should be noted that incongruencies between geochemical data and grain size or magnetic susceptibly is due to the exclusion of sampling points exhibiting low validity (validity =0) or total counts (<1600 kcps). Additionally, grain size measurements are presented as the center of their 0.5 cm continous-sampling interval, thus resulting to a slight offset of 0.25 cm between a grain size and magnetic susceptibility.

2014-2015 Sediment Budget Year

C4_15

Visual Stratigraphy

C4_15 is 9.6 cm long, the bottom of the sediment trap is a dark mud and homogeneous in appearance (Figure 3.2). From 8.3-6 cm the sediment is visibly coarser with an erosive base. The next two cm are a homogeneous mud. The upper 4 cm consist of a blackish (5y 2.5/2) bedded coarse grained layer and an undulating base.

Grain Size and Geochemical Composition

C4_15 is divided into four units based on grain size and chemical composition (Figure 3.2).

Unit IV (9.5 to 5.75 cm), corresponding to a peak in grain size, exhibits a relatively low average ratio of Fe/Ti (23.8) with a decreasing trend, while zirconium, silica and calcium exhibited a relative increase. Zirconium and silica shows an initial increase from the base to 8.1 cm, followed by a saw tooth pattern of peaks and troughs. There appear to be two background curves from 8.1 cm to 7.15 cm and from 7.15 cm to 5.85 cm, however there is an overall decreasing trend from 8.1 cm to 5.85 cm. Calcium and the Ca/Ti ratio show similar increasing trends from the base until 6 cm.

Unit III (5.75 to 4.40 cm), corresponds to another peak in grain size and MS, and is characterized by an increase in the ratio of iron to titanium, a decrease in zirconium and silica, and a peak in calcium at 5.4 cm and Ca/Ti has peaks at both 5.4cm and 4.85 cm.

Unit II (4.40-3.75 cm) exhibits a small median grain size and low MS readings. There is a peak in Fe/Ti followed by a sharp decrease, relatively low and then sharply increasing zirconium and steadily increasing Si. Calcium and Ca/Ti have a small peak at 4.25 cm.

Unit I (3.75-0.0 cm) exhibits a gradual peak in grain size and MS, corresponding to a low ratio of iron to titanium. Zirconium and silica kcps were relatively high, but began to decrease from 0.75 cm to the surface, following the decreasing grain size. Calcium and the ratio of calcium to titanium show 3 clustered regions of similar values: 3.75- 2.85 cm, 2.80-1.70 cm, and a peak from 1.65-0.75 cm. Throughout C4_15, but particularly in unit I, Ca/Ti exhibits a generally more peaked profile than Ca.

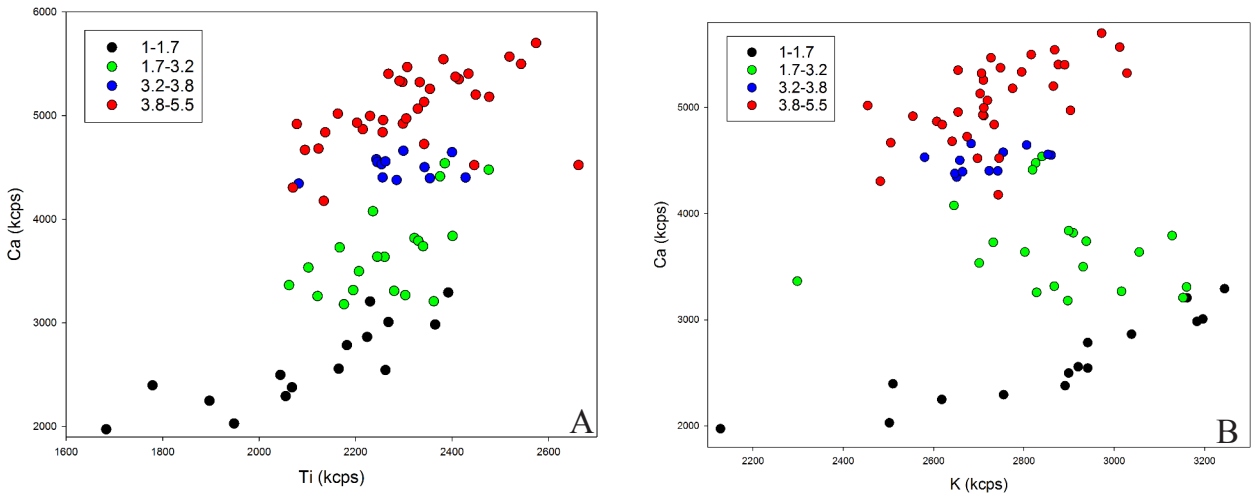

Figure 3.1: Scatter plots of the elemental content (kcps) suggest a change in elemental composition between visual stratigraphic units. This is best exemplified in receiving tube D4_15. Points are grouped by the depths (in cm) of changes in the visual stratigraphy observed in D4_15.

D4_15

Visual Stratigraphy

D4_15 is 5.5 cm in length and predominantly characterized by a series of alternating lighter and darker layers (Figure 3.3). The bottom 1.7 cm consists of light colored homogeneous mud, with subparallel bedding from 4.0-4.5 cm. This was topped by a visibly coarse layer, from 3.8-3.7 cm, with an undulating upper boundary. Above the undulation, a 0.5 cm dark bed was overlaid by a lighter bed from 3.2 cm to 2.8 cm, and a dark coarse bed from 2.8 cm to 1.7 cm. This was followed by very thinly laminated light and dark layers from 1.7-0.9 cm, followed by a lightly colored 0.2 cm bed with a homogeneous texture. Finally, the upper 0.7 cm are described as a black mud (5y 2.5/2) with a disturbed sediment surface.

Grain Size and Geochemical composition

D4_15 is also divided into 4 units (Figure 3.3).

Unit IV (5.5 cm to 4.5 cm) had a decreasing grain size and a peak in MS. The ratio of Fe/Ti exhibits some variability but little overall change. Zirconium decreased from the base until 5.25 cm, and then peaked at 4.9 cm. Silica first peaked at 5.45 cm and then again at 5.0 cm and 4.85 cm. Calcium shows a general increase at 5.25 cm, however Ca/Ti shows a more peaked increase.

Unit III (4.5 cm to 2.75 cm) corresponds to a general increase in grain size and decrease in MS. Within unit III there are 2 peaked areas of Fe/Ti, one from 4.5 cm to 3.85 cm, and a second from 3.85 to 3.00 cm. The trough between these two peaks corresponds to a peak in both Zr and Si. Silica increase more than Zr, and appear slightly offset within unit III. There is one apparent peak in calcium from 4.3 cm to 3.9 cm, however the relationship between calcium and titanium exhibits a more peaked profile.

Unit II (2.75 cm to 1.25 cm) corresponds to a peak in grain size, and shows a general increase in the ratio of Fe/Ti as well as Zr. Silica, calcium and Ca/Ti all exhibit a decreasing trend, with silica and Ca/Ti being more peaked than calcium alone.

Unit I (1.25 cm to 0.0 cm) is missing elemental data due to the sloping sediment surface at the top of the sample (Figure 3.6). This uneven surface resulted in non-valid measurements. Unit 1 starts begins with a relatively constant grain size of 11.2 microns followed by a decrease from 0.25 cm to the surface.

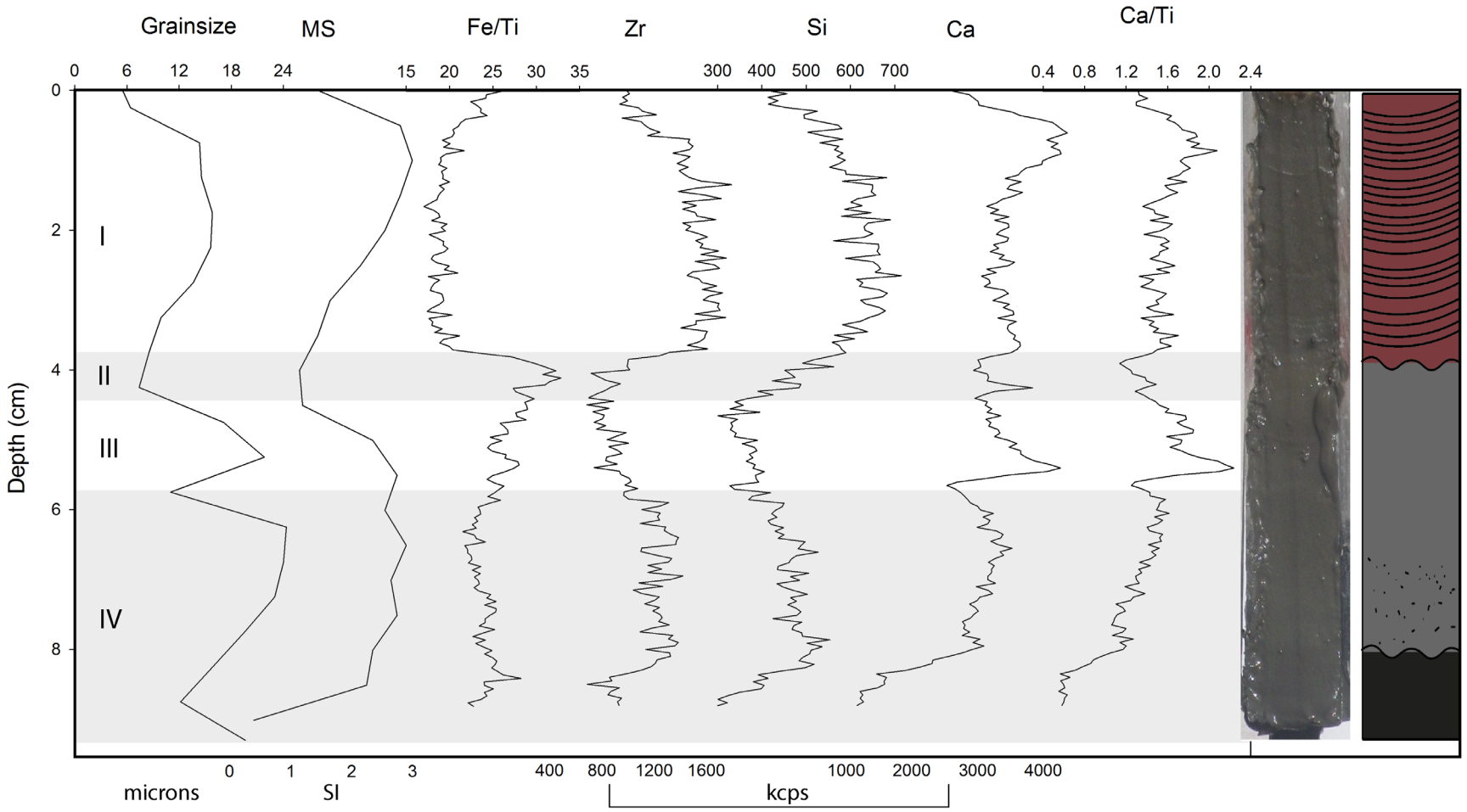

Figure 3.2: Composite log of receiving tube C4_15. Units are divided based on grain size and Fe/Ti.

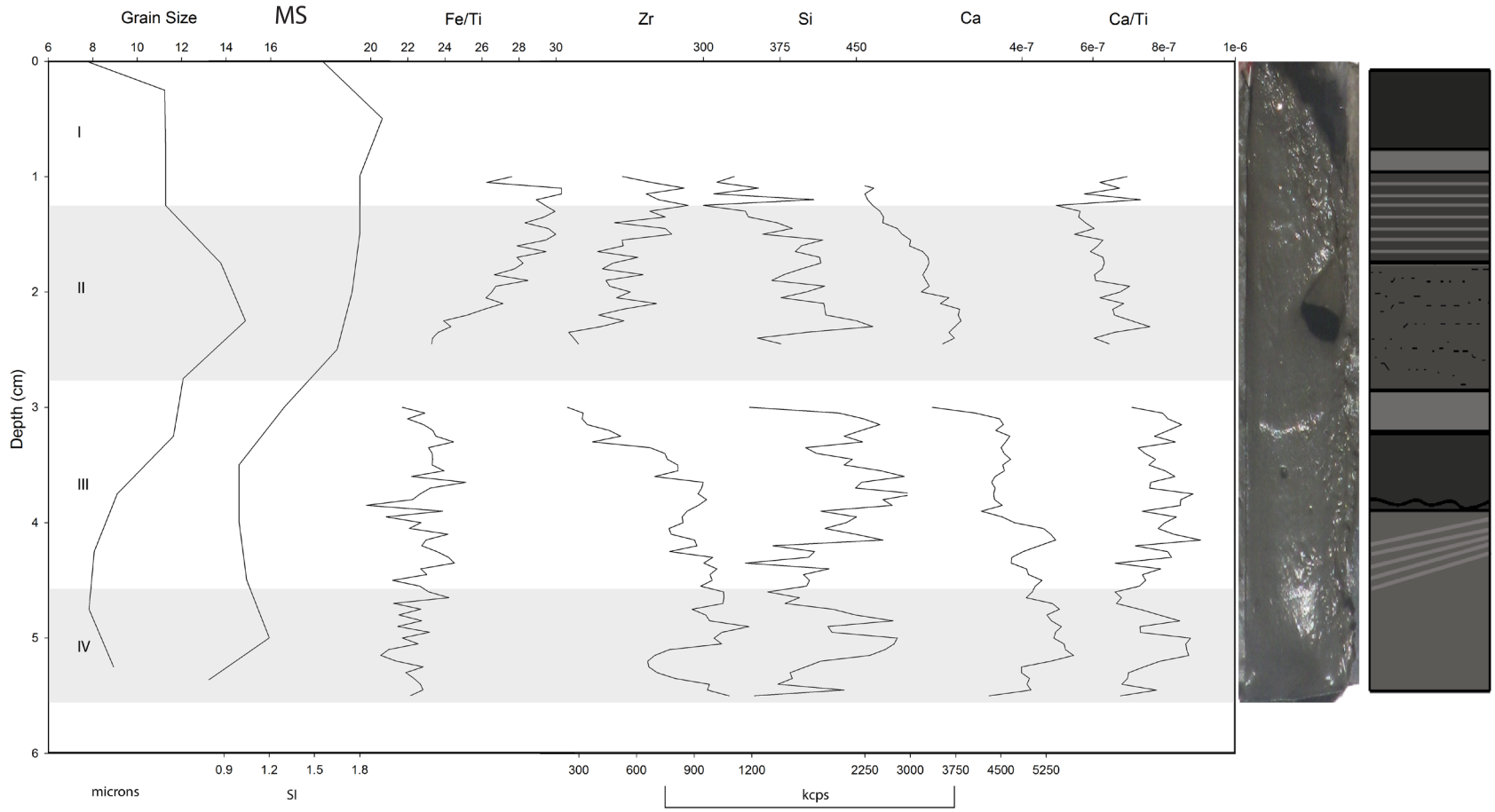

Figure 3.3: Composite log of receiving tube D4_15. Units are divided based on grain size and Fe/Ti.

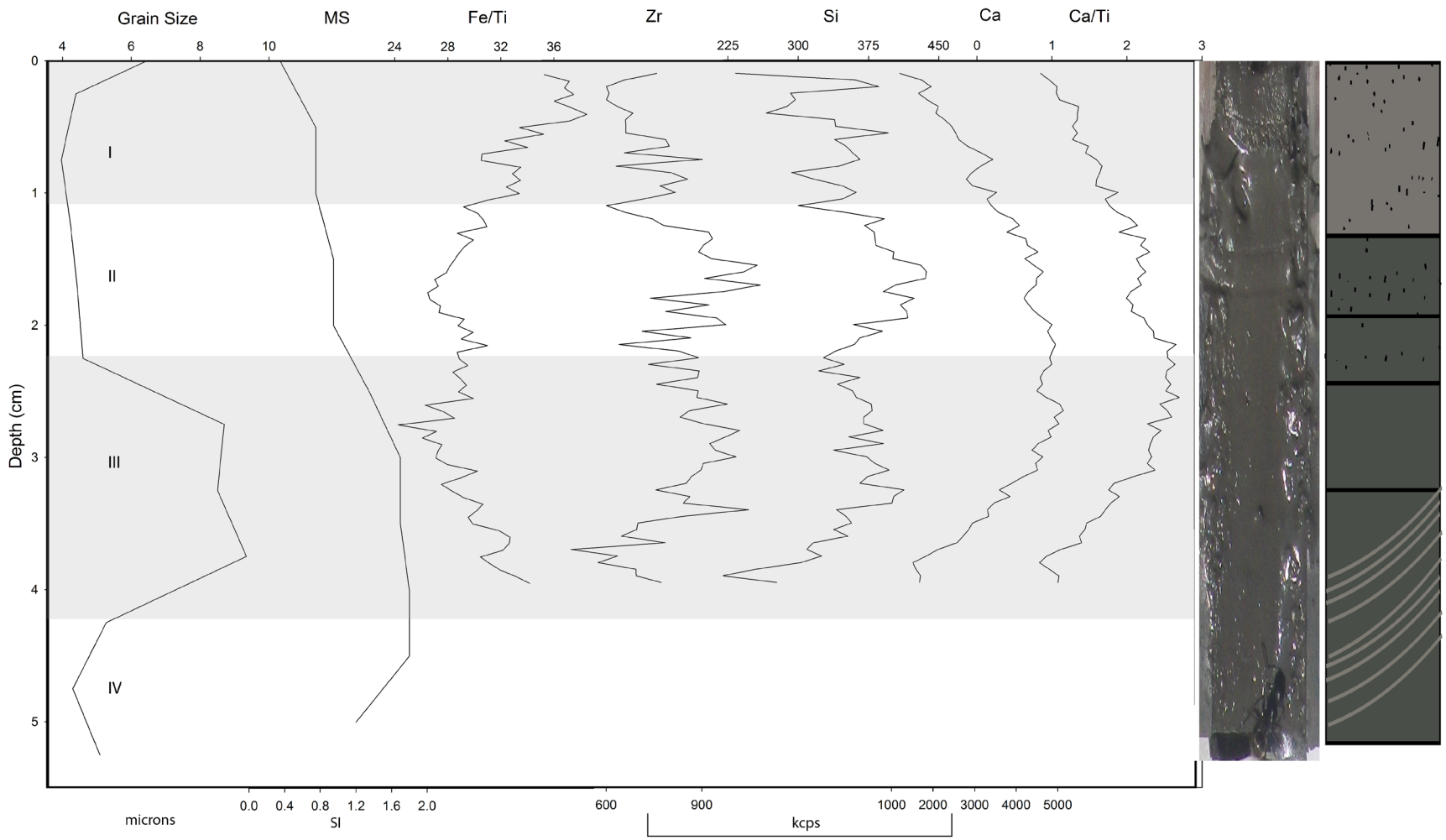

Figure 3.4: Composite log of receiving tube H5_15. Units are divided based on grain size and Fe/Ti.

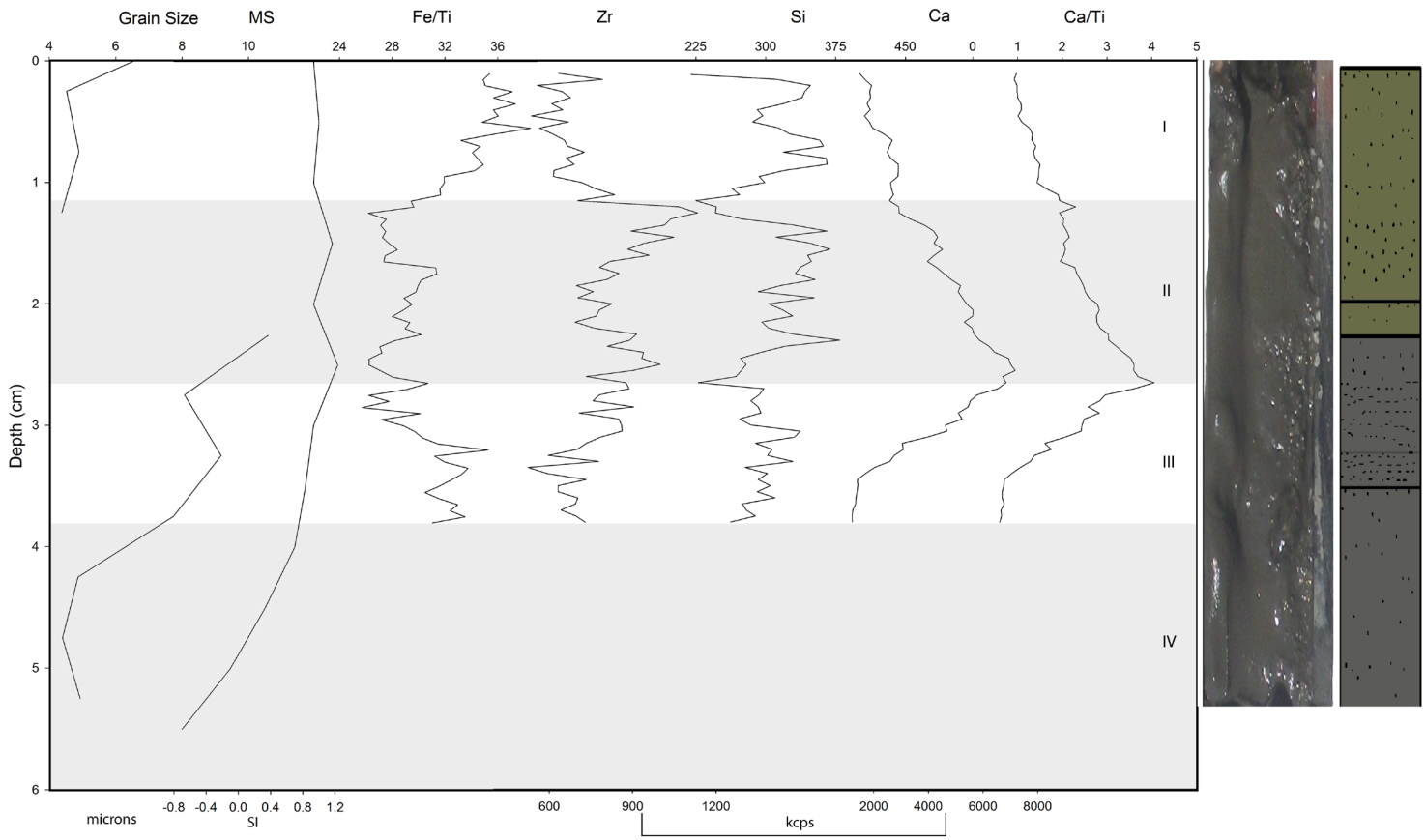

Figure 3.5: Composite log of receiving tube G5_15. Units are divided based on grain size and Fe/Ti.

H5_15

Visual Stratigraphy

The bottom 2.1 cm of H5_15 is a black (5Y 2.5/2) mud with faint inclinded bedding (Figure 3.4). The following 1.9 cm is also a black mud, but contains black specks that show an upwards increase in abundance. The upper 1.3 cm of H5_15 is a very dark gray (5y 3/1) mud with black specks.

Grain Size and Geochemical Composition

H5_15 again was divided into four units (Figure 3.4).

Unit IV (5.25 cm to 4.25 cm) is characterized by a decreasing in grain size. There is no geochemical data associated with this unit.

Unit III (4.25 cm to 2.25 cm) corresponds to 2 peaks in grain size and increased MS measurements. It exhibited a consistent decrease in Fe/Ti. Additionally, counts of Zr decrease from 3.95 cm to 3.70 cm and then increase to peak at 3.40 cm. Si, Ca, and Ca/Ti all show an increasing trend in unit III.

Unit II (2.25 cm to 1.1 cm) consists of a small median grain size (3.5 microns) and a slight peak in MS. Fe/Ti increase while Ca shows an overall decreasing trend. This corresponded to elevated counts of Zr and Si.

Unit I (1.1 cm to 0.0 cm) has an increase in grain size, a decrease in MS and a general increase in Fe/Ti, and a general decrease in Ca. Zr peaked from 1.0 cm to 0.5 cm and Si peak at 0.55 cm and 0.20 cm.

G5_15

Visual Stratigraphy

Sediment trap G5_15 is 5.5 cm in total length (Figure 3.5). The bottom 1.9 cm consists of a homogeneous black mud (5y 2.5/2), followed by 1.3 cm of differently textured sediment with stripes of black grains. Fine-grained dark olive gray (5y 3/2) mud, from 2.3 cm to 2.0 cm, is topped by coarser grained bed containing black specks.

Grain Size and Geochemical Composition

G5_15 is also divided into four units (Figure 3.5).

Unit IV (5.5 cm to 3.8 cm) is defined by a relatively fine median grain size and increasing MS measurements. There is no geochemical data available from 3.80 cm to the base.

Unit III (3.8 cm to 2.65 cm) corresponds to a peak in grain size, a more gently increasing MS measurement, and decreasing Fe/Ti. Zr shows a general increase and Si remains fairly constant but peaked. Ca/Ti and Ca increase sharply, with Ca increasing by approximately 7000 kcps.

Unit II (2.65 cm to 1.15 cm) covers a gap in the grain size record, but shows both a decrease and a local peak in MS readings. The trough of the MS readings corresponds to an elevated Fe/Ti ratio, while the peaks in MS correspond to peaks in Zr. Silica shows slight inverse relationship with Zr. Calcium and Ca/Ti both show a decrease throughout unit II.

Unit I has a small median grain size, followed by an increase of ~2 microns from 0.25 cm to the top. The fine grain size corresponds to an elevated Fe/Ti ratio, a decreasing Zr trend, and decreasing Ca. The Si appears to correspond to changes in grain size.

2013-2014 Sediment Budget Year

All 2014 samples were split over one year ago, resulting in drier and sometimes cracked sediment.

C3_14

Visual Stratigraphy

C3_14 is 24 cm in length and exhibited cracks at 0.8 cm, 1.9 cm, 5.3 cm, 6.6 cm, 8 cm, 8.9 cm, 10.1 cm, 10.9 cm, 12.8 cm, 15-15.6 cm, 17-17.2 cm, 18.8 cm, 20.3-20.8 cm and 23-24 cm. In general, the base of the core was drier, resulting in dry crumbling homogeneous mud from 24-22 cm. 22-20.5 cm was dark gray in color and appeared to retain some moisture. 20.5-18.1 cm exhibits a change in color and from 18.1-17.5 cm there is a change in texture, becoming coarser in appearance. From 17.5 cm until 5.6 cm is a dark gray homogeneous mud containing a depression extending from 17-9 cm. 5.6-4.4 cm consists of interspersed coarser grained sediment, followed by a homogeneous mud from 4.4-4.0 cm. From 4.0 until 3.3 there are a series 0.05 cm thick coarse laminations with a gritty appearance; one at 3.9cm, the seconds at 3.7 cm, and the third at 3.3 cm. The top 3.3 cm are a dark gray mud (10YR 4/1) with a coarser grayish brown (10YR 5/2) bed extending from 0.7-1.0 cm.

Grain Size and Geochemical Composition:

C3_14 was divided into five units (Figure 3.6).

Unit V (23.75 cm to 17.75 cm) was defined by the both the grain size and the lack of geochemical data, due to cracks in the sediment. These cracks resulted in infinite values for the constituents, and thus were excluded. Unit V has two instinct areas of increased grain size.

Unit IV (17.75 cm to 12.75 cm) exhibits two increases in median grain size. Fe/Ti shows a parabolic decrease, Zr shows an initial increase alternating to a decreasing trend. Si, Ca and Ca/Ti all exhibit an increasing trend.

Unit III (12.75 cm to 5.75 cm) is predominantly characterized by the steady relationship between iron and titanium. The decreasing grain size trend has two peaks at 8.25 cm and 6.75 cm. Zr, Si, and Ca follow the same trend. First they are decreasing, then there is a sudden increase at 9.4 cm, followed again by an overall decrease in kcps. Ca/Ti did not exhibit this rapid increase.

Unit II (5.75 cm to 2.25 cm) corresponded to the smallest median grain size of the sediment trap. As the grain size dipped, the higher ratios of Fe/Ti was observed. Fe/Ti and Zr appear to be covariant within unit II. Si and Ca both exhibit increasing trends while Ca/ti exhibited a peaked decreasing trend.

Unit I (2.25 cm to 0.0 cm) was defined by a spike in grain size. This grain size peak corresponded to peaks in Zr, Si, Ca, Ca/Ti but also a trough in Fe/Ti.

D3_14

Visual Stratigraphy

Receiving tube D3_14 is 10 cm in total length and contains a series of light (10YR 6/1) and dark (10YR 3/1) layers (Figure 3.7) . The bottom 6.4 cm of D3_14 consists of a banded mud, with a light gray layer at 4 cm. There are gaps in the sediment at 6.3 and 7.3 cm, as well as holes in the sediment near the base from 9-10 cm. From 3.6-2.1 the sediment appeared to be drying out with depth. There is a gap in the sediment from 2.1-1.9 cm followed by wetter dark gray mud from 1.9 cm to 1.2 cm. This is followed by an erosional base and 0.2 cm of lighter colored sediment. The top centimeter is characterized by interlayering of dark mud and coarse sand layers.

Grain Size and Geochemical Composition

Unit V (9.15 cm to 6.85 cm) experienced an increase in Fe/Ti, and a decrease in Zr and Si (Figure 3.7). Ca and Ca/Ti exhibited two areas of peaked values at 8.5 cm and 7.4 cm.

Unit IV (6.85 cm to 4.65 cm) experienced a decreasing trend in Zr, Si, and Fe/Ti. There was a large peak in Ca content centered around 5.8 cm depth.

Unit III (4.65 cm to 3.5 cm) continued the decreasing Zr and Ti trends of Unit IV. Fe/Ti was variable and Ca appeared steady, yet it increased relative to Ti.

Unit II (3.5 cm to 1.80 cm) exhibits a major peak in Ca relative to Ti. Fe also increases relative to Ti. Zr and Si appear to decrease slightly.

Unit I (1.80 cm to 0.0 cm) experienced a decrease in Fe/Ti, and increases in all other parameters, with a peak in Si at 0.5 cm.

H3_14

Visual Stratigraphy

Receiving tube H3_14 shows a prominent separation of 2.8 cm between the sediment and the zorbitrol. It has a total sediment thickness of 7.5 cm and there is a 0.8 cm crack at the base (Figure 3.8). An orange gray mud extended from 6.7 cm to 3.8 cm with coarser sand beds at 6.0 cm, 5.4 cm and 5.1 cm. This is followed by a darker gray mud from 3.8 cm to 1.6 cm. The upper 1.6 cm is also dark orange-gray in color with cracking at the surface due to increasing dryness towards the top.

Grain Size and Geochemical Composition

From the base of H3_14 to the start of Unit IV the grain size increased (Figure 3.8).

Unit IV (6.0 cm to 4.25 cm) exhibits a decrease in grain size, but an increase in Fe/Ti. Zr appears to be relatively constant and Si appears to increase. Ca and Ca/Ti both show a large increase, but Ca/Ti appears more peaked.

Unit III (4.25 cm to 2.75 cm) is characterized by a small median grain size, a steadily decreasing Ca content and an increase in Fe/Ti.

Unit II (2.75 cm to 1.25 cm) was characterized by an increase in grain size, and a general peak in Fe/Ti. Zr content was relatively stable, and silica showed an increasing trend. There is an increase in Ca content at the bottom of the unit.

Unit I (1.25 cm to 0.0 cm) contains a large peak in calcium at the bottom of the unit, and a second peak in calcium at the top of the unit. Fe/Ti decreases while Zr has increasing trend and Si appears to increase but remains variable.

G3_14

Visual Stratigraphy

Similarly to H3_14, G3_14 has also pulled away from the zorbitrol at the surface, leaving a gap of 3.0 cm. The total sediment thickness in sediment trap G3_14 is 6 cm. The bottom 3.2 cm are dry and coarse with a few small fine layers interspersed From 2.8 cm to 1.3 cm, a homogeneous mud appears to have retained more moisture than the layer below.The top 1.3 cm are characterized by dry crumbled sediment. Gaps are present and it has pulled apart from the sides of the receiving tube.

Grain Size and Geochemical composition

G3_14 appears to have 3 distinct units (Figure 3.9).

Unit III (4.75 cm to 3.25 cm) is characterized by a smooth decreasing trend in all parameters except Fe/Ti. Fe/Ti begins a steadily increasing trend, which continues throughout unit II.

Unit II (3.25 cm to 1.05 cm) is characterized by a fine median grain size (<3 microns) and an increasing Fe/Ti ratio. Ca and Ca/Ti are slightly decreasing and low. Zr and Si show a little overall change but have a moderate degree of variability and low kcps values.

Unit I (1.05 cm to 0.0 cm) has a high median grain size, and a decreasing Fe/Ti content. There are two apparent peaks in Ca and Ca/Ti. Si and Zr increase from Unit II to Unit I, but decrease towards the top of the sediment trap.

2011-2012 Sediment Budget Year

C3_12

Visual Stratigraphy

Sediment trap C3_12 has a total sediment thickness of 8.4 cm. The bottom 4 cm are bluish gray in color with drier fissuring sediment from 8.4 cm to 7.0 cm. From 4.4 to 1.0 cm is an orange-gray mud that appears to be fining upwards. This layer is topped by an uneven boundary. The upper centimeter is a homogeneous brown coarse grained layer.

Grain Size and Geochemical composition

C3_12 was divided into four units (Figure 3.10)

Unit IV (9.5 cm to 5.75 cm) exhibits a peak in all elemental profiles corresponding to increased grain size from 7.0 cm to 6.0 cm.

Unit III (5.75 cm to 3.70 cm) corresponds to fine-grained sedimentation (4.9 microns). The fine grain size corresponds to decreased Ca, but variable Si content.

Unit II (3.70 cm to 1.65 cm) and corresponds to the coarsest grain size (19 microns). Unit II shows an overall increase in Ca, Zr, Si. Iron-titanium ratios show a general decrease throughout the unit.

Unit I (1.65 cm to 0.0 cm) Unit I was characterized by increasing MS, and Fe/Ti but the remaining parameters follow a decreasing trend.

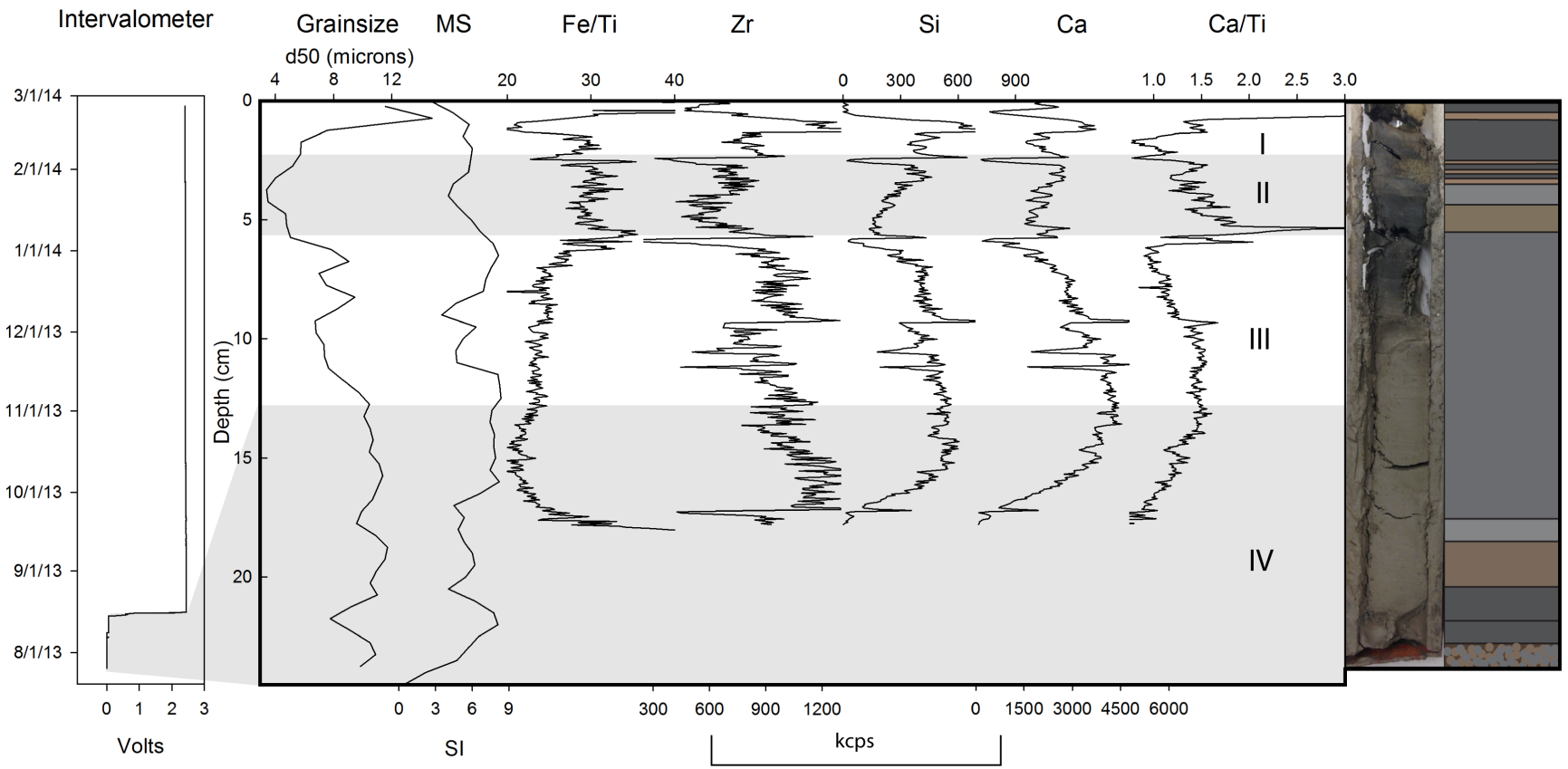

Figure 3.6: Composite log of receiving tube C3_14. Units are divided based on grain size and Fe/Ti.

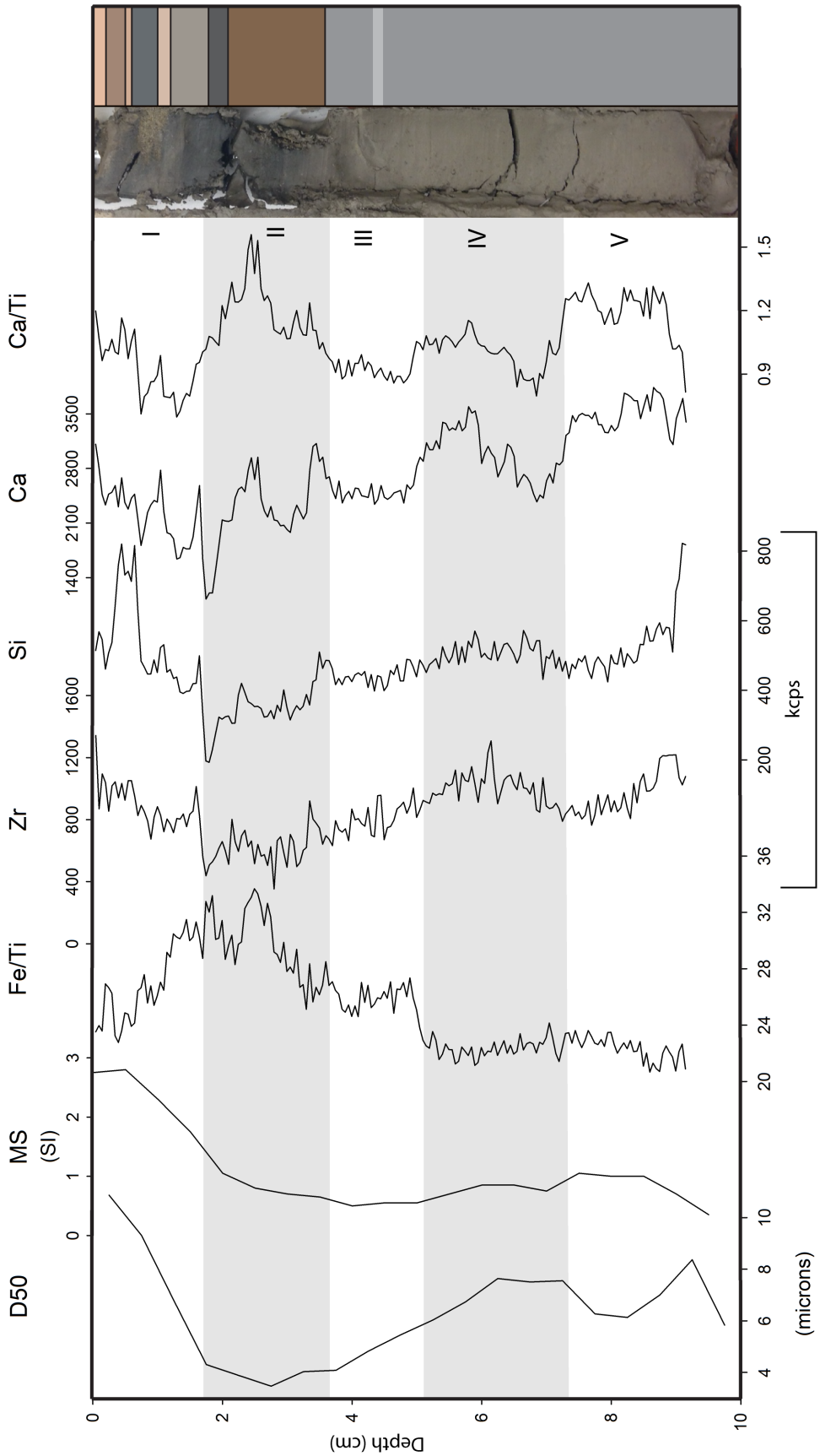

Figure 3.7: Composite log of receiving tube D3_14. Units are divided based on grain size and Fe/Ti.

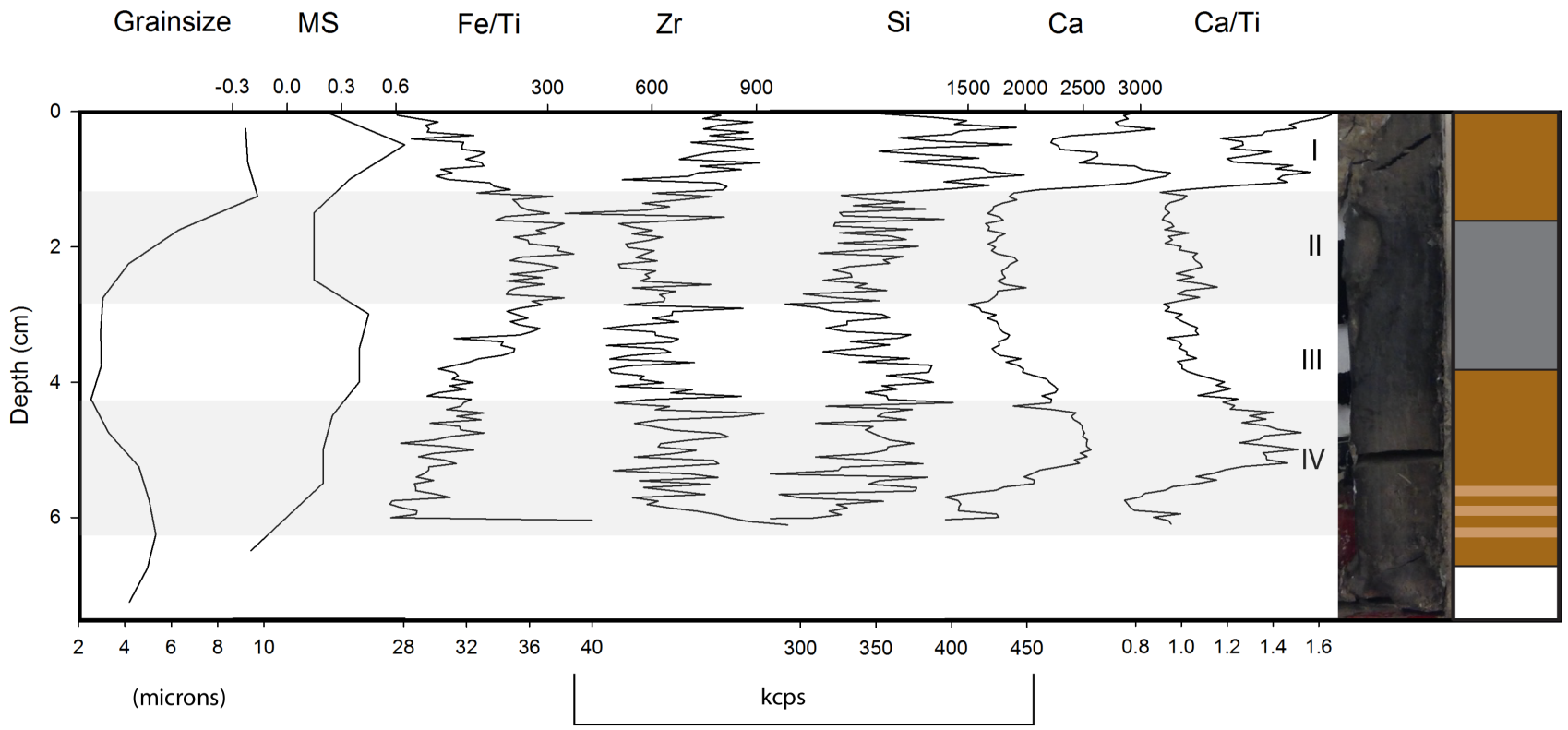

Figure 3.8: Composite log of receiving tube H3_14. Units are divided based on grain size and Fe/Ti.

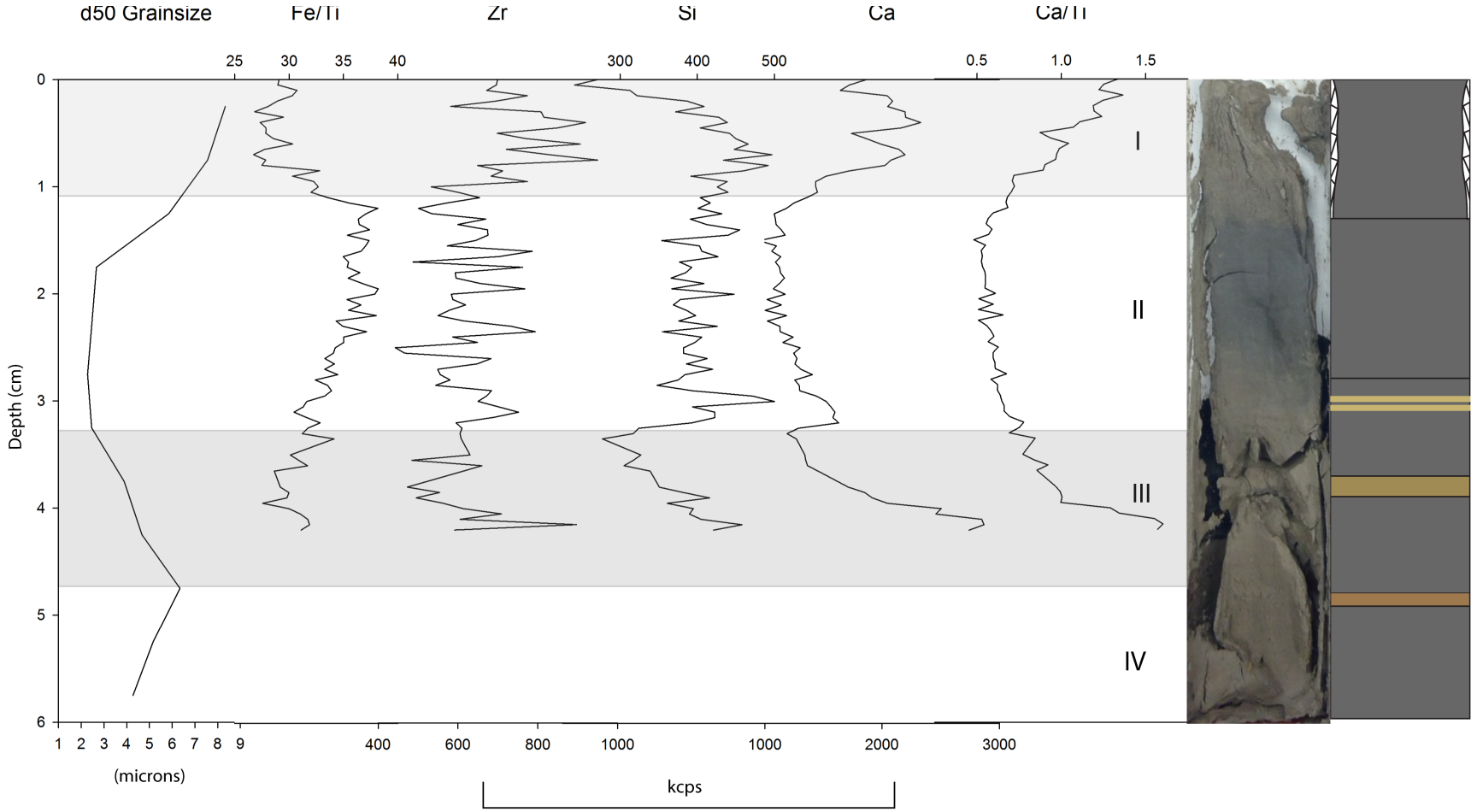

Figure 3.9: Composite log of sediment trap Composite log of receiving tube G3_14. Units are divided based on grain size and Fe/Ti.

D3_12

Visual Stratigraphy

The sediment trap D3_12 is 5.8 cm in total length, and most notable for the presence of a series of coarse red laminations (10 YR 4/2) located at 5.5 cm 1.2 cm, and 0.6 cm (Figure 3.12). From 5.8 cm to 4.1 cm, the sediment was greenish brown in color. This graded into a gray brown layer from 4.1 cm to 1.5 cm. This bed was the wettest sediment in the receiving tube. There is a sharp boundary between the wet gray layer and the visibly coarser green brown layer at 1.5 cm.

Grain Size and Geochemical composition

D3_12 was divided into four units (Figure 3.11).

Unit IV (5.65 cm to 4.70 cm) is characterized by a high Fe/Ti ratio and an increasing trend in the remaining elements.

Unit III (4.70 cm to 2.10 cm), contains two peaks in grain size. These two peaks, 4.25 cm and 2.75 cm, reached a grain size of 8.20 microns and corresponded to general increases in the counts of Zr and Si.

Unit II (2.75 cm to 1.05 cm) corresponds to a slight overall increase in Fe/Ti ratios and to consistent low Zr counts. Ca shows a decreasing and then increasing trend, with a peak in Si coincident with the transition of unit I and unit II.

Unit I extends from 1.05 cm to the top. Unit I contains peaks in Fe/Ti, Ca, and Si content. Zirconium exhibits a slight increasing trend.

H4_12

Visual Stratigraphy

The total sediment thickness at H4_12 is 5 cm. From 5.0 cm to 3.7 cm there is a visibly coarse orange gray homogeneous mud (Figure 3.12). This is overlain by a fine blue gray mud from 3.7 cm to 0.9 cm, it is also the wettest layer. The upper 1.25 cm of sediment are green gray in color and contain distinct undulating boundaries, and a coarse bed from 0.9 cm to 0.3 cm. Additionally, the sediment from H4_12 was most notable for a strong effervescence during sample preparation for grain-size analysis.

Grain Size and Geochemical composition

Receiving tube H4_12 can be divided into four units (Figure 3.12).

Unit IV (5.0 cm to 3.25 cm) is characterized by decreasing grain size and minimal XRF data due to the low validity counts associated with an uneven sample surface.

Unit III spans a peak in grain size, and low Fe/Ti ratios. Unit III shows variable Zr counts, which shows no trend in counts. In addition to Zr, Si and Ca counts show a general increasing then decreasing trend. A peak in Ca content occurs at the top of the unit.

Unit II describes the finest grain size. The fine Grain size corresponding to a local peak in Fe/Ti, and an increase in Si relative to Unit III. Unit II also exhibits a deviation between Ca and Ca/Ti.

Unit I describes the peak in grain size at the top of the receiving tube. This peak grain size coincides with peak Fe/Ti content, increased Si, and increasing Ca content.

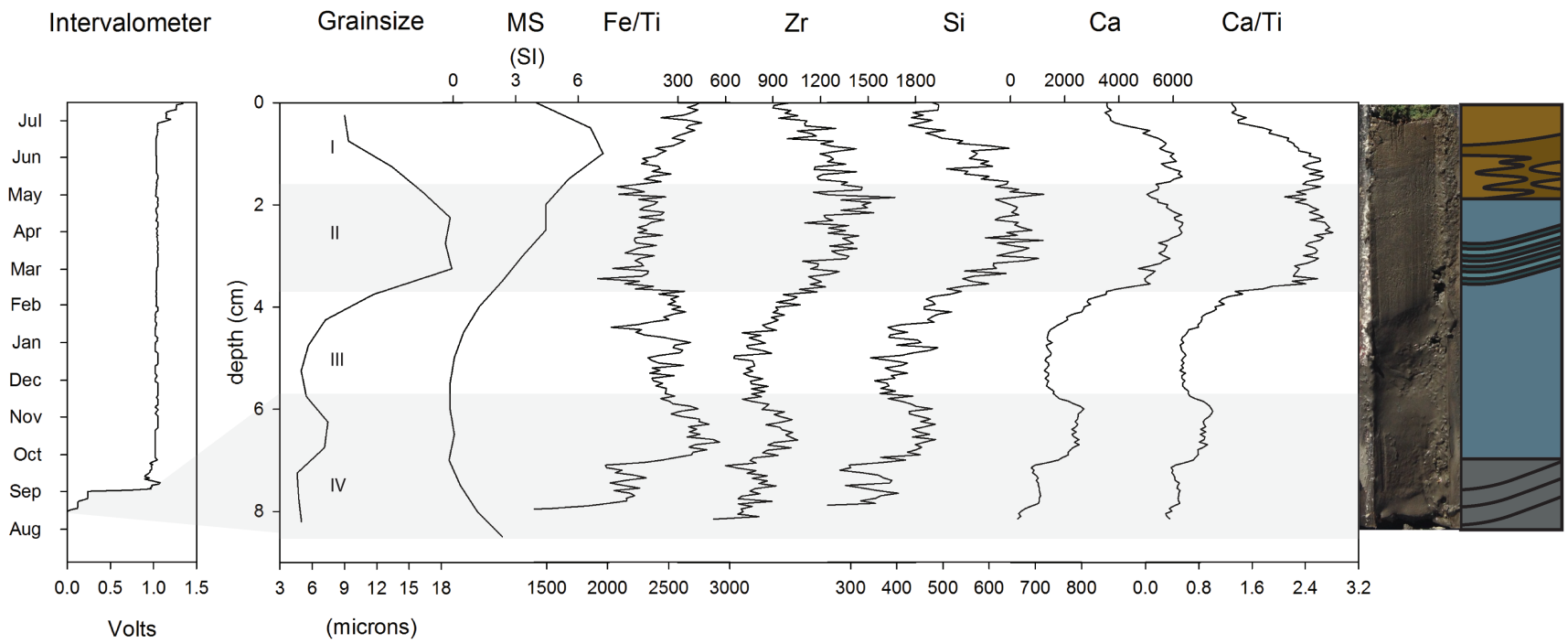

Figure 3.10: Composite log of receiving tube C3_12 Units are divided based on grain size and Fe/Ti.

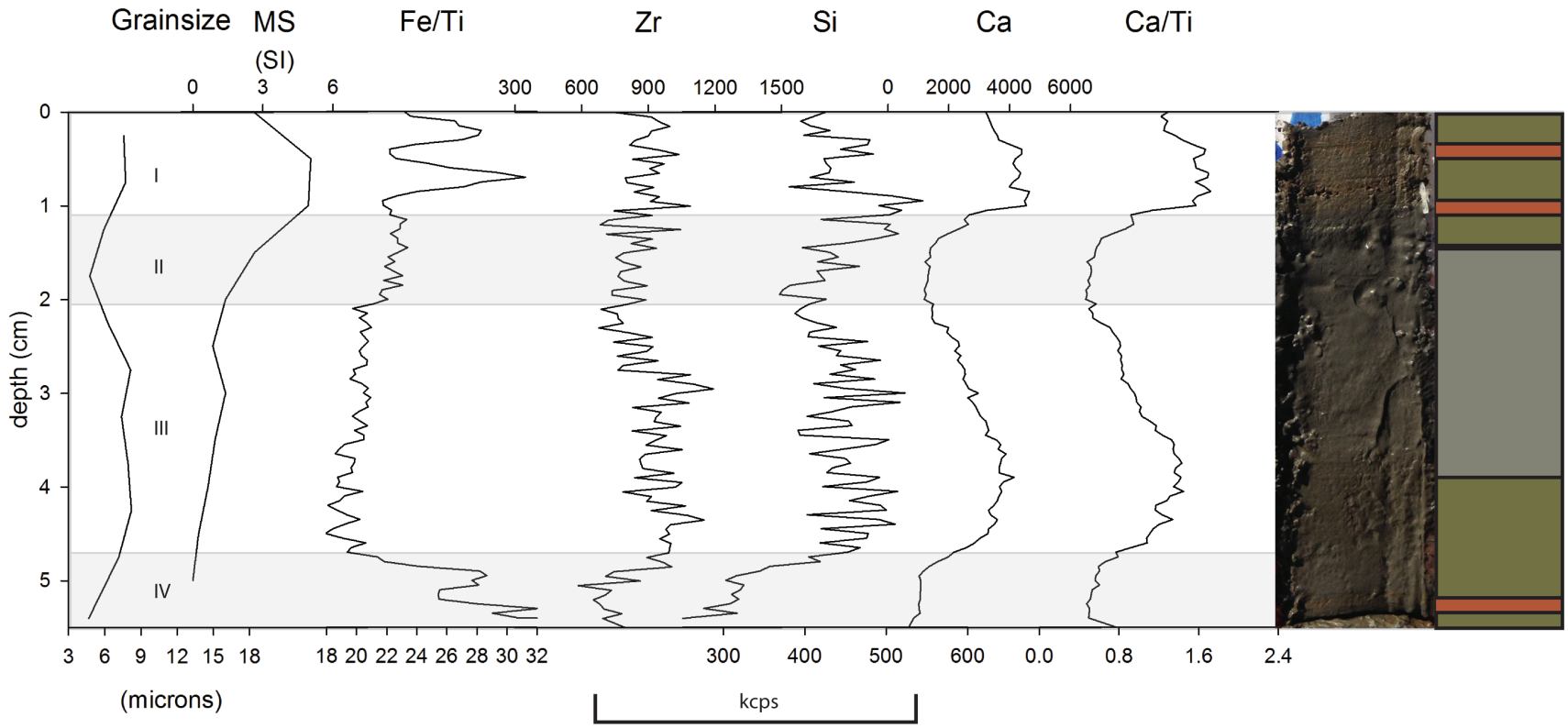

Figure 3.11: Composite log of receiving tube D3_12. Units are divided based on grain size and Fe/Ti.

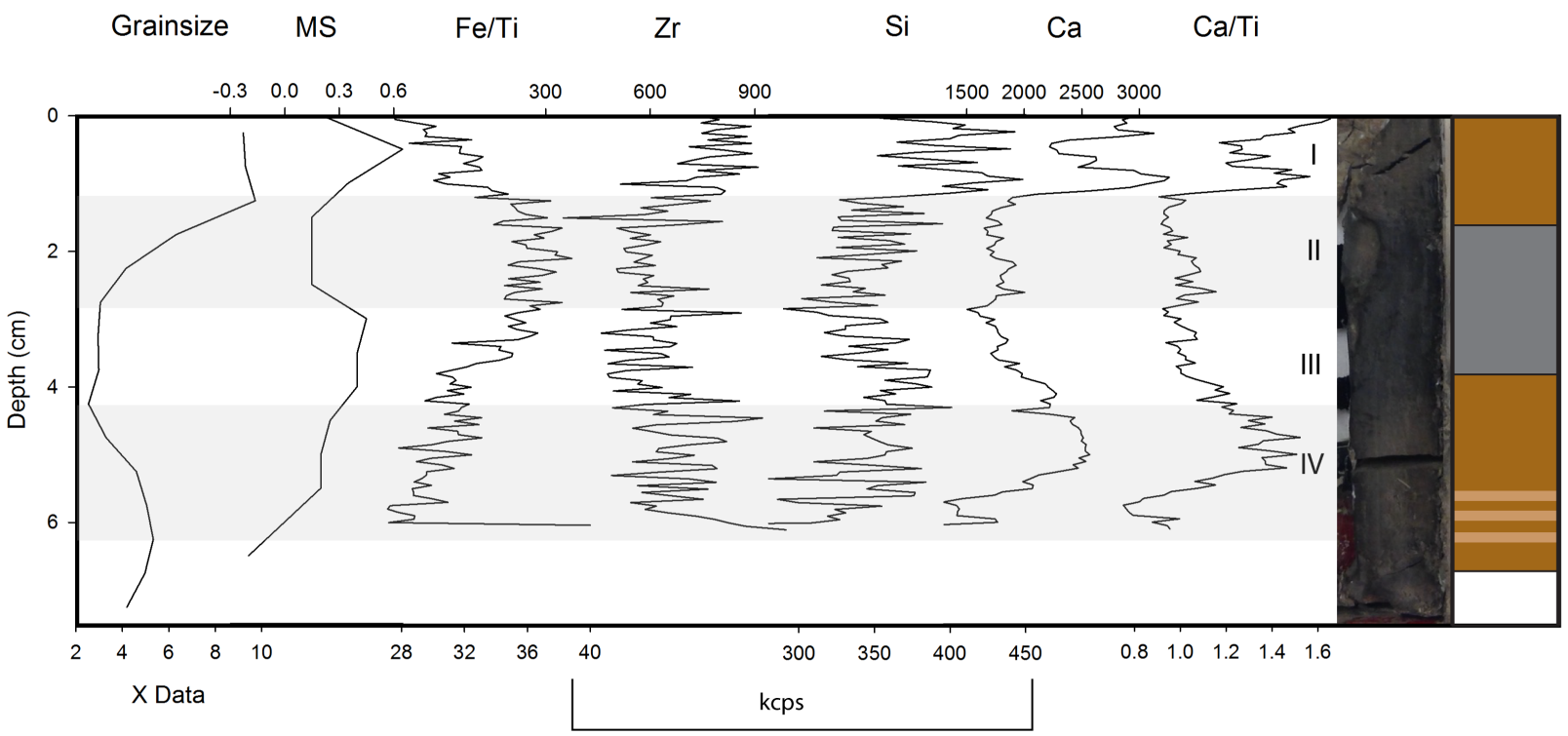

Figure 3.12: Composite log of receiving tube H4_12. Units are divided based on grain size and Fe/Ti.

G4_12

Visual Stratigraphy:

G4_12 has a total sediment thickness of 5.1 cm. From 5.1 cm to 3.5 cm, is a relatively coarse and wet green gray homogeneous mud. There is 0.1 cm finer layer at 4.2 cm. Above a sharp boundary at 3.5 cm, there is a very wet blue gray mud until a disturbed upper boundary at 1 cm. From 1 cm to the top, G4_12 contains a green gray mud that was the coarsest and driest when first split open. There are thin (<.3 cm) red sediment layers at 0.8 cm and 0.0 cm. There is an undulating boundary below these layers.

Grain Size and Geochemical composition:

G4_12 is divided into three units (Figure 3.13).

Unit III, (4.75 cm to 3.1 cm) corresponds to the finest grain size within the receiving tube. The sediment within this unit also contained too many cracks to provide geochemical data.

Unit II (3.1 cm to 0.9 cm) corresponds to increasing grain size, and two regions of peaked Zr and Ca content from 2.35 cm to 1.60 cm and 1.3 cm to 0.9 cm.

Unit I, the top 0.9 cm, covers a large peak in Fe/Ti content. This unit also corresponds to decreasing Ca and Si content.

Weather Conditions

From 7/20/2014 until 9/17/2014 average daily temperatures were above freezing, resulting in 60 degree days above freezing. From 9/18/14 until 10/28/14, average daily temperatures fluctuated around freezing, associated with 18 and 23 days respectively. Afterward, below freezing temperatures dominated the weather record until late May. Of the 69 days spanning 5/16/2015 until 7/24/2015, 63 were above freezing. The warmest daily average temperature recorded was 10.04°C on 7/9/15, and the coldest was -21.3°C on 2/22/15. Throughout the year there were a total of 155 days with average temperatures above freezing.

There were multiple notable precipitation events throughout the late summer and fall (Figure 3.14). From 7/23/14 through 8/1/14, 10.8 mm of rain was measured in Linnédalen. From 8/26/14 through 8/31/14, 38.4 mm of precipitation was measured. And from 9/5/14 to 9/16/14, 99.6 mm of precipitation was collected, with 42.6mm of the precipitation on 9/13/14 alone. The early October precipitation event, 10/2/14 to 10/6/14, corresponded with average temperatures above freezing and 33 mm of precipitation were recorded. A late November precipitation event, 11/22/14 to 11/27/14, again corresponded to above freezing temperatures and 56.4 mm of precipitation were measured. During the winter months, rain events still occurred. Both 1/22/15 and 2/16/15 experienced the deposition of 18.2 mm and 45.2 mm, respectively, of precipitation over two days with average daily temperatures above freezing. Similar events occurred in March and April. There were few precipitation events in the spring and early summer. Most notable are 4/16/15 and 6/27/15 with 6.4 mm and 10.6 mm of precipitation respectively. Throughout the year these precipitation events correspond to changes in lake stage (Figure 3.15).

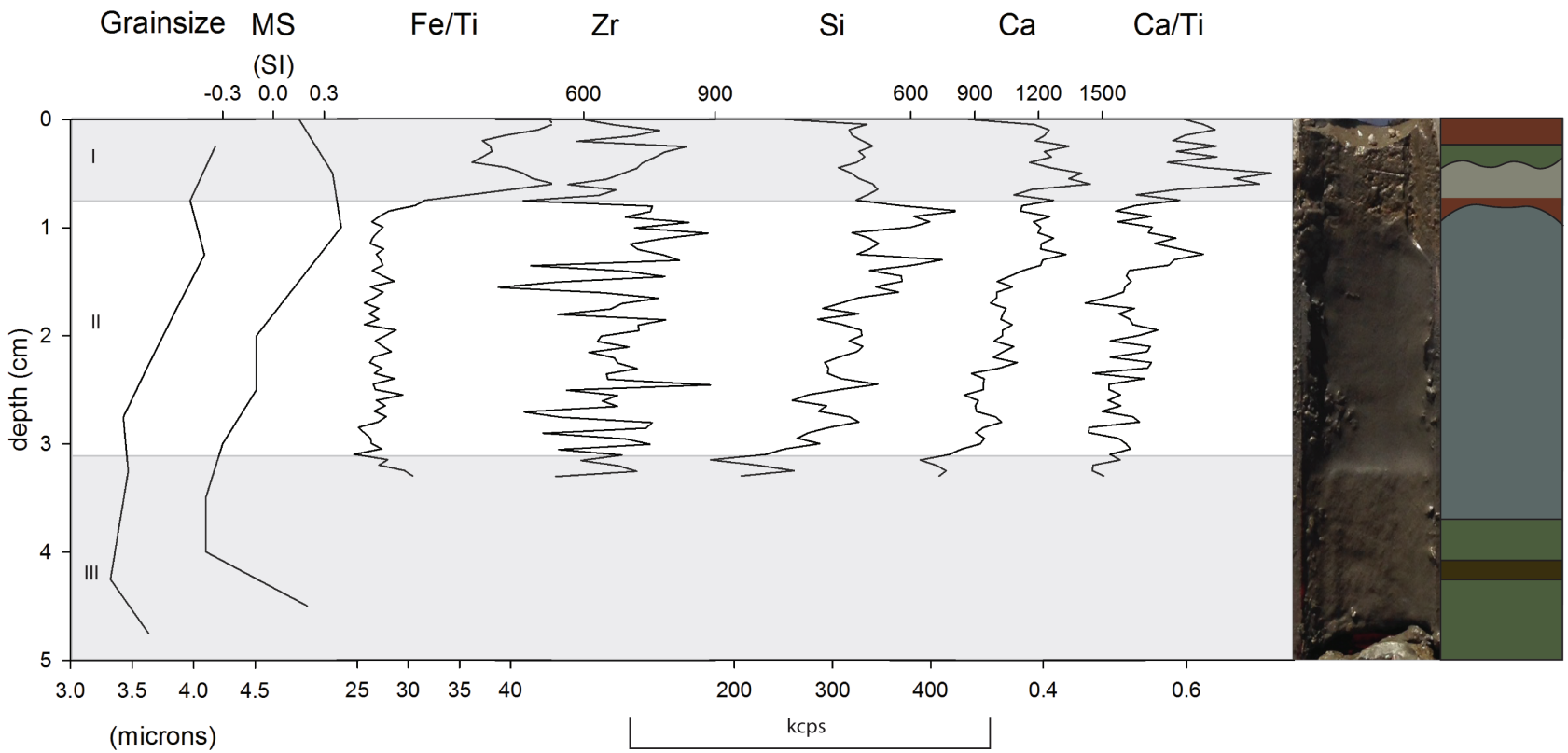

Figure 3.13: Composite log of receiving tube G4_12. Units are divided based on grain size and Fe/Ti.

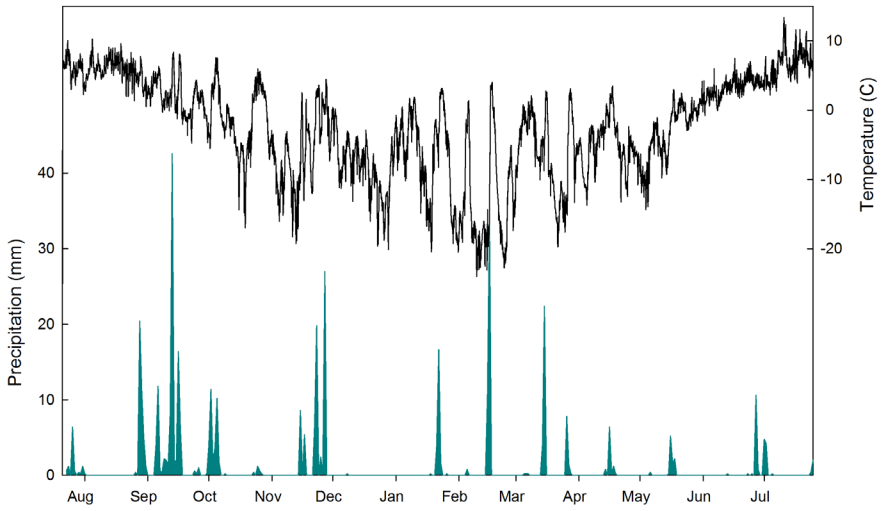

Figure 3.14: July 2014-July 2015 air temperature and precipitation record for Linnédalen

Lake Stage

The corrected water level (Figure 3.15) shows a general decrease until 8/28/14. There are five increases in lake level before November, with peaks corresponding to 8/30/14, 9/9/14, 9/14/14, 9/17/14, and 10/7/14. From November to May, there are two notable increases in lake stage, the first on 11/27/14 and the other on 2/13/15. The lake stage increases from 5/14/15 until it peakes at 6/5/15, with a secondary peak at 6/9/15. This is followed by an overall parabolic decrease in the lake stage with minor increases in June.

Water Column

The water column was well mixed during the ice-free period from late-July through early October (Figure 3.16a. The water temperature from late-July through mid-September was above 4°C (Figure 3.16 b). As the lake cools down from September to November, there was a notable pulse of warm water in mid-October (Figure 3.16 a,b). Throughout the winter the lake was thermally stratified with the warmest water at the bottom of the lake. This stratification continued into the spring, with periodic warm surface water pulses from mid-June until late July.

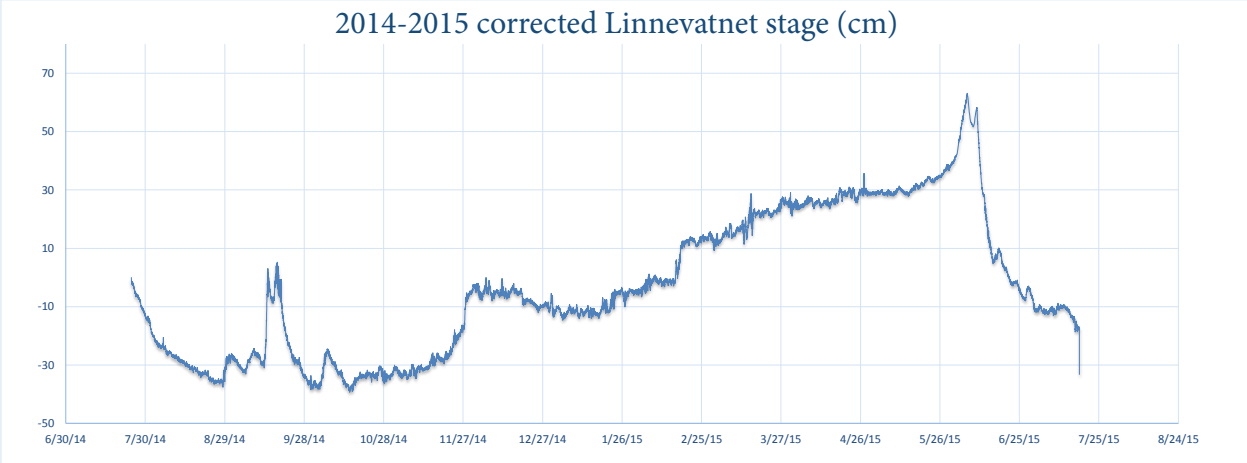

Figure 3.15: Linnevatnet lake stage, or relative water level, corrected for changes in barometic pressure based on pressure data from Gruvefjellet (Steve Roof).

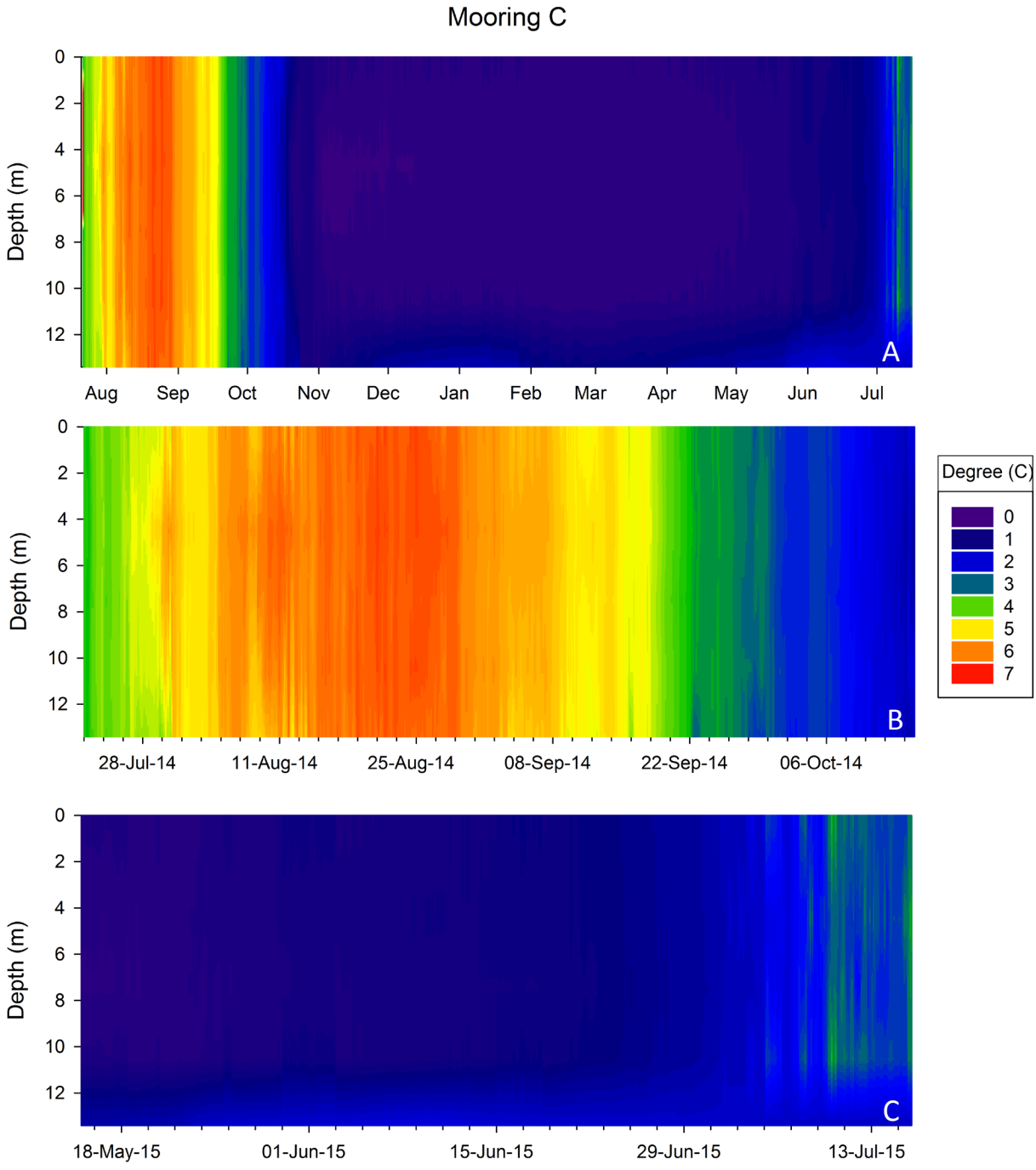

Figure 3.16: Contoured plot of water temperatures measured during the July 2014-July 2015 period at Mooring C, the most proximal site. Annually (A), distinct phases of the water column can be observed. The water column is warm and mixed in the summer (B), stratified during the winter, and beginning to mix again in the spring (C).

Meteorological conditions during summer/fall (2014) precipitation events

Late July storm.

From 7/23/14 to 8/1/14, 10.8 mm of precipitation were measured in Linnédalen, the least of all Summer-Fall 2014 storms. The majority of this precipitation was deposited on July 26th (6.4 mm). Throughout the storm period, the river and air temperature followed a diurnal peaked trends (Figure 3.17). River temperature ranged from 9.3°C on 7/30/14 to 3.6°C on 7/31/14. The fluctuations in both observations showed diurnal variations. Following the peak in precipitation, there were a series of warm surface water pulses that reached the deep basin. These pulses are coincident with the diurnally peaked river temperatures. After the storm, the water column was is homogeneously mixed.

Late August storm.

Over the 6 day period from 8/26/14-8/31/14 38.4 mm of precipitation was measured. At this time, both the river and the air temperature show diurnal variations (Figure 3.18). The onset of the precipitation event corresponds to a decrease in the diurnal amplitude. During the storm, the maximum river temperature was 6.1°C on 8/26/14 and the minimum was 1.3°C on 8/30/14. Prior to the onset of precipitation, Linnévatnet experienced pulses of warm surface water corresponding to peak temperatures. The distal basin is stratified, with cool bottom water (4.5°C) overlain by warm surface water (>6°C). Following peak precipitation, the lake became isothermal. The deep basin appears to have begun stratifying after 8/29/14, and the eastern sub-basin experienced cold water bottom pulses. The air temperature peaks are suppressed after the storm.

Mid-September storm:

The largest precipitation event of 2014 occurred over 17 days from 9/5/14-9/17/14. A net precipitation of 99.6 mm was deposited. There were three peaks in precipitation on 9/6/14, 9/13/14 and 9/16/14, with the deposition of 11.8 mm, 42.6 mm and 16.4 mm of precipitation respectively. The Linnévatnet water column goes isothermal following each precipitation peaks (Figure 3.19). Throughout this event, there are a series of cold water pulses, most notably on 9/15/14, which extend into the deep basin (site H).

There is a correlation between river and air temperatures, as they both exhibit a similar diurnal variation pattern. Precipitation peaks corresponded to a deviation from this pattern. For example, before to the onset of precipitation, air temperature fluctuated between 0.5°C and 4.5°C. During precipitation peaks, temperature increased to fluctuating between 4.7°C and 8.2°C, often without diurnal variation. Following each peak in precipitation, the temperature dropped to 0°C with small amplitude diurnal variations and a decreasing trend. After the storm, the river temperature also dropped to 0°C.

Early October Storm

A net precipitation of 33 mm was recorded in Linnédalen from 9/30/14 to 10/6/14. Both the air temperature and the lake temperature exhibited a general decreasing trend during this period (Figure 3.20). The lake was isothermal following following peaks in precipitation, and over the course of the storm event, two days maintained average temperatures belowing freezing.

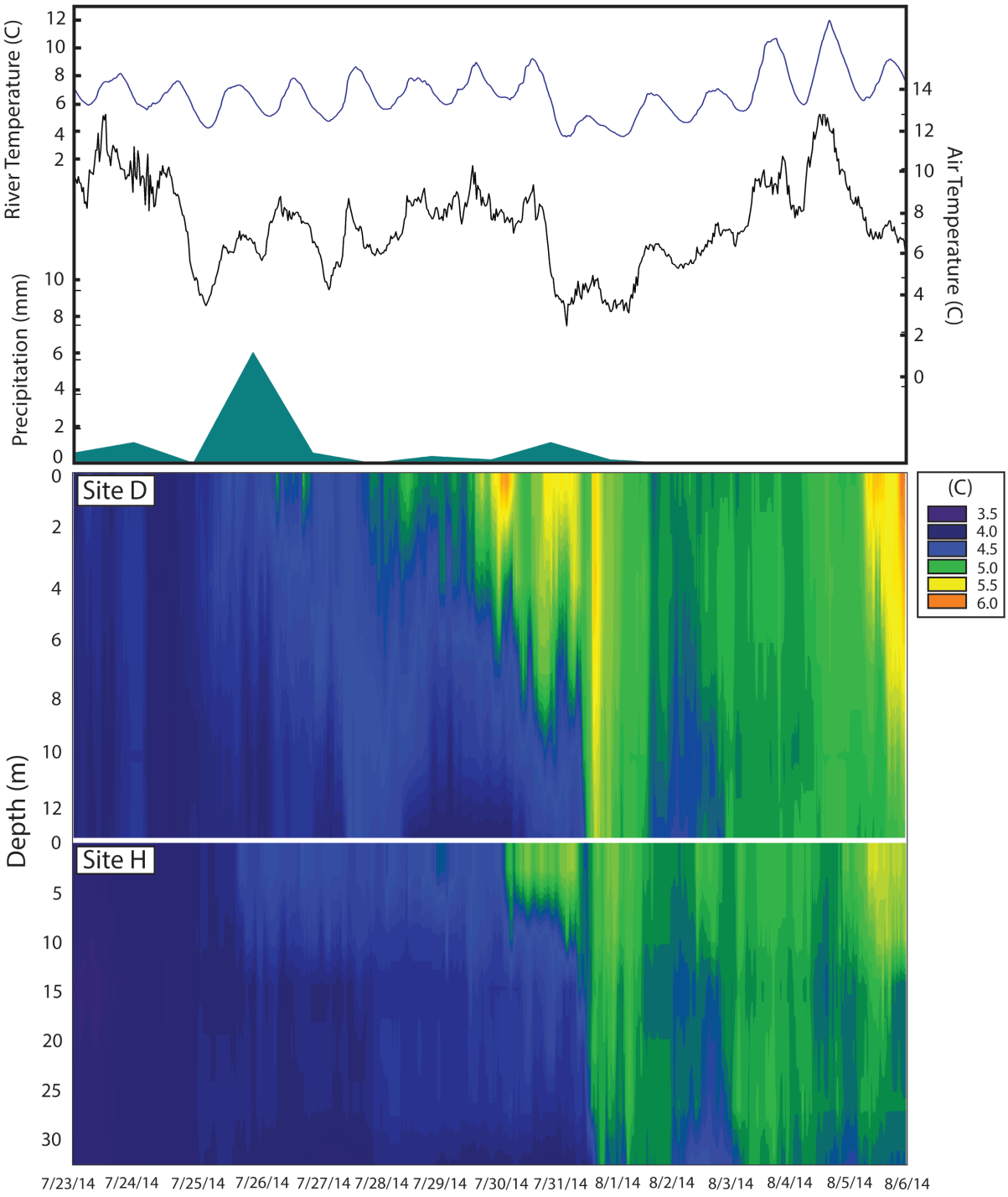

Figure 3.17: Meteorological conditions during the late July 2014 precipitation event. Water temperatures show the conditions both in the shallow eastern sub-basin (Site D), and the distal basin (Site H).

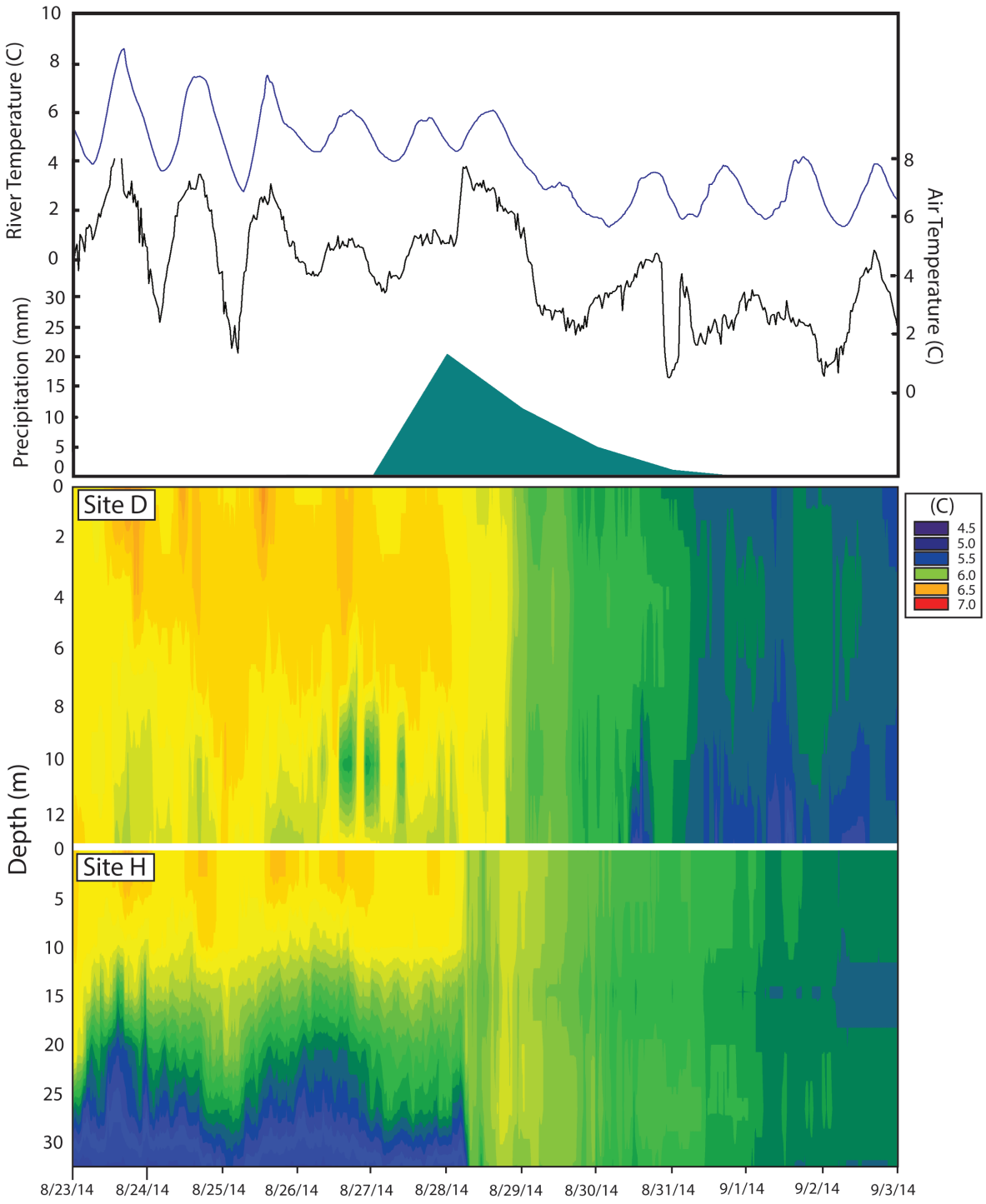

Figure 3.18: Meteorological conditions surrounding the late August 2015 precipitation event.

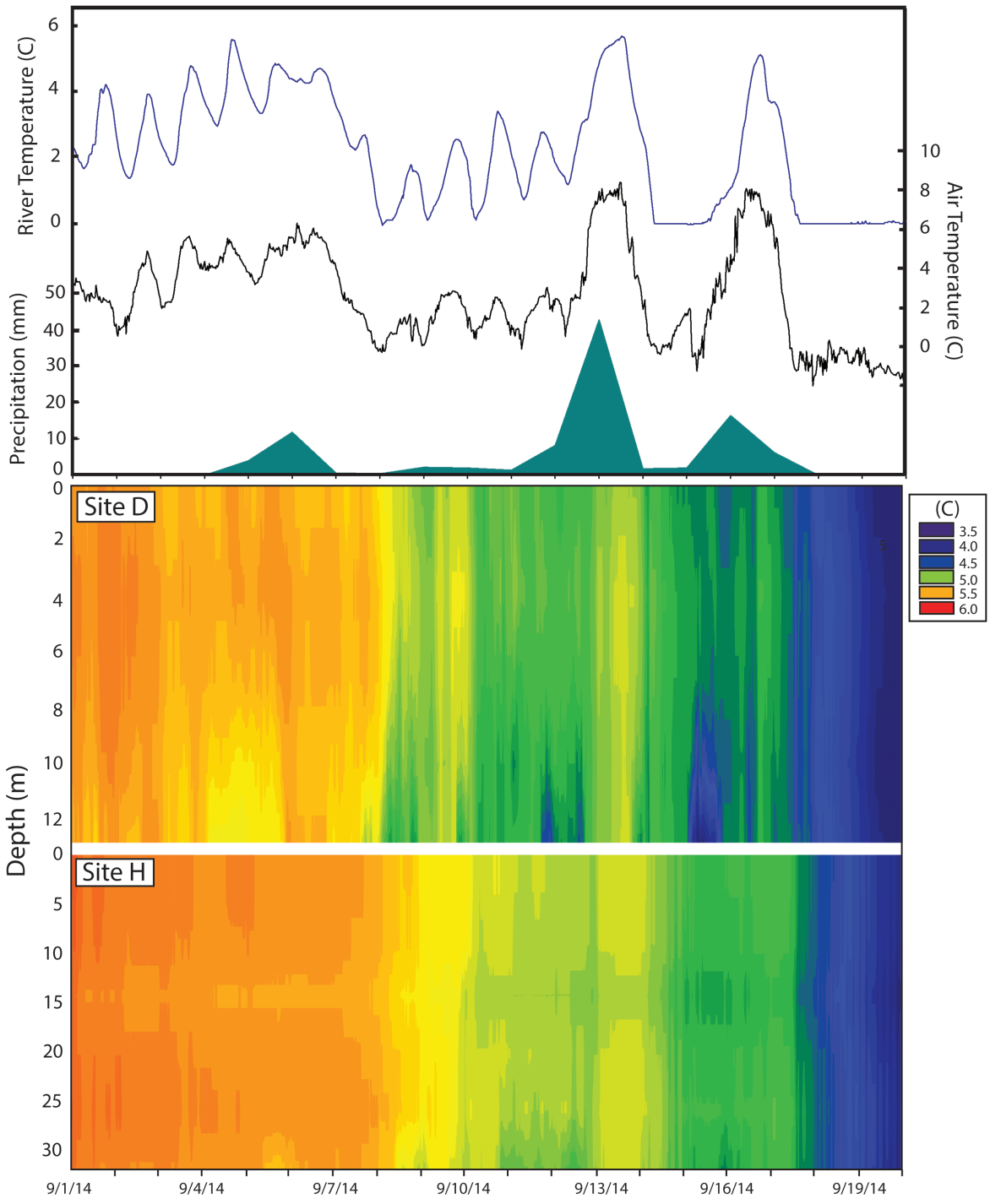

Figure 3.19:Meteorological conditions during the mid September 2014 precipitation event.

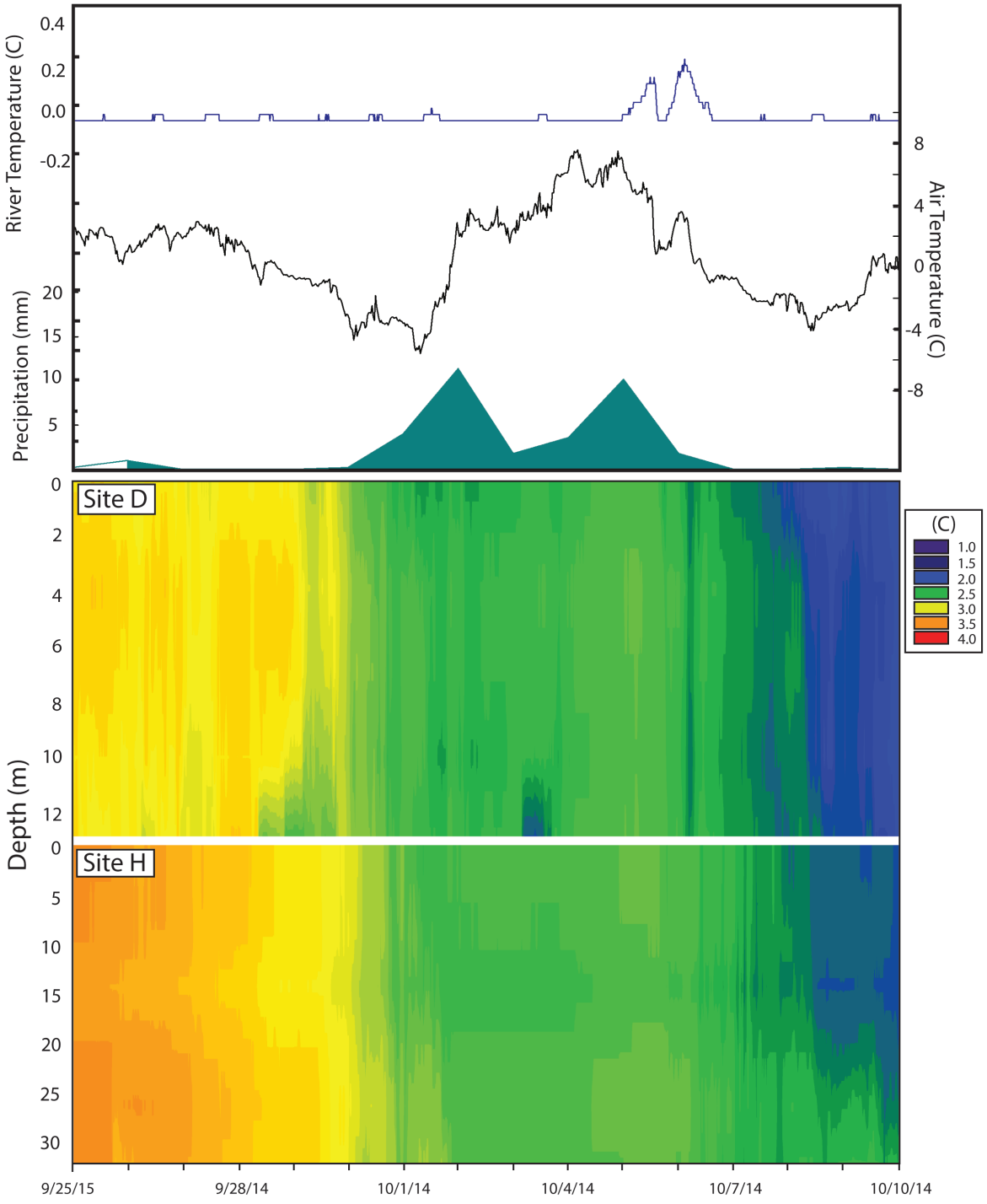

Figure 3.20:Meteorological conditions surrounding the early October 2015 precipitation event.

Principle Component Analysis

Assuming that the Principle Component (PC) best describes the maximum variability across all selected elements at each 0.5 mm depth interval, the relationship between a single elemental constituent and the PC expresses how well that elemental constituent describes the overall variation. It is similar to a correlation between the variation and each element.

Mooring C shows similar variation across the three years (table 3.1), as the bulk of annual sediment composition is well described by similar constituents in all three data sets. C4_15 exhibits a variety of relationships between constituents and variability (table 3.1). The variability most closely corresponds to changes in potassium, magnesium, iron, and rubidium, but there is also a moderate inverse relationship with zirconium, silica, and calcium. All elemental constituents of C3_14 are well described by PC 1. The strongest elemental relationships are iron, potassium, and rubidium; while strontium and zirconium are least related to the overall variance of C3_14. The variance in C3_13 is well described by a combination of PC1 and PC2, but it is also is subject to multiple inverse relationships. Calcium, and zirconium showed strong inverse relationship with PC1 (>0.9).

Mooring D exhibits variation between the years. D4_15 has the strongest relationship between PC1 and iron, potassium and magnesium. The remaining variability (PC2) is best described by titanium, silica, and calcium. Similar to C3_14, the variation in D3_14 is well described by all the constituent elements. However titanium shows the strongest correlation to overall variability, and manganese has a relatively weak relationship. Variation in D3_12 is best described by titanium, calcium, and silica. The correlations between constituents and PC1 shows a greater inter-annual difference at mooring D than at mooring C.

Mooring site H shows a similar trend in correlations across the years. H5_15 and H4_12 both show the strongest relationship between variability and silica content. H3_14 shows the strongest relationship with potassium. All three years also exhibit a strong relationship with titanium and calcium.

Sediment traps at mooring site G show some inter-annual consistency. Changes in potassium describe the majority of sediment variation across all three years. Iron content is also strongly correlated in G5_15 and G3_14, and somewhat correlated in G4_12. Ti shows a decreasing relationship across the years, where it related to the most variation in G4_12, but only has a moderate PC1 value (0.65) are G5_15.

	C4_15		C3_14		C3_13	
	PC 1	PC 2	PC 1	PC 2	PC 1	PC 2
Al	0.35	0.204	**0.738**	0.245	0.237	0.385
Si	**-0.615**	**0.679**	**0.955**	0.192	**-0.733**	**0.522**
K	**0.933**	0.24	**0.957**	0.188	**0.733**	**0.57**
Ca	**-0.536**	0.215	**0.873**	0.246	**-0.909**	0.342
Ti	0.373	**0.862**	**0.973**	0.135	0.164	**0.844**
Mn	**0.717**	0.33	**0.927**	0.085	-0.26	**0.513**
Fe	**0.917**	0.205	**0.979**	0.0498	**0.765**	0.443
Rb	**0.807**	0.00113	**0.764**	**-0.534**	**0.858**	0.0798
Sr	0.455	-0.233	**0.505**	**-0.72**	**0.829**	-0.0864
Zr	**-0.746**	**0.543**	**0.604**	-0.408	**-0.921**	0.169

	H5_15		H3_14		H4_13	
	PC 1	PC 2	PC 1	PC 2	PC 1	PC 2
Al	0.173	0.139	**0.528**	0.168	0.385	0.0774
Si	**0.91**	-0.029	**0.926**	-0.187	**0.895**	0.0536
K	0.442	0.689	**0.945**	0.0895	**0.553**	**-0.576**
Ca	**0.823**	-0.446	**0.705**	-0.392	**0.887**	0.318
Ti	**0.897**	0.108	**0.92**	-0.126	**0.883**	-0.172
Mn	0.434	0.459	**0.601**	0.142	**0.52**	0.308
Fe	0.192	**0.896**	**0.83**	0.328	**0.739**	**0.506**
Rb	0.0148	**0.59**	0.0633	**0.793**	0.387	**-0.64**
Sr	-0.122	**0.655**	-0.176	**0.568**	0.385	**-0.545**
Zr	**0.582**	**-0.57**	-0.232	-0.362	0.137	0.244

	D4_15		D3_14		D3_13	
	PC 1	PC 2	PC 1	PC 2	PC 1	PC 2
Al	0.257	0.0309	**0.529**	-0.126	0.245	**0.523**
Si	-0.0867	**0.85**	**0.713**	**-0.572**	**0.826**	0.361
K	**0.8**	0.439	**0.915**	0.195	0.342	**0.755**
Ca	-0.498	**0.774**	**0.749**	-0.222	**0.868**	-0.246
Ti	0.147	**0.923**	**0.946**	-0.171	**0.861**	0.319
Mn	**0.724**	0.098	**0.567**	**0.573**	**0.566**	**-0.531**
Fe	**0.918**	0.0186	**0.889**	0.218	0.425	-0.184
Rb	0.364	-0.217	**0.799**	0.232	-0.22	**0.715**
Sr	**0.616**	0.107	**0.504**	**0.599**	-0.331	**0.72**
Zr	-0.422	0.264	**0.698**	-0.548	**0.627**	0.0464

	G5_15		G3_14		G4_13	
	PC 1	PC 2	PC 1	PC 2	PC 1	PC 2
Al	0.419	-0.361	0.576	0.333	0.171	**0.693**
Si	**0.535**	**0.577**	**0.568**	**0.7**	**0.819**	0.441
K	**0.961**	0.0265	**0.977**	0.0135	**0.919**	0.0793
Ca	-0.416	**0.83**	**-0.6**	**0.714**	**0.87**	-0.215
Ti	**0.652**	**0.594**	**0.821**	0.401	**0.938**	0.133
Mn	0.14	**0.788**	**0.746**	0.0907	0.0993	**-0.516**
Fe	**0.942**	0.000766	**0.973**	-0.039	**0.628**	**-0.54**
Rb	0.369	-0.113	**0.832**	-0.323	**0.503**	0.0784
Sr	**0.615**	0.0191	**0.752**	-0.263	0.441	-0.12
Zr	-0.567	0.539	-0.108	0.616	0.345	-0.251

Table 3.1: First and second resultant principle components, PC1 and PC2 respectively, for each receiving tube used in this study. PC values |>0.5| are bolded.

Chapter 4

Discussion

Differentiation of Sedimentary Layers.

The receiving tube stratigraphy is interpreted both in terms of events (Figure 4.1) and seasons (Figure 4.2). Sedimentary units were divided based upon grain size, geochemical profiles and continuity across the basin. Thus within a given unit, there can be multiple sedimentation events (Figure 4.1). A change in event resolution is pronounced in the inter-comparison between proximal and distal grain size and Zr profiles (Figures 4.1 and 4.2) similar to the model presented by Smith and Ashley (1985, p.194). Each year is represented by a July-July sediment budget, extending from summer sedimentation at the base of the sediment receiving tube, overlain by fall-winter and spring events. (Figure 4.2). Sediment seasonality was delineated based on assumptions of seasonal depositional conditions. For example, in a glacially influenced environment it is commonly anticipated that the deposition of the coarsest sediment relates to the spring freshet (Leeman and Niessen, 1994; Zolitschka et al., 2015). This coarse sedimentation is thus expected to correspond to the top of the receiving tubes (Figure 4.2). During colder months, lake ice halts the wind-driven circulation of the lake and allows fine grained sediment to settle out of the water column (Ojala et al., 2012). This settling forms the classic "winter layer" of a clastic varve (Zolitschka et al., 2015), found below the coarse freshet (Figure 4.2). In Svalbard, glacially dominated fluvial sedimentation forms the 'summer' varve lamination (Rutter et al., 2011). Additional coarse-grained sedimentation is associated with rainfall-induced discharge (Zolitschka et al., 2015; Ojala et al., 2012).These precipitation driving runoff events are either seen within or above the melt-induced units, suggesting an increasing dominance of late season precipitation driven sedimentation as glacio-fluvial influence decreases (Chutko and Lamoureux, 2008).

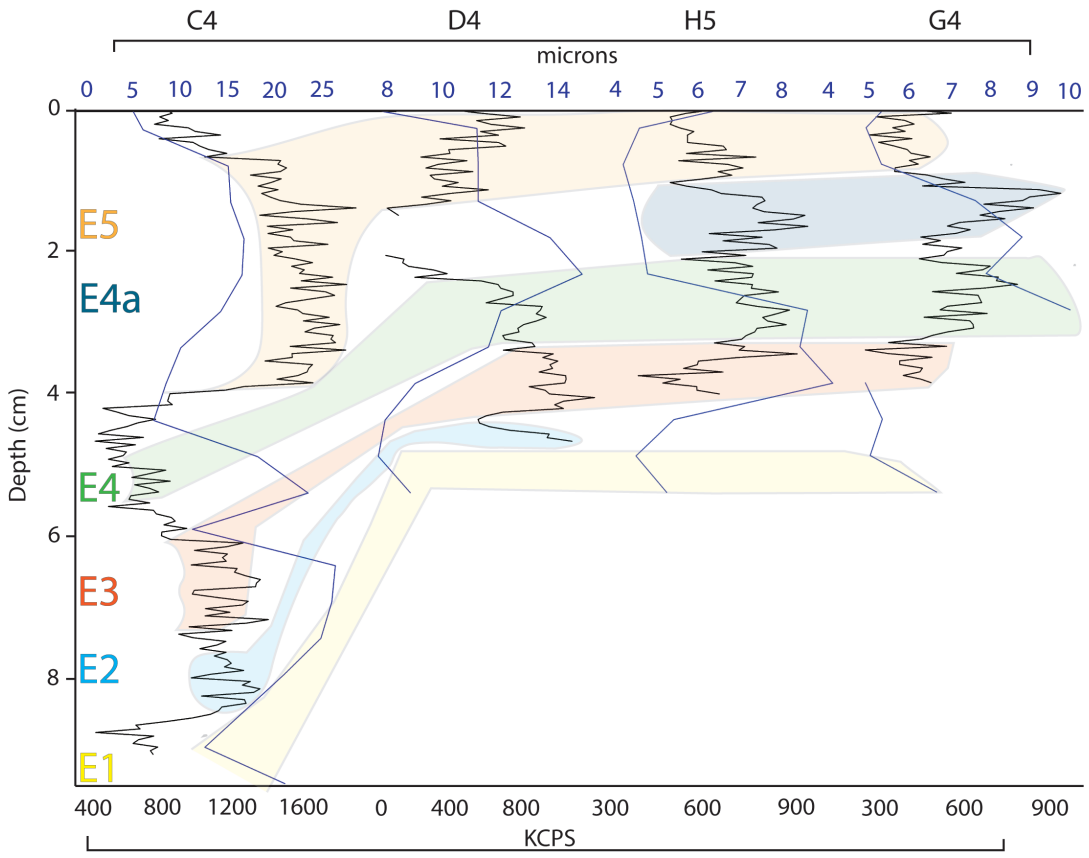

Figure 4.1: Event interpretation of '14-'15 sedimentation year, determined by peaks in Zr (black). Grain size (blue) is presented for visual comparison.

Interpretation of Sedimentation Events

The Zr record for 2014-2015 shows at least 5 sedimentation events (Figure 4.1). The timing of these events was constrained by the intervalometer (Figure 4.3). In the previous year, Walther (2015) found the intervalometer to record a change of 0.6 Volts for every 2 cm of sediment thickness deposited in the receiving tube. By comparison, there is a notable decrease in sediment thickness collected by the intervalometer, relative to sediment trap C4, attributed to the larger receiving tube diameter and smaller funnel size of the intervalometer. Walther (2015) recorded a 45 cm sediment thickness in C4_14, but only 9.5 cm in the intervalometer, resulting in a 4.7x decrease between the two. When this conversion is applied to the 2015 samples, the ~2.5 cm of sediment in the intervalometer should equate to approximately 12 cm of sediment in C4_15 tubes. However, C4_15 received 9.5 cm of sediment resulting in a 3.8x decrease from receiving tube to intervalometer. Despite this incongruence and the possibility that the intervelometer could have been compromised, the time stamp of sedimentation, recorded as changes in voltage, are assumed to accurately represent the timing of sedimentation in Linnévatnet during this study. It should also be noted that not all sedimentation events each year may be captured by the intervalometer due to its location in the lake at mooring C, as occasionally plumes may bypass this area of the lake (Werner, personal communication).

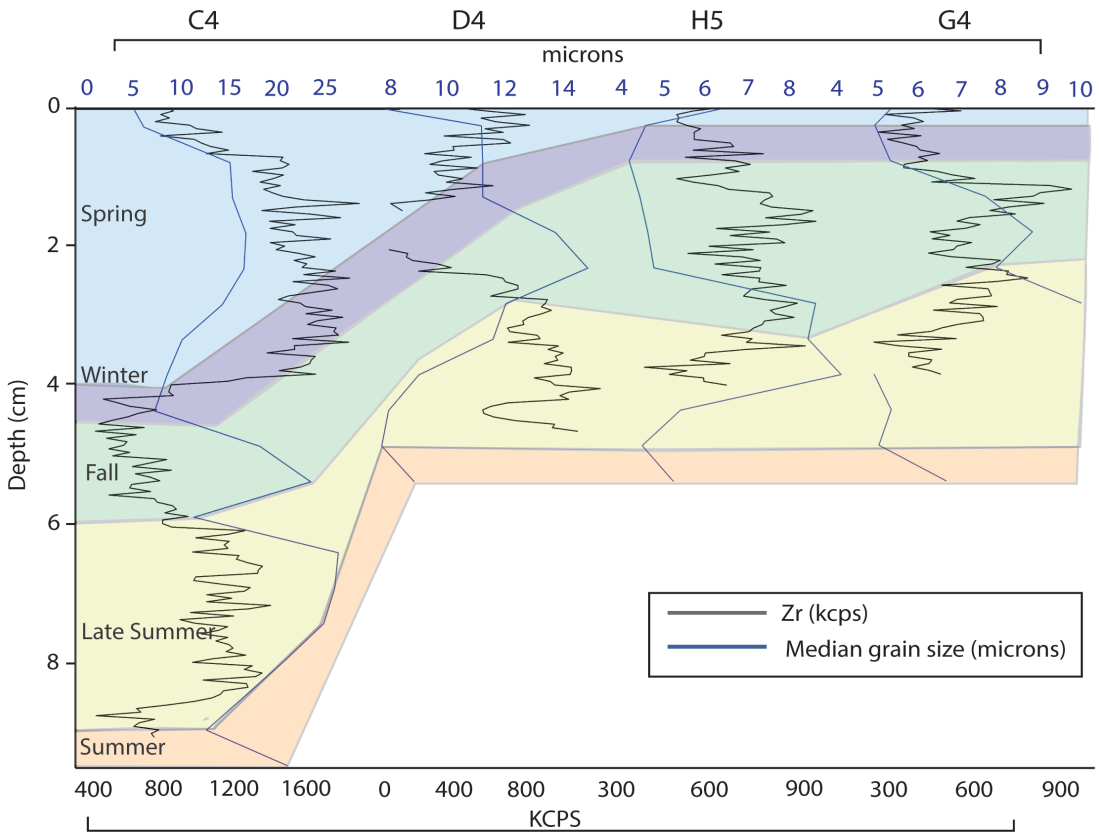

Figure 4.2: Seasonal interpretation of '14-'15 sedimentation year, determined by peaks in grain size (blue). Zr content is presented for visual comparison (black).

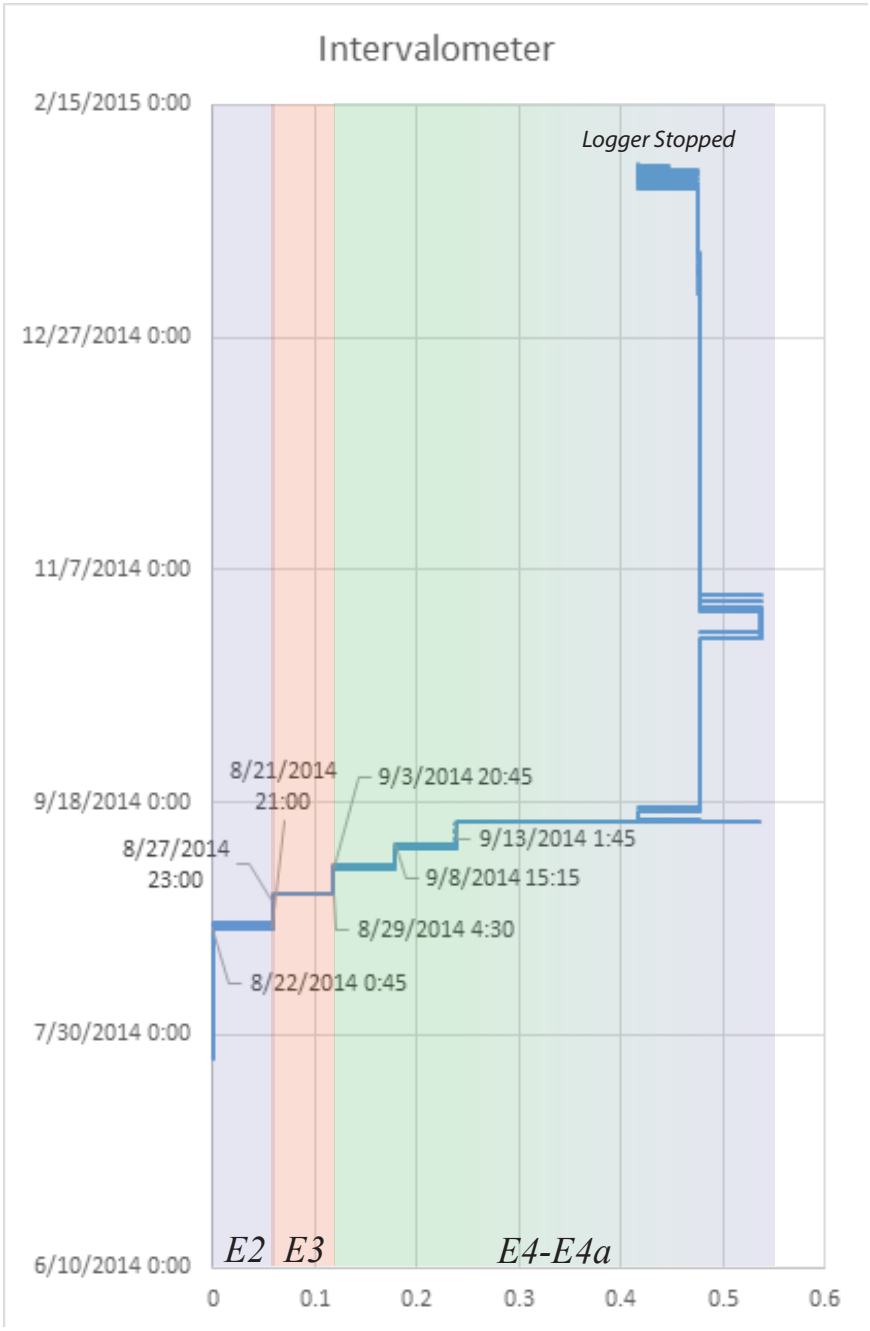

Figure 4.3: The change in voltage of the intervalometer, showing the timing of sedimentation from July 2014 - February 2015. Three sedimentation events were recorded by the intervalometer across the basin. The thickest sediment deposition corresponds to the September storm (E4-E4a). Note: voltage values can decrease due to the settling of fine sediment within the receiving tube.

Summer 2014/*Event 1*

The increased grain size at the base of all 2015 sediment traps was designated as Event 1 (E1). E1 is interpreted as sedimentation associated with the 7/24/14 to 8/1/14 precipitation event (Figure 3.15). The sediment traps were deployed during this precipitation event, thus the decrease in grain size represents the sediment settling after the event. During E1, the river was diurnally influenced (2°C fluctuation) and the lake temperature was increasing. These diurnal influences are the result of solar insolation, which suggests the presence of melt-influenced sedimentation during such precipitation events (Chutko and Lamoureux, 2008). At the beginning of the storm event, the river temperature was approximately 2x that of the lake resulting in an overflow of the inflowing warm water pulses (Figure 3.15). This stratification is supported by the presence of a sediment plume (Figure 4.4a), and turbid surface waters (Figure 4.4b) suggesting a consistency with the Carmack et al. (1979) model for spring sediment currents. The rapid decrease in turbiditiy (Figure 4.4b-c) supports this overflow model, because as grains settle out of an overflow, the surface turbidity should decrease. The series of cold bottom water pulses (Figure 3.15), prominent at the proximal sites, are interpreted as sediment-laden fluvial input from a combination of both diurnally influenced meltwater and precipitation runoff.

Late-Summer 2014/*Events 2 - Event 3*

The Summer-Late Summer unit (Figure 4.2) contains multiple sediment pulses (Figure 4.1). These pulses, differentiated by peaks in Zr, are present across the lake, but appear more distinctly within the distal basin. These Zr peaks correspond to both warm weather, Event 2 (E2), and a rain storm, Event 3 (E3). E2 is associated with the stretch of warm dry weather in August, when large diurnal fluctuations (4°C) in river temperature suggest the basin is still subject to nival melt and its ability to transport sediment. Overall, the summer sedimentation is represented by a large volume of coarse sediment deposition, attributed to the contribution of this glaciofluvial sediment from Linnéelva (Snyder et al., 2000; Arnold, 2009). Continuous clastic sedimentary input (Lewkowicz and Wolfe, 1991) may be diluting the signal of E2 and E3 in the proximal basin. This dilution is common in the Linnévatnet sediment record, as the thickest sediment deposits occur in the eastern sub-basin (Figure 1.8) near the mouth of Linnéelva (Svendsen and Mangerud, 1997). When turbid water from Linnéelva enters the lake, the decrease in energy between the two systems causes the largest particles to begin settling out of suspension (Smith and Ashley, 1985). This process has caused the buildup of the delta at the mouth of Linnéelva. The finer grains remaining in suspension can be distributed distally in the lake by wind or water currents (Figure 4.5). Thus distal sediment traps exhibit distinctive grain size and Zr peaks, associated with large melting or storm events, because they were not diluted by the daily coarse-grained sediment pulses from Linnéelva.

Event 3

The first major fall precipitation event, E3, lasted from 8/28/14 to 9/1/14. This late August storm occurred while the lake was slightly stratified, with a 2°C difference in the deep basin (Figure 3.16). The precipitation caused the lake to go isothermal. The decrease in the amplitude of diurnal changes during the storm, the deposition of snow in the highlands (Figure 4.6), and the suppression of the air, stream, and lake temperatures suggests a transition into the fall season.

Figure 4.4: (A) Linnéelva swollen with discharge during the late July storm. The lake water is turbid and a reddish brown sediment plume can be seen hugging the western eastern shore. (B) A down lake view of the turbid lake water. The lake shore is blurry, possibly suggesting an interaction between the sediment fans and the lake water. (C) Following the peak in precipitation, the lake appears less turbid.

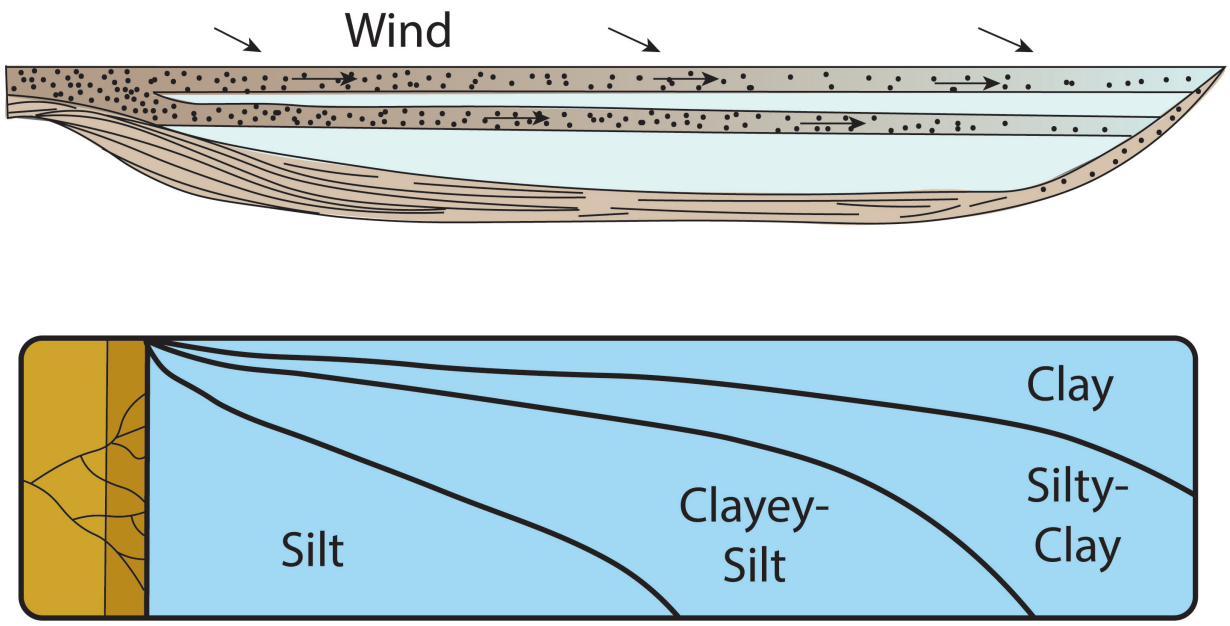

Figure 4.5: The sediment dispersal in a narrow glacier-fed lake, dominated by overflow-interflow, results in a proximal-distal thinning (A) and a distally finning (B) distribution of sedimentation. (Modified from Smith and Ashley, 1985)

Fall/*Event 4 - Event 4a*

Two major precipitation events occurred in Fall 2014 (Figure 4.2), the first in mid-September and the second in early October. In mid-September, precipitation event (E4) totaled almost 100 mm of precipitation over the course of 14 days. Before the storm, the river was still strongly influenced by diurnal fluctuations but the warm air during peak precipitation disrupted these variations. Following each precipitation peak, the amplitude of diurnal variation decreases. By the end of the storm, the river temperature remained near freezing and air temperature showed less diurnal influence, marking the end of the ablation season (Chutko and Lamoureux, 2008).

The combination of heavy precipitation and a decreasing temperature trend may explain the jump in coarse-grained sedimentation associated with E4 throughout the basin. Considering an average temperature lapse rate of -0.5°C/100 m (Christiansen et al., 2013), the near freezing valley floor temperatures during the onset of precipitation corresponded to solid precipitation up slope. The presence of snow in the mountains (Figure 4.7a) suggests the storage of precipitation within the watershed system (Nowak and Hodson, 2013). Subsequent rain events resulted in the melting of the snow, and the release of this 'stored' precipitation. These rain-on-snow events produced significant runoff which in turn increased the lake water level by over 34 cm (Figure 4.8). The resulting extensive flooding of Linnéelva and stream flow over the alluvial fans (Figure 4.7b) is believed to have transported a heavy sediment load. Previous hydrological studies in Northern Spitsbergen noted that the combination of late season snowmelt and rain events resulted in suspended sediment concentrations up to 8x higher than during snow melt alone (Bogen and Bonsnes, 2003). During E4, the increased sediment load generated large sediment plumes which extended down the lake (Figure 4.7c), propelled by the wind and Coriolis forcing. The second precipitation event of the fall occurred from 9/29/14 until 10/6/14. The net accumulation of this rain on snow event was <40 mm. Prior to the storm, the landscape was covered in a layer of snow (Figure 4.9a),

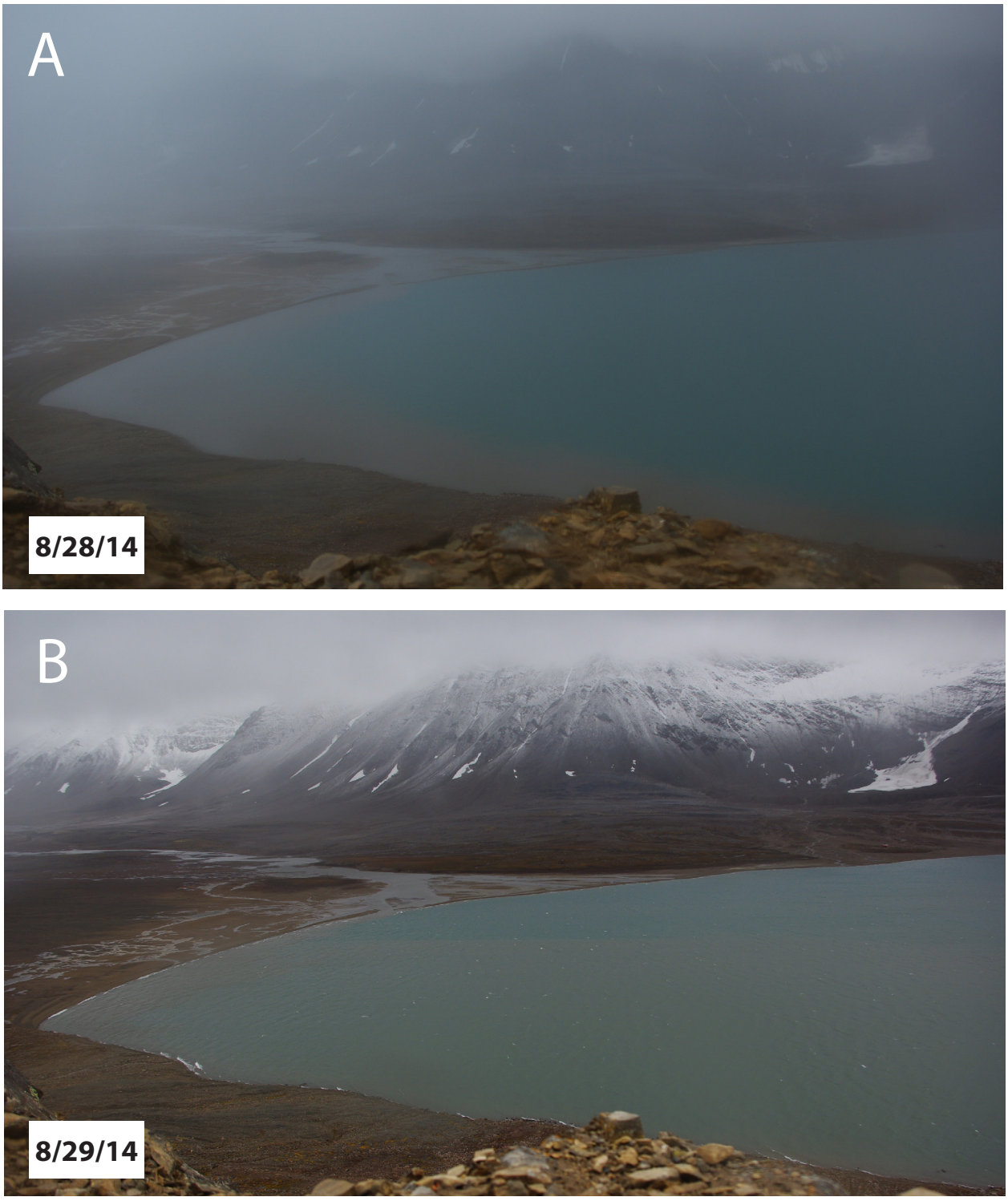

Figure 4.6: Timelapse photographs of the sediment plume entering the lake, hugging eastern shore of the lake (A) during the peak in precipitation of the event and flowing more difussely (B) across the lake as an overflow -note the presence of strong wind seen by the white-caps on the water and waves along the shore.

Figure 4.7: (A) The Linnéelva inflow the day before the 9/13/14 precipitation event. Note: the presence of snow on the hillside. (B) The Linnéelva inflow during peak precipitation. Note: the absence of snow, the flooding of Linnéelva, and the streams of water flowing over the 'twin fans' and from the western cirque glacier across the lake.

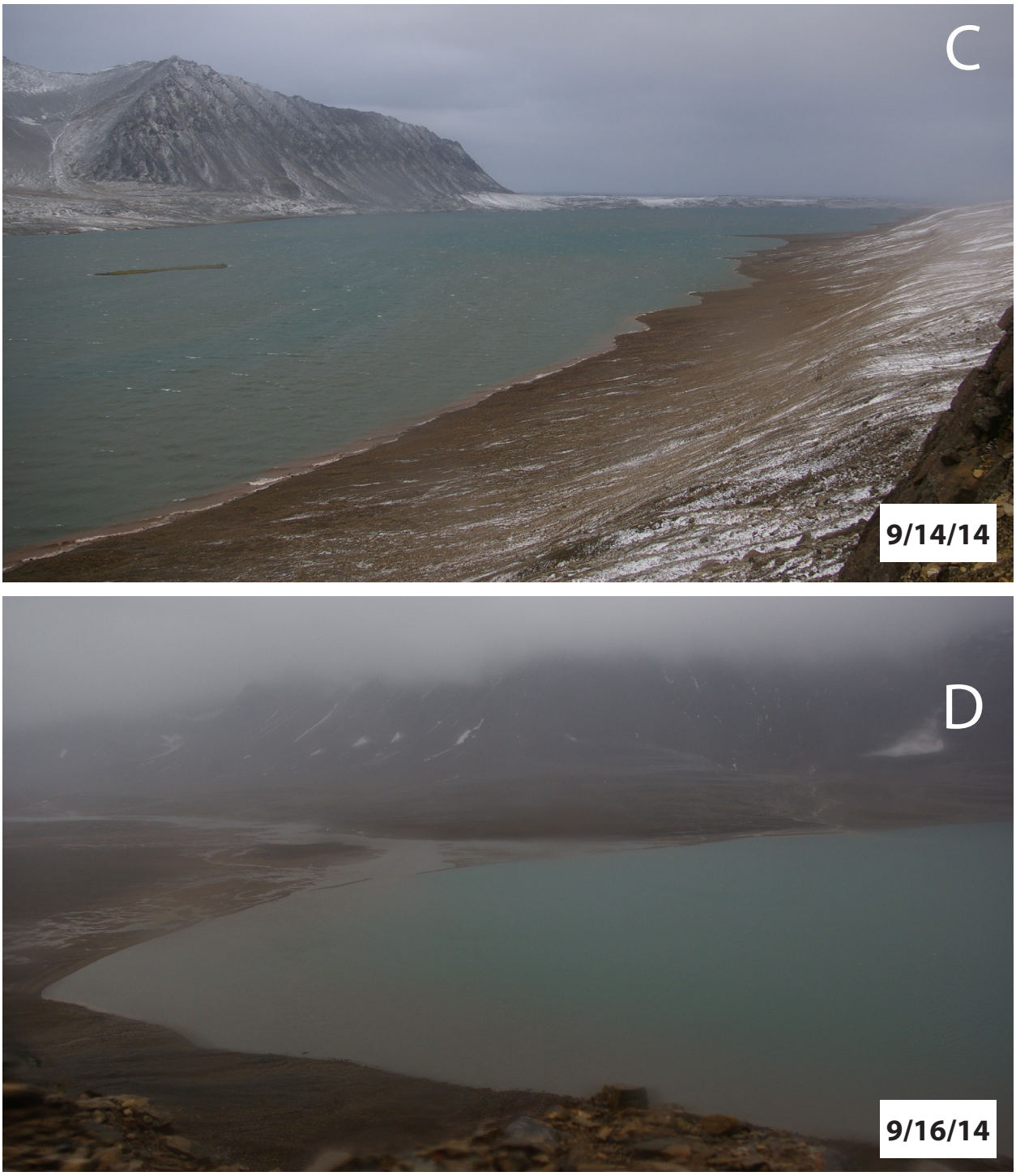

Figure 4.7: (C) Downlake view of the wind-driven transport of a sediment overflow. (D) Linnéelva, still flooding the delta, formed a visible sediment plume in the lake. Note: there is continued inflow of water from the western cirque glacier.

which melted during the event (Figure 4.9b). Similar to E4, this storm experienced a period of increased water storage within the system as snow. Following peak precipitation and increasing temperatures, the 10/3/14 cold bottom water pulse suggests a period of sediment delivery in association with this storm. However this rain-on-snow event (Figure 4.9b) may not be as strongly reflected in the sediment record as E4, due to ice in the river channel. Most rivers in Svalbard freeze completely during the winter, and during the freeze up process, ice can block the river (Killingtveit et al., 2003). Throughout the October storm, Linnéelva maintained below- to near-freezing temperatures (<0.3°C), and is suspected to be filled with ice (Werner, personal communication).

When examining the grain size of the receiving tubes, E4 is interpreted as a separate peak from the earlier two storms, despite E3 occurring only days before the onset of E4. It is suspected that the fluvial channel system was exhausted of coarse sediment during a period of persistent warm temperatures in August (E2), resulting in an underrepresentation of E3 in the sedimentary record. This is based on the interpretation of E3 as a glacio-fluvially dominated precipitation event, and thus flushing of the river channel by prior glaciofluvial processes may have resulted in a sediment deprevation. Comparatively, E4 engaged other sediment sources, such as the thawed permafrost active layer, across the watershed. Additionally, the E4 grain size peak did not necessarily correspond to peaks in Zr. Proximally, counts of Zr were low relative to the summer sedimentation. However, at the distal moorings, Zr and grain size peaked congruently. All moorings had similar Zr content of approximately 700-900 kcps relating to E4, supporting the idea sediment source around the lake, such as the alluvial fans and solifluction sheets, were activate during these storms.

A second but related event unit (E4a) occurs in the distal basin, where there is a peak in Zr corresponding to fining grain size (Figure 4.1). While Zr is typically analogous to coarse detrital sediment (Cuven et al., 2010), these peaks are attributed to the settling of finer sediments through the water column following E4. Walther (2015) describes a thick fine-grained unit above the major 2014 season storm deposit, which corresponds to stable or elevated Zr counts in the 2014 receiving tubes (Figures 3.6-3.9).

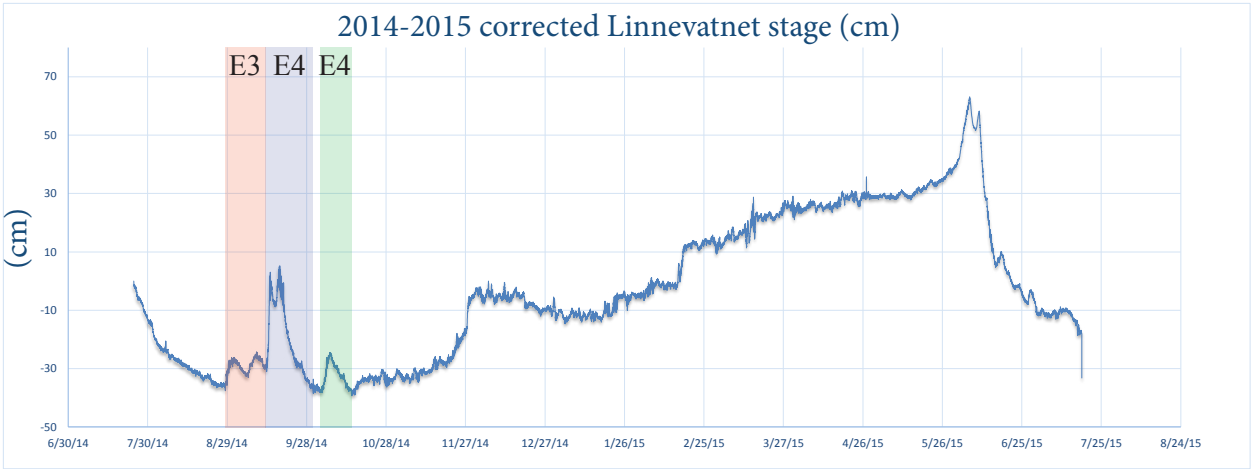

Figure 4.8: Interpretation of fall sedimentation events in relation to changes in lake stage. The precipitation events caused notable increases in surface level during an overall low lake stage.

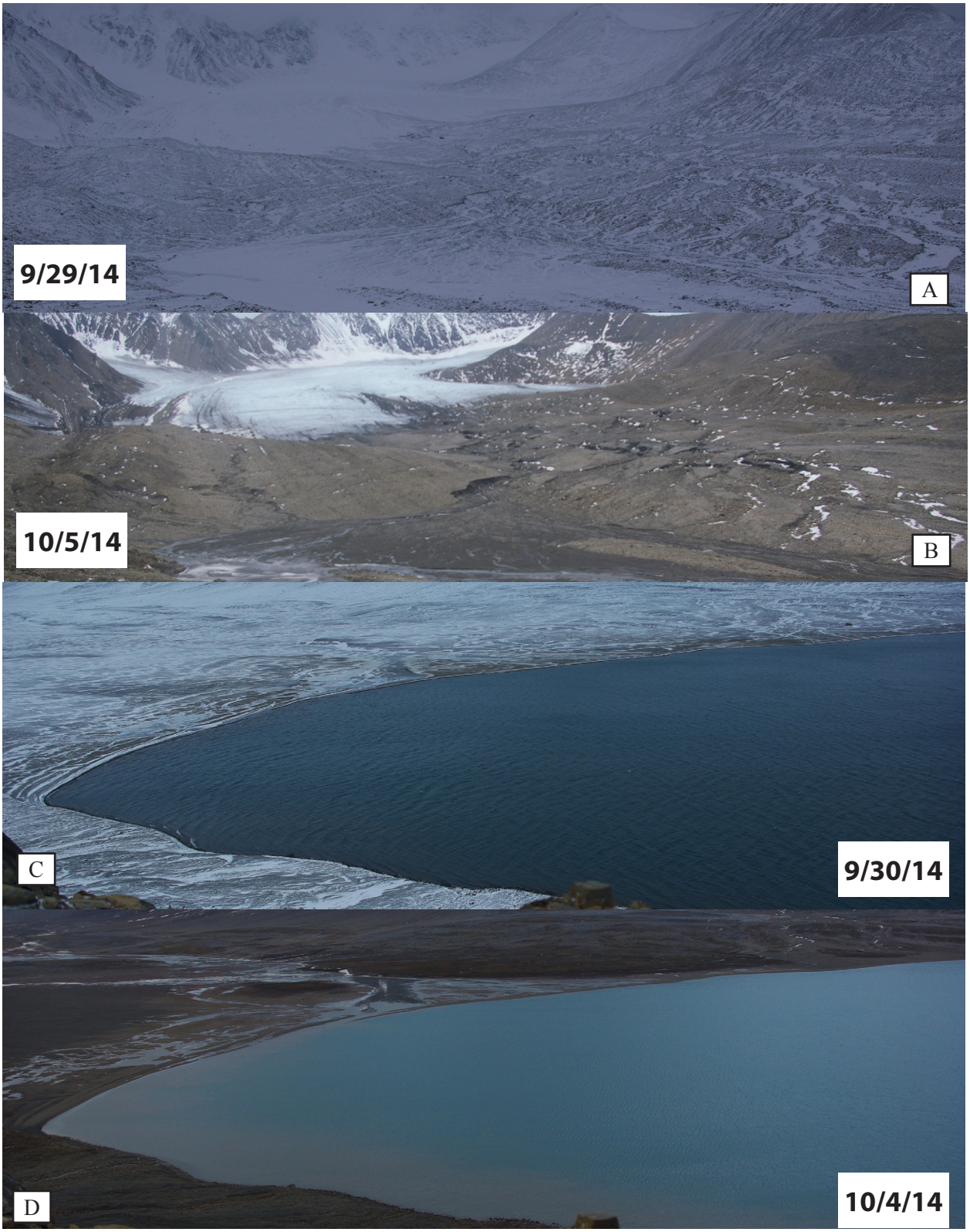

Figure 4.9: Time lapse images of the glacier front (A,B) and the linneleva inlet (C,D). During this early October precipitation event, the snow disappeared from the highlands (B) and a sediment plume hugged the east coast of the lake (D).

Winter

Across the basin, winter sedimentation was difficult to discern in the sediment traps. The winter layer is associated with the finest sedimention of the year (Zolitschka et al., 2015) yet in some sediment traps there is a complete lack of fine (<6 μm) sediment. Thus the winter layer was delineated based on peaks in the Fe/Ti ratio (Cuven et al., 2010). C4_15 and G5_15 exemplify the inverse relationship between the fine (Fe/Ti ratios) and coarse (Zr) grain size analogues. Site D lacks fine sediment, and has concurrent peaks in Fe/Ti and Zr. This grain size anomaly is attributed to extraneous outsized plastic particles from the sample splitting process. Additionally, increased Fe/Ti and Zr, combined with decreased Si, suggest Zr is influenced by other factors.

Spring/ *Event 5*

The coarser silt deposit overlying the winter layer in C4_15 is interpreted as the spring freshet. The spring corresponds to the coarsest yearly sediment deposition in a glacially influenced environment due to rapid snowmelt (Francus et al., 2008; Leeman and Niessen, 1994). The distal thinning observed in the spring layer supports this interpretation as spring sedimentation predominantly reaches the deep basin by overflows (Francus et al., 2008).

Comparison to 2012 and 2014 sedimentation records

There is a high variability of annual sedimentation in High Arctic locations (Bogen, 2003), and Linnévatnet is no different. Over the three years included in this study, there is variation of accumulated sediment thicknesses, but the timing of precipitation events is relatively similar. The 2011-2012 sedimentation year was characterized by a heavy September (8/31/11-9/7/11) precipitation event which contributed to approximately 50% of the annual accumulated sediment thickness (Obermeyer, 2012). The 2013-2014 sediment year was dominated by a late August sedimentation event. Walther (2015) found that 57% of the annual sediment load was associated with an August storm (8/8/13-8/18/13). The 2014-2015 year also saw up to 50% of the net annual accumulation associated with late summer-fall events. However, while the fall of 2014 saw a precipitation event of the same magnitude as both 2011 and 2013, no singular sediment depositional event represents ≥50% of the annual sedimentation. The total sediment thickness at site C4 from 2014-2015 was 9.5 cm, while the 2013-2014 C4 yield was over 45 cm (Walther, 2015). One explanation for this decrease is a potential flushing of the fluvial system by the August 2013 event. Bogen et al. (2003) found that major floods can flush waterways and exhaust sediment sources, in turn reducing the sediment readily available for transport (Lewkowicz and Wolfe, 1991). It should also be noted that the August ‘13 sedimentation event coincided with the largest annual glacial retreat since 2004 (Figure 4.10). Thus freshly exposed sediment in the glacial forefield would have been readily available for transportation.

Influence of changing hydrology

In western Svalbard, glaciers are retreating at an accelerated rate (Kohler et al., 2007);(Figure 4.10). In addition to increasing annual runoff by up to 20% (Hagen et al., 2003), the retreat of glaciers has shifted the storage of water into non-glacial flow paths, such as snow, permafrost, or ground icings (Nowak and Hodson, 2013). This change in storage capacity is notable during

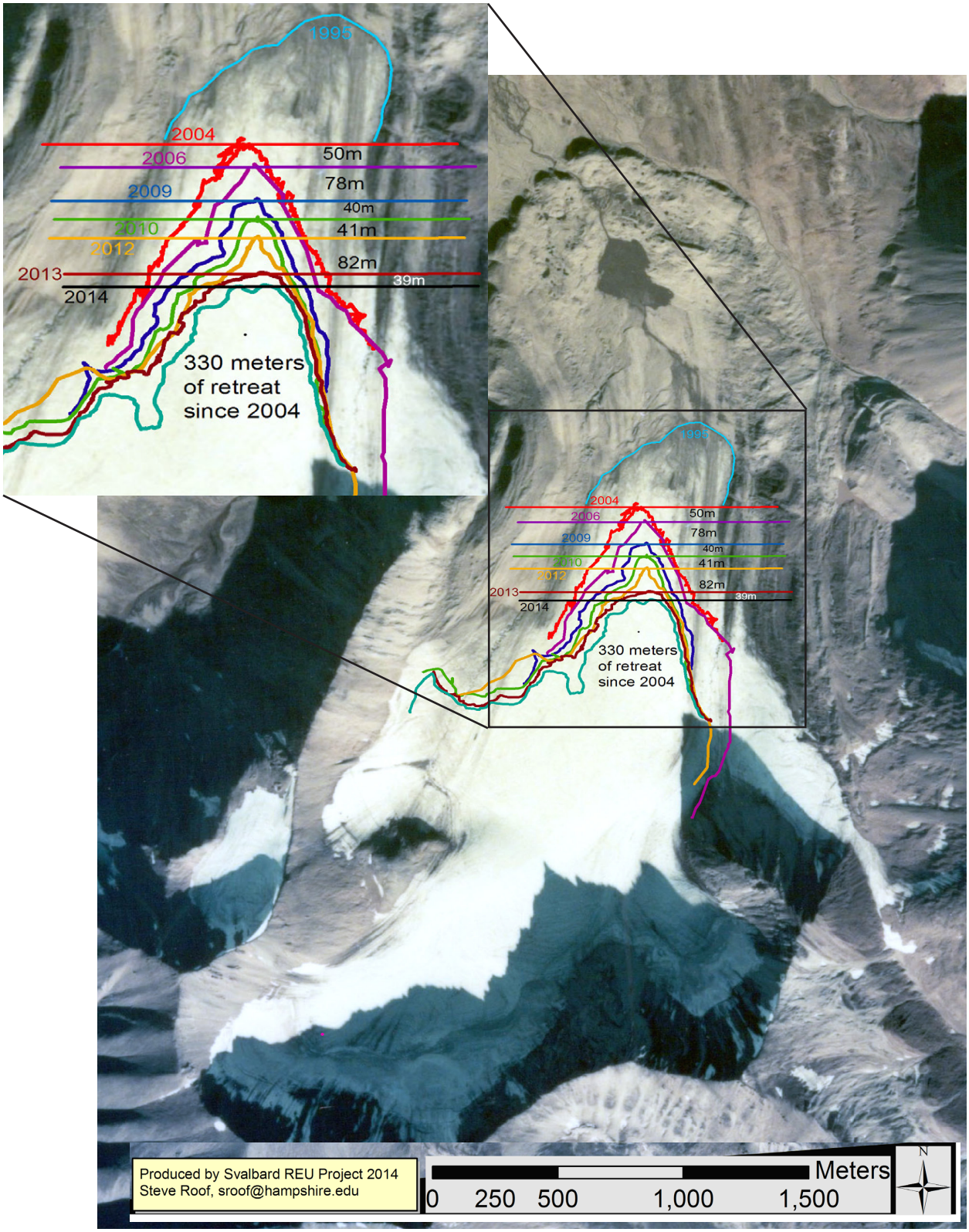

Figure 4.10: The retreat of Linnébreen since 2004 in meters. The glacier has retreated over 330m over the last 12 years. (From Roof, 2014; Modified by Walther, 2015)

the hydrological shoulder seasons (SS) from April-May and September-October. In Svalbard, SS precipitation can account for up to 26% of a catchment's annual discharge (Nowak and Hodson, 2013). Over the last decade, an increasing fraction of this precipitation has been deposited as rain. Nowak and Hodson (2013) noted that this change is most prominent during the fall, because September precipitation has the largest influence on catchment hydrology. The average September air temperature fluctuates around 0°C., thus controlling whether precipitation will be deposition as rain or snow.

During a SS event, the deposition of snow and ice holds the precipitation in the catchment without transporting sediment into Linnévatnet. However, if there is a rain on snow event, the solid precipitation can be converted into water and is then available to entrain sediment as it flows towards the lake. Thus, the early fall storage of snow in a basin may later increase the active runoff, adding to the runoff of a particular event. This model is most applicable for the 9/4/14-9/18/14 storm events (E4). Assuming the storage of ~20 mm of precipitated snow across the landscape, the subsequent 40 mm of rainfall deposited in 1 day, should cause the system to respond as if ~60 mm of precipitation had fallen in a single day (Figure 4.7). This increase of energy within the system allows for the greater mobilization of sediment across the basin and not just through Linnéelva.

Geochemical Interpretation

The annual geochemical interpretation is characterized by Principal Component Analysis (PCA) where the element's relation to the Principle Components, PC1 and PC2 values, represents the amount of variance that elemental constituent accounts for within the bulk sediment sample.

Multiple factors need to be taken into consideration in order to interpret the geochemical data. First, the 2014 samples were dry and cracked, having been split the previous year. Second, both the 2012 and 2014 ITRAX receiving tube scans were run without the application of the plastic film to prevent drying during the XRF analysis, thus exacerbating this problem. These cracks and changes in sediment surface impact the elemental counts (kcps), introducing an artificial variability which could strongly impact the outcomes of the PCA. Finally, the relative difference between the sediment traps in this study needs to be considered. For 2015, the bottom-most samples were analyzed for XRF data, while the 2012 and 2014 samples utilized traps situated 3 m to 18 m above the lake bottom, due to destructive sampling in previous studies. The difference in sediment thickness between the samples at a mooring, was ≤ 20 cm (Walther, 2015). This water column position discrepancy may preclude sedimentation associated with either underflows or turbidity currents (Smith and Ashley, 1985) from being captured in the upper traps.

While all three years experienced similar timings of large precipitation events, they exhibited geochemical variations between themselves (Table 3.1). Across the three sampling years, mooring D exhibited the greatest inter-annual variability, attributed predominantly to its position in the water column. The PC1 values of Si, Ti, and Ca show little change between D3_12 and D3_14, but they both vary significantly from D4_15. The two D3 samples were located 3 m above the lake floor.

All four 2013-2014 samples showed similar strong correlations to PC1. Assuming sediment delivery is compositionally similar for a single event, the high covariance is explained by ≥50% of the 2013-2014 sediment budget deposition occurring in association with the August 8th storm

(Walther, 2015). During the earlier 2 years, the variability of sediment geochemistry changed throughout the basin. This is to be expected, because during a less extreme precipitation year than 2013-2014, sedimentation may vary in its point sourcing around the lake (e.g. Linnéelva, solifluction, wave reworking). If this source change is not proportional (i.e. increase in sediment source does not always cause an increase in a second source) this source variability should be represented by lower correlations between the individual elements, of annually resolved samples, with PC1. Thus it stands to reason that it may be possible to determine a large storm layer based on the strong covariance of elemental constituents in a single varve.

Sediment Provenance

Principle component analysis was also used to experimentally examine the geochemistry associated with each event in 2014-2015, and each season in 2011-2012 and 2013-2014. The relationship between elements during an event were ***interpreted*** as follows: if a suite of elements have a strong correlation to the variance (PC value approaches |1|) within an event, they are assumed to be the dominant elemental constituents for that event. Elements which cluster together vary together, and point to a common source. Lower PC values suggest higher variability, and thus allude to the influence of different point sources.

Linnéelva is the main sediment source for Linnévatnet (Svendsen and Mangerud, 1997). Perreault (2006) found more than 50% of the coarse-grained material entering the lake from Linnéelva to be quartz and muscovite. Thus it could be assumed that the elemental signature of Linnéelva is represented by Si and the major elemental constituents associated with aluminosilicate rich sediment such as Ti, Al, K and Fe (Martin-Puertas et al., 2011). However, the exact geochemical signature of Linnéelva is suspected to be more complicated, but it is currently poorly constrained. The river's sediment budget may ultimately be attributed to glacial erosion by Linnébreen (Svendsen et al., 1989). The glacier overlies quartzite bedrock, and thus could be expected to contribute mainly Si, Ti and Zr to the river's sediment load. Runoff from the series of cirque glaciers and nival patches in the hills surrounding upper Linnédalen may also be contributing sediment associated with both the carbonate and metamorphic bedrock to the river's sediment load. Additionally, the deposition of glaciomarine sediment (Mangerud et al., 1987) following the deglaciation of Linnédalen [12,300-9600 BP] (Svendsen et al., 1989), may have developed a mixture of various lithologies in the valley (Retelle, personal communication) accessible to Linnéelva by erosion. To the east of Linnéelva, the 'twin fan' leads down from the carbonate rich eastern valley wall. This fan is fed by snow melt, groundwater, and it has been related to a thermal spring (Snyder et al., 2000). The fan is also subject to periodic icings throughout the winter. Gypsum ($CaSO_4 \cdot 2(H_2O)$) crystals are commonly observed forming on these twin fans (Snyder et al., 2000) suggesting it is another point source of Ca to both Linnéelva and the proximal basin of Linnévatnet. Changes in the relative combination of these sources may create a dynamic and variable geochemical signature within Linnéelva.

Based on the preeminence of quartzite-rich glacially eroded sediment, for the purpose of an exploratory analysis, it is assumed that a strong covariance of Si, Ti, Zr, K, Fe and Al* represents a dominant influence of Linnéelva on event sedimentation. In examining the relation of elements during E2 (Figure 4.11), when sedimentation was dominated by Linnéelva input, this assumption holds true. Fe, Ti, Zr and Si vary together (Appendix A, p.103), and have resultant PC1 values >0.82, demonstrating the dominance of Linnéelva on sediment variability. It should be noted that Ca and Sr covary, inversely to this Linnéelva signature.

During E3, precipitation began to influence the glaciofluvial dominance on sedimentation. Fe, Ti, and Al exhibit a strong covariance (Appendix A, pg. 108), yet the influence of these 'Linnéelva' elements on the

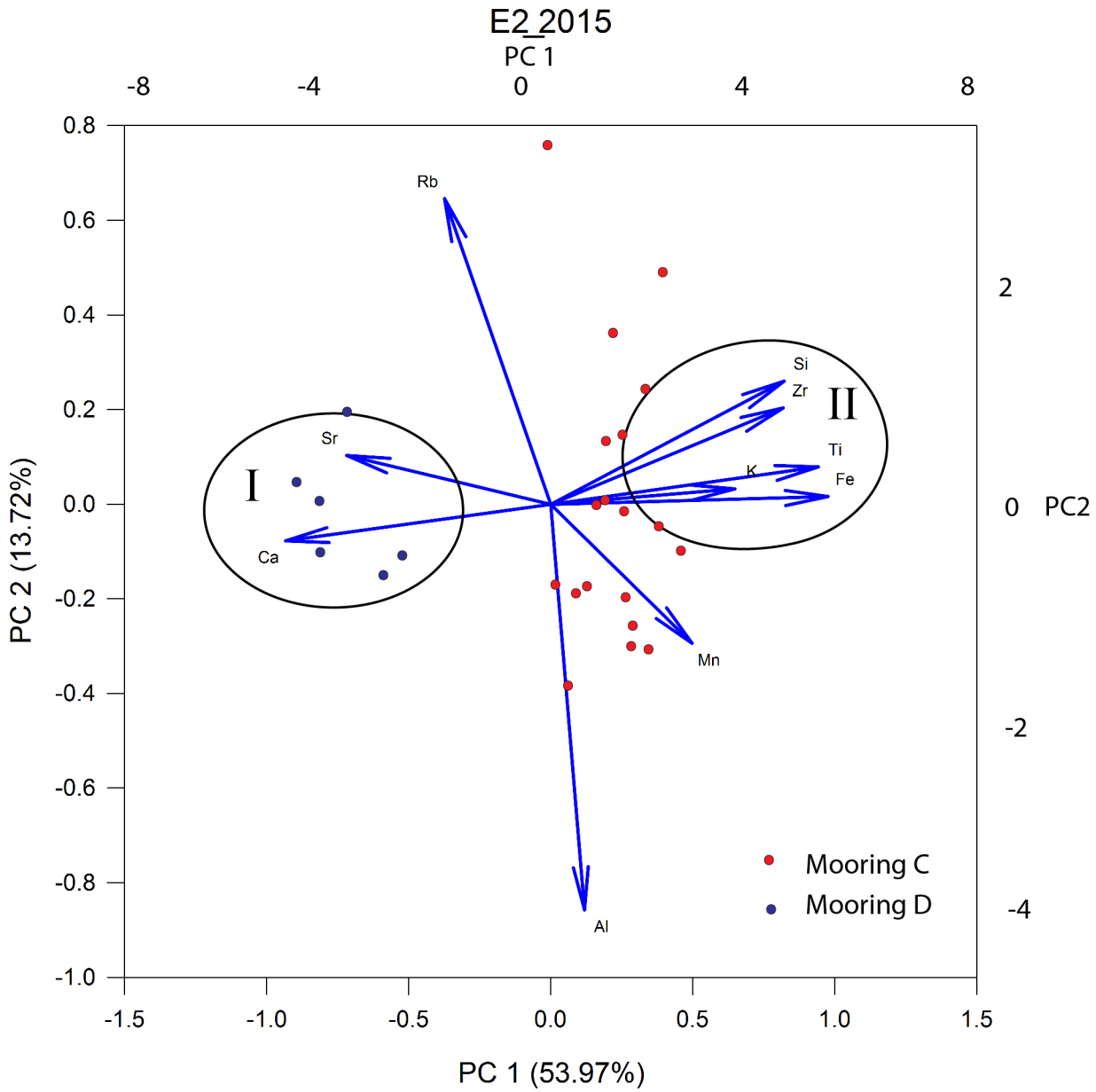

Figure 4.11: PCA Biplot of E2. The fit of each elementals to the resultant PC is presented by vectors related to the left and bottom axis. The relationship of each sampling point to the calculated PC is represented by the 'scores' or dots ploted against the top and right axis. No coordinate rotation has been applied to the data. This applies for all following Biplots.

overall sedimentation is decreased (PC1≤0.60) relative to the E2 event which was controlled by glacial meltwater alone. Additionally, the strong covariance of Ca, Sr and Rb combined with a highly fitted correlation matrix [r>0.69] (Appendix A, pg. 108) suggests a point source of Ca active during this event. Thus, the changes between E2 and E3 demonstrate a notable change in geochemical signature between *glacially dominated* fluvial input and *glacially influenced* fluvial input into the lake.

**Al is at the low end of the detectability scale for Mo X-ray tubes, and thus it has a high noise to signal ratio (Cuven et al., 2015). Al also exhibits low correlations when examining the fitted correlation matrix (Appendix A), thus in this study it is not expected to exhibit strong covariance.*

If E2 is considered a glacially dominated end member, then E4 should represent the precipitation dominated end of the seasonal sedimentation influence spectrum; meaning all sedimentary transport channels are mobilized during the event. The visible runoff down the alluvial fans on both the eastern and western shores of Linnédalen (Figure 4.7b) provides evidence of sediment transport from distinctive point sources. The provenance from east and west fans is reflected in the event's PCA with a wide variation among all elemental constituents (Figure 4.13), even among coarse-grained analogs (Cuven, 2010). E4 resulted in two or 3 general clusterings of elemental data. First, Ca, Mn, Si and Rb are clustered together. This clusters relation to the 'score' of sample points suggest a connection with sedimentation at Mooring sites G and H. Second, moorings C and D may have a dominant influence on the clustering of Ti and Si, .

The settling of fine-grained E4 sediment in the distal basin (E4a) resulted in three clusters of elemental constituents (Figure 4.14). Cluster II suggests that the elements associated with Linnéelva dominated the overall variation. This seems possible, particularly considering the fine grain size associated with E4a (Figure 4.1). During E4, assuming all sediment transport mechanisms were mobilized, coarse-grained material deposited in the deep basin may have been from a local point source along the valley walls, thus explaining the variation seen in E4 throughout the basin. However, the fine sediment from Linnéelva, transported by sediment plumes down the lake (Figure 4.7c) was allowed to settle slowly out of the water column over time developing sedimentary unit E4a. The settling of fine grained sedimentation is a mixture of the entire lake, and not a point source. In which case, the fine grained material associated with the storm event is related to Linnéelva.

There are similarities between the winter sedimentation in the proximal basin (Figure 4.15) and E4a (Figure 4.14) in the distal basin, signifying that the unit interpretation of unit E4 overlaps with, or grades into, the winter unit. During the winter, the low variance suggests that a well-mixed suspended sediment content is deposited in specific geochemical compositions, which vary relative to each other. Because the rate of settling is related to grain size, Zr should be inversely related to the variation in sediment geochemistry during this period. Once the coarse sediment (which may be related to a local point source) is deposited, the entire lake should be subject to the homogeneous deposition, under the ice. And the determinant factor in the elemental variation of this homogeneous deposition would be tied to the changes in grain size, as that is the major factor influencing winter sedimentation under the ice (Gilbert, 2003).

Sediment Provenance in '11-'12 and '13-'14

When the '13-'14 sediment traps were analyed at an annual resolution, there was a strong covariance across the lake (Table 3.1). If each season is examined (Figure 4.16) separately, a similar low variability is seen throughout the year (Figure 4.18). This is because the summer sedimentation was dominated by a large event deposit, which resulted in the settling of associated fines throughout the year (Walther, 2015). Thus it appears that large episodic events can control the sediment geochemistry throughout the year. In '11-'12 seasonal sediment stratigraphy (Figure 4.17) suggests a 'normal' year with a precipitation-induced sediment unit during the late summer season (Obermyer, 2012). While '11-'12 showed a greater degree of variability between elements than '13-'14 (Figure 4.19), there may be a relationship between certain elements that persists throughout the year. For example, the component vectors for Si and K are inversely related from the summer through the winter, but this relationship changes during spring sedimentation, suggesting the possibility of a seasonal sedimentation signature in the lake.

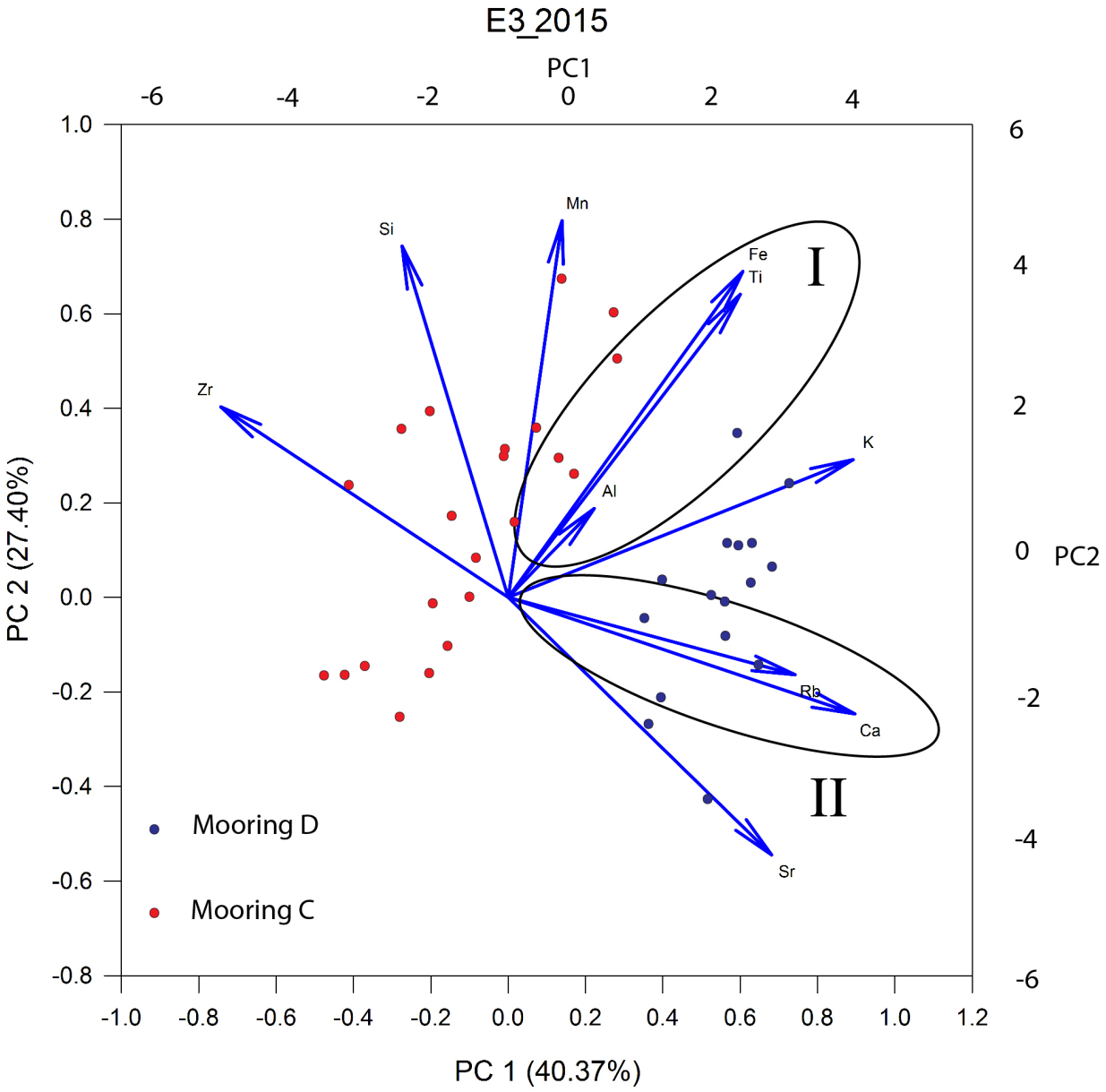

Figure 4.12: PCA Biplot of E3.

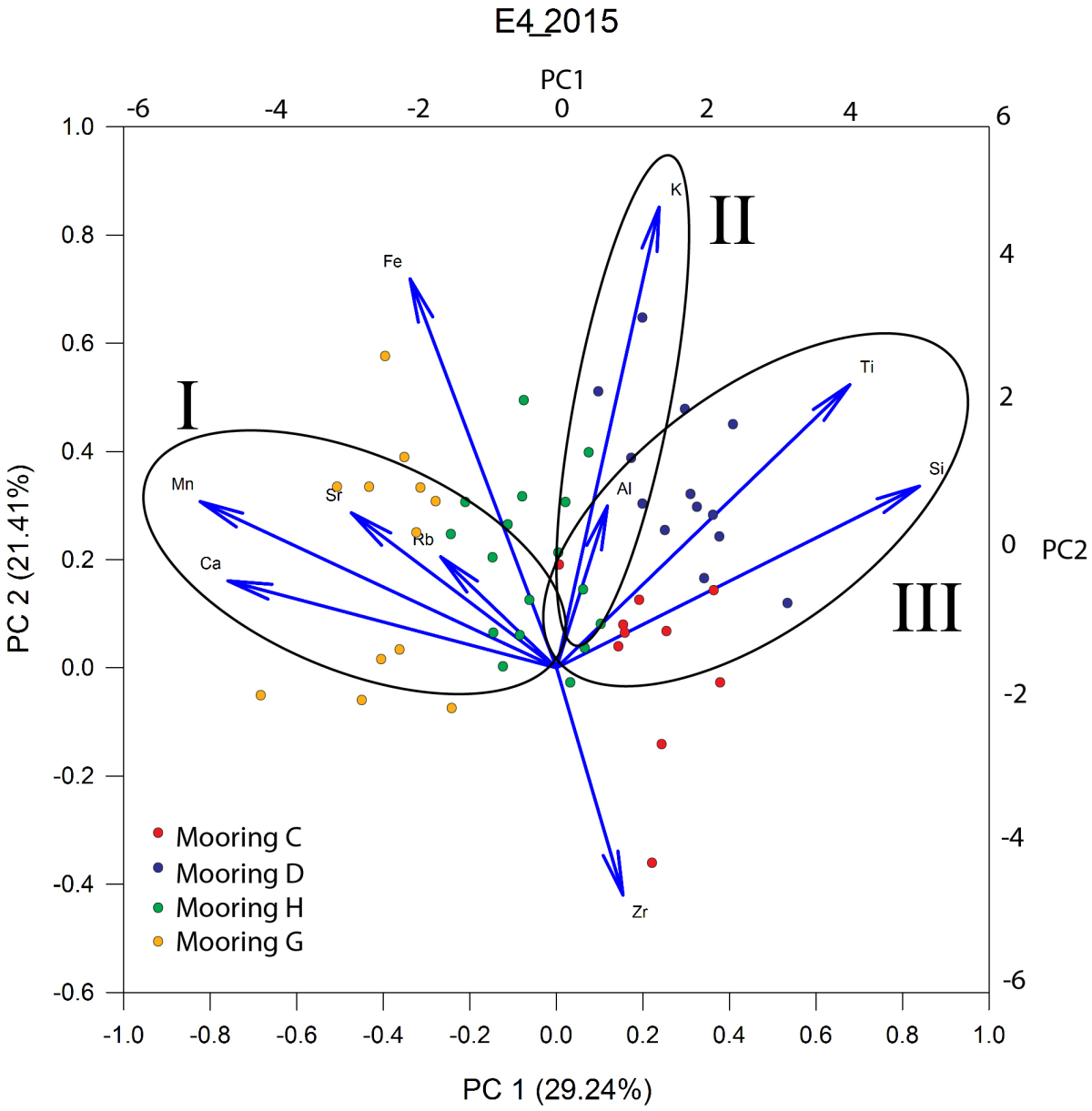

Figure 4.13: PCA Biplot of E4.

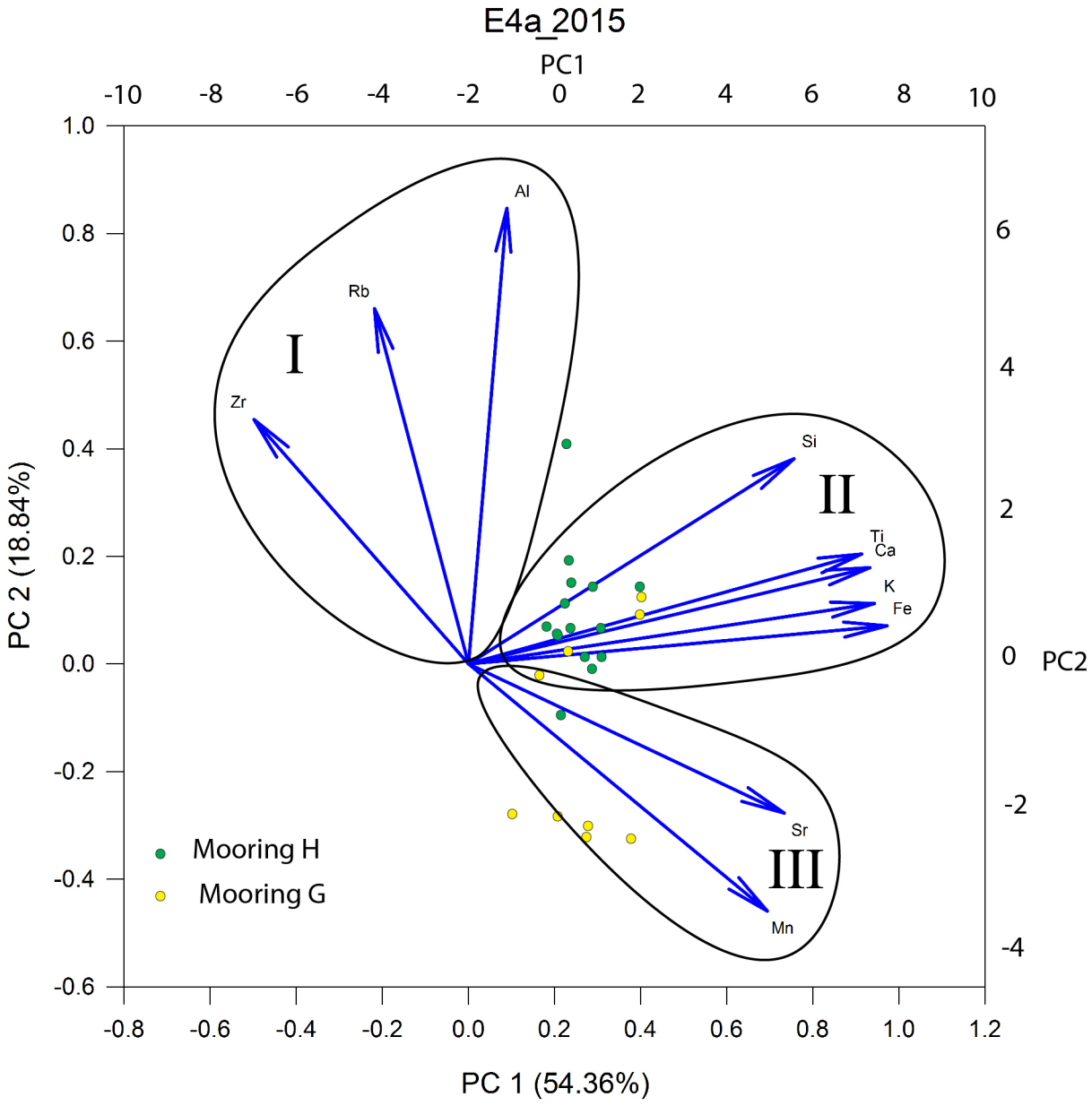

Figure 4.14: PCA Biplot of E4a.

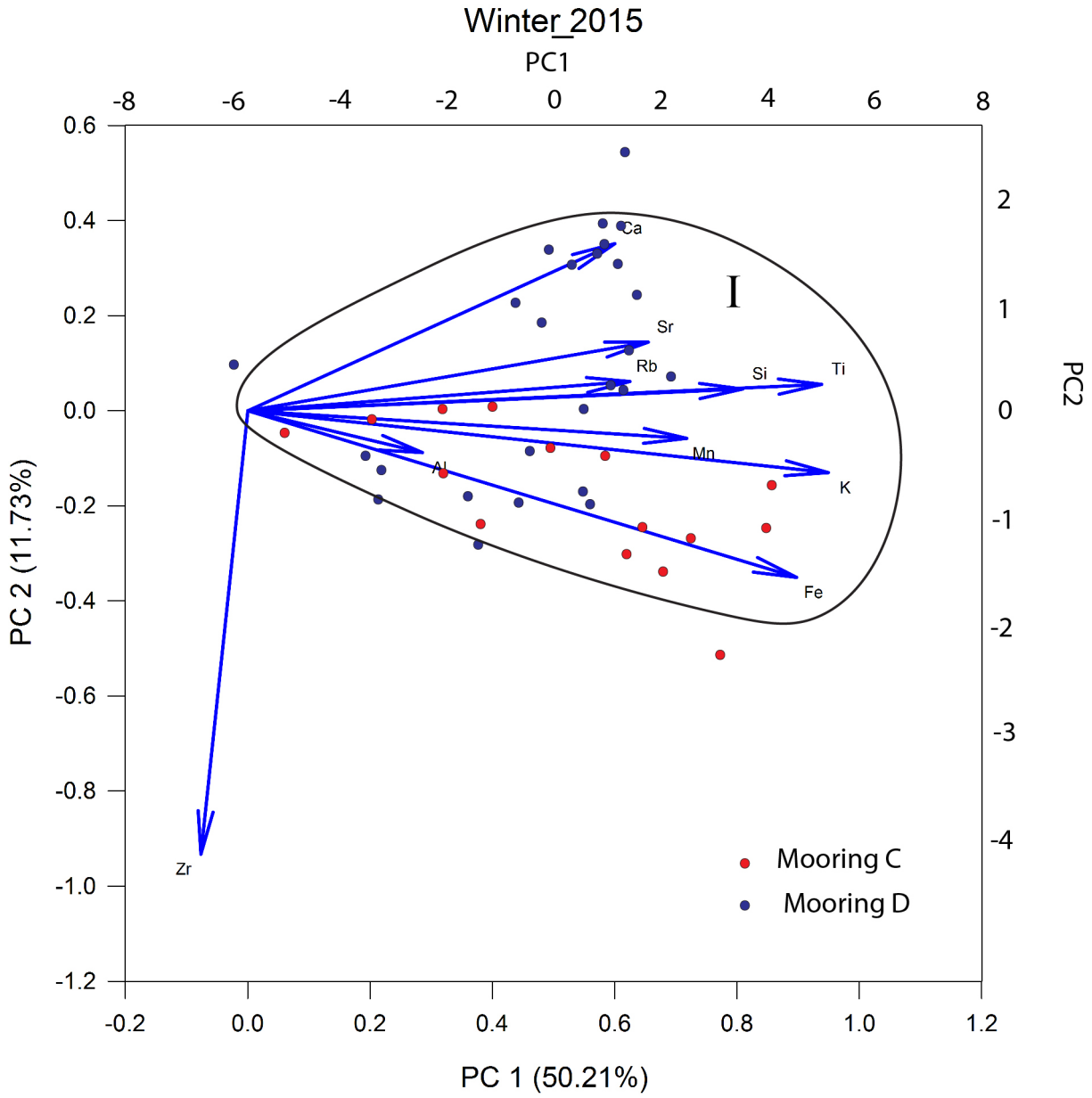

Figure 4.15: PCA Biplot of Winter sedimentation.

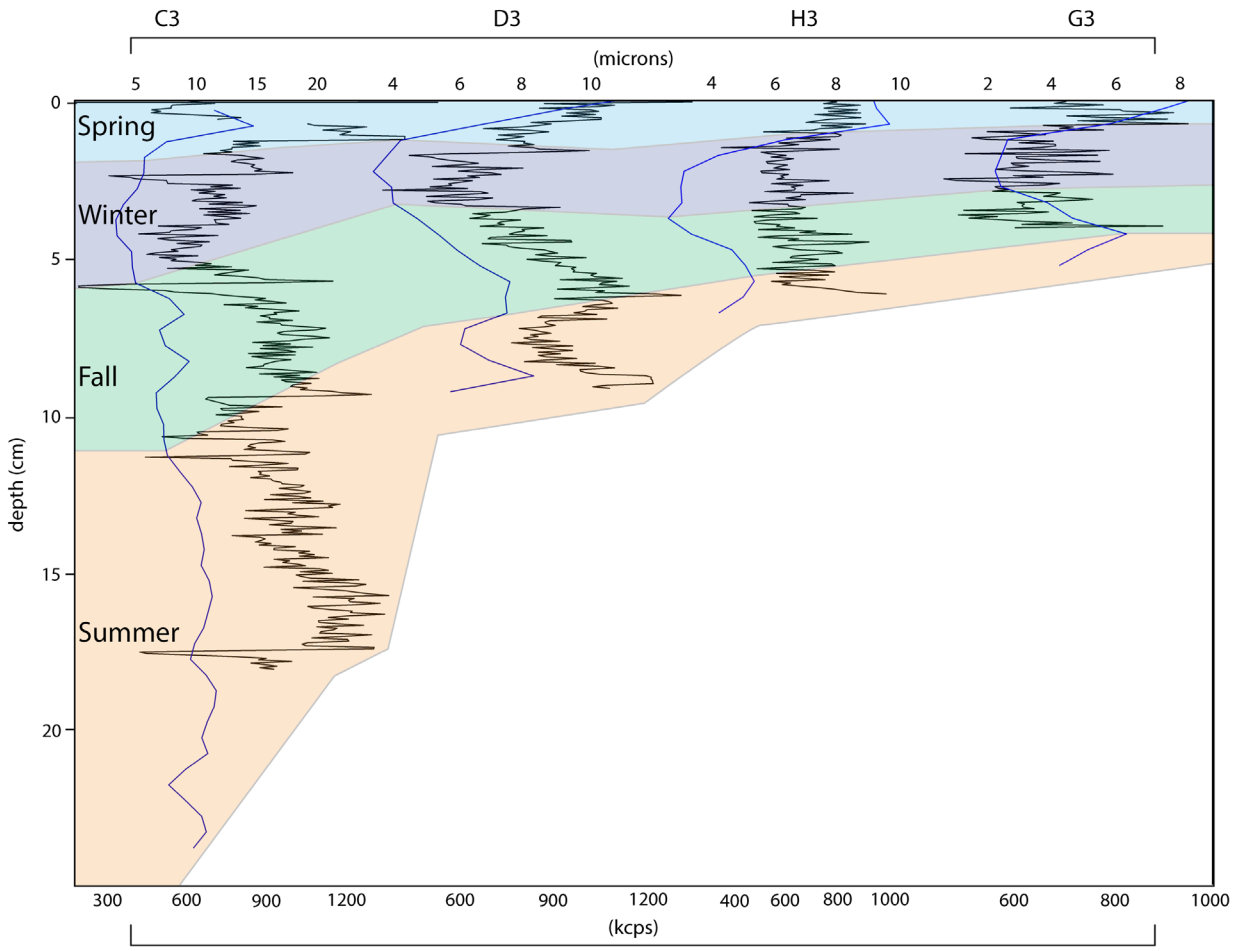

Figure 4.16: The seasonal interpretation of 2013-2014 receiving tubes determined by peaks in grain size (blue). Zr content is presented for visual comparison (black).

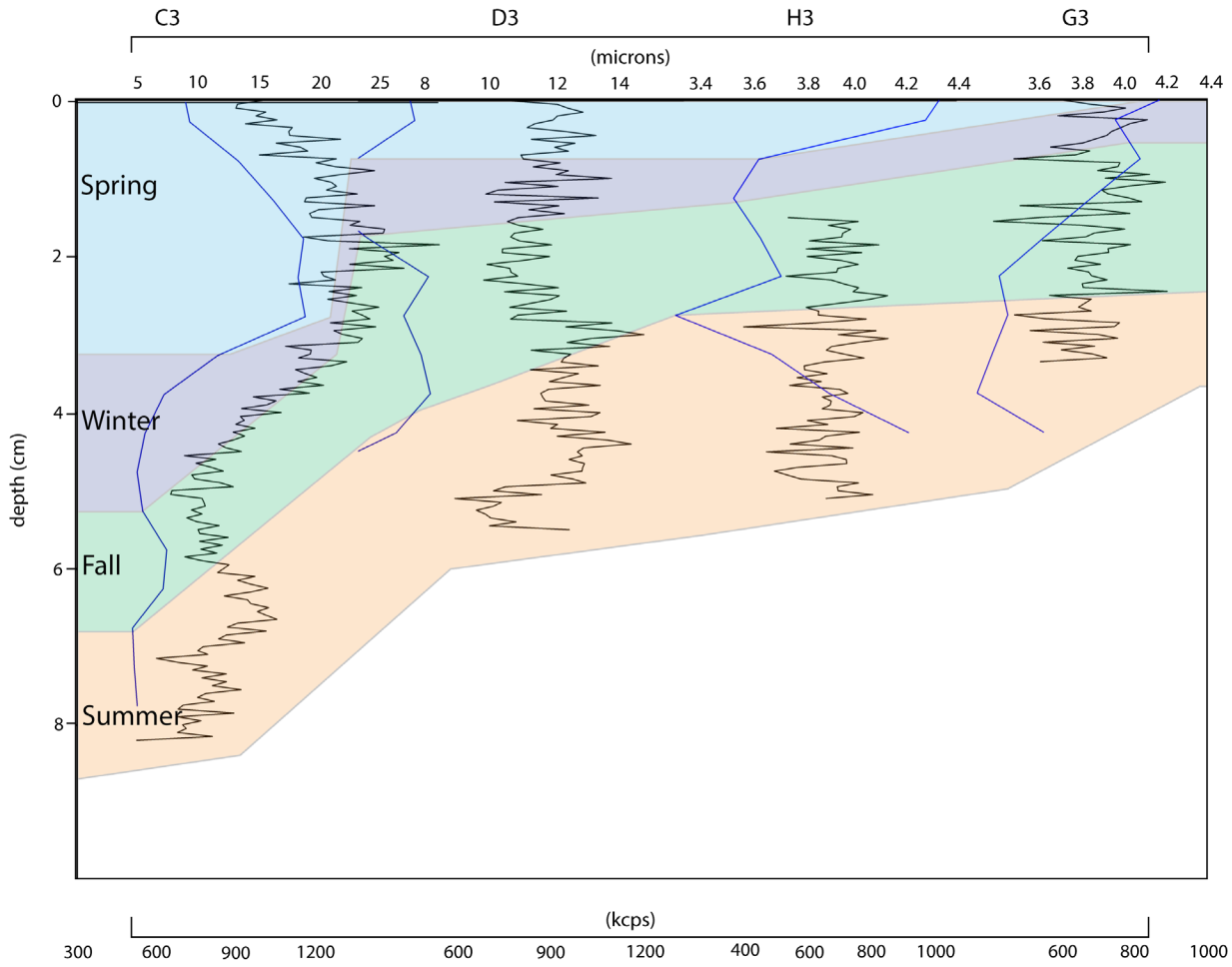

Figure 4.17: The seasonal interpretation of 2013-2014 receiving tubes determined by peaks in grain size (blue). Zr content is presented for visual comparison (black).

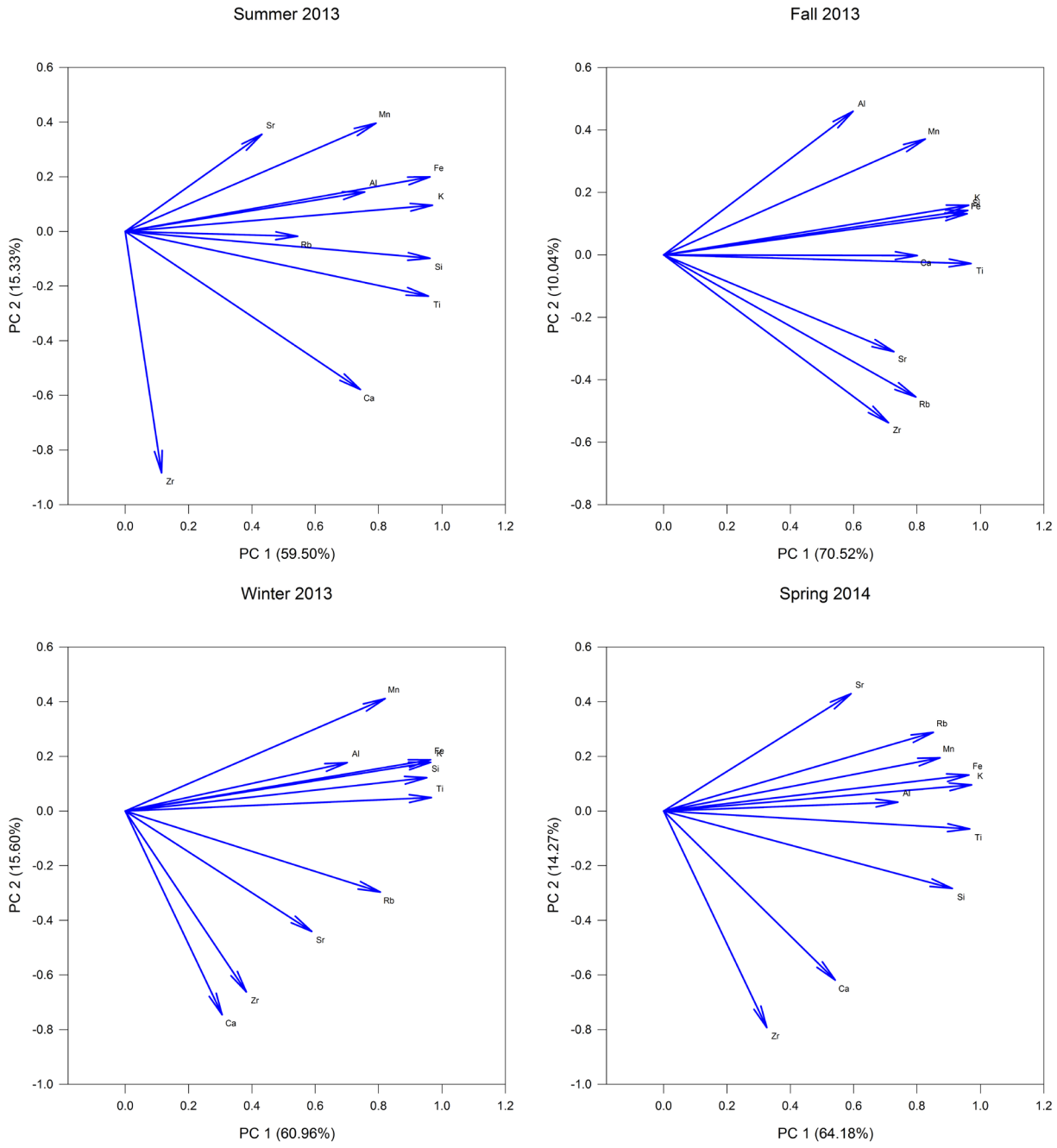

Figure 4.18: 2013-2014 seasonal elemental vector Biplots. There is a strong covariance between most elemental constituents throughout the year.

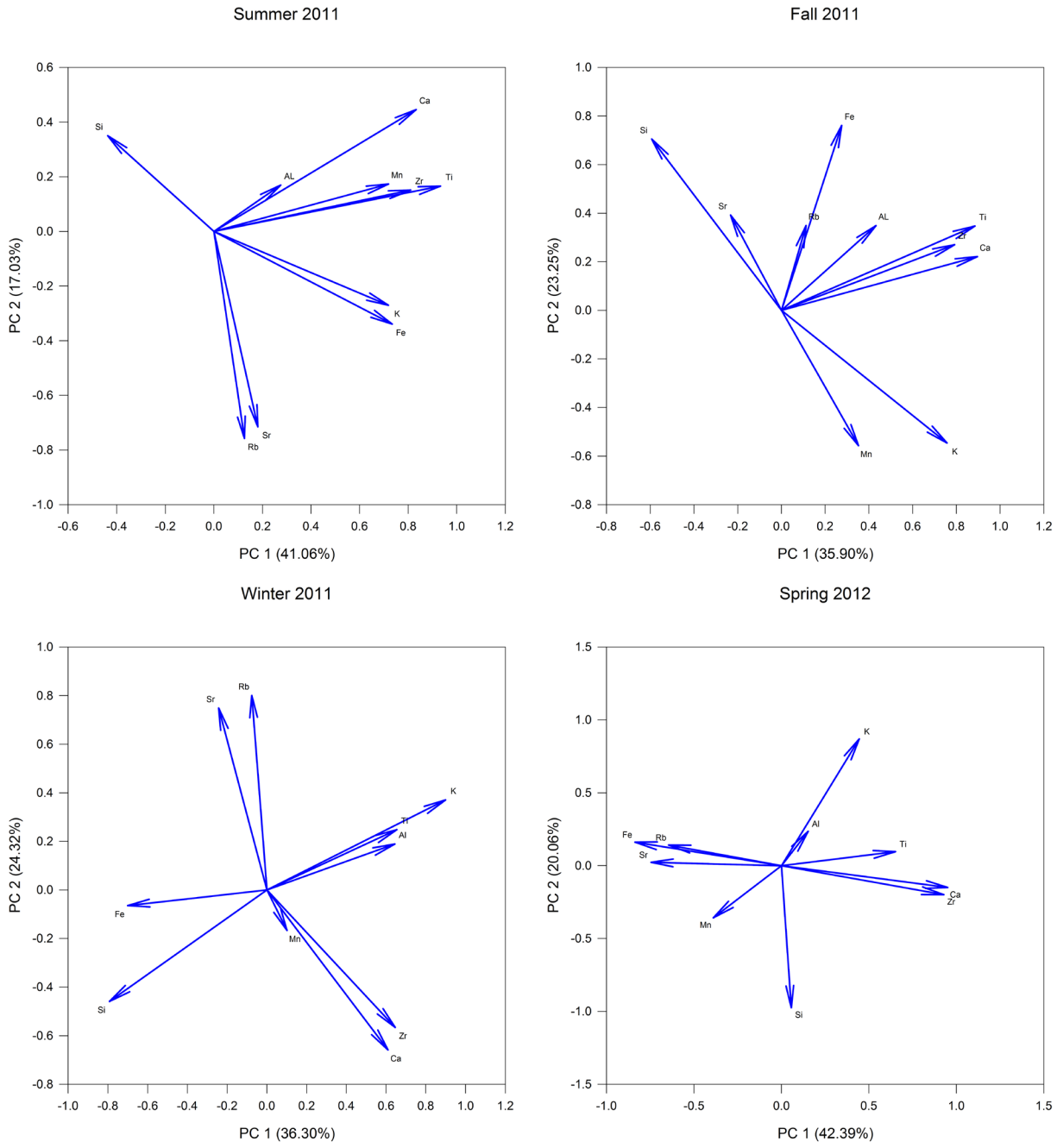

Figure 4.19: 2013-2014 seasonal elemental vector Biplots.

Conclusions

Three years of sediment deposition from High Arctic lake, Linnévatnet, were analyzed in order to understand the relationship between hydrometeorological conditions and seasonal sedimentation. Heavy late-season precipitation events occurred each year (‘11-‘12, ‘13-‘14, ‘14-‘15). These similar meteorological conditions resulted in different sedimentary deposits, suggesting the presence of a large inter-annual variability. This variability is attributed to changes in basin storage capacity. The timing of precipitation during the shoulder season, as later events were more likely to experience the storage of water in the system as snow, which can then be released during a rain-on-snow event, amplifying the flow during such events. These late season, multi-day heavy precipitation events can result in the activation of the valley side alluvial fans in Linnédalen, and sediment point sources around the lake. Within the ‘14-‘15 recieving tubes, increased precipitation corresponded to a decreased component loadings of relationship between ‘linneelva’ elements and PC1.

An idealized Linneelva signature (covariance between Fe, Ti, Zr and Si) was present in the ‘14-‘15 samples, but was not well defined in ‘11-‘12 or ‘13-‘14. In ‘14-‘15, greater variation among elemental relationships, as described by PCA results, during storm events relative to E2 showed a potential for determining the geochemical signatures of both Linnéelva and the various point sources around the lake. Additionally, the subannual variablity in fall sediment chemistry supports the activation of alternative sediment sources during large precipitation events.

Thus, large episodic events exhibit a dominance on the variability of annual sediment geochemistry. A single dominant source likely results in high covariance between its constituent elements. The settling of sediment from large storms influences the relationship between the entire year’s geochemistry. Thus larger storms have an annual signature, which may be useful in determining large storm events in the paleorecord.

Future studies

This study suggests the potential for establishing a geochemical signature of seasonal events within the lake system, but there is a need for better constraints. The use of ICP-AMS to determine bulk sediment composition (Cuven et al., 2010) is recommended to better understand the quantitative elemental concentrations. This would allow for the better determination of what is truly present in the samples and discerning the relationship between the signal-noise ratio and the element near the detection limit of the ITRAX scanner.

Additionally, redundancy analysis as suggested by Martin-puertas et al. (2011) may help to determine the relationship between geochemical analysis and mineralogical analysis. This will allow the information presented in this study to be paired with more concrete conclusions.

Works cited:

Akerman, H. J., 2005, Relations between slow slope processes and active-layer thickness 1972–2002, Kapp Linné, Svalbard: Norwegian Journal of Geography, v. 59, no. 2, p. 116-128.

Asper, V., 1987, A Review of Sediment Trap Technique: Marine Technology Society Journal, v. 21, p. 18-25.

Arnold, M., 2009, Sedimentation in High-Arctic Lake, Linnèvatnet, Svalbard: A Modern Process Study Using Sediment Traps: Bates College Unpublished Thesis.

Bakke, J., Lie, Ø., Heegaard, E., Dokken, T., Haug, G., Birks, H., Dulski, P., and Nilsen, T., Rapid oceanic and atmospheric changes at the end of the Younger Dryas cold period, in Proceedings EGU General Assembly Conference Abstracts2009, Volume 11, p. 14016.

Benn, D., and Evans, D. J., 2014, Glaciers and glaciation, Routledge.

Blair, T. C., and McPherson, J. G., 1994, Alluvial fans and their natural distinction from rivers based on morphology, hydraulic processes, sedimentary processes, and facies assemblages: Journal of sedimentary research, v. 64, no. 3.

Bogen, J., and Bønsnes, T. E., 2003, Erosion and sediment transport in High Arctic rivers, Svalbard: Polar Research, v. 22, no. 2, p. 175-189.

Boyum, A., and Kjensmo, J., Physiography of Lake Linnévatn, Western Spitsbergen, in Proceedings Proceedings: 20 th Congress, Internationale Vereinigung fur Theoretische und Angewandte Limnologie1978.

British Ocean Sediment Core Research Facility (BOSCORF), 2012, ITRAX-High-resolution XRF analysis of sediment coures. [webpage] http://www.boscorf.org/instruments/itrax-high-resolution-xrf-analysis-sediment-cores.

Bradley, R. S., and England, J. H., 2008, The Younger Dryas and the sea of ancient ice: Quaternary Research, v. 70, no. 1, p. 1-10.

Carmack, E. C., Gray, C. B., Pharo, C. H., and Daley, R. J., 1979, Importance of lake-river interaction on seasonal patterns in the general circulation of Kamloops Lake, British Columbia: Limnol. Oceanogr, v. 24, no. 4, p. 634-644.

Christiansen, H. H., 2010, The thermal state of permafrost in the nordic area during the international polar year 2007-2009: Permafrost and periglacial processes, v. 21, no. 2, p. 156-181.

Christiansen, H. H., Humlum, O., and Eckerstorfer, M., 2013, Central Svalbard 2000–2011 Meteorological Dynamics and Periglacial Landscape Response: Arctic, Antarctic, and Alpine Research, v. 45, no. 1, p. 6-18.

Chutko, K. J., and Lamoureux, S. F., 2008, Identification of coherent links between interannual sedimentary structures and daily meteorological observations in Arctic proglacial lacustrine varves: potentials and limitations: Canadian Journal of Earth Sciences, v. 45, no. 1, p. 1-13.

Croudace, I. W., Rindby, A., and Rothwell, R. G., 2006, ITRAX: description and evaluation of a new multi-function X-ray core scanner: Geological Society, London, Special Publications, v. 267, no. 1, p. 51-63.

Cuven, S., Francus, P., Crémer, J. F., and Bérubé, F., 2015, Optimization of Itrax Core Scanner Protocols for the Micro X-Ray Fluorescence Analysis of Finely Laminated Sediment: A Case Study of Lacustrine Varved Sediment from the High Arctic, Micro-XRF Studies of Sediment Cores, Springer, p. 279-303.

Cuven, S., Francus, P., and Lamoureux, S. F., 2010, Estimation of grain size variability with micro X-ray fluorescence in laminated lacustrine sediments, Cape Bounty, Canadian High Arctic: Journal of Paleolimnology, v. 44, no. 3, p. 803-817.

Dallman, W.K., Hjelle, A., Andresen, A., Ohta, Y., Salvigsen, O., 1992, Geological Map of Svalbard 1:100 000 B9G Isfjorden: Norsk Polar Institutt, Temakart nr. 16

De Haas, T., Kleinhans, M. G., Carbonneau, P. E., Rubensdotter, L., and Hauber, E., 2015, Surface morphology of fans in the high-Arctic periglacial environment of Svalbard: Controls and processes: Earth-Science Reviews, v. 146, p. 163-182.

Divine, D., Isaksson, E., Martma, T., Meijer, H. A., Moore, J., Pohjola, V., van de Wal, R. S., and Godtliebsen, F., 2011, Thousand years of winter surface air temperature variations in Svalbard and northern Norway reconstructed from ice core data: Polar Research, v. 30.

Dowey, C. W., and Retelle, M. J., 2013, 600 Years of Late Holocene Climate Variability Inferred from a Varved Proglacial Sediment Record Linnévatnet, Svalbard, Norway.

Dunteman, G. H., 1989, Principal components analysis, Sage.

Eckerstorfer, M., and Christiansen, H. H., 2011, The “high Arctic maritime snow climate” in central Svalbard: Arctic, Antarctic, and Alpine Research, v. 43, no. 1, p. 11-21.
Eckerstorfer, M., Christiansen, H. H., Vogel, S., and Rubensdotter, L., 2013, Snow cornice dynamics as a control on plateau edge erosion in central Svalbard: Earth Surface Processes and Landforms, v. 38, no. 5, p. 466-476.
Førland, E., Hanssen-Bauer, I., and Nordli, P., 1997, Climate statistics and longterm series of temperature and precipitation at Svalbard and Jan Mayen: DNMI report, v. 21, no. 97, p. 43.
Forman, S., Lubinski, D., Ingólfsson, Ó., Zeeberg, J., Snyder, J., Siegert, M., and Matishov, G., 2004, A review of postglacial emergence on Svalbard, Franz Josef Land and Novaya Zemlya, northern Eurasia: Quaternary Science Reviews, v. 23, no. 11, p. 1391-1434.
Forman, S. L., 1989, Late Weichselian glaciation and deglaciation of Forlandsundet area, western Spitsbergen, Svalbard: Boreas, v. 18, no. 1, p. 51-60.
Francus, P., Bradley, R. S., Lewis, T., Abbott, M., Retelle, M., and Stoner, J. S., 2008, Limnological and sedimentary processes at Sawtooth Lake, Canadian High Arctic, and their influence on varve formation: Journal of Paleolimnology, v. 40, no. 3, p. 963-985.
Gilbery, R., 2003, Lacustrine sedimentation. In Encyclopedia of sedimentology and sedimentary Rocks. *Edited by* G.V. Middleton. Kluwer Academic Publishers, Dordrecht, The Netherlands, p. 404-408.
Gogolek, W. L., W., 1980, Preliminary geomorphological characteristic of Lindalens (Spitsbergen, Svalbard Archipelago): Polish Polar Research v. 1, no. 4, p. 7-19.
Hagen, J. O., Melvold, K., Pinglot, F., and Dowdeswell, J. A., 2003, On the net mass balance of the glaciers and ice caps in Svalbard, Norwegian Arctic: Arctic, Antarctic, and Alpine Research, v. 35, no. 2, p. 264-270.
Hald, M., Andersson, C., Ebbesen, H., Jansen, E., Klitgaard-Kristensen, D., Risebrobakken, B., Salomonsen, G. R., Sarnthein, M., Sejrup, H. P., and Telford, R. J., 2007, Variations in temperature and extent of Atlantic Water in the northern North Atlantic during the Holocene: Quaternary Science Reviews, v. 26, no. 25, p. 3423-3440.
Hanssen-Bauer, I., 2002, Temperature and precipitation in Svalbard 1912–2050: measurements and scenarios: Polar Record, v. 38, no. 206, p. 225-232.
Hjelle, A., Lauritzen, O, Salvigsen, O., and Winsnes, T.S., 1986, Geological map, Svalbard 1:100.000, sheet B10G Van Mijenfjorden. *Norsk polarinstitutt Temakart No. 2*
Hodgkins, R., 1997, Glacier Hydrology in Svalbard, Norwegian High Arctic: Quaternary Science Reviews, v. 16, p. 957-973.
Hodson, A., 1994, Climate, hydrology and sediment transfer process interactions in a sub-polar glacier basin, Svalbard: University of Southampton.
Hodson, A., 1998, Suspended sediment yield and transfer processes in a small High-Artic glacier basin, Svalbard: Hydrological processes, v. 12, no. 1, p. 73-86.
Hodson, A., Tranter, M., Gurnell, A., Clark, M., and Hagen, J. O., 2002, The hydrochemistry of Bayelva, a high Arctic proglacial stream in Svalbard: Journal of Hydrology, v. 257, no. 1, p. 91-114.
Humlum, O., 2002, Modelling late 20th century precipitation in Nordenskiold Land, Svalbard, by geographic means: Norsk Geografisk Tidsskrift-Norwegian Journal of Geography, v. 56, p. 96-103.
Humlum, O., 2005, holocene permafrost aggradation in Svalbard, in Harris, C. M., J. B., ed., Cryospheric Systems: Glaciers and Permafrost, Volume 242: London, Geological Society, London, Special Publications, p. 119-130.
Humlum, O., Christiansen, H. H., and Juliussen, H., 2007, Avalanche-derived rock glaciers in Svalbard: Permafrost and Periglacial Processes, v. 18, no. 1, p. 75-88.
Humlum, O., Instanes, A., and Sollid, J. L., 2003, Permafrost in Svalbard: a review of research history, climatic background and engineering challenges: Polar research, v. 22, no. 2, p. 191-215.
Humlum, O. E., B.; Hormes, A.; Fjordheim, K.; Hansen, O.; Heinemeier, J., 2005, Late-Holocene glacier growth in Svalbard, documented by subglacial relict vegetation and living soil microbes: The Holocene, v. 15, no. 3, p. 396-407.
Humlum, O. I., A.; Sollid, J. L., 2003, Permafrost in Svalbard: a review of research history, climatic background and engineering challenges: Polar Research, v. 22, no. 2, p. 191-215.
Hurrell, J. W., and Van Loon, H., 1997, Decadal variations in climate associated with the North Atlantic Oscillation, Climatic Change at High Elevation Sites, Springer, p. 69-94.
Hurrell, J. W., Kushnir, Y., and Visbeck, M., 2001, The north Atlantic oscillation: Science, v. 291, no. 5504, p. 603-605.
Ingolfsson, O., 2011, Fingerprints of Quaternary glaciations on Svalbard: Geological Society, London, Special Publications, v. 354, no. 1, p. 15-31.

Ingólfsson, Ó., and Landvik, J. Y., 2013, The Svalbard–Barents Sea ice-sheet – Historical, current and future perspectives: Quaternary Science Reviews, v. 64, p. 33-60.
IPCC, 2014, Climate Change 2014: Synthesis Report. Contribution of Working Groups I, II and III to the Fifth Assessment Report of the Intergovernmental Panel on Climate Change [Core Writing Team, R.K. Pachauri and L.A. Meyer (eds.)]. IPCC, Geneva, Switzerland, 151 pp.
Killingtveit, Å. P., L.E.; Sand, K, 2003, Water Balance investigations in Svalbard: polar research, v. 22, no. 2, p. 161-174.
Kohler, J., 2007, Acceleration in thinning rate on western Svalbard glaciers: Geophysical research letters, v. 34, no. 18.
Lamb, H. H., 1985, Climatic history and the future, Princeton, N.J, Princeton University Press, v. Book, Whole.
Larsson, S., 1982, Geomorphological Effects on the Slopes of Longyear Valley, Spitsbergen, after a Heavy Rainstorm in July 1972: Geografiska Annaler. Series A, Physical Geography,, v. 64, no. 3/4, p. 105-125.
Leemann, A., and Niessen, F., 1994, Holocene glacial activity and climatic variations in the Swiss Alps: reconstructing a continuous record from proglacial lake sediments: The Holocene, v. 4, no. 3, p. 259-268.
Lewkowicz, A. G., and Wolfe, P. M., 1991, Sediment transport in Hot Weather Creek, Ellesmere Island, NWT, Canada, 1990-1991: Arctic and Alpine Research, p. 213-226.
Liestøl, O., 1977, Pingos, springs, and permafrost in Spitsbergen. Nor. Polarinst. Aarbk 1975, 7-29.
Mangerud, J., and Landvik, J. Y., 2007, Younger Dryas cirque glaciers in western Spitsbergen: smaller than during the Little Ice Age: Boreas, v. 36, no. 3, p. 278-285.
Mangerud, J., Svendsen, J.I., 1990, Deglaciation chronology inferred from marine sediments in a proglacial lake basin, western Spitsbergen, Svalbard: Boreas, v. 19, p. 249-272.
Mangerud, J. B., M.; Elgersma, A; Helliksen, D.; Landvik, J.Y.; Lycke, A.K.; Lonne, I.; Salvigsen, O.; Sandahl, T.; Sejrup, H.P., 1987, The Late WEichselian glacial maximum in western Svalbard: Polar research, v. 5, p. 275-278.
Mann, M., Zhang, Z., Rutherford, S., Bradley, R., Hughes, M., Shindell, D., Ammann, C., Faluvegi, G., Ni, F., 2009, Global Signatures and Dynamical Origins of the Late Ice Age and Medieval Climate Anomaly: Science, v. 326 p.1256-1260.
Martín-Puertas, C., Valero-Garcés, B. L., Mata, M. P., Moreno, A., Giralt, S., Martínez-Ruiz, F., and Jiménez-Espejo, F., 2011, Geochemical processes in a Mediterranean Lake: a high-resolution study of the last 4,000 years in Zonar Lake, southern Spain: Journal of Paleolimnology, v. 46, no. 3, p. 405-421.
National Research Council of Canada (NRCC), 1988, Glossary of Permafrost and Related Ground-Ice Terms. http://globalcryospherewatch.org/reference/glossary_docs/permafrost_and_ground_terms_canada.pdf (Accessed October 2015.
Nelson, A., 2010, A Varved Sediment Aanalysis of 1,000 Years of Climate Change: Linnevatnet, Svalbard: Bates College Unpublished Thesis.
Nowak, A., and Hodson, A., 2013, Hydrological response of a High-Arctic catchment to changing climate over the past 35 years: a case study of Bayelva watershed, Svalbard: Polar Research, v. 32, no. 0.
Nuth, C., Moholdt, G., Kohler, J., Hagen, J. O., and Kääb, A., 2010, Svalbard glacier elevation changes and contribution to sea level rise: Journal of Geophysical Research, v. 115, no. F1.
Obermeyer, D.A., amd Kaufman, D.S, 2013, Hydroclimatic Variability Inferred from Subannual Sediment Pulses in Lake Linnevatnet, Svalbard, 43rd Arctic Workshop, Boulder, CO [Poster].
Ohta, Y., Hjelle, A., Andresen, A., Dallmann, W.K. and Salvigsen, O., 1992. Geological map of Svalbard, scale 1: 100.000, sheet B9G Isfjorden, Temakart 16. Norsk Polarinstitutt, Oslo, Norway.
Ojala, A. E. K., Francus, P., Zolitschka, B., Besonen, M., and Lamoureux, S. F., 2012, Characteristics of sedimentary varve chronologies – A review: Quaternary Science Reviews, v. 43, p. 45-60.
Perreault, L., 2006, Mineralogical Analysis of Primary and Secondary Source Sediments to Linnevatnet, Spitsbergen, Svalbard: Unpublished Bates College Thesis.
Retelle, M., 2015, Personal Communication.
Røthe, T. O., Bakke, J., Vasskog, K., Gjerde, M., D'Andrea, W. J., and Bradley, R. S., 2015, Arctic Holocene glacier fluctuations reconstructed from lake sediments at Mitrahalvøya, Spitsbergen: Quaternary Science Reviews, v. 109, p. 111-125.
Rothwell, R. G., Croudace, I., W., 2015, Twenty years of XRF core scanning marine sediments: What do geochemical proxies tell us?, Micro-XRF Studies of Sediment Cores, Springer, p. 25-102.
Rubensdotter, L., Romundset, A., Farnsworth, W.R., and Christiansen, H.H., 2015, Landforms andsediments in

Bjordalen-Vestpynten. Svalbard. Quaternary geological map, 1:10 000. Geological survey of Norway. ISBN 978-82-7385-158-1.
Rubensdotter, L., and Rosqvist, G., 2009, Influence of geomorphological setting, fluvial-, glaciofluvial-and mass-movement processes on sedimentation in alpine lakes: The Holocene, v. 19, no. 4, p. 665-678.
Rutter, N., Hodson, A., Irvine-Fynn, T., and Solås, M. K., 2011, Hydrology and hydrochemistry of a deglaciating high-Arctic catchment, Svalbard: Journal of Hydrology, v. 410, no. 1, p. 39-50.
Serreze, M. C., Carse, F., Barry, R. G., and Rogers, J. C., 1997, Icelandic low cyclone activity: Climatological features, linkages with the NAO, and relationships with recent changes in the Northern Hemisphere circulation: Journal of Climate, v. 10, no. 3, p. 453-464.
Serreze, M., Walsh, J., Chapin Iii, F., Osterkamp, T., Dyurgerov, M., Romanovsky, V., Oechel, W., Morison, J., Zhang, T., and Barry, R., 2000, Observational evidence of recent change in the northern high-latitude environment: Climatic Change, v. 46, no. 1-2, p. 159-207.
Serreze, M. C., and Barry, R. G., 2011, Processes and impacts of Arctic amplification: A research synthesis: Global and Planetary Change, v. 77, no. 1, p. 85-96.
Smith, N.D., and Ashley, G., 1985, Proglacial lacustrine environments. Ch. 4, in Glacial Sedimentary Environments, eds. Ashley, G., Shaw, J., and Smith, N.D.; S.E.P.M. short course no. 16, p. 135-215.
Snyder, J. A. M., G. H.; Werner, A.; Jull, A. J. T.; Stafford, T. W.;, 1994, AMS-radiocarbon dating of organic-poor lake sediment, an example from Linnévatnet, Spitsbergen, Svalbard: The Holocene, v. 4, no. 4, p. 413-421.
Snyder, J. A. W., A.; Miller, G. H., 2000, Holocene cirque glacier activity in western Spitsbergen, Svalbard: sediment records from proglacial Linnévatnet: The Holocene, v. 10, no. 5, p. 555-563.
Spielhagen, R. F., Werner, K., Sørensen, S. A., Zamelczyk, K., Kandiano, E., Budeus, G., Husum, K., Marchitto, T. M., and Hald, M., 2011, Enhanced modern heat transfer to the Arctic by warm Atlantic water: Science, v. 331, no. 6016, p. 450-453.
Svendsen, J. I., and Mangerud, J., 1997, Holocene glacial and climatic variations on Spitsbergen, Svalbard: The Holocene, v. 7, no. 1, p. 45-57.
Svendsen, J. I. M., J.; Miller, G. H., 1987, Postglacial marine and lacustrine sediments in Lake Linnevatnet, Svalbard: Polar research, v. 5, p. 281-283.
-, 1989, Denudation rates in the Arctic estimated from lake sediments on Spitsbergen, Svalbard: Paleogeography, Palaeoclimatology, Palaeoecology, v. 76, p. 153-168.
Tomkins, J. D., Antoniades, D., Lamoureux, S. F., and Vincent, W. F., 2008, A simple and effective method for preserving the sediment–water interface of sediment cores during transport: Journal of Paleolimnology, v. 40, no. 1, p. 577-582.
Trouet, V., Esper, J., Graham, N. E., Baker, A., Scourse, J. D., and Frank, D. C., 2009, Persistent positive North Atlantic Oscillation mode dominated the medieval climate anomaly: science, v. 324, no. 5923, p. 78-80.
van der Bilt, W. G. M., Bakke, J., Vasskog, K., D'Andrea, W. J., Bradley, R. S., and Ólafsdóttir, S., 2015, Reconstruction of glacier variability from lake sediments reveals dynamic Holocene climate in Svalbard: Quaternary Science Reviews, v. 126, p. 201-218.
Walther, T., 2015, Analysis of sediment traps in Linnévatnet, Svalbard for reconstruction of annual sediment flux and lacustrine processes [Bachelors: Bates College].
Werner, A., 1993, Holocene moraine chronology, Spitsbergen, Svalbard: lichenometric evidence for multiple Neoglacial advances in the Arctic: The Holocene, v. 3, no. 2, p. 128-137.
-, 2016. Personal Communication
Woo, M. K., Kane, D. L., Carey, S. K., and Yang, D., 2008, Progress in permafrost hydrology in the new millennium: Permafrost and Periglacial Processes, v. 19, no. 2, p. 237-254.
Woo, M.-k., and McCann, B. S., 1994, Climatic variability, climatic change, runoff, and suspended sediment regimes in northern Canada: Physical Geography, v. 15, no. 3, p. 201-226.
Worsley, D., 2008, The post-Caledonian development of Svalbard and the western Barents Sea: Polar Research, v. 27, no. 3, p. 298-317.
Zolitschka, B., Francus, P., Ojala, A. E., and Schimmelmann, A., 2015, Varves in lake sediments–a review: Quaternary Science Reviews, v. 117, p. 1-41.

Appendix: A

The results for each run of PCA* for each unit in each years

- Principle Component Results output by SigmaPlot.
- Component Vector Loadings
- Component Scores

*each sample consisted of a combination of data points across the lake based on the division of units. The spread of data selection can be seen in the Component Scores as the data points are labeled with their Mooring.

Contents

E2_2015.....105
E3_2015 110
E4_2015 115
E4a_2015 120
Winter_2015 125
Summer_2013 130
Fall_2013 135
Winter_2013 140
Spring_2014 145
Summer_2011 150
Fall_2011 155
Winter_2011 160
Spring_2012 165

E2_2015

Principal Components Analysis Monday, March 21, 2016, 8:49:41 PM

Data source: E2

Normality Test (Henze-Zinkler):

Statistic = 1.022 Failed (P < 0.050)

Descriptive Statistics:

Variable	Mean	Std Dev
Al	1.530	0.209
Si	2.664	0.0505
K	3.457	0.0320
Ca	3.510	0.102
Ti	3.390	0.0324
Mn	2.676	0.0678
Fe	4.768	0.0467
Rb	2.985	0.0495
Sr	2.694	0.0756
Zr	3.057	0.0855

Total Observations	25
Missing	0
Valid Observations	25

An observation is missing if any worksheet cell in its row has a non-numeric value.

Correlation Matrix:

	Al	Si	K	Ca	Ti	Mn	Fe	Rb	Sr	Zr
Al	1.000									
Si	-0.161	1.000								
K	0.242	0.370	1.000							
Ca	-0.101	-0.786	-0.581	1.000						
Ti	0.0619	0.722	0.719	-0.841	1.000					
Mn	0.236	0.431	0.0985	-0.433	0.332	1.000				
Fe	0.129	0.780	0.731	-0.907	0.934	0.454	1.000			
Rb	-0.337	-0.246	0.0282	0.271	-0.290	-0.212	-0.315	1.000		
Sr	-0.0227	-0.442	-0.411	0.549	-0.706	-0.275	-0.669	0.426	1.000	
Zr	-0.0487	0.723	0.310	-0.832	0.729	0.374	0.747	-0.214	-0.489	1.000

Total Variance: = 10.000

Eigenvalues of the Correlation Matrix:

	Eigenvalue	Difference	Proportion(%)	Cumulative(%)
1	5.397	4.026	53.973	53.973
2	1.372	0.274	13.716	67.689
3	1.098	0.222	10.977	78.666
4	0.876	0.342	8.760	87.425
5	0.534	0.177	5.338	92.763
6	0.357	0.194	3.568	96.331
7	0.163	0.0577	1.630	97.961

8	0.105	0.0373	1.053	99.014
9	0.0680	0.0373	0.680	99.694
10	0.0306	--	0.306	100.000

If two or more eigenvalues have the same value, then the corresponding principal components are not well-defined and any interpretation of them is suspect.

Number of In-Model Principal Components = 3

The in-model components correspond to all eigenvalues greater than or equal to the average eigenvalue. When analyzing the correlation matrix, the average eigenvalue is always 1.0. This criterion can be changed in the Test Options dialog on the Criterion panel. The variance of each principal component equals its corresponding eigenvalue.

Chi-Square Tests for the Equality of Eigenvalues:

Hypothesis: All eigenvalues are equal.
Statistic = 206.979
Degrees of freedom = 45.000
P value = <0.001

There is a significant difference in the eigenvalues. A principal components analysis can be conducted.

Hypothesis: The last 7 eigenvalues are equal.
Statistic = 69.924
Degrees of freedom = 29.230
P value = <0.001

There is a significant difference in the last 7 eigenvalues. You may want to include additional principal components in your model by changing the settings in the Test Options dialog on the Criterion panel.

Eigenvectors of the Correlation Matrix:

	PC 1	PC 2	PC 3
Al	0.0513	-0.732	0.319
Si	0.354	0.222	-0.254
K	0.279	0.0280	0.688
Ca	-0.402	-0.0659	0.00221
Ti	0.406	0.0674	0.156
Mn	0.214	-0.251	-0.367
Fe	0.420	0.0141	0.117
Rb	-0.161	0.551	0.367
Sr	-0.309	0.0881	0.0400
Zr	0.352	0.174	-0.227

Each principal component is a linear combination of the original variables, after each original variable has been standardized to have unit variance. The coefficients of this linear combination are the entries in the corresponding column of the above table. These coefficients provide the interpretation of the principal components in terms of the original variables.

Standard Errors for the Eigenvector Entries:

	PC 1	PC 2	PC 3
Al	0.111	0.316	0.700
Si	0.0574	0.255	0.251
K	0.0810	0.620	0.0787

Ca	0.0333	0.105	0.156
Ti	0.0323	0.167	0.144
Mn	0.0901	0.449	0.628
Fe	0.0205	0.124	0.0646
Rb	0.101	0.401	0.663
Sr	0.0686	0.260	0.472
Zr	0.0567	0.241	0.229

Component Loadings:

	PC 1	**PC 2**	**PC 3**
Al	0.119	-0.857	0.335
Si	0.822	0.260	-0.266
K	0.649	0.0328	0.720
Ca	-0.934	-0.0771	0.00232
Ti	0.942	0.0790	0.164
Mn	0.498	-0.294	-0.385
Fe	0.976	0.0165	0.122
Rb	-0.374	0.646	0.385
Sr	-0.718	0.103	0.0419
Zr	0.819	0.204	-0.238

If the principle components are standardized to have unit variance, the loadings are the coefficients of the linear combination of in-model principal components used to approximate the original variables. If a correlation matrix is analyzed, then the loadings equal the correlations between the original variables and the principal components.

Fitted Correlation Matrix:

	Al	**Si**	**K**	**Ca**	**Ti**	**Mn**	**Fe**	**Rb**	**Sr**	**Zr**
Al	0.861									
Si	-0.214	0.813								
K	0.290	0.350	0.941							
Ca	-0.0445	-0.788	-0.607	0.878						
Ti	0.0995	0.751	0.732	-0.885	0.921					
Mn	0.183	0.435	0.0362	-0.443	0.383	0.482				
Fe	0.143	0.774	0.722	-0.913	0.941	0.434	0.969			
Rb	-0.469	-0.242	0.0557	0.300	-0.238	-0.524	-0.308	0.705		
Sr	-0.160	-0.575	-0.433	0.663	-0.662	-0.404	-0.695	0.351	0.529	
Zr	-0.156	0.789	0.367	-0.781	0.748	0.439	0.774	-0.266	-0.577	0.768

This is an estimate of the correlation matrix that results by approximating the original variables with the in-model principal components.

Component Loading Vectors

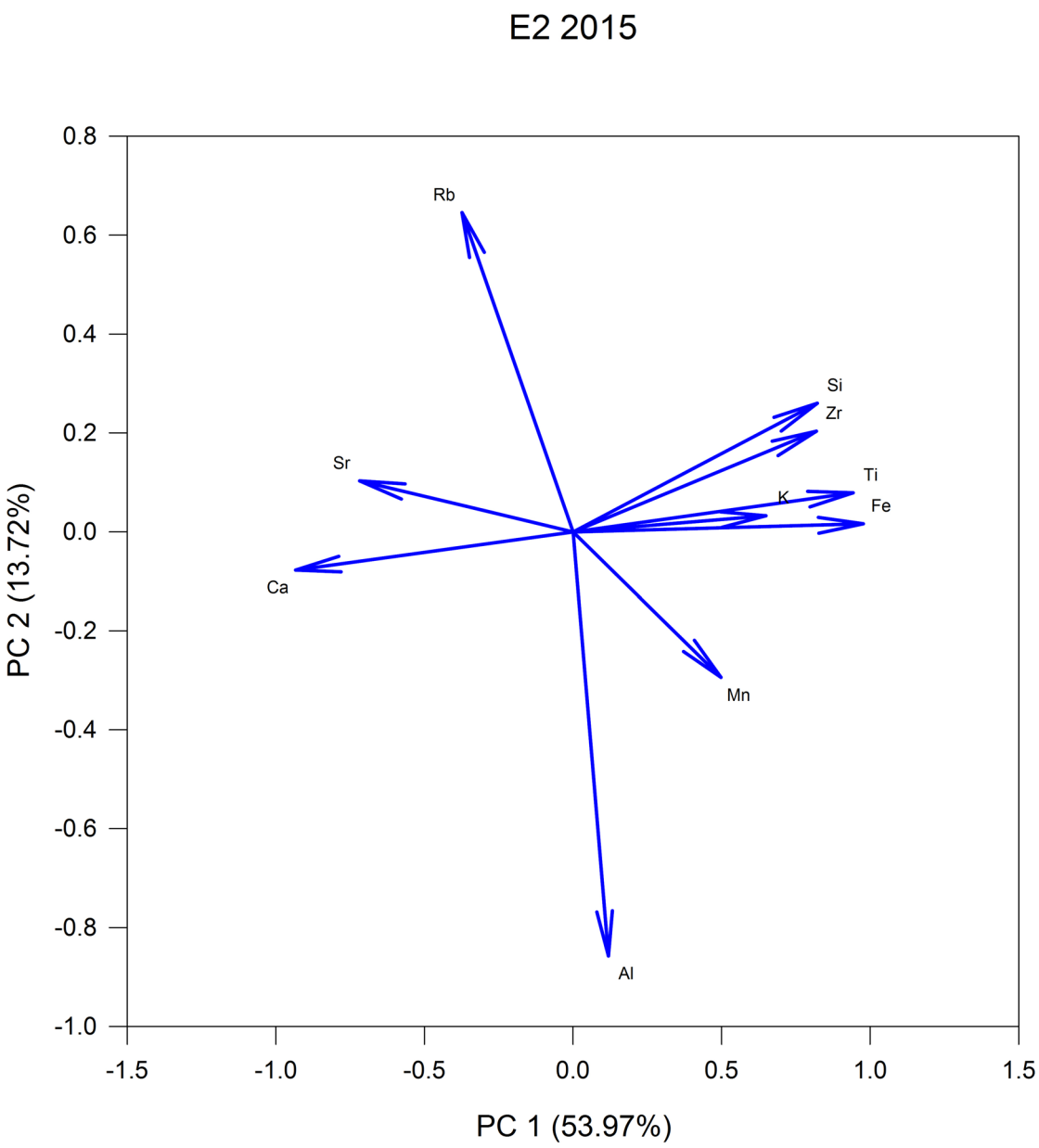

Component Scores

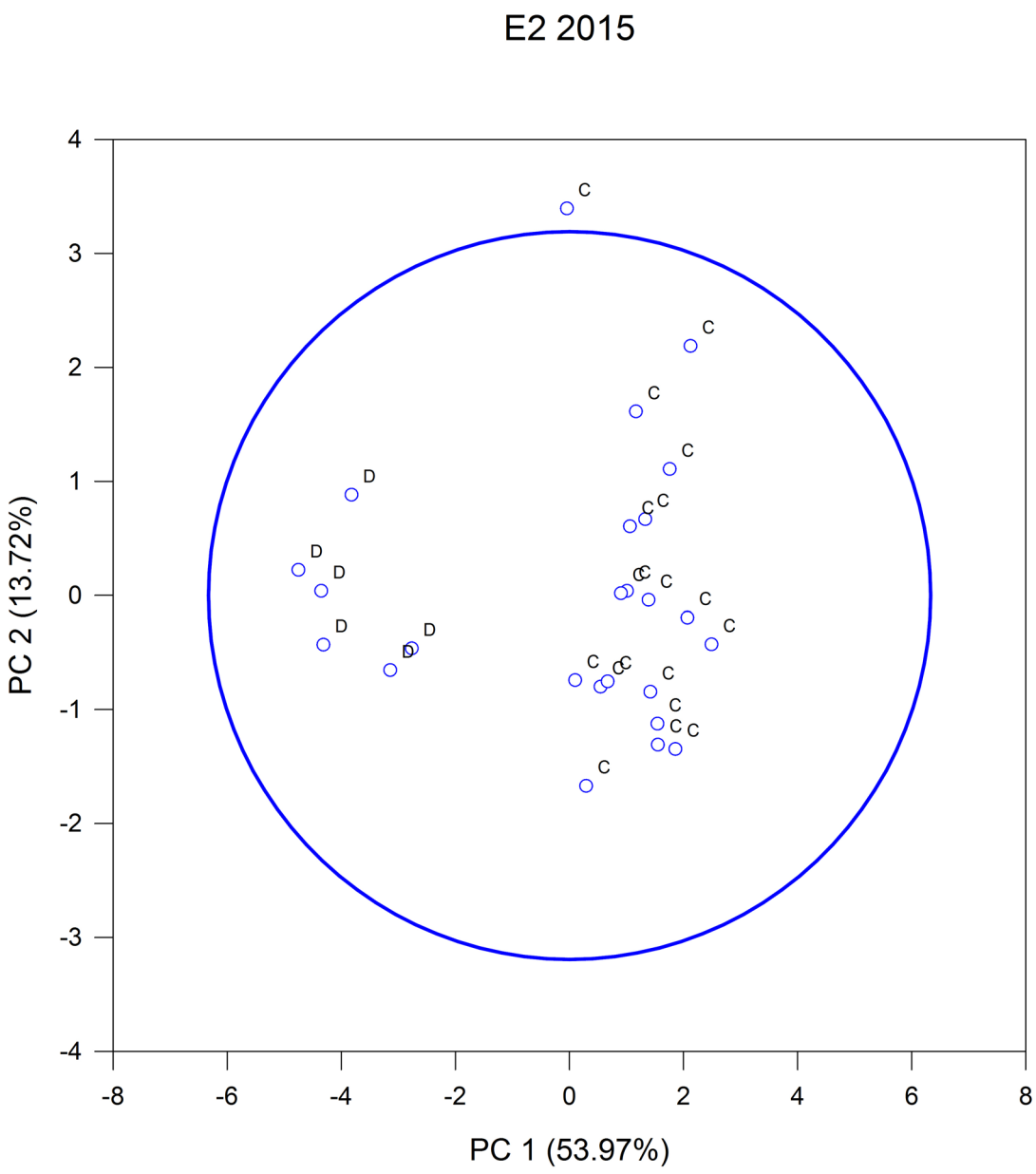

E3_2015

Principal Components Analysis Monday, March 21, 2016, 8:47:22 PM

Data source: E3

Normality Test (Henze-Zinkler):

Statistic = 0.997 Failed (P < 0.050)

Descriptive Statistics:

Variable	Mean	Std Dev
Al	1.431	0.209
Si	2.643	0.0404
K	3.403	0.0329
Ca	3.591	0.105
Ti	3.351	0.0301
Mn	2.671	0.0633
Fe	4.710	0.0216
Rb	2.951	0.0589
Sr	2.722	0.0874
Zr	3.059	0.0571

Total Observations	39
Missing	0
Valid Observations	39

An observation is missing if any worksheet cell in its row has a non-numeric value.

Correlation Matrix:

	Al	Si	K	Ca	Ti	Mn	Fe	Rb	Sr	Zr
Al	1.000									
Si	0.115	1.000								
K	0.196	0.00898	1.000							
Ca	0.158	-0.389	0.763	1.000						
Ti	0.109	0.254	0.657	0.380	1.000					
Mn	0.0967	0.461	0.336	-0.0594	0.472	1.000				
Fe	0.163	0.215	0.735	0.313	0.841	0.557	1.000			
Rb	0.291	-0.276	0.522	0.541	0.276	-0.0302	0.341	1.000		
Sr	-0.0623	-0.520	0.420	0.713	0.0840	-0.279	0.0185	0.626	1.000	
Zr	-0.0539	0.413	-0.570	-0.811	-0.140	0.171	-0.111	-0.496	-0.591	1.000

Total Variance: = 10.000

Eigenvalues of the Correlation Matrix:

	Eigenvalue	Difference	Proportion(%)	Cumulative(%)
1	4.037	1.297	40.373	40.373
2	2.740	1.705	27.401	67.774
3	1.036	0.429	10.355	78.130
4	0.607	0.120	6.070	84.199
5	0.487	0.0279	4.865	89.064
6	0.459	0.157	4.586	93.650
7	0.301	0.107	3.015	96.665

8	0.194	0.103	1.942	98.608
9	0.0917	0.0441	0.917	99.524
10	0.0476	--	0.476	100.000

If two or more eigenvalues have the same value, then the corresponding principal components are not well-defined and any interpretation of them is suspect.

Number of In-Model Principal Components = 3

The in-model components correspond to all eigenvalues greater than or equal to the average eigenvalue. When analyzing the correlation matrix, the average eigenvalue is always 1.0. This criterion can be changed in the Test Options dialog on the Criterion panel. The variance of each principal component equals its corresponding eigenvalue.

Chi-Square Tests for the Equality of Eigenvalues:

Hypothesis: All eigenvalues are equal.
Statistic = 272.875
Degrees of freedom = 45.000
P value = <0.001

There is a significant difference in the eigenvalues. A principal components analysis can be conducted.

Hypothesis: The last 7 eigenvalues are equal.
Statistic = 69.892
Degrees of freedom = 28.300
P value = <0.001

There is a significant difference in the last 7 eigenvalues. You may want to include additional principal components in your model by changing the settings in the Test Options dialog on the Criterion panel.

Eigenvectors of the Correlation Matrix:

	PC 1	PC 2	PC 3
Al	0.111	0.114	-0.915
Si	-0.137	0.449	-0.0970
K	0.444	0.176	0.0656
Ca	0.446	-0.149	0.0382
Ti	0.299	0.387	0.180
Mn	0.0693	0.481	0.0935
Fe	0.302	0.417	0.109
Rb	0.369	-0.0986	-0.285
Sr	0.339	-0.329	0.106
Zr	-0.370	0.244	-0.0486

Each principal component is a linear combination of the original variables, after each original variable has been standardized to have unit variance. The coefficients of this linear combination are the entries in the corresponding column of the above table. These coefficients provide the interpretation of the principal components in terms of the original variables.

Standard Errors for the Eigenvector Entries:

	PC 1	PC 2	PC 3
Al	0.112	0.154	0.0674
Si	0.193	0.0918	0.196
K	0.0783	0.186	0.0998

Ca	0.0694	0.188	0.125
Ti	0.165	0.135	0.134
Mn	0.205	0.0746	0.181
Fe	0.175	0.132	0.130
Rb	0.0738	0.173	0.201
Sr	0.142	0.150	0.146
Zr	0.111	0.164	0.181

Component Loadings:

	PC 1	PC 2	PC 3
Al	0.223	0.188	-0.931
Si	-0.275	0.743	-0.0987
K	0.892	0.292	0.0668
Ca	0.896	-0.246	0.0389
Ti	0.600	0.641	0.183
Mn	0.139	0.797	0.0952
Fe	0.607	0.690	0.111
Rb	0.742	-0.163	-0.290
Sr	0.681	-0.544	0.107
Zr	-0.743	0.403	-0.0494

If the principle components are standardized to have unit variance, the loadings are the coefficients of the linear combination of in-model principal components used to approximate the original variables. If a correlation matrix is analyzed, then the loadings equal the correlations between the original variables and the principal components.

Fitted Correlation Matrix:

	Al	Si	K	Ca	Ti	Mn	Fe	Rb	Sr	Zr
Al	0.952									
Si	0.171	0.637								
K	0.191	-0.0348	0.885							
Ca	0.117	-0.433	0.730	0.865						
Ti	0.0838	0.293	0.735	0.387	0.805					
Mn	0.0925	0.544	0.363	-0.0676	0.612	0.663				
Fe	0.161	0.335	0.750	0.378	0.827	0.644	0.856			
Rb	0.404	-0.296	0.595	0.694	0.288	-0.0543	0.305	0.661		
Sr	-0.0511	-0.602	0.456	0.748	0.0794	-0.329	0.0496	0.563	0.771	
Zr	-0.0434	0.509	-0.548	-0.767	-0.197	0.213	-0.178	-0.603	-0.731	0.718

This is an estimate of the correlation matrix that results by approximating the original variables with the in-model principal components.

Component Loading Vectors

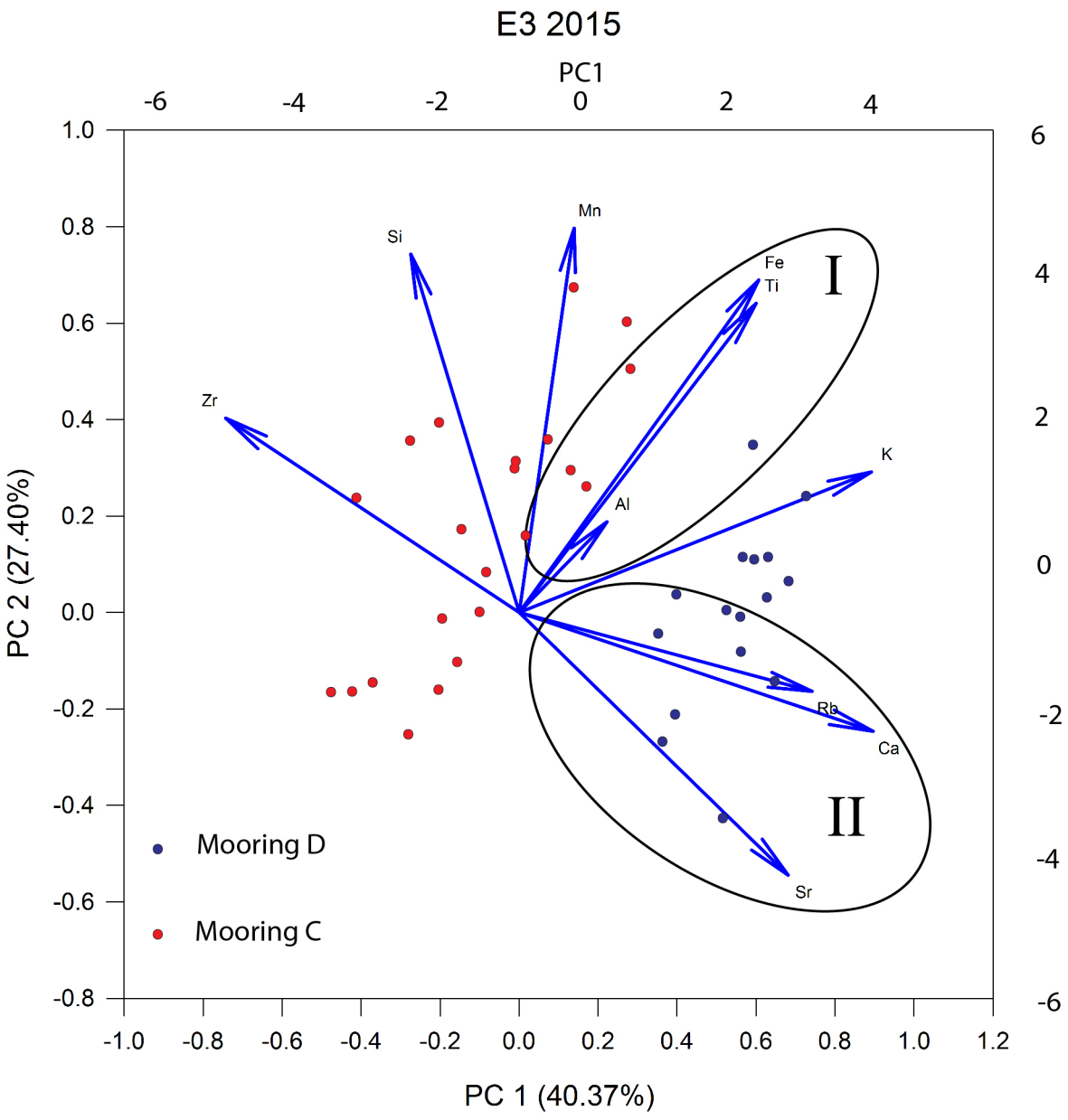

Component Scores

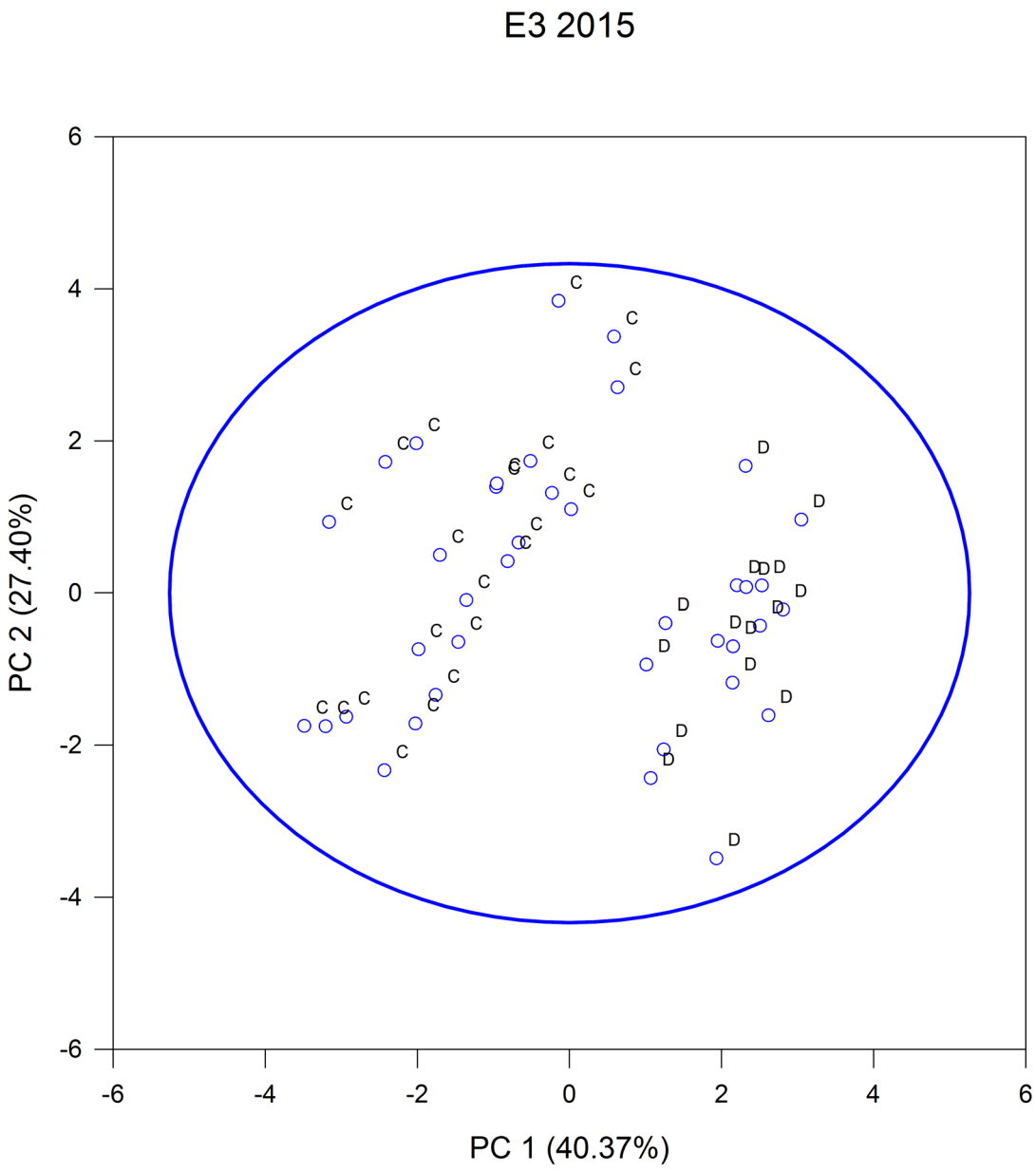

E4_2015

Principal Components Analysis Monday, March 21, 2016, 8:02:57 PM

Data source: Data 1 in Notebook1

Normality Test (Henze-Zinkler):

Statistic = 1.036 Failed (P < 0.050)

Descriptive Statistics:

Variable	Mean	Std Dev
Al	1.417	0.240
Si	2.560	0.0764
K	3.411	0.0235
Ca	3.669	0.0771
Ti	3.305	0.0425
Mn	2.729	0.0659
Fe	4.724	0.0127
Rb	2.967	0.0424
Sr	2.791	0.0452
Zr	2.939	0.0434

Total Observations	56
Missing	3
Valid Observations	53

An observation is missing if any worksheet cell in its row has a non-numeric value.

Correlation Matrix:

	Al	Si	K	Ca	Ti	Mn	Fe	Rb	Sr	Zr
Al	1.000									
Si	0.192	1.000								
K	0.0697	0.426	1.000							
Ca	-0.232	-0.536	0.0168	1.000						
Ti	0.0978	0.707	0.567	-0.269	1.000					
Mn	0.0637	-0.505	0.0354	0.666	-0.368	1.000				
Fe	0.236	-0.0626	0.465	0.286	0.0444	0.429	1.000			
Rb	0.137	-0.0979	-0.00612	0.0104	-0.132	0.251	0.212	1.000		
Sr	0.0808	-0.282	0.0972	0.279	-0.103	0.373	0.251	0.126	1.000	
Zr	0.0883	0.0463	-0.324	-0.160	-0.0679	-0.214	-0.139	-0.0805		
-0.00672	1.000									

Total Variance: = 10.000

Eigenvalues of the Correlation Matrix:

	Eigenvalue	Difference	Proportion(%)	Cumulative(%)
1	2.924	0.783	29.242	29.242
2	2.141	0.838	21.410	50.653
3	1.303	0.334	13.033	63.685
4	0.969	0.212	9.692	73.377
5	0.757	0.0612	7.570	80.947
6	0.696	0.205	6.958	87.905

7	0.491	0.213	4.906	92.810
8	0.277	0.0331	2.775	95.585
9	0.244	0.0472	2.444	98.029
10	0.197	--	1.971	100.000

If two or more eigenvalues have the same value, then the corresponding principal components are not well-defined and any interpretation of them is suspect.

Number of In-Model Principal Components = 3

The in-model components correspond to all eigenvalues greater than or equal to the average eigenvalue. When analyzing the correlation matrix, the average eigenvalue is always 1.0. This criterion can be changed in the Test Options dialog on the Criterion panel. The variance of each principal component equals its corresponding eigenvalue.

Chi-Square Tests for the Equality of Eigenvalues:

Hypothesis: All eigenvalues are equal.
Statistic = 175.826
Degrees of freedom = 45.000
P value = <0.001

There is a significant difference in the eigenvalues. A principal components analysis can be conducted.

Hypothesis: The last 7 eigenvalues are equal.
Statistic = 51.788
Degrees of freedom = 26.820
P value = 0.003

There is a significant difference in the last 7 eigenvalues. You may want to include additional principal components in your model by changing the settings in the Test Options dialog on the Criterion panel.

Eigenvectors of the Correlation Matrix:

	PC 1	PC 2	PC 3
Al	0.0688	0.205	0.659
Si	0.491	0.230	0.0441
K	0.139	0.582	-0.208
Ca	-0.444	0.110	-0.311
Ti	0.397	0.358	-0.140
Mn	-0.482	0.210	0.0258
Fe	-0.198	0.492	0.160
Rb	-0.157	0.141	0.431
Sr	-0.277	0.196	0.164
Zr	0.0900	-0.287	0.407

Each principal component is a linear combination of the original variables, after each original variable has been standardized to have unit variance. The coefficients of this linear combination are the entries in the corresponding column of the above table. These coefficients provide the interpretation of the principal components in terms of the original variables.

Standard Errors for the Eigenvector Entries:

	PC 1	PC 2	PC 3
Al	0.154	0.200	0.165
Si	0.108	0.221	0.123

K	0.260	0.0946	0.175
Ca	0.0873	0.223	0.151
Ti	0.166	0.188	0.162
Mn	0.102	0.218	0.130
Fe	0.225	0.123	0.192
Rb	0.132	0.188	0.327
Sr	0.127	0.179	0.286
Zr	0.167	0.169	0.307

Component Loadings:

	PC 1	PC 2	PC 3
Al	0.118	0.299	0.752
Si	0.839	0.336	0.0503
K	0.237	0.852	-0.237
Ca	-0.759	0.161	-0.355
Ti	0.678	0.524	-0.160
Mn	-0.824	0.308	0.0294
Fe	-0.339	0.719	0.182
Rb	-0.268	0.206	0.492
Sr	-0.474	0.287	0.187
Zr	0.154	-0.420	0.464

If the principle components are standardized to have unit variance, the loadings are the coefficients of the linear combination of in-model principal components used to approximate the original variables. If a correlation matrix is analyzed, then the loadings equal the correlations between the original variables and the principal components.

Fitted Correlation Matrix:

	Al	Si	K	Ca	Ti	Mn	Fe	Rb	Sr	Zr
Al	0.670									
Si	0.237	0.819								
K	0.105	0.474	0.838							
Ca	-0.308	-0.601	0.0408	0.728						
Ti	0.116	0.737	0.645	-0.374	0.760					
Mn	0.0173	-0.586	0.0594	0.664	-0.402	0.774				
Fe	0.313	-0.0330	0.489	0.308	0.118	0.506	0.665			
Rb	0.400	-0.131	-0.00515	0.0618	-0.153	0.298	0.328	0.356		
Sr	0.171	-0.292	0.0874	0.340	-0.201	0.484	0.401	0.278	0.342	
Zr	0.242	0.0113	-0.431	-0.349	-0.190	-0.242	-0.269	0.101	-0.106	0.415

This is an estimate of the correlation matrix that results by approximating the original variables with the in-model principal components.

Component Loading Vectors

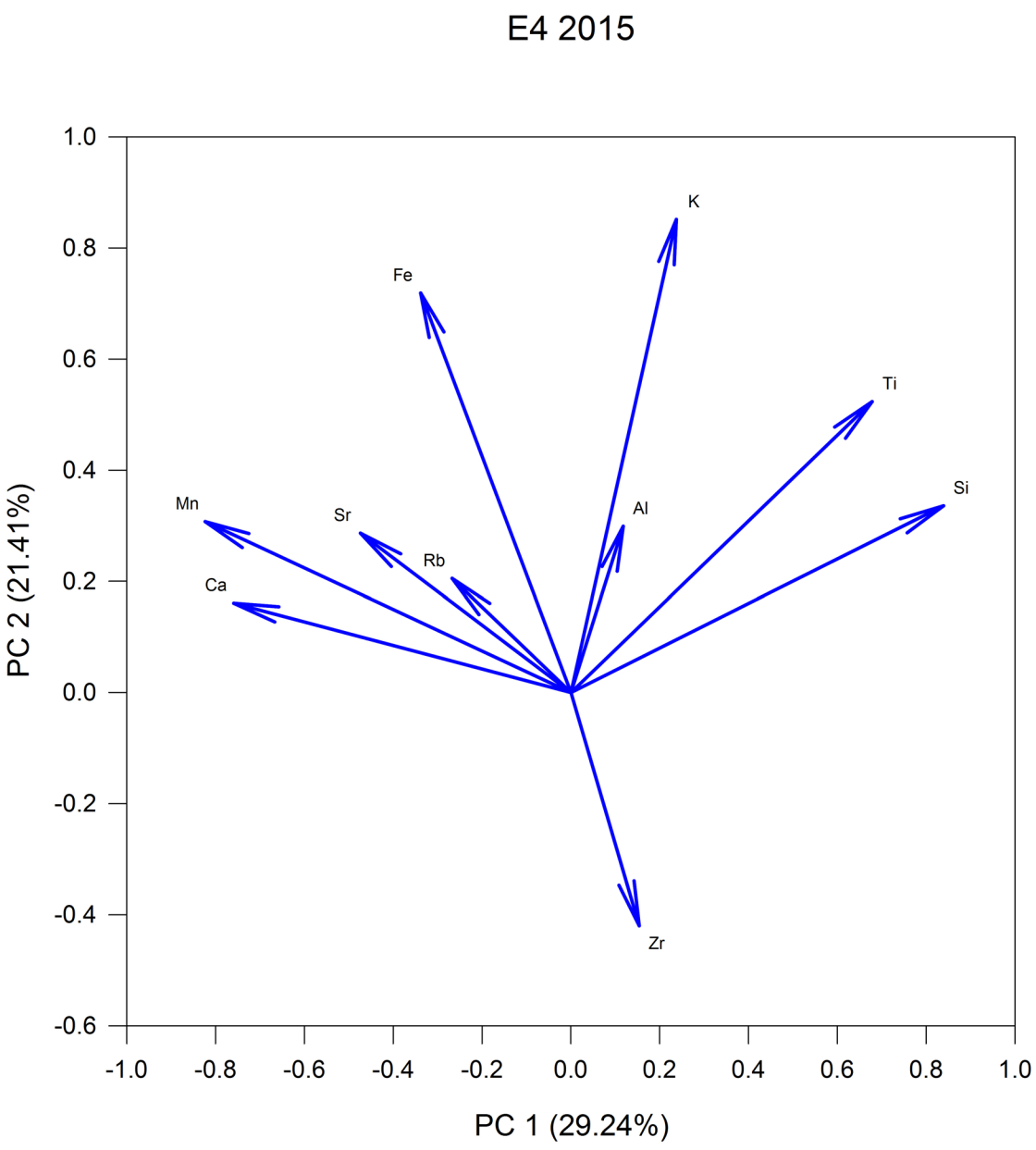

Component Scores

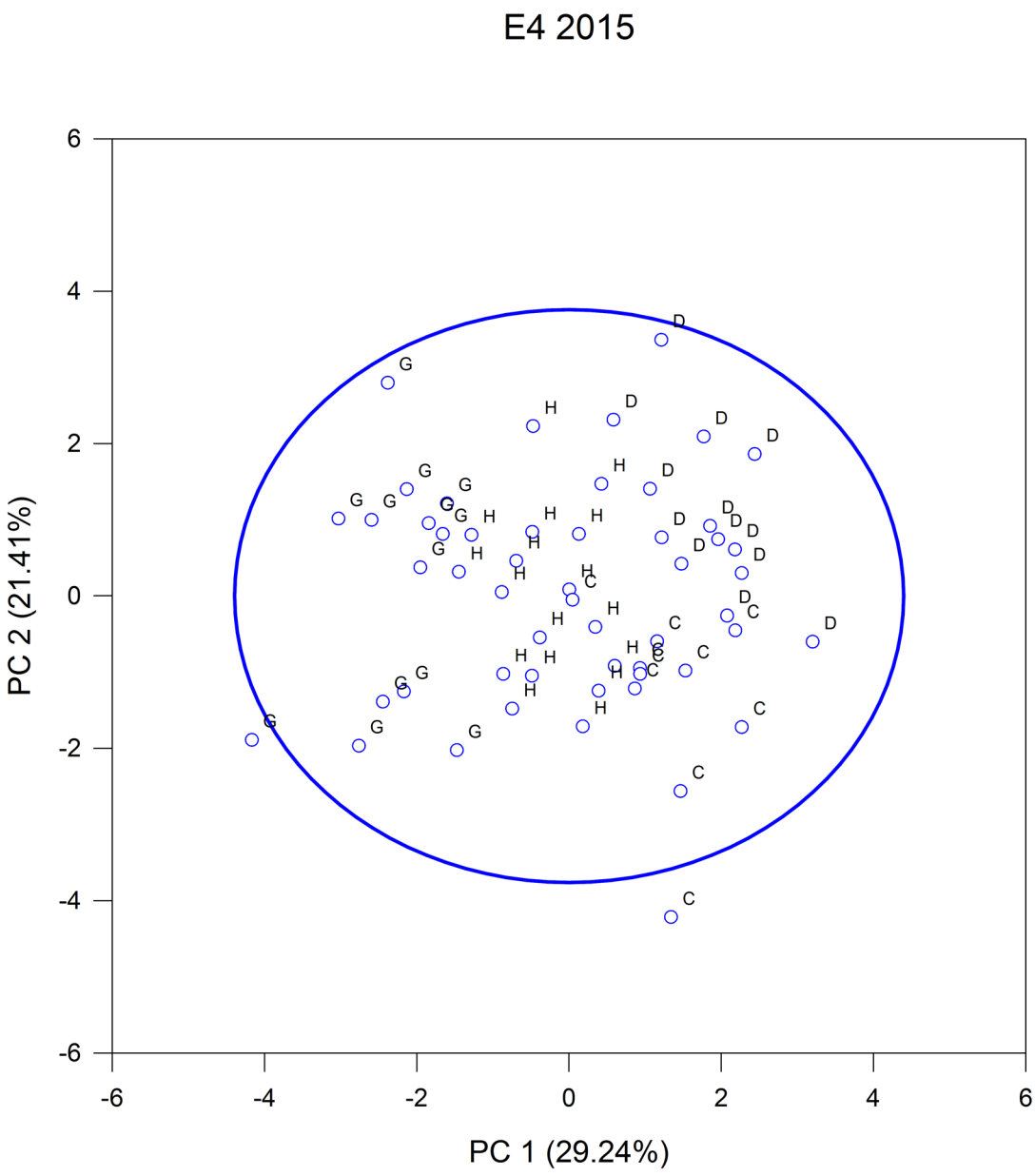

E4a_2015

Principal Components Analysis Monday, March 21, 2016, 8:41:38 PM

Data source: E4a

Normality Test (Henze-Zinkler):

Statistic = 0.977 Passed (P = 0.222)

Descriptive Statistics:

Variable	Mean	Std Dev
Al	1.503	0.172
Si	2.565	0.0619
K	3.415	0.0495
Ca	3.623	0.0470
Ti	3.299	0.0359
Mn	2.728	0.0837
Fe	4.747	0.0419
Rb	2.984	0.0387
Sr	2.793	0.0439
Zr	2.970	0.0465

Total Observations	27
Missing	2
Valid Observations	25

An observation is missing if any worksheet cell in its row has a non-numeric value.

Correlation Matrix:

	Al	Si	K	Ca	Ti	Mn	Fe	Rb	Sr	Zr
Al	1.000									
Si	0.339	1.000								
K	0.167	0.671	1.000							
Ca	0.238	0.735	0.911	1.000						
Ti	0.201	0.784	0.829	0.869	1.000					
Mn	-0.232	0.165	0.667	0.601	0.503	1.000				
Fe	0.154	0.699	0.961	0.921	0.876	0.655	1.000			
Rb	0.297	-0.0353	-0.0989	-0.157	-0.0333	-0.434	-0.124	1.000		
Sr	-0.295	0.454	0.645	0.566	0.607	0.572	0.659	-0.133	1.000	
Zr	0.267	-0.312	-0.327	-0.293	-0.393	-0.350	-0.487	0.362	-0.359	1.000

Total Variance: = 10.000

Eigenvalues of the Correlation Matrix:

	Eigenvalue	Difference	Proportion(%)	Cumulative(%)
1	5.436	3.552	54.364	54.364
2	1.884	1.033	18.843	73.207
3	0.851	0.0720	8.515	81.722
4	0.779	0.311	7.795	89.516
5	0.469	0.232	4.687	94.203
6	0.237	0.0842	2.371	96.574
7	0.153	0.0429	1.529	98.104

8	0.110	0.0460	1.100	99.204
9	0.0641	0.0485	0.641	99.844
10	0.0156	--	0.156	100.000

If two or more eigenvalues have the same value, then the corresponding principal components are not well-defined and any interpretation of them is suspect.

Number of In-Model Principal Components = 2

The in-model components correspond to all eigenvalues greater than or equal to the average eigenvalue. When analyzing the correlation matrix, the average eigenvalue is always 1.0. This criterion can be changed in the Test Options dialog on the Criterion panel. The variance of each principal component equals its corresponding eigenvalue.

Chi-Square Tests for the Equality of Eigenvalues:

Hypothesis: All eigenvalues are equal.
Statistic = 234.925
Degrees of freedom = 45.000
P value = <0.001

There is a significant difference in the eigenvalues. A principal components analysis can be conducted.

Hypothesis: The last 8 eigenvalues are equal.
Statistic = 94.614
Degrees of freedom = 35.363
P value = <0.001

There is a significant difference in the last 8 eigenvalues. You may want to include additional principal components in your model by changing the settings in the Test Options dialog on the Criterion panel.

Eigenvectors of the Correlation Matrix:

	PC 1	PC 2
Al	0.0381	0.617
Si	0.324	0.278
K	0.404	0.0819
Ca	0.400	0.130
Ti	0.392	0.149
Mn	0.298	-0.334
Fe	0.417	0.0517
Rb	-0.0938	0.481
Sr	0.315	-0.202
Zr	-0.214	0.331

Each principal component is a linear combination of the original variables, after each original variable has been standardized to have unit variance. The coefficients of this linear combination are the entries in the corresponding column of the above table. These coefficients provide the interpretation of the principal components in terms of the original variables.

Standard Errors for the Eigenvector Entries:

	PC 1	PC 2
Al	0.122	0.121
Si	0.0715	0.129
K	0.0325	0.0951

Ca	0.0371	0.0930
Ti	0.0413	0.0922
Mn	0.0808	0.137
Fe	0.0220	0.0843
Rb	0.113	0.181
Sr	0.0704	0.153
Zr	0.0944	0.182

Component Loadings:

	PC 1	**PC 2**
Al	0.0888	0.847
Si	0.756	0.382
K	0.943	0.112
Ca	0.933	0.179
Ti	0.914	0.205
Mn	0.694	-0.459
Fe	0.973	0.0709
Rb	-0.219	0.660
Sr	0.734	-0.277
Zr	-0.499	0.454

If the principle components are standardized to have unit variance, the loadings are the coefficients of the linear combination of in-model principal components used to approximate the original variables. If a correlation matrix is analyzed, then the loadings equal the correlations between the original variables and the principal components.

Fitted Correlation Matrix:

	Al	**Si**	**K**	**Ca**	**Ti**	**Mn**	**Fe**	**Rb**	**Sr**	**Zr**
Al	0.725									
Si	0.390	0.717								
K	0.179	0.756	0.902							
Ca	0.234	0.774	0.900	0.902						
Ti	0.255	0.769	0.885	0.889	0.877					
Mn	-0.327	0.350	0.603	0.565	0.540	0.693				
Fe	0.146	0.763	0.925	0.920	0.903	0.643	0.951			
Rb	0.540	0.0866	-0.132	-0.0858	-0.0646	-0.455	-0.166	0.484		
Sr	-0.169	0.449	0.661	0.635	0.613	0.636	0.694	-0.343	0.615	
Zr	0.340	-0.204	-0.419	-0.384	-0.362	-0.555	-0.453	0.409	-0.492	0.455

This is an estimate of the correlation matrix that results by approximating the original variables with the in-model principal components.

Component Loading Vectors

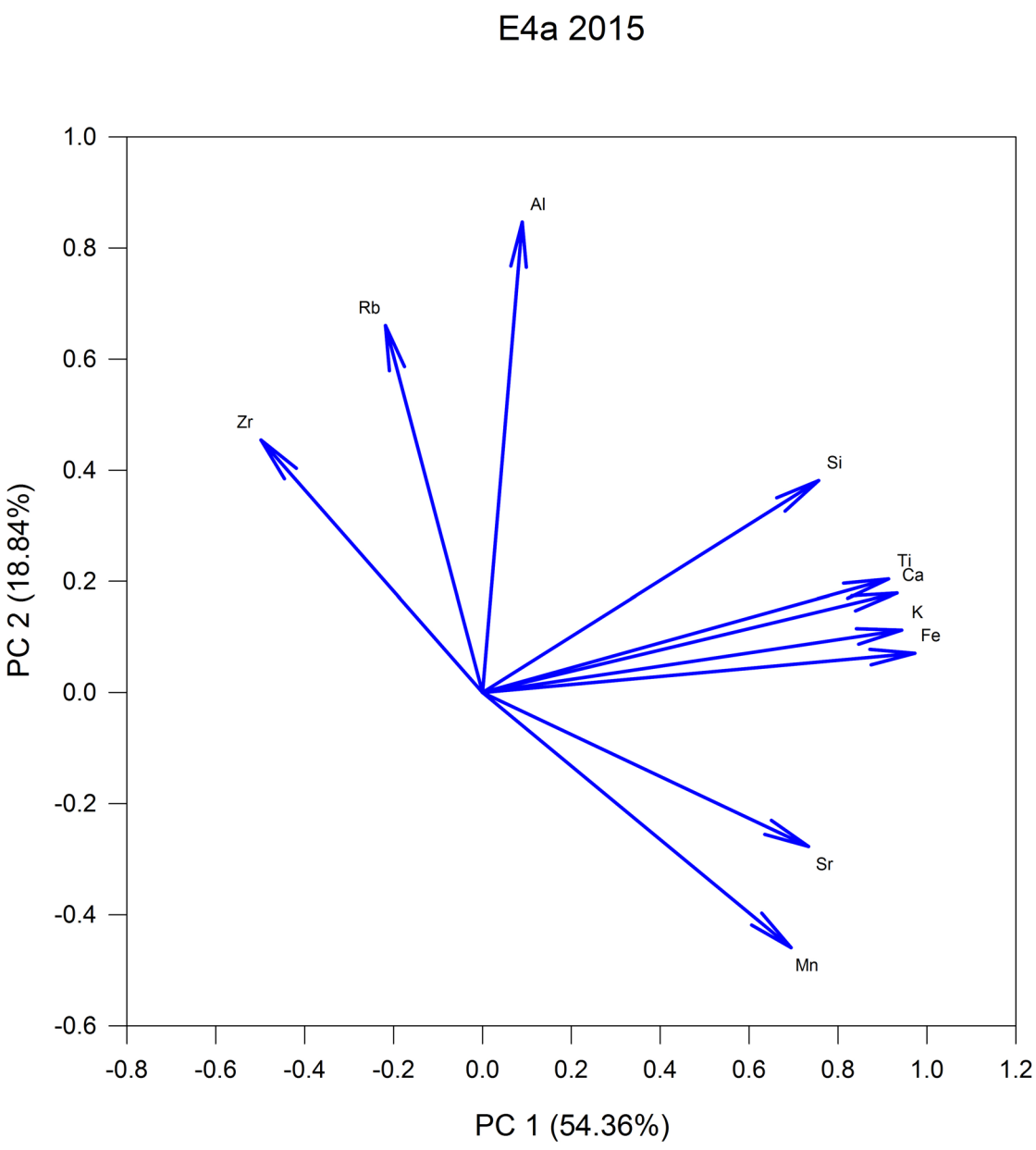

Component Scores

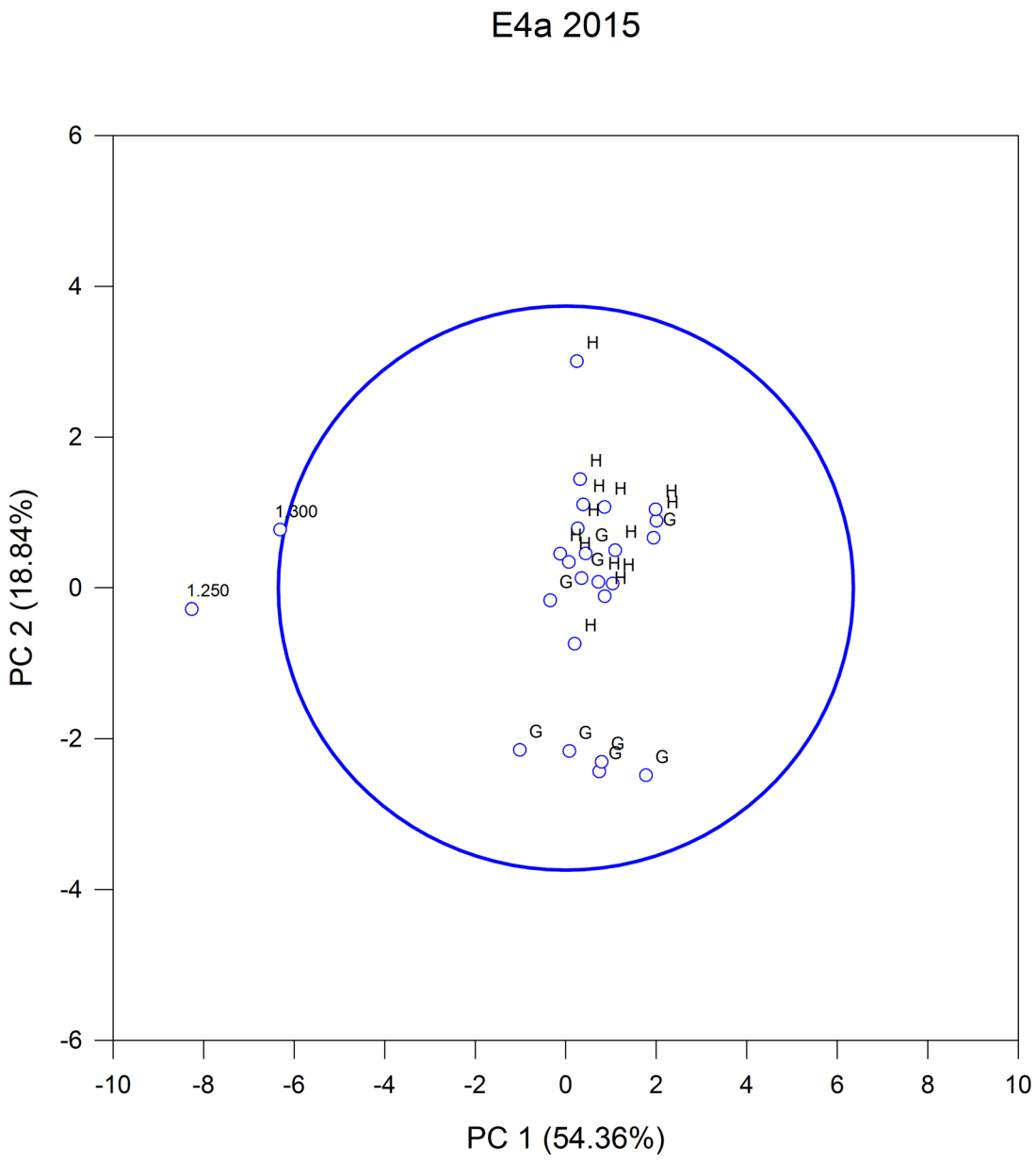

Winter_2015

Principal Components Analysis Monday, March 21, 2016, 8:29:04 PM

Data source Winter

Normality Test (Henze-Zinkler):

Statistic = 0.956 Passed (P = 0.643)

Descriptive Statistics:

Variable	Mean	Std Dev
Al	1.532	0.184
Si	2.586	0.0555
K	3.470	0.0478
Ca	3.480	0.0717
Ti	3.338	0.0437
Mn	2.716	0.0842
Fe	4.793	0.0491
Rb	3.003	0.0491
Sr	2.825	0.0679
Zr	2.816	0.110

Total Observations	41
Missing	0
Valid Observations	41

An observation is missing if any worksheet cell in its row has a non-numeric value.

Correlation Matrix:

	Al	Si	K	Ca	Ti	Mn	Fe	Rb	Sr	Zr
Al	1.000									
Si	0.308	1.000								
K	0.180	0.710	1.000							
Ca	0.124	0.583	0.526	1.000						
Ti	0.232	0.732	0.930	0.618	1.000					
Mn	0.136	0.470	0.656	0.140	0.582	1.000				
Fe	0.233	0.671	0.924	0.364	0.821	0.680	1.000			
Rb	0.107	0.479	0.487	0.297	0.436	0.487	0.536	1.000		
Sr	0.0926	0.319	0.612	0.308	0.650	0.443	0.498	0.317	1.000	
Zr	-0.00791	-0.0736	0.0342	-0.163	-0.108	-0.138	0.204	-0.111	-0.144	1.000

Total Variance: = 10.000

Eigenvalues of the Correlation Matrix:

	Eigenvalue	Difference	Proportion(%)	Cumulative(%)
1	5.021	3.848	50.213	50.213
2	1.173	0.142	11.732	61.946
3	1.031	0.126	10.312	72.258
4	0.905	0.147	9.054	81.312
5	0.758	0.243	7.581	88.892
6	0.515	0.245	5.153	94.046
7	0.270	0.0446	2.703	96.749

8	0.226	0.158	2.257	99.006
9	0.0673	0.0353	0.673	99.680
10	0.0320	--	0.320	100.000

If two or more eigenvalues have the same value, then the corresponding principal components are not well-defined and any interpretation of them is suspect.

Number of In-Model Principal Components = 3

The in-model components correspond to all eigenvalues greater than or equal to the average eigenvalue. When analyzing the correlation matrix, the average eigenvalue is always 1.0. This criterion can be changed in the Test Options dialog on the Criterion panel. The variance of each principal component equals its corresponding eigenvalue.

Chi-Square Tests for the Equality of Eigenvalues:

Hypothesis: All eigenvalues are equal.
Statistic = 300.950
Degrees of freedom = 45.000
P value = <0.001

There is a significant difference in the eigenvalues. A principal components analysis can be conducted.

Hypothesis: The last 7 eigenvalues are equal.
Statistic = 121.778
Degrees of freedom = 25.556
P value = <0.001

There is a significant difference in the last 7 eigenvalues. You may want to include additional principal components in your model by changing the settings in the Test Options dialog on the Criterion panel.

Eigenvectors of the Correlation Matrix:

	PC 1	PC 2	PC 3
Al	0.127	-0.0810	0.697
Si	0.361	0.0422	0.298
K	0.424	-0.120	-0.0623
Ca	0.268	0.324	0.383
Ti	0.419	0.0514	0.0392
Mn	0.320	-0.0534	-0.373
Fe	0.400	-0.324	-0.0721
Rb	0.279	0.0569	-0.185
Sr	0.292	0.133	-0.292
Zr	-0.0342	-0.861	0.0971

Each principal component is a linear combination of the original variables, after each original variable has been standardized to have unit variance. The coefficients of this linear combination are the entries in the corresponding column of the above table. These coefficients provide the interpretation of the principal components in terms of the original variables.

Standard Errors for the Eigenvector Entries:

	PC 1	PC 2	PC 3
Al	0.0827	0.926	0.758
Si	0.0467	0.386	0.193
K	0.0250	0.127	0.221

Ca	0.0681	0.568	0.754
Ti	0.0268	0.137	0.223
Mn	0.0572	0.522	0.500
Fe	0.0375	0.107	0.397
Rb	0.0635	0.371	0.463
Sr	0.0618	0.429	0.375
Zr	0.0896	0.209	1.093

Component Loadings:

	PC 1	**PC 2**	**PC 3**
Al	0.285	-0.0878	0.708
Si	0.809	0.0457	0.302
K	0.949	-0.130	-0.0633
Ca	0.600	0.351	0.389
Ti	0.938	0.0556	0.0398
Mn	0.718	-0.0579	-0.379
Fe	0.897	-0.351	-0.0732
Rb	0.625	0.0616	-0.188
Sr	0.655	0.144	-0.297
Zr	-0.0766	-0.932	0.0986

If the principle components are standardized to have unit variance, the loadings are the coefficients of the linear combination of in-model principal components used to approximate the original variables. If a correlation matrix is analyzed, then the loadings equal the correlations between the original variables and the principal components.

Fitted Correlation Matrix:

	Al	**Si**	**K**	**Ca**	**Ti**	**Mn**	**Fe**	**Rb**	**Sr**	**Zr**
Al	0.590									
Si	0.441	0.748								
K	0.237	0.743	0.921							
Ca	0.416	0.619	0.499	0.635						
Ti	0.291	0.773	0.881	0.598	0.885					
Mn	-0.0582	0.463	0.713	0.263	0.655	0.662				
Fe	0.235	0.688	0.902	0.387	0.819	0.692	0.933			
Rb	0.0395	0.451	0.597	0.323	0.582	0.516	0.553	0.430		
Sr	-0.0359	0.447	0.621	0.328	0.610	0.574	0.559	0.474	0.538	
Zr	0.130	-0.0748	0.0421	-0.335	-0.120	-0.0384	0.251	-0.124	-0.214	0.885

This is an estimate of the correlation matrix that results by approximating the original variables with the in-model principal components.

Component Loading Vectors

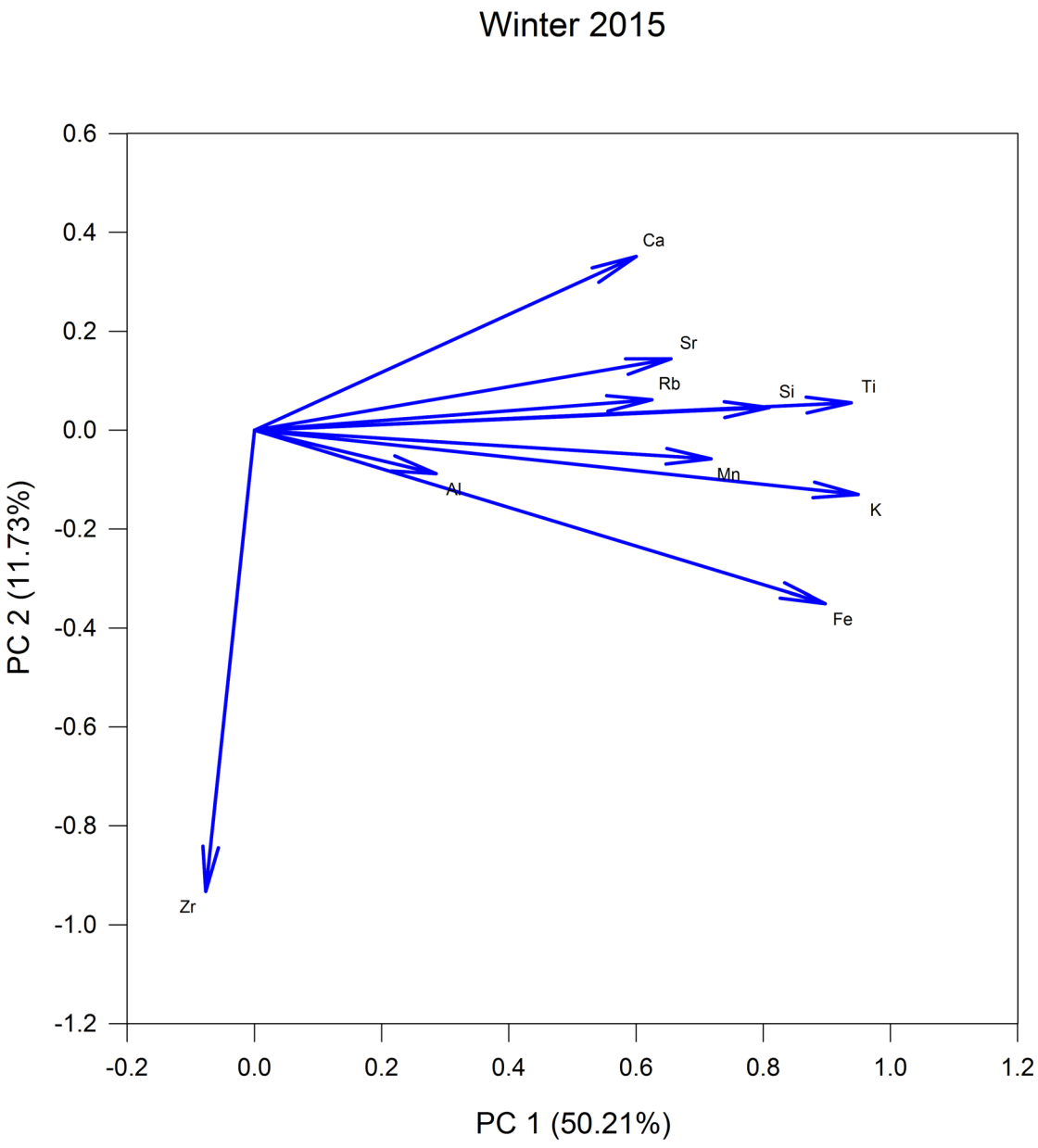

Component Scores

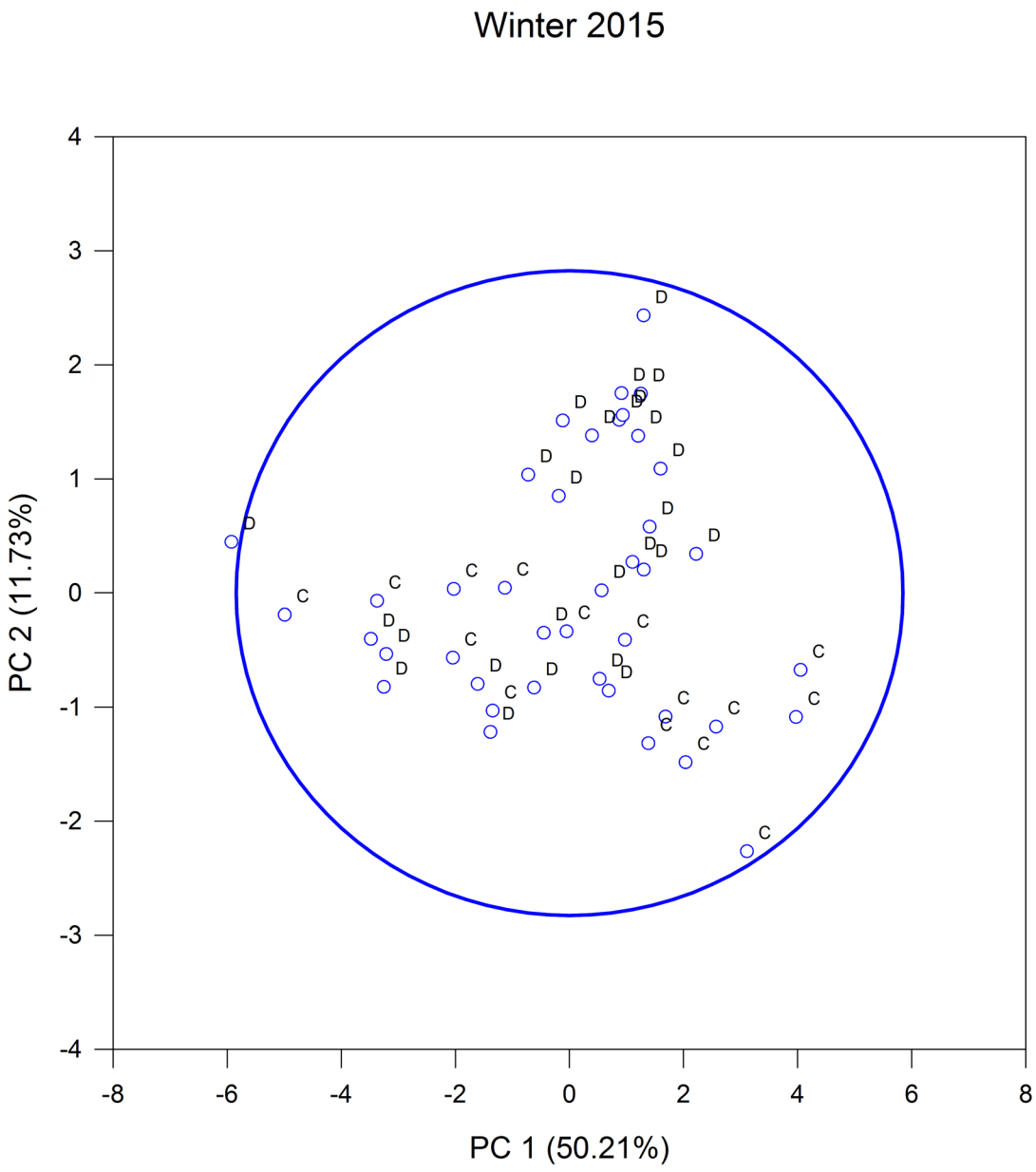

Summer_2013

Principal Components Analysis Friday, March 25, 2016, 3:23:29 AM

Data source: Summer 2013

Normality Test (Henze-Zinkler):

Statistic = 1.940 Failed ($P < 0.050$)

Descriptive Statistics:

Variable	Mean	Std Dev
Al	1.668	0.207
Si	2.613	0.223
K	3.473	0.207
Ca	3.384	0.263
Ti	3.355	0.176
Mn	2.677	0.151
Fe	4.761	0.142
Rb	3.026	0.0692
Sr	2.789	0.0796
Zr	2.941	0.112

Total Observations	287
Missing	18
Valid Observations	269

An observation is missing if any worksheet cell in its row has a non-numeric value.

Correlation Matrix:

	Al	Si	K	Ca	Ti	Mn	Fe	Rb	Sr	Zr
Al	1.000									
Si	0.680	1.000								
K	0.702	0.957	1.000							
Ca	0.484	0.798	0.686	1.000						
Ti	0.657	0.963	0.928	0.871	1.000					
Mn	0.576	0.723	0.798	0.349	0.647	1.000				
Fe	0.703	0.919	0.973	0.593	0.881	0.853	1.000			
Rb	0.292	0.389	0.433	0.252	0.463	0.356	0.497	1.000		
Sr	0.307	0.288	0.355	0.0128	0.288	0.337	0.424	0.595	1.000	
Zr	-0.0447	0.134	-0.0353	0.472	0.270	-0.219	-0.0833	0.284	-0.00825	1.000

Total Variance: = 10.000

Eigenvalues of the Correlation Matrix:

	Eigenvalue	Difference	Proportion(%)	Cumulative(%)
1	5.950	4.417	59.500	59.500
2	1.533	0.238	15.334	74.835
3	1.295	0.824	12.952	87.787
4	0.471	0.128	4.713	92.500
5	0.343	0.0849	3.433	95.933
6	0.258	0.167	2.584	98.517
7	0.0917	0.0639	0.917	99.434

8	0.0278	0.0112	0.278	99.712
9	0.0166	0.00440	0.166	99.878
10	0.0122	--	0.122	100.000

If two or more eigenvalues have the same value, then the corresponding principal components are not well-defined and any interpretation of them is suspect.

Number of In-Model Principal Components = 3

The in-model components correspond to all eigenvalues greater than or equal to the average eigenvalue. When analyzing the correlation matrix, the average eigenvalue is always 1.0. This criterion can be changed in the Test Options dialog on the Criterion panel. The variance of each principal component equals its corresponding eigenvalue.

Chi-Square Tests for the Equality of Eigenvalues:

Hypothesis: All eigenvalues are equal.
Statistic = 4020.136
Degrees of freedom = 45.000
P value = <0.001

There is a significant difference in the eigenvalues. A principal components analysis can be conducted.

Hypothesis: The last 7 eigenvalues are equal.
Statistic = 1426.530
Degrees of freedom = 27.128
P value = <0.001

There is a significant difference in the last 7 eigenvalues. You may want to include additional principal components in your model by changing the settings in the Test Options dialog on the Criterion panel.

Eigenvectors of the Correlation Matrix:

	PC 1	PC 2	PC 3
Al	0.310	0.117	0.112
Si	0.394	-0.0791	0.140
K	0.398	0.0775	0.117
Ca	0.304	-0.467	0.181
Ti	0.392	-0.191	0.0674
Mn	0.324	0.320	0.103
Fe	0.394	0.161	0.0460
Rb	0.223	-0.0140	-0.641
Sr	0.177	0.287	-0.632
Zr	0.0470	-0.713	-0.306

Each principal component is a linear combination of the original variables, after each original variable has been standardized to have unit variance. The coefficients of this linear combination are the entries in the corresponding column of the above table. These coefficients provide the interpretation of the principal components in terms of the original variables.

Standard Errors for the Eigenvector Entries:

	PC 1	PC 2	PC 3
Al	0.0181	0.0609	0.0676
Si	0.00792	0.0541	0.0343
K	0.00711	0.0465	0.0336

Ca	0.0217	0.0681	0.170
Ti	0.00920	0.0305	0.0711
Mn	0.0183	0.0486	0.120
Fe	0.00833	0.0256	0.0610
Rb	0.0258	0.233	0.0319
Sr	0.0281	0.230	0.108
Zr	0.0327	0.112	0.258

Component Loadings:

	PC 1	**PC 2**	**PC 3**
Al	0.756	0.144	0.127
Si	0.962	-0.0980	0.159
K	0.970	0.0960	0.133
Ca	0.742	-0.578	0.206
Ti	0.957	-0.237	0.0767
Mn	0.791	0.396	0.117
Fe	0.962	0.200	0.0524
Rb	0.544	-0.0174	-0.729
Sr	0.431	0.355	-0.720
Zr	0.115	-0.883	-0.349

If the principle components are standardized to have unit variance, the loadings are the coefficients of the linear combination of in-model principal components used to approximate the original variables. If a correlation matrix is analyzed, then the loadings equal the correlations between the original variables and the principal components.

Fitted Correlation Matrix:

	Al	**Si**	**K**	**Ca**	**Ti**	**Mn**	**Fe**	**Rb**	**Sr**	**Zr**
Al	0.608									
Si	0.733	0.960								
K	0.764	0.945	0.967							
Ca	0.504	0.804	0.692	0.928						
Ti	0.699	0.956	0.915	0.863	0.977					
Mn	0.670	0.741	0.821	0.382	0.672	0.797				
Fe	0.763	0.914	0.959	0.609	0.877	0.846	0.968			
Rb	0.316	0.409	0.429	0.264	0.469	0.338	0.482	0.828		
Sr	0.286	0.266	0.357	-0.0335	0.273	0.397	0.448	0.753	0.830	
Zr	-0.0851	0.141	-0.0200	0.524	0.292	-0.300	-0.0843	0.332	-0.0137	0.914

This is an estimate of the correlation matrix that results by approximating the original variables with the in-model principal components.

Component Loading Vectors

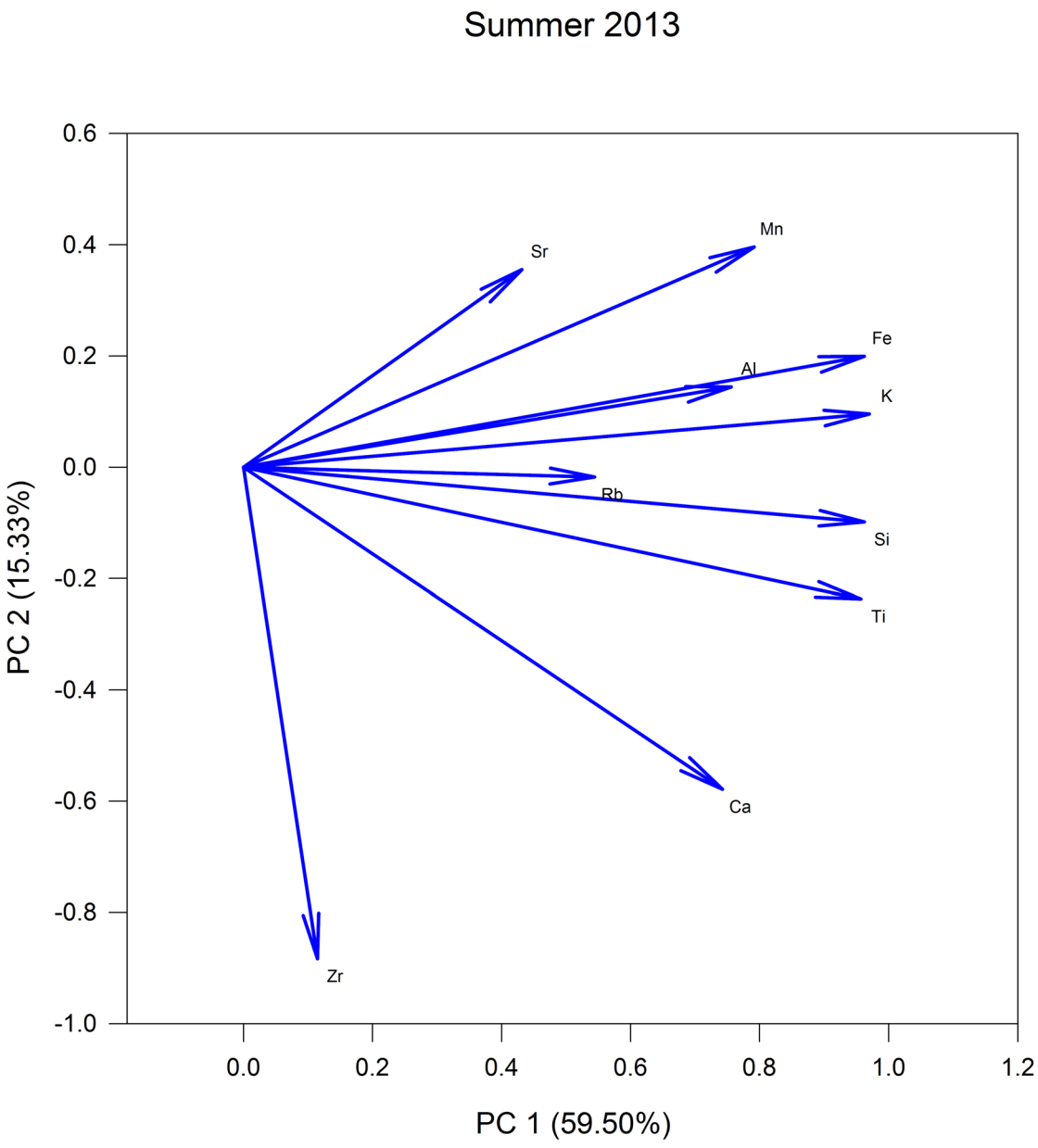

Component Scores

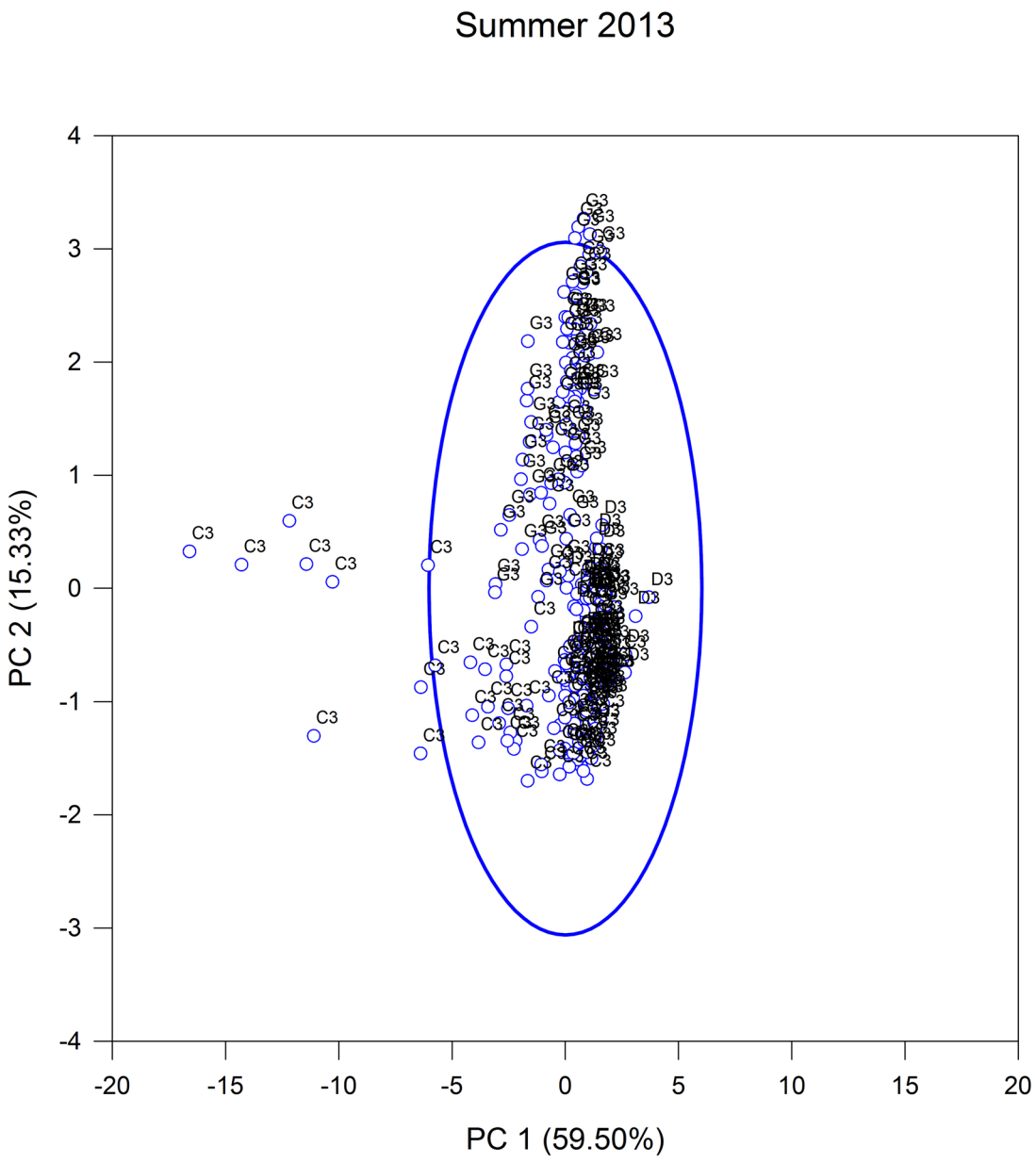

Fall_2013

Principal Components Analysis Friday, March 25, 2016, 3:19:11 AM

Data source: Fall 2013

Normality Test (Henze-Zinkler):

Statistic = 1.423 Failed ($P < 0.050$)

Descriptive Statistics:

Variable	Mean	Std Dev
Al	1.675	0.187
Si	2.583	0.155
K	3.478	0.133
Ca	3.390	0.142
Ti	3.347	0.143
Mn	2.650	0.127
Fe	4.767	0.118
Rb	3.027	0.101
Sr	2.783	0.111
Zr	2.901	0.113

Total Observations	234
Missing	3
Valid Observations	231

An observation is missing if any worksheet cell in its row has a non-numeric value.

Correlation Matrix:

	Al	Si	K	Ca	Ti	Mn	Fe	Rb	Sr	Zr
Al	1.000									
Si	0.566	1.000								
K	0.571	0.959	1.000							
Ca	0.429	0.781	0.726	1.000						
Ti	0.523	0.943	0.947	0.811	1.000					
Mn	0.495	0.839	0.854	0.631	0.767	1.000				
Fe	0.566	0.947	0.981	0.670	0.921	0.855	1.000			
Rb	0.381	0.665	0.694	0.520	0.767	0.455	0.720	1.000		
Sr	0.329	0.611	0.650	0.422	0.638	0.513	0.691	0.740	1.000	
Zr	0.255	0.612	0.557	0.663	0.712	0.382	0.556	0.733	0.501	1.000

Total Variance: = 10.000

Eigenvalues of the Correlation Matrix:

	Eigenvalue	Difference	Proportion(%)	Cumulative(%)
1	7.052	6.048	70.519	70.519
2	1.004	0.311	10.041	80.560
3	0.693	0.104	6.928	87.488
4	0.589	0.320	5.888	93.376
5	0.269	0.0817	2.685	96.062
6	0.187	0.0650	1.869	97.930
7	0.122	0.0814	1.219	99.149

8	0.0405	0.00699	0.405	99.554
9	0.0335	0.0224	0.335	99.889
10	0.0111	--	0.111	100.000

If two or more eigenvalues have the same value, then the corresponding principal components are not well-defined and any interpretation of them is suspect.

Number of In-Model Principal Components = 2

The in-model components correspond to all eigenvalues greater than or equal to the average eigenvalue. When analyzing the correlation matrix, the average eigenvalue is always 1.0. This criterion can be changed in the Test Options dialog on the Criterion panel. The variance of each principal component equals its corresponding eigenvalue.

Chi-Square Tests for the Equality of Eigenvalues:

Hypothesis: All eigenvalues are equal.
Statistic = 3433.802
Degrees of freedom = 45.000
P value = <0.001

There is a significant difference in the eigenvalues. A principal components analysis can be conducted.

Hypothesis: The last 8 eigenvalues are equal.
Statistic = 1302.897
Degrees of freedom = 33.853
P value = <0.001

There is a significant difference in the last 8 eigenvalues. You may want to include additional principal components in your model by changing the settings in the Test Options dialog on the Criterion panel.

Eigenvectors of the Correlation Matrix:

	PC 1	**PC 2**
Al	0.225	0.459
Si	0.361	0.142
K	0.363	0.159
Ca	0.301	-0.00204
Ti	0.365	-0.0275
Mn	0.311	0.370
Fe	0.361	0.131
Rb	0.300	-0.454
Sr	0.274	-0.309
Zr	0.267	-0.536

Each principal component is a linear combination of the original variables, after each original variable has been standardized to have unit variance. The coefficients of this linear combination are the entries in the corresponding column of the above table. These coefficients provide the interpretation of the principal components in terms of the original variables.

Standard Errors for the Eigenvector Entries:

	PC 1	**PC 2**
Al	0.0222	0.107
Si	0.00743	0.0284
K	0.00730	0.0269

Ca	0.0161	0.107
Ti	0.00622	0.0304
Mn	0.0154	0.0526
Fe	0.00770	0.0371
Rb	0.0168	0.0578
Sr	0.0188	0.112
Zr	0.0197	0.0757

Component Loadings:

	PC 1	**PC 2**
Al	0.598	0.460
Si	0.960	0.142
K	0.963	0.159
Ca	0.801	-0.00205
Ti	0.970	-0.0276
Mn	0.826	0.371
Fe	0.958	0.132
Rb	0.796	-0.455
Sr	0.726	-0.310
Zr	0.709	-0.537

If the principle components are standardized to have unit variance, the loadings are the coefficients of the linear combination of in-model principal components used to approximate the original variables. If a correlation matrix is analyzed, then the loadings equal the correlations between the original variables and the principal components.

Fitted Correlation Matrix:

	Al	**Si**	**K**	**Ca**	**Ti**	**Mn**	**Fe**	**Rb**	**Sr**	**Zr**
Al	0.569									
Si	0.639	0.942								
K	0.649	0.947	0.952							
Ca	0.478	0.768	0.770	0.641						
Ti	0.568	0.927	0.930	0.777	0.942					
Mn	0.664	0.845	0.854	0.660	0.791	0.819				
Fe	0.633	0.938	0.943	0.767	0.926	0.840	0.935			
Rb	0.267	0.699	0.694	0.638	0.785	0.489	0.703	0.841		
Sr	0.292	0.653	0.650	0.582	0.713	0.485	0.655	0.719	0.624	
Zr	0.177	0.604	0.598	0.569	0.703	0.386	0.609	0.809	0.682	0.792

This is an estimate of the correlation matrix that results by approximating the original variables with the in-model principal components.

Component Loading Vectors

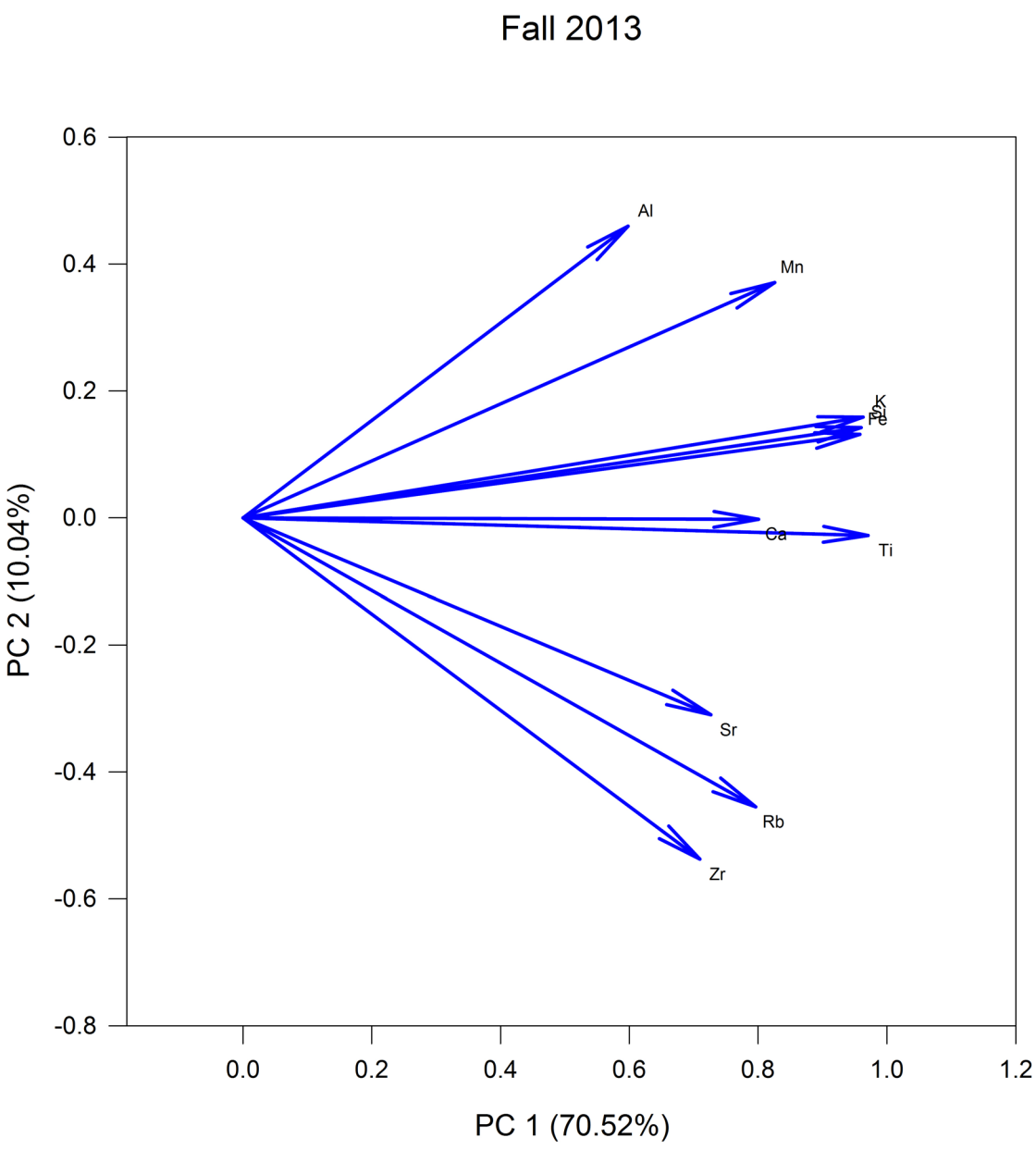

Component Scores

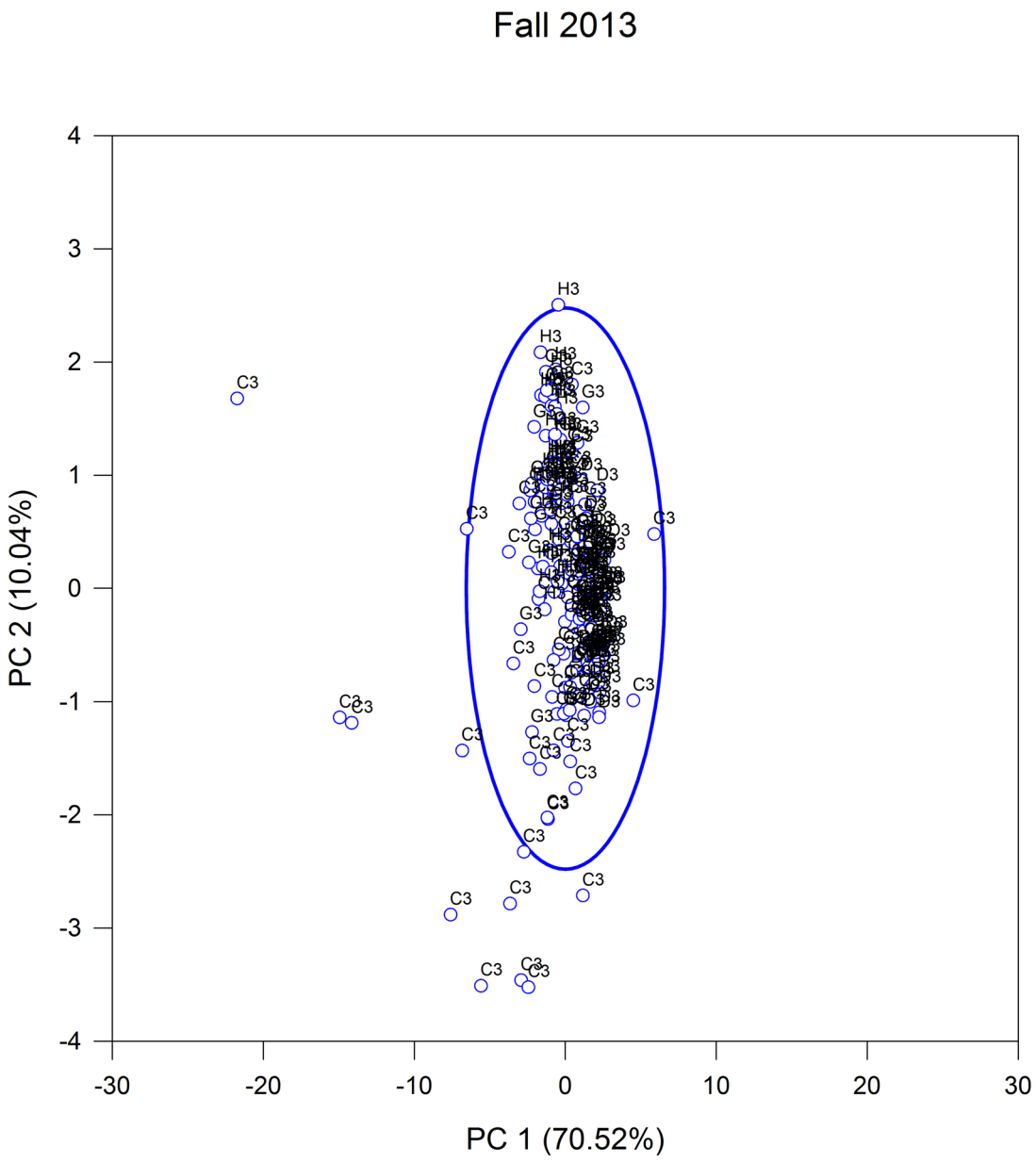

Winter_2013

Principal Components Analysis Friday, March 25, 2016, 3:17:42 AM

Data source: Winter 2013

Normality Test (Henze-Zinkler):

Statistic = 1.285 Failed ($P < 0.050$)

Descriptive Statistics:

Variable	Mean	Std Dev
Al	1.619	0.234
Si	2.499	0.145
K	3.438	0.151
Ca	3.251	0.146
Ti	3.223	0.128
Mn	2.612	0.182
Fe	4.732	0.142
Rb	2.997	0.0839
Sr	2.805	0.0884
Zr	2.797	0.0825

Total Observations	194
Missing	1
Valid Observations	193

An observation is missing if any worksheet cell in its row has a non-numeric value.

Correlation Matrix:

	Al	Si	K	Ca	Ti	Mn	Fe	Rb	Sr	Zr
Al	1.000									
Si	0.678	1.000								
K	0.669	0.963	1.000							
Ca	0.165	0.243	0.211	1.000						
Ti	0.649	0.962	0.966	0.332	1.000					
Mn	0.530	0.769	0.834	-0.118	0.777	1.000				
Fe	0.654	0.934	0.979	0.171	0.944	0.873	1.000			
Rb	0.403	0.682	0.682	0.318	0.711	0.574	0.709	1.000		
Sr	0.233	0.430	0.445	0.359	0.481	0.375	0.468	0.670	1.000	
Zr	0.198	0.287	0.235	0.395	0.308	0.0919	0.245	0.476	0.332	1.000

Total Variance: = 10.000

Eigenvalues of the Correlation Matrix:

	Eigenvalue	Difference	Proportion(%)	Cumulative(%)
1	6.096	4.536	60.957	60.957
2	1.560	0.768	15.601	76.558
3	0.792	0.153	7.920	84.478
4	0.639	0.201	6.394	90.872
5	0.438	0.206	4.382	95.253
6	0.232	0.0759	2.320	97.573
7	0.156	0.109	1.561	99.134

8	0.0466	0.0185	0.466	99.600
9	0.0281	0.0162	0.281	99.881
10	0.0119	--	0.119	100.000

If two or more eigenvalues have the same value, then the corresponding principal components are not well-defined and any interpretation of them is suspect.

Number of In-Model Principal Components = 2

The in-model components correspond to all eigenvalues greater than or equal to the average eigenvalue. When analyzing the correlation matrix, the average eigenvalue is always 1.0. This criterion can be changed in the Test Options dialog on the Criterion panel. The variance of each principal component equals its corresponding eigenvalue.

Chi-Square Tests for the Equality of Eigenvalues:

Hypothesis: All eigenvalues are equal.
Statistic = 2576.330
Degrees of freedom = 45.000
P value = <0.001

There is a significant difference in the eigenvalues. A principal components analysis can be conducted.

Hypothesis: The last 8 eigenvalues are equal.
Statistic = 1139.227
Degrees of freedom = 34.111
P value = <0.001

There is a significant difference in the last 8 eigenvalues. You may want to include additional principal components in your model by changing the settings in the Test Options dialog on the Criterion panel.

Eigenvectors of the Correlation Matrix:

	PC 1	**PC 2**
Al	0.284	0.142
Si	0.385	0.0978
K	0.390	0.143
Ca	0.124	-0.597
Ti	0.391	0.0395
Mn	0.332	0.329
Fe	0.390	0.150
Rb	0.326	-0.237
Sr	0.239	-0.353
Zr	0.155	-0.530

Each principal component is a linear combination of the original variables, after each original variable has been standardized to have unit variance. The coefficients of this linear combination are the entries in the corresponding column of the above table. These coefficients provide the interpretation of the principal components in terms of the original variables.

Standard Errors for the Eigenvector Entries:

	PC 1	**PC 2**
Al	0.0234	0.0686
Si	0.00988	0.0289
K	0.00925	0.0244

Ca	0.0351	0.0622
Ti	0.00809	0.0281
Mn	0.0203	0.0373
Fe	0.00929	0.0228
Rb	0.0199	0.0486
Sr	0.0281	0.0717
Zr	0.0333	0.0629

Component Loadings:

	PC 1	**PC 2**
Al	0.701	0.177
Si	0.952	0.122
K	0.964	0.178
Ca	0.306	-0.745
Ti	0.966	0.0493
Mn	0.820	0.411
Fe	0.964	0.188
Rb	0.805	-0.296
Sr	0.589	-0.440
Zr	0.382	-0.662

If the principle components are standardized to have unit variance, the loadings are the coefficients of the linear combination of in-model principal components used to approximate the original variables. If a correlation matrix is analyzed, then the loadings equal the correlations between the original variables and the principal components.

Fitted Correlation Matrix:

	Al	**Si**	**K**	**Ca**	**Ti**	**Mn**	**Fe**	**Rb**	**Sr**	**Zr**
Al	0.522									
Si	0.688	0.921								
K	0.707	0.939	0.961							
Ca	0.0821	0.200	0.162	0.649						
Ti	0.686	0.925	0.940	0.258	0.936					
Mn	0.648	0.831	0.864	-0.0559	0.813	0.842				
Fe	0.708	0.940	0.963	0.155	0.940	0.868	0.964			
Rb	0.512	0.730	0.723	0.467	0.763	0.539	0.720	0.736		
Sr	0.335	0.507	0.489	0.508	0.547	0.302	0.485	0.605	0.541	
Zr	0.150	0.283	0.250	0.610	0.336	0.0412	0.244	0.504	0.516	0.584

This is an estimate of the correlation matrix that results by approximating the original variables with the in-model principal components.

Component Loading Vectors

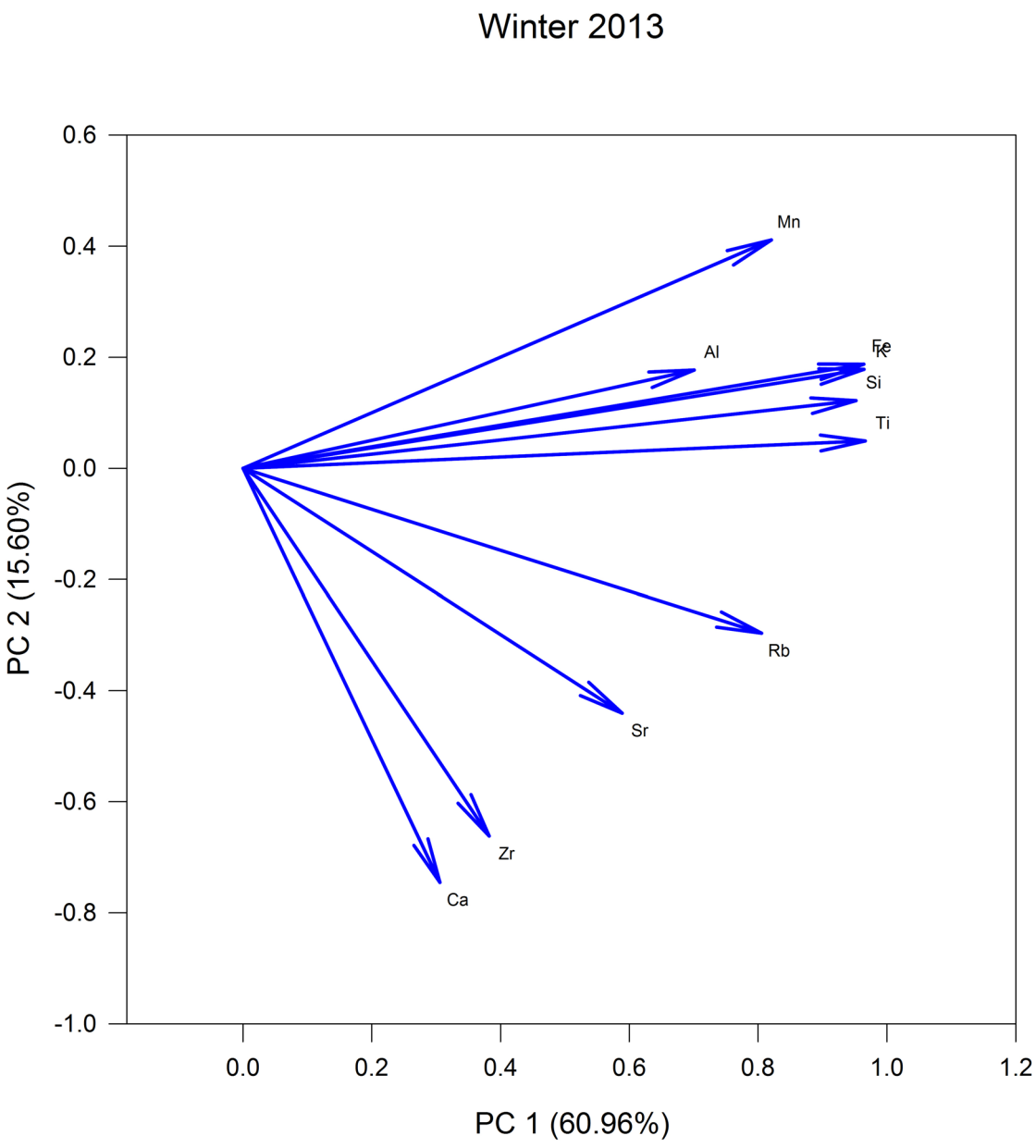

Component Scores

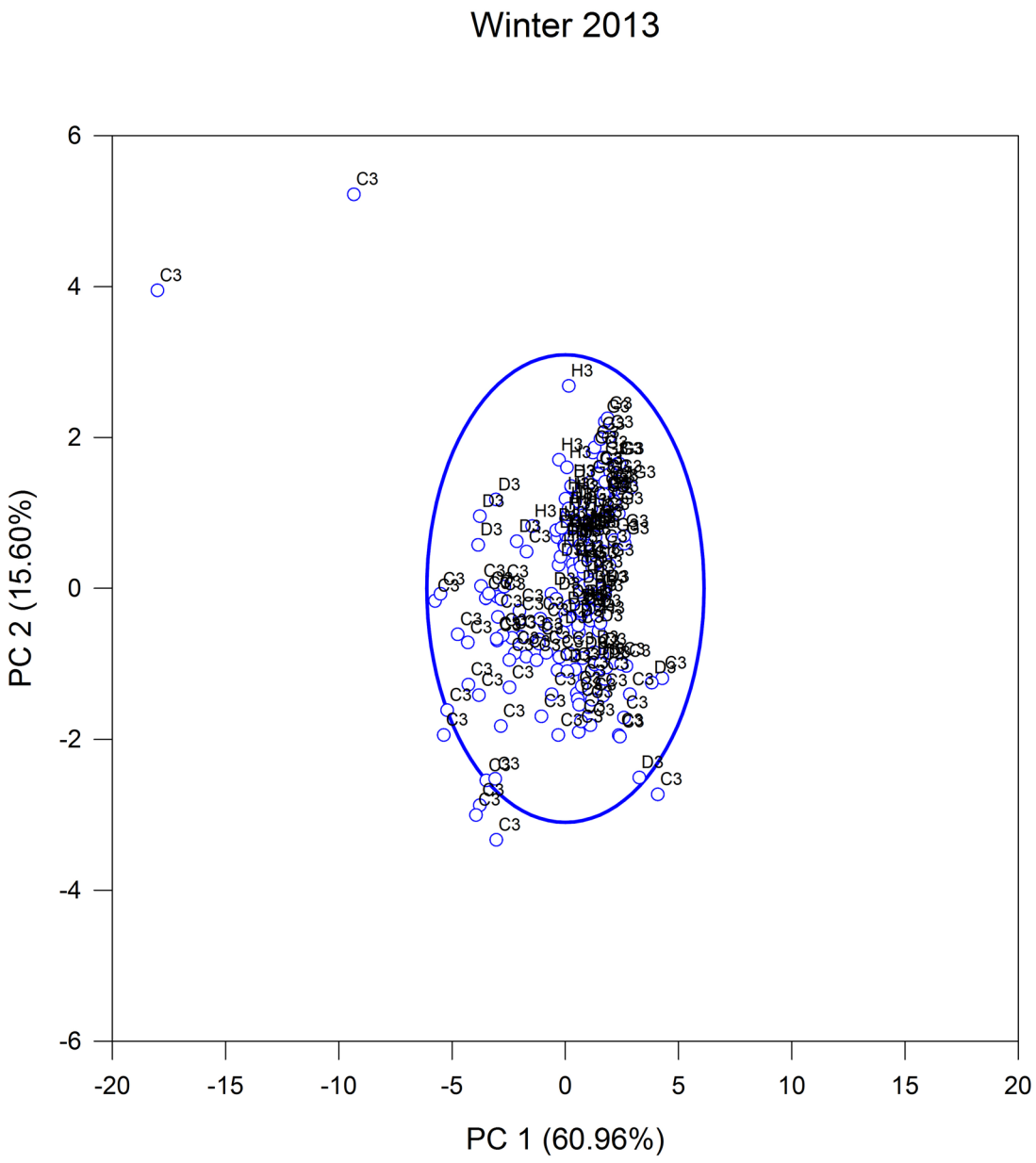

Spring_2014

Principal Components Analysis Friday, March 25, 2016, 3:16:08 AM

Data source: Spring 2014

Normality Test (Henze-Zinkler):

Statistic = 1.251 Failed ($P < 0.050$)

Descriptive Statistics:

Variable	Mean	Std Dev
Al	1.675	0.181
Si	2.623	0.234
K	3.440	0.259
Ca	3.352	0.123
Ti	3.286	0.240
Mn	2.578	0.261
Fe	4.731	0.210
Rb	2.983	0.102
Sr	2.769	0.0821
Zr	2.926	0.0863

Total Observations	110
Missing	10
Valid Observations	100

An observation is missing if any worksheet cell in its row has a non-numeric value.

Correlation Matrix:

	Al	Si	K	Ca	Ti	Mn	Fe	Rb	Sr	Zr
Al	1.000									
Si	0.626	1.000								
K	0.648	0.875	1.000							
Ca	0.353	0.640	0.438	1.000						
Ti	0.624	0.922	0.978	0.503	1.000					
Mn	0.621	0.721	0.869	0.388	0.818	1.000				
Fe	0.639	0.851	0.995	0.416	0.969	0.869	1.000			
Rb	0.612	0.669	0.837	0.209	0.803	0.696	0.840	1.000		
Sr	0.438	0.364	0.525	0.183	0.443	0.525	0.531	0.639	1.000	
Zr	0.229	0.469	0.209	0.471	0.351	0.0802	0.174	0.161	-0.00897	1.000

Total Variance: = 10.000

Eigenvalues of the Correlation Matrix:

	Eigenvalue	Difference	Proportion(%)	Cumulative(%)
1	6.418	4.991	64.176	64.176
2	1.427	0.770	14.270	78.446
3	0.657	0.0923	6.570	85.016
4	0.565	0.0758	5.646	90.662
5	0.489	0.263	4.888	95.550
6	0.226	0.0885	2.255	97.805
7	0.137	0.0665	1.370	99.175

8	0.0705	0.0618	0.705	99.881
9	0.00869	0.00544	0.0869	99.968
10	0.00324	--	0.0324	100.000

If two or more eigenvalues have the same value, then the corresponding principal components are not well-defined and any interpretation of them is suspect.

Number of In-Model Principal Components = 2

The in-model components correspond to all eigenvalues greater than or equal to the average eigenvalue. When analyzing the correlation matrix, the average eigenvalue is always 1.0. This criterion can be changed in the Test Options dialog on the Criterion panel. The variance of each principal component equals its corresponding eigenvalue.

Chi-Square Tests for the Equality of Eigenvalues:

Hypothesis: All eigenvalues are equal.
Statistic = 1542.748
Degrees of freedom = 45.000
P value = <0.001

There is a significant difference in the eigenvalues. A principal components analysis can be conducted.

Hypothesis: The last 8 eigenvalues are equal.
Statistic = 739.086
Degrees of freedom = 34.000
P value = <0.001

There is a significant difference in the last 8 eigenvalues. You may want to include additional principal components in your model by changing the settings in the Test Options dialog on the Criterion panel.

Eigenvectors of the Correlation Matrix:

	PC 1	**PC 2**
Al	0.292	0.0275
Si	0.360	-0.237
K	0.384	0.0802
Ca	0.214	-0.518
Ti	0.381	-0.0544
Mn	0.344	0.163
Fe	0.380	0.110
Rb	0.336	0.241
Sr	0.234	0.359
Zr	0.128	-0.663

Each principal component is a linear combination of the original variables, after each original variable has been standardized to have unit variance. The coefficients of this linear combination are the entries in the corresponding column of the above table. These coefficients provide the interpretation of the principal components in terms of the original variables.

Standard Errors for the Eigenvector Entries:

	PC 1	**PC 2**
Al	0.0289	0.0894
Si	0.0189	0.0380
K	0.0104	0.0377

Ca	0.0398	0.0784
Ti	0.0112	0.0413
Mn	0.0211	0.0544
Fe	0.0119	0.0389
Rb	0.0235	0.0556
Sr	0.0369	0.103
Zr	0.0460	0.0730

Component Loadings:

	PC 1	**PC 2**
Al	0.739	0.0329
Si	0.911	-0.283
K	0.972	0.0958
Ca	0.542	-0.618
Ti	0.966	-0.0650
Mn	0.872	0.195
Fe	0.964	0.132
Rb	0.851	0.288
Sr	0.592	0.429
Zr	0.325	-0.792

If the principle components are standardized to have unit variance, the loadings are the coefficients of the linear combination of in-model principal components used to approximate the original variables. If a correlation matrix is analyzed, then the loadings equal the correlations between the original variables and the principal components.

Fitted Correlation Matrix:

	Al	**Si**	**K**	**Ca**	**Ti**	**Mn**	**Fe**	**Rb**	**Sr**	**Zr**
Al	0.548									
Si	0.664	0.910								
K	0.722	0.858	0.954							
Ca	0.380	0.669	0.467	0.676						
Ti	0.712	0.898	0.933	0.563	0.937					
Mn	0.652	0.740	0.867	0.352	0.830	0.799				
Fe	0.717	0.841	0.949	0.440	0.922	0.866	0.946			
Rb	0.639	0.694	0.855	0.283	0.803	0.799	0.858	0.807		
Sr	0.452	0.417	0.616	0.0550	0.543	0.600	0.627	0.627	0.534	
Zr	0.215	0.521	0.240	0.666	0.366	0.129	0.209	0.0488	-0.147	0.733

This is an estimate of the correlation matrix that results by approximating the original variables with the in-model principal components.

Component Loading Vectors

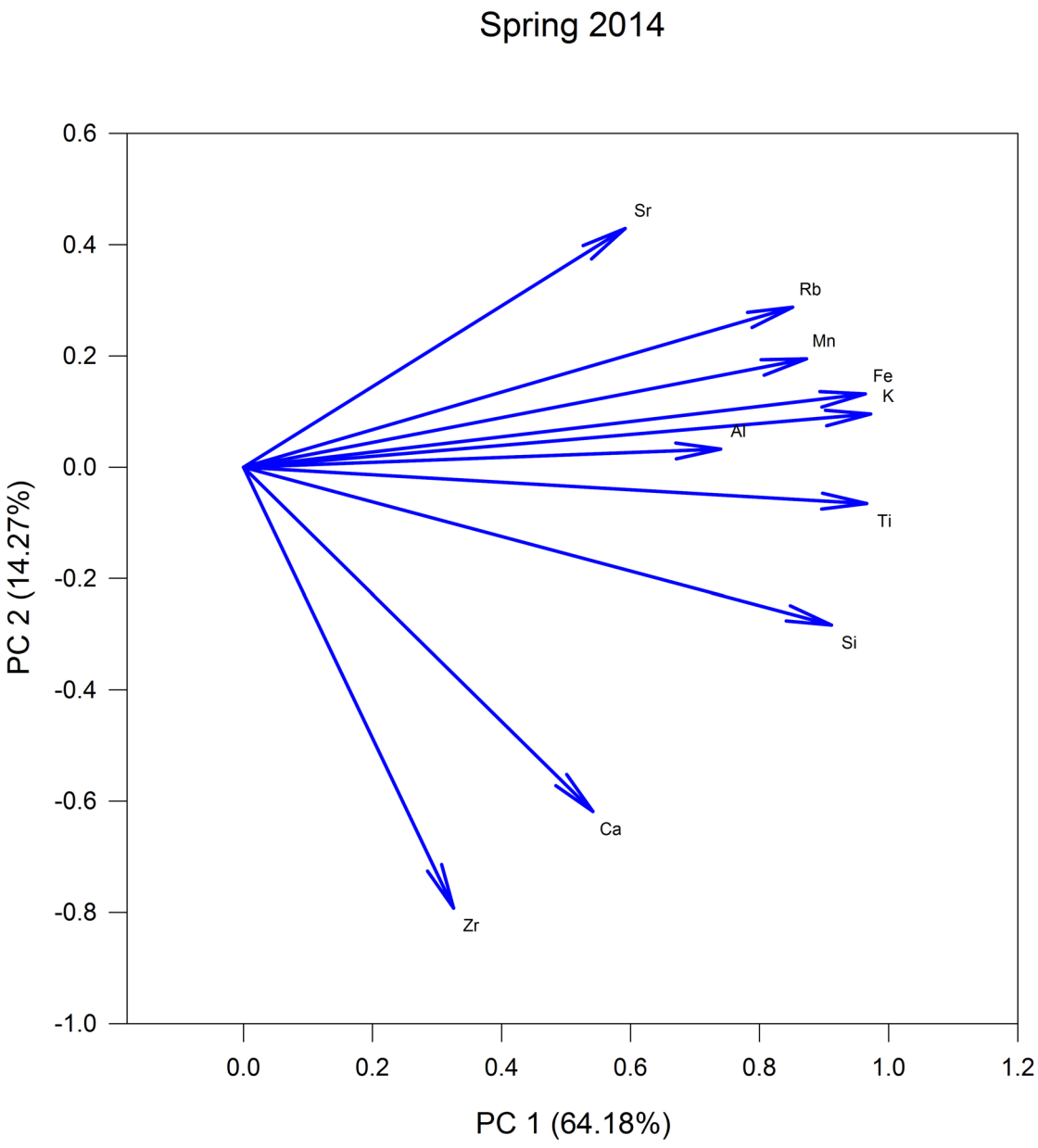

Component Scores

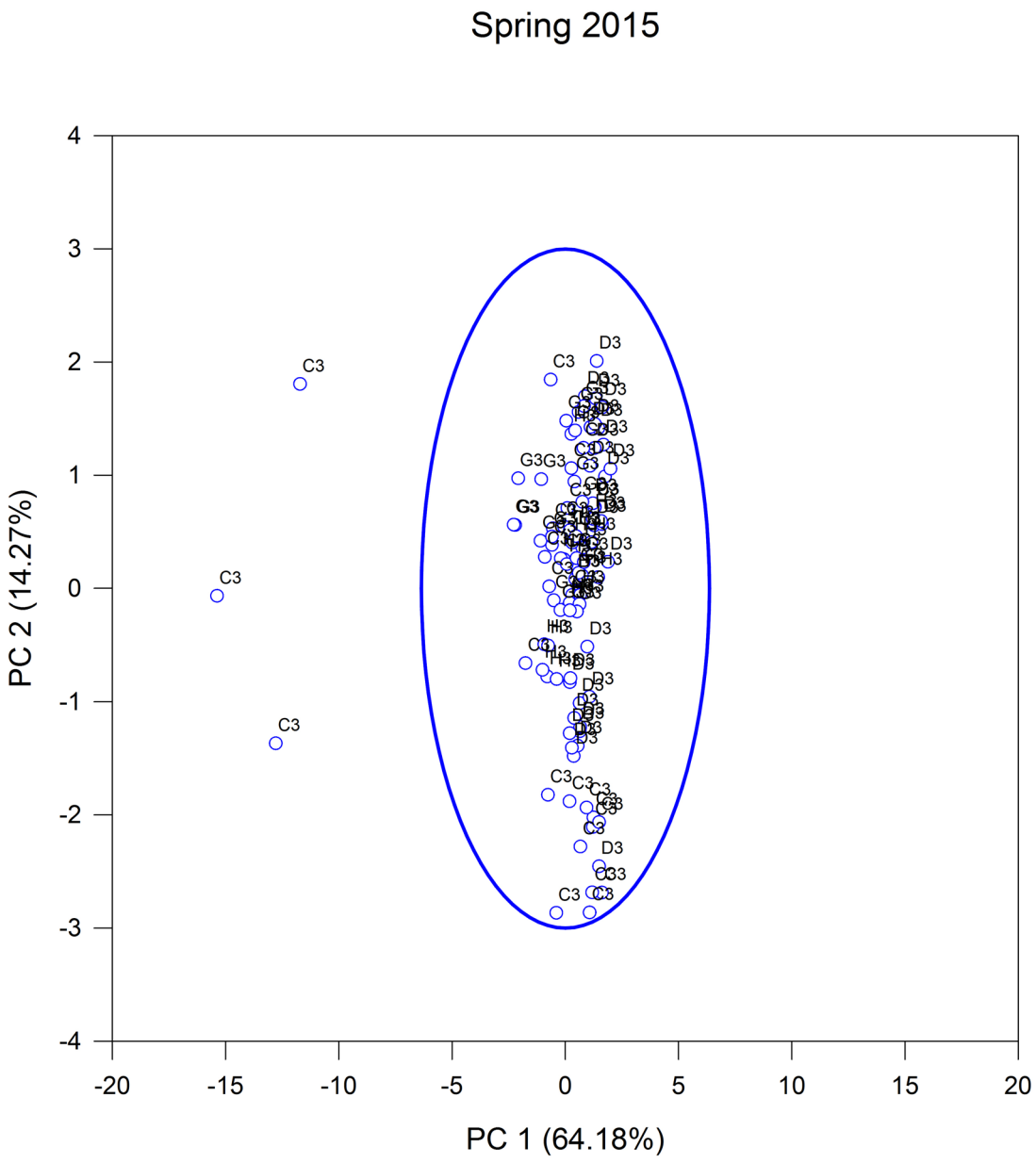

Summer_2011

Principal Components Analysis Friday, March 25, 2016, 2:53:13 AM

Data source: Summer 2011

Normality Test (Henze-Zinkler):

Statistic = 1.160 Failed ($P < 0.050$)

Descriptive Statistics:

Variable	Mean	Std Dev
AL	1.539	0.217
Si	2.727	0.403
K	3.243	0.437
Ca	3.108	0.260
Ti	3.316	0.0930
Mn	2.434	0.132
Fe	4.710	0.0415
Rb	3.021	0.0467
Sr	2.841	0.0529
Zr	2.880	0.0902

Total Observations	84
Missing	5
Valid Observations	79

An observation is missing if any worksheet cell in its row has a non-numeric value.

Correlation Matrix:

	AL	Si	K	Ca	Ti	Mn	Fe	Rb	Sr	Zr
AL	1.000									
Si	0.111	1.000								
K	0.0501	-0.898	1.000							
Ca	0.283	-0.0928	0.400	1.000						
Ti	0.309	-0.163	0.501	0.904	1.000					
Mn	0.143	-0.0506	0.286	0.677	0.684	1.000				
Fe	0.197	-0.319	0.521	0.378	0.647	0.511	1.000			
Rb	0.0137	0.0411	0.0369	-0.148	0.104	0.0919	0.349	1.000		
Sr	0.0648	-0.0419	0.0950	-0.0591	0.117	0.0672	0.256	0.539	1.000	
Zr	0.102	-0.297	0.512	0.745	0.773	0.452	0.416	-0.0198	0.114	1.000

Total Variance: = 10.000

Eigenvalues of the Correlation Matrix:

	Eigenvalue	Difference	Proportion(%)	Cumulative(%)
1	4.106	2.403	41.063	41.063
2	1.703	0.0727	17.034	58.097
3	1.631	0.738	16.308	74.405
4	0.892	0.237	8.925	83.329
5	0.655	0.230	6.554	89.883
6	0.425	0.0837	4.254	94.138

7	0.342	0.162	3.417	97.555
8	0.179	0.142	1.795	99.350
9	0.0371	0.00929	0.371	99.721
10	0.0279	--	0.279	100.000

If two or more eigenvalues have the same value, then the corresponding principal components are not well-defined and any interpretation of them is suspect.

Number of In-Model Principal Components = 3

The in-model components correspond to all eigenvalues greater than or equal to the average eigenvalue. When analyzing the correlation matrix, the average eigenvalue is always 1.0. This criterion can be changed in the Test Options dialog on the Criterion panel. The variance of each principal component equals its corresponding eigenvalue.

Chi-Square Tests for the Equality of Eigenvalues:

Hypothesis: All eigenvalues are equal.
Statistic = 645.201
Degrees of freedom = 45.000
P value = <0.001

There is a significant difference in the eigenvalues. A principal components analysis can be conducted.

Hypothesis: The last 7 eigenvalues are equal.
Statistic = 292.312
Degrees of freedom = 27.342
P value = <0.001

There is a significant difference in the last 7 eigenvalues. You may want to include additional principal components in your model by changing the settings in the Test Options dialog on the Criterion panel.

Eigenvectors of the Correlation Matrix:

	PC 1	PC 2	PC 3
AL	0.136	0.130	0.306
Si	-0.216	0.268	0.622
K	0.354	-0.207	-0.466
Ca	0.411	0.342	0.108
Ti	0.460	0.127	0.160
Mn	0.355	0.133	0.219
Fe	0.362	-0.260	0.0867
Rb	0.0619	-0.580	0.350
Sr	0.0891	-0.548	0.290
Zr	0.400	0.116	-0.0425

Each principal component is a linear combination of the original variables, after each original variable has been standardized to have unit variance. The coefficients of this linear combination are the entries in the corresponding column of the above table. These coefficients provide the interpretation of the principal components in terms of the original variables.

Standard Errors for the Eigenvector Entries:

	PC 1	PC 2	PC 3
AL	0.0726	0.806	0.375
Si	0.0818	1.607	0.694

K	0.0624	1.204	0.537
Ca	0.0477	0.285	0.884
Ti	0.0285	0.418	0.333
Mn	0.0500	0.574	0.357
Fe	0.0498	0.239	0.676
Rb	0.0876	0.906	1.499
Sr	0.0842	0.753	1.416
Zr	0.0392	0.141	0.313

Component Loadings:

	PC 1	**PC 2**	**PC 3**
AL	0.275	0.170	0.391
Si	-0.437	0.350	0.795
K	0.718	-0.270	-0.595
Ca	0.833	0.446	0.138
Ti	0.933	0.166	0.204
Mn	0.719	0.174	0.280
Fe	0.734	-0.339	0.111
Rb	0.125	-0.757	0.448
Sr	0.180	-0.715	0.371
Zr	0.810	0.152	-0.0542

If the principle components are standardized to have unit variance, the loadings are the coefficients of the linear combination of in-model principal components used to approximate the original variables. If a correlation matrix is analyzed, then the loadings equal the correlations between the original variables and the principal components.

Fitted Correlation Matrix:

	AL	**Si**	**K**	**Ca**	**Ti**	**Mn**	**Fe**	**Rb**	**Sr**	**Zr**
AL	0.258									
Si	0.250	0.945								
K	-0.0813	-0.881	0.943							
Ca	0.358	-0.0984	0.396	0.911						
Ti	0.364	-0.187	0.504	0.879	0.939					
Mn	0.337	-0.0308	0.303	0.715	0.757	0.626				
Fe	0.188	-0.352	0.553	0.475	0.651	0.500	0.666			
Rb	0.0811	0.0357	0.0286	-0.172	0.0828	0.0841	0.398	0.789		
Sr	0.0733	-0.0347	0.102	-0.117	0.125	0.109	0.416	0.730	0.681	
Zr	0.227	-0.344	0.573	0.735	0.769	0.594	0.537	-0.0375	0.0177	0.682

This is an estimate of the correlation matrix that results by approximating the original variables with the in-model principal components.

Component Loading Vectors

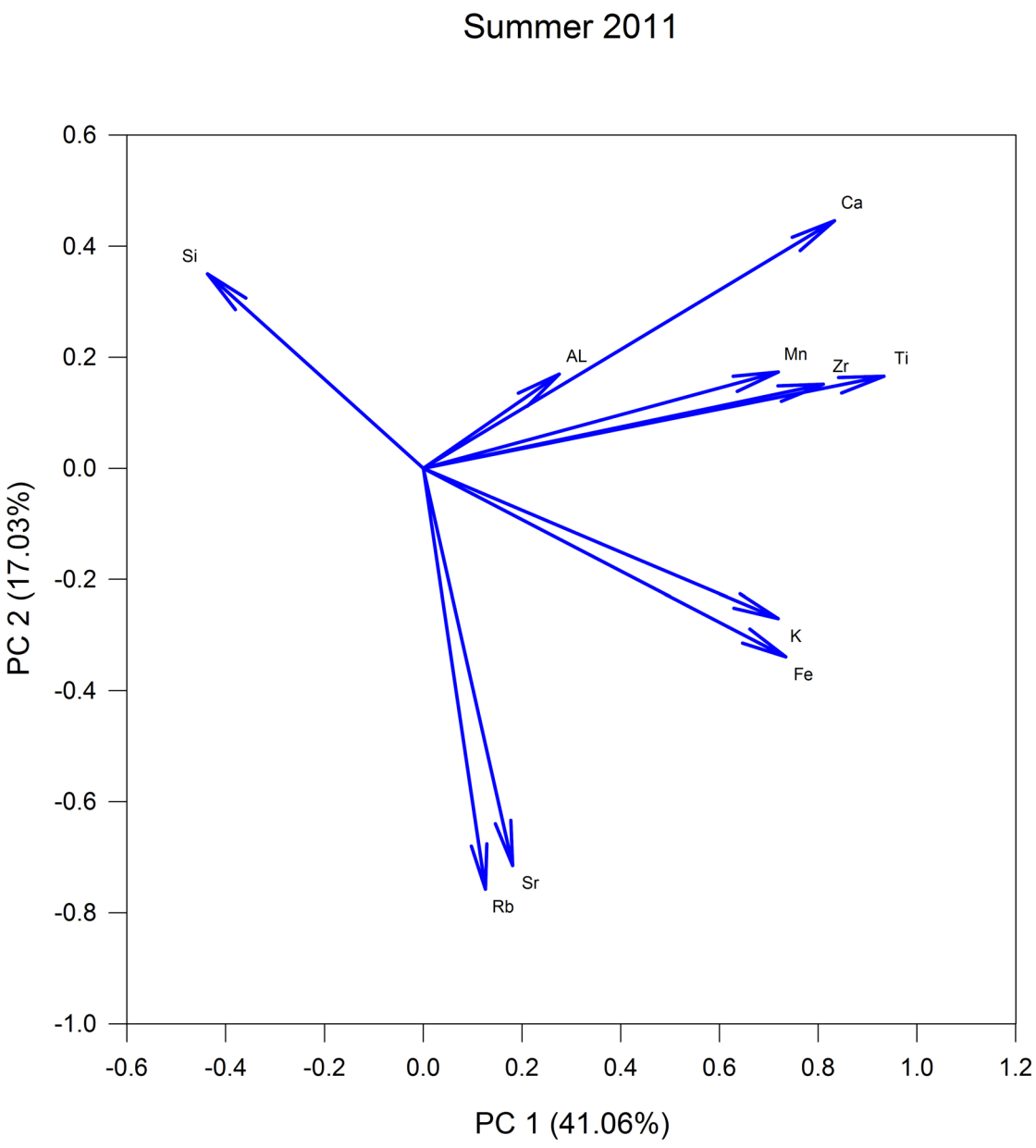

Component Scores

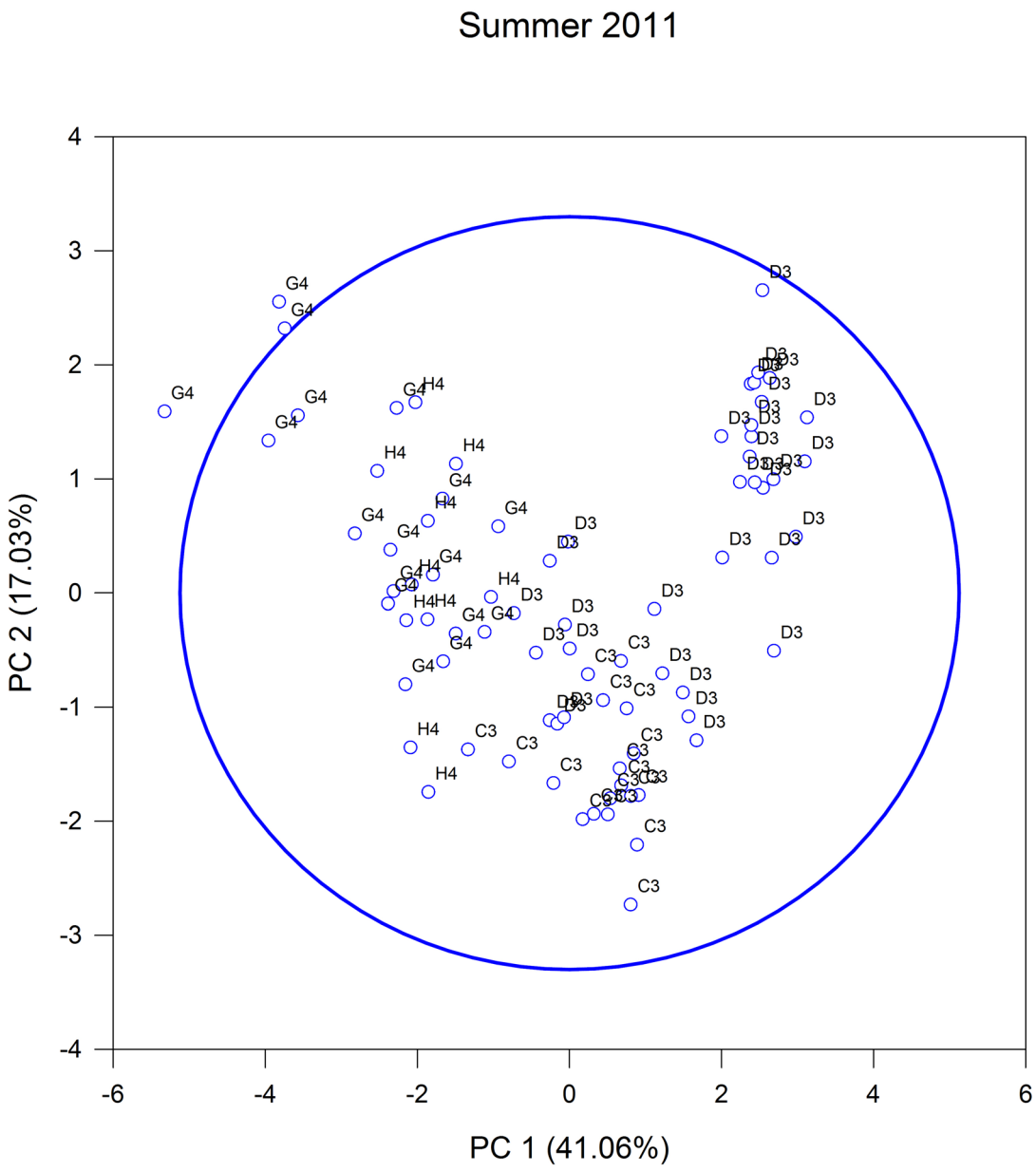

Fall_2011

Principal Components Analysis Friday, March 25, 2016, 2:55:58 AM

Data source: Fall 2011

Normality Test (Henze-Zinkler):

Statistic = 1.269 Failed ($P < 0.050$)

Descriptive Statistics:

Variable	Mean	Std Dev
AL	1.613	0.204
Si	2.832	0.420
K	3.237	0.438
Ca	3.184	0.195
Ti	3.364	0.0779
Mn	2.502	0.115
Fe	4.741	0.0356
Rb	3.045	0.0410
Sr	2.846	0.0548
Zr	2.884	0.0863

Total Observations	135
Missing	0
Valid Observations	135

An observation is missing if any worksheet cell in its row has a non-numeric value.

Correlation Matrix:

	AL	Si	K	Ca	Ti	Mn	Fe	Rb	Sr	Zr
AL	1.000									
Si	-0.0254	1.000								
K	0.137	-0.968	1.000							
Ca	0.365	-0.307	0.496	1.000						
Ti	0.400	-0.254	0.474	0.890	1.000					
Mn	-0.0380	-0.438	0.418	0.198	0.110	1.000				
Fe	0.240	0.345	-0.174	0.384	0.540	-0.261	1.000			
Rb	0.0372	0.0823	-0.0308	0.0774	0.182	-0.0602	0.157	1.000		
Sr	0.0613	0.253	-0.237	-0.172	-0.124	-0.219	0.0961	0.232	1.000	
Zr	0.350	-0.233	0.394	0.750	0.725	0.134	0.280	0.187	-0.0153	1.000

Total Variance: = 10.000

Eigenvalues of the Correlation Matrix:

	Eigenvalue	Difference	Proportion(%)	Cumulative(%)
1	3.590	1.265	35.904	35.904
2	2.325	1.222	23.250	59.154
3	1.103	0.244	11.030	70.184
4	0.859	0.169	8.592	78.776
5	0.690	0.0485	6.901	85.677
6	0.642	0.156	6.416	92.093
7	0.485	0.265	4.852	96.944

8	0.220	0.137	2.197	99.141
9	0.0827	0.0795	0.827	99.968
10	0.00320	--	0.0320	100.000

If two or more eigenvalues have the same value, then the corresponding principal components are not well-defined and any interpretation of them is suspect.

Number of In-Model Principal Components = 3

The in-model components correspond to all eigenvalues greater than or equal to the average eigenvalue. When analyzing the correlation matrix, the average eigenvalue is always 1.0. This criterion can be changed in the Test Options dialog on the Criterion panel. The variance of each principal component equals its corresponding eigenvalue.

Chi-Square Tests for the Equality of Eigenvalues:

Hypothesis: All eigenvalues are equal.
Statistic = 1206.810
Degrees of freedom = 45.000
P value = <0.001

There is a significant difference in the eigenvalues. A principal components analysis can be conducted.

Hypothesis: The last 7 eigenvalues are equal.
Statistic = 704.699
Degrees of freedom = 27.329
P value = <0.001

There is a significant difference in the last 7 eigenvalues. You may want to include additional principal components in your model by changing the settings in the Test Options dialog on the Criterion panel.

Eigenvectors of the Correlation Matrix:

	PC 1	PC 2	PC 3
AL	0.228	0.229	-0.0770
Si	-0.313	0.463	-0.179
K	0.399	-0.358	0.155
Ca	0.473	0.145	-0.116
Ti	0.467	0.228	-0.0731
Mn	0.186	-0.365	0.0904
Fe	0.145	0.499	-0.219
Rb	0.0592	0.229	0.700
Sr	-0.123	0.257	0.605
Zr	0.418	0.177	0.0868

Each principal component is a linear combination of the original variables, after each original variable has been standardized to have unit variance. The coefficients of this linear combination are the entries in the corresponding column of the above table. These coefficients provide the interpretation of the principal components in terms of the original variables.

Standard Errors for the Eigenvector Entries:

	PC 1	PC 2	PC 3
AL	0.0661	0.0844	0.268
Si	0.0936	0.0700	0.0946
K	0.0733	0.0843	0.0865

Ca	0.0348	0.0968	0.0633
Ti	0.0475	0.0942	0.0656
Mn	0.0833	0.0708	0.172
Fe	0.103	0.0548	0.119
Rb	0.0736	0.0929	0.167
Sr	0.0746	0.0889	0.177
Zr	0.0450	0.0908	0.0833

Component Loadings:

	PC 1	**PC 2**	**PC 3**
AL	0.432	0.349	-0.0809
Si	-0.594	0.705	-0.188
K	0.757	-0.546	0.163
Ca	0.896	0.222	-0.121
Ti	0.884	0.347	-0.0768
Mn	0.352	-0.557	0.0949
Fe	0.276	0.761	-0.230
Rb	0.112	0.349	0.735
Sr	-0.233	0.393	0.635
Zr	0.792	0.271	0.0912

If the principle components are standardized to have unit variance, the loadings are the coefficients of the linear combination of in-model principal components used to approximate the original variables. If a correlation matrix is analyzed, then the loadings equal the correlations between the original variables and the principal components.

Fitted Correlation Matrix:

	AL	**Si**	**K**	**Ca**	**Ti**	**Mn**	**Fe**	**Rb**	**Sr**	**Zr**
AL	0.315									
Si	0.00479	0.885								
K	0.124	-0.865	0.897							
Ca	0.474	-0.353	0.537	0.866						
Ti	0.509	-0.266	0.468	0.879	0.909					
Mn	-0.0496	-0.620	0.586	0.181	0.111	0.443				
Fe	0.403	0.417	-0.244	0.443	0.526	-0.348	0.708			
Rb	0.111	0.0415	0.0139	0.0886	0.164	-0.0851	0.128	0.675		
Sr	-0.0151	0.296	-0.287	-0.199	-0.119	-0.240	0.0887	0.578	0.612	
Zr	0.429	-0.296	0.466	0.758	0.787	0.137	0.403	0.250	-0.0204	0.708

This is an estimate of the correlation matrix that results by approximating the original variables with the in-model principal components.

Component Loading Vectors

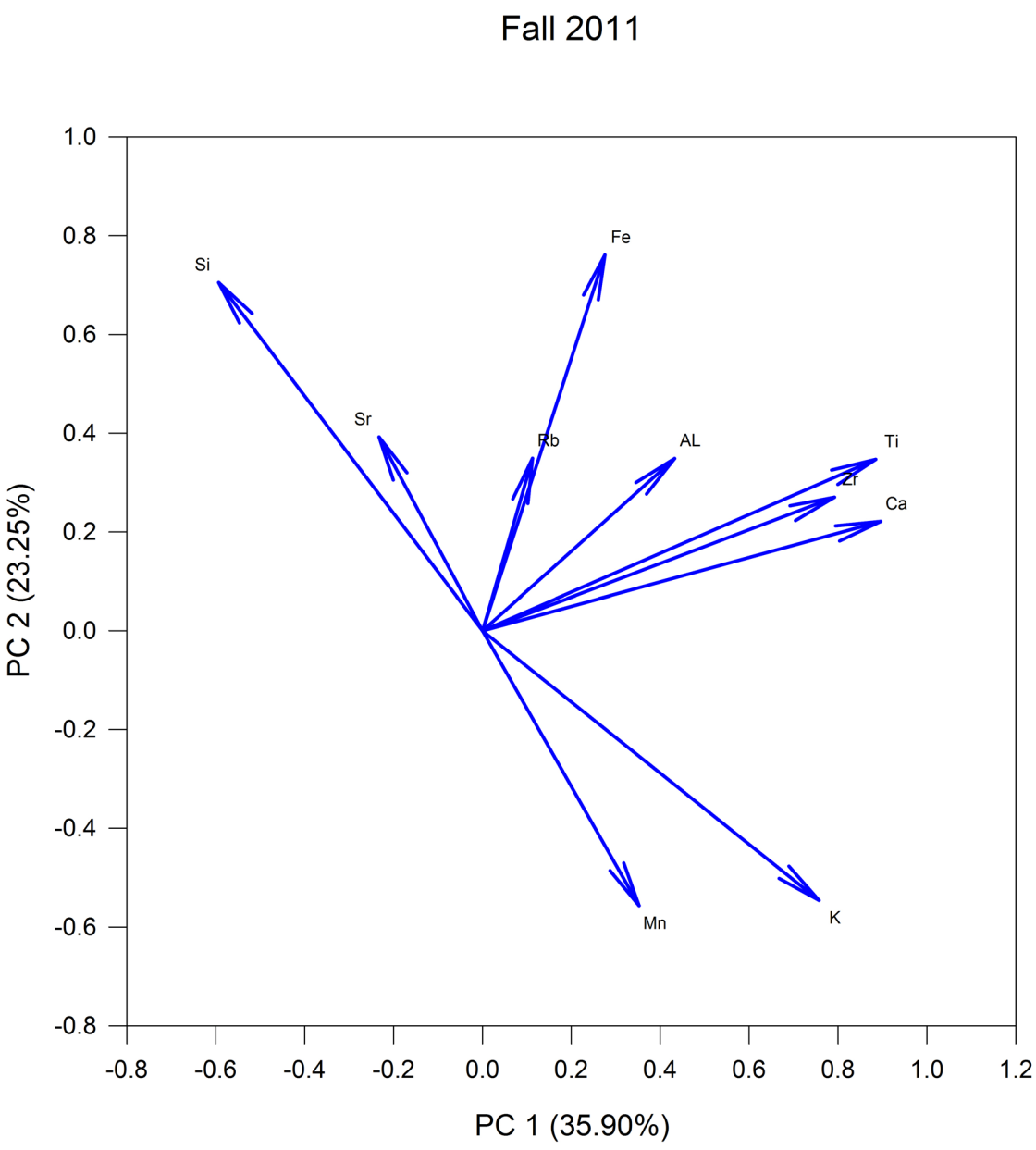

Component Scores

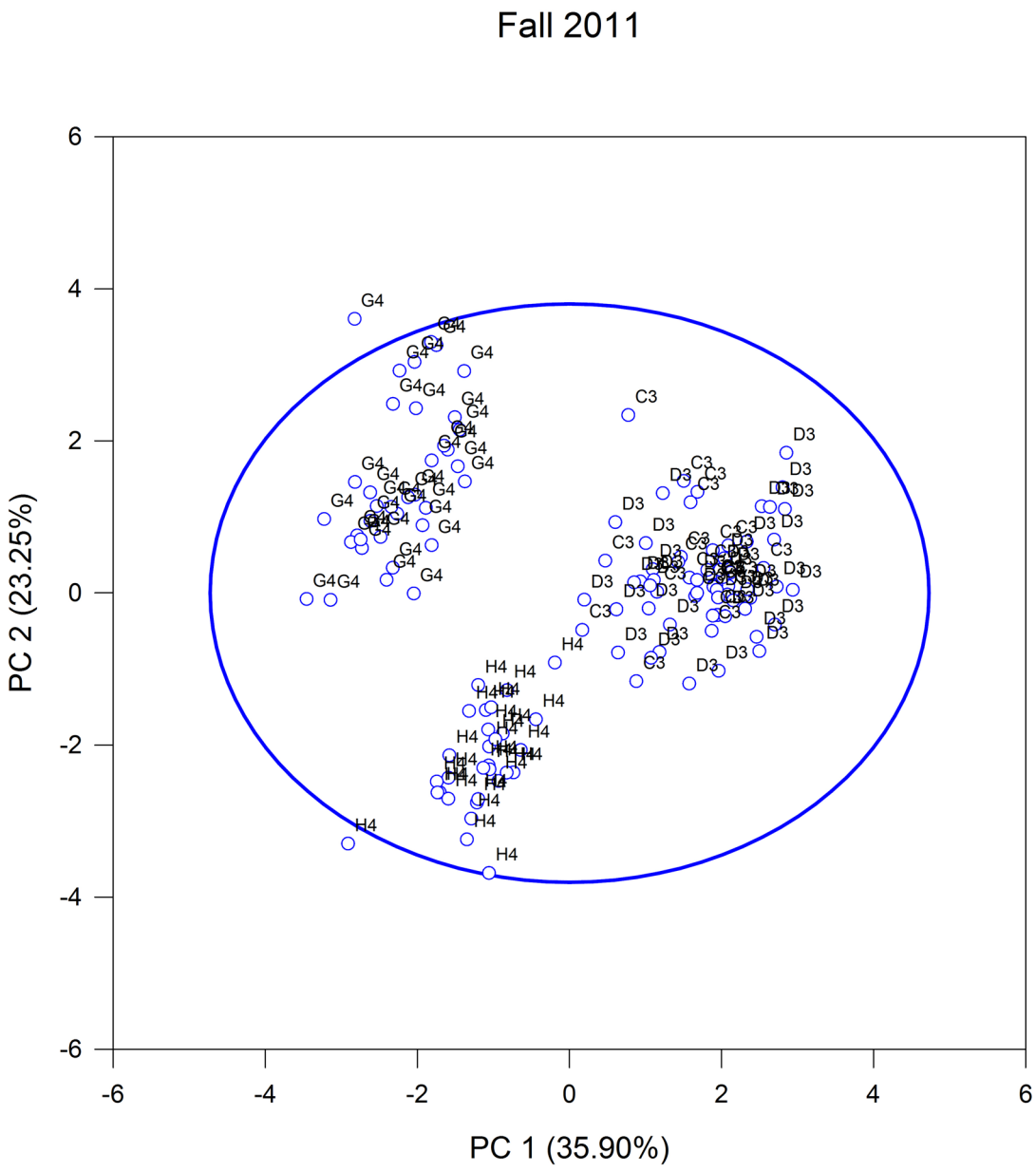

Winter_2011

Principal Components Analysis Friday, March 25, 2016, 2:57:28 AM

Data source: Winter 2011

Normality Test (Henze-Zinkler):

Statistic = 1.392 Failed ($P < 0.050$)

Descriptive Statistics:

Variable	Mean	Std Dev
Al	1.636	0.174
Si	2.752	0.290
K	3.378	0.350
Ca	3.289	0.237
Ti	3.370	0.0546
Mn	2.531	0.177
Fe	4.786	0.0578
Rb	3.041	0.0637
Sr	2.844	0.0611
Zr	2.921	0.0882

Total Observations	96
Missing	0
Valid Observations	96

An observation is missing if any worksheet cell in its row has a non-numeric value.

Correlation Matrix:

	Al	Si	K	Ca	Ti	Mn	Fe	Rb	Sr	Zr
Al	1.000									
Si	-0.416	1.000								
K	0.523	-0.960	1.000							
Ca	0.261	-0.112	0.290	1.000						
Ti	0.526	-0.454	0.634	0.394	1.000					
Mn	0.0618	0.0219	-0.00753	0.173	0.0327	1.000				
Fe	-0.273	0.736	-0.701	-0.207	-0.0702	0.0117	1.000			
Rb	0.118	-0.208	0.177	-0.489	0.280	-0.0365	0.195	1.000		
Sr	0.00335	-0.0826	0.0210	-0.547	0.0120	0.0210	0.0924	0.514	1.000	
Zr	0.313	-0.171	0.315	0.766	0.283	0.207	-0.380	-0.342	-0.463	1.000

Total Variance: = 10.000

Eigenvalues of the Correlation Matrix:

	Eigenvalue	Difference	Proportion(%)	Cumulative(%)
1	3.630	1.198	36.299	36.299
2	2.432	1.161	24.321	60.620
3	1.271	0.288	12.712	73.332
4	0.983	0.412	9.831	83.163
5	0.572	0.125	5.716	88.878
6	0.447	0.0364	4.466	93.345
7	0.410	0.263	4.103	97.447

8	0.148	0.0475	1.475	98.922
9	0.100	0.0923	1.000	99.923
10	0.00774	--	0.0774	100.000

If two or more eigenvalues have the same value, then the corresponding principal components are not well-defined and any interpretation of them is suspect.

Number of In-Model Principal Components = 3

The in-model components correspond to all eigenvalues greater than or equal to the average eigenvalue. When analyzing the correlation matrix, the average eigenvalue is always 1.0. This criterion can be changed in the Test Options dialog on the Criterion panel. The variance of each principal component equals its corresponding eigenvalue.

Chi-Square Tests for the Equality of Eigenvalues:

Hypothesis: All eigenvalues are equal.
Statistic = 820.355
Degrees of freedom = 45.000
P value = <0.001

There is a significant difference in the eigenvalues. A principal components analysis can be conducted.

Hypothesis: The last 7 eigenvalues are equal.
Statistic = 412.853
Degrees of freedom = 28.471
P value = <0.001

There is a significant difference in the last 7 eigenvalues. You may want to include additional principal components in your model by changing the settings in the Test Options dialog on the Criterion panel.

Eigenvectors of the Correlation Matrix:

	PC 1	**PC 2**	**PC 3**
Al	0.338	0.121	0.294
Si	-0.416	-0.294	0.271
K	0.472	0.238	-0.121
Ca	0.320	-0.422	0.210
Ti	0.343	0.159	0.483
Mn	0.0530	-0.107	0.369
Fe	-0.368	-0.0412	0.549
Rb	-0.0400	0.513	0.299
Sr	-0.128	0.480	0.0794
Zr	0.339	-0.363	0.124

Each principal component is a linear combination of the original variables, after each original variable has been standardized to have unit variance. The coefficients of this linear combination are the entries in the corresponding column of the above table. These coefficients provide the interpretation of the principal components in terms of the original variables.

Standard Errors for the Eigenvector Entries:

	PC 1	**PC 2**	**PC 3**
Al	0.0590	0.112	0.121
Si	0.0802	0.115	0.0760
K	0.0623	0.122	0.0632

Ca	0.111	0.0919	0.0911
Ti	0.0675	0.122	0.129
Mn	0.0781	0.113	0.348
Fe	0.0568	0.130	0.104
Rb	0.136	0.0613	0.105
Sr	0.128	0.0631	0.149
Zr	0.0972	0.0961	0.0950

Component Loadings:

	PC 1	**PC 2**	**PC 3**
Al	0.643	0.189	0.331
Si	-0.792	-0.459	0.305
K	0.899	0.371	-0.136
Ca	0.609	-0.658	0.237
Ti	0.654	0.249	0.544
Mn	0.101	-0.166	0.416
Fe	-0.700	-0.0642	0.619
Rb	-0.0762	0.800	0.337
Sr	-0.243	0.749	0.0895
Zr	0.646	-0.565	0.140

If the principle components are standardized to have unit variance, the loadings are the coefficients of the linear combination of in-model principal components used to approximate the original variables. If a correlation matrix is analyzed, then the loadings equal the correlations between the original variables and the principal components.

Fitted Correlation Matrix:

	Al	**Si**	**K**	**Ca**	**Ti**	**Mn**	**Fe**	**Rb**	**Sr**	**Zr**
Al	0.559									
Si	-0.495	0.931								
K	0.603	-0.924	0.964							
Ca	0.346	-0.108	0.271	0.861						
Ti	0.648	-0.466	0.605	0.364	0.785					
Mn	0.171	0.123	-0.0277	0.270	0.251	0.211				
Fe	-0.258	0.773	-0.738	-0.238	-0.137	0.198	0.878			
Rb	0.214	-0.204	0.182	-0.493	0.333	-0.000618	0.211	0.760		
Sr	0.0151	-0.124	0.0471	-0.620	0.0760	-0.112	0.178	0.648	0.628	
Zr	0.355	-0.209	0.351	0.799	0.358	0.217	-0.329	-0.455	-0.568	0.756

This is an estimate of the correlation matrix that results by approximating the original variables with the in-model principal components.

Component Loading Vectors

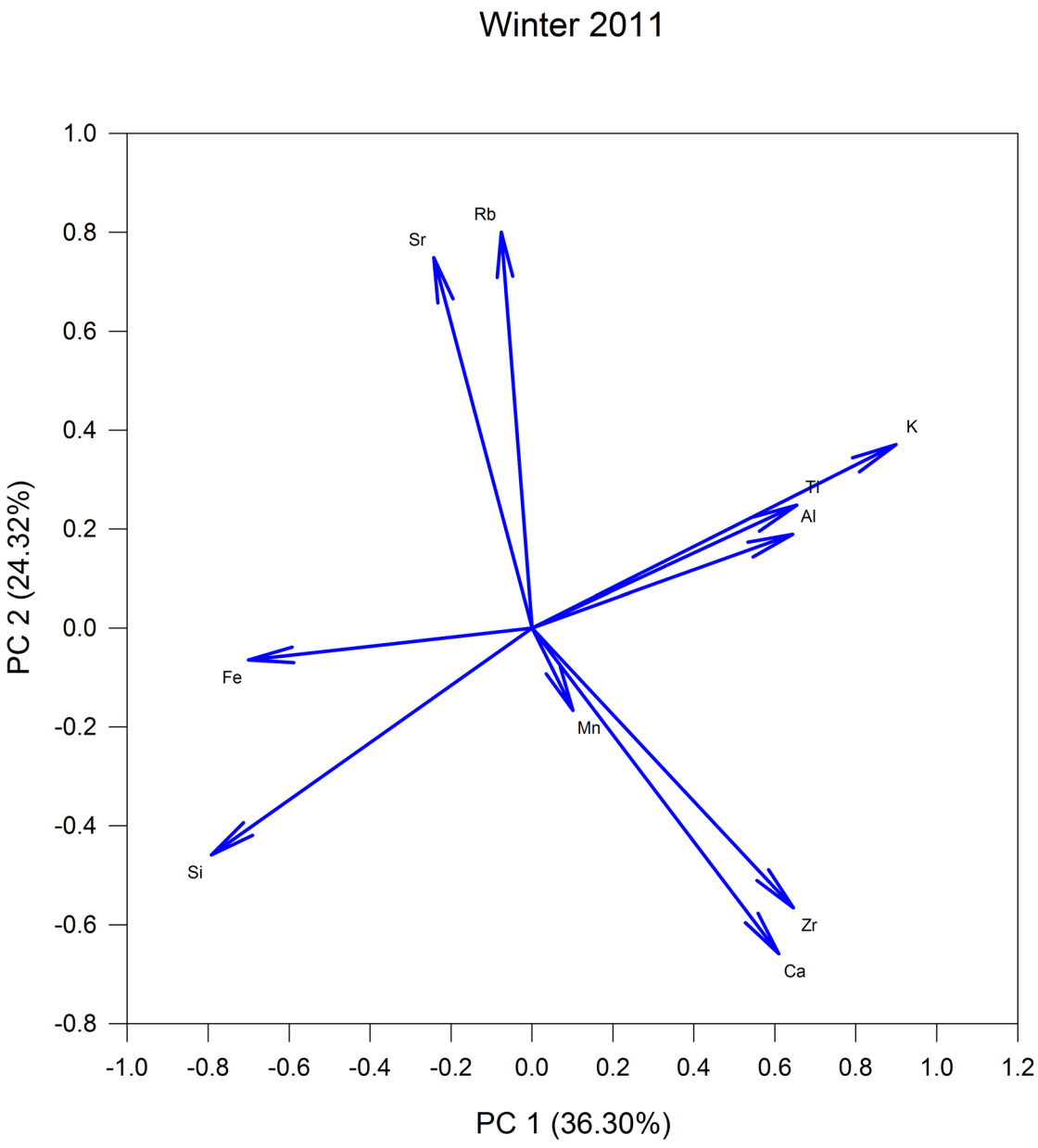

Component Scores

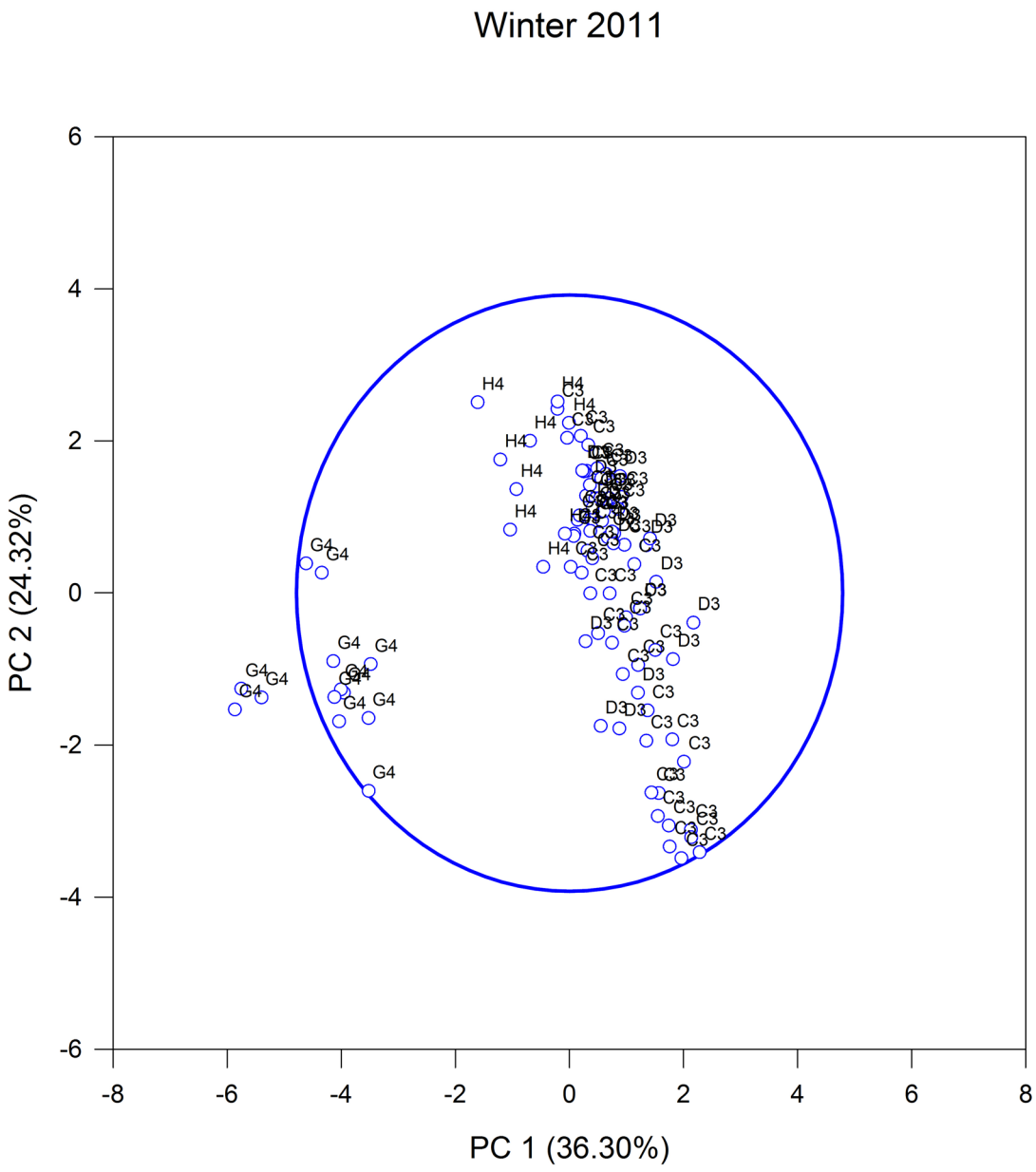

Spring_2012

Principal Components Analysis

Friday, March 25, 2016, 3:00:17 AM

Data Source: Spring 2011

Normality Test (Henze-Zinkler):

Statistic = 1.291 Failed ($P < 0.050$)

Descriptive Statistics:

Variable	Mean	Std Dev
Al	1.547	0.178
Si	2.723	0.196
K	3.398	0.209
Ca	3.533	0.291
Ti	3.361	0.0586
Mn	2.643	0.156
Fe	4.762	0.0771
Rb	2.969	0.0582
Sr	2.767	0.0804
Zr	3.006	0.127

Total Observations	104
Missing	0
Valid Observations	104

An observation is missing if any worksheet cell in its row has a non-numeric value.

Correlation Matrix:

	Al	Si	K	Ca	Ti	Mn	Fe	Rb	Sr	Zr
Al	1.000									
Si	-0.107	1.000								
K	0.190	-0.845	1.000							
Ca	0.0969	0.209	0.313	1.000						
Ti	0.154	-0.0297	0.402	0.719	1.000					
Mn	0.0238	0.253	-0.374	-0.245	0.0315	1.000				
Fe	-0.0162	-0.174	-0.247	-0.787	-0.282	0.374	1.000			
Rb	-0.0117	-0.111	-0.164	-0.538	-0.258	0.227	0.537	1.000		
Sr	-0.195	-0.0581	-0.287	-0.678	-0.462	0.150	0.515	0.372	1.000	
Zr	0.0704	0.251	0.245	0.904	0.533	-0.355	-0.842	-0.554	-0.622	1.000

Total Variance: = 10.000

Eigenvalues of the Correlation Matrix:

	Eigenvalue	Difference	Proportion(%)	Cumulative(%)
1	4.239	2.233	42.394	42.394
2	2.006	0.769	20.062	62.456
3	1.237	0.372	12.369	74.825
4	0.864	0.246	8.644	83.470
5	0.619	0.131	6.188	89.658
6	0.488	0.0978	4.876	94.534
7	0.390	0.296	3.899	98.433

8	0.0940	0.0458	0.940	99.373
9	0.0483	0.0338	0.483	99.855
10	0.0145	--	0.145	100.000

If two or more eigenvalues have the same value, then the corresponding principal components are not well-defined and any interpretation of them is suspect.

Number of In-Model Principal Components = 3

The in-model components correspond to all eigenvalues greater than or equal to the average eigenvalue. When analyzing the correlation matrix, the average eigenvalue is always 1.0. This criterion can be changed in the Test Options dialog on the Criterion panel. The variance of each principal component equals its corresponding eigenvalue.

Chi-Square Tests for the Equality of Eigenvalues:

Hypothesis: All eigenvalues are equal.
Statistic = 954.834
Degrees of freedom = 45.000
P value = <0.001

There is a significant difference in the eigenvalues. A principal components analysis can be conducted.

Hypothesis: The last 7 eigenvalues are equal.
Statistic = 465.587
Degrees of freedom = 29.116
P value = <0.001

There is a significant difference in the last 7 eigenvalues. You may want to include additional principal components in your model by changing the settings in the Test Options dialog on the Criterion panel.

Eigenvectors of the Correlation Matrix:

	PC 1	PC 2	PC 3
Al	0.0740	0.167	0.521
Si	0.0272	-0.688	0.0411
K	0.216	0.614	0.0219
Ca	0.462	-0.105	0.0951
Ti	0.317	0.0685	0.462
Mn	-0.189	-0.252	0.592
Fe	-0.407	0.114	0.250
Rb	-0.313	0.100	0.201
Sr	-0.362	0.0166	-0.209
Zr	0.451	-0.140	-0.0745

Each principal component is a linear combination of the original variables, after each original variable has been standardized to have unit variance. The coefficients of this linear combination are the entries in the corresponding column of the above table. These coefficients provide the interpretation of the principal components in terms of the original variables.

Standard Errors for the Eigenvector Entries:

	PC 1	PC 2	PC 3
Al	0.0637	0.140	0.224
Si	0.0889	0.0231	0.144
K	0.0795	0.0351	0.132

Ca	0.0201	0.0661	0.0586
Ti	0.0473	0.117	0.131
Mn	0.0624	0.133	0.119
Fe	0.0332	0.0819	0.0732
Rb	0.0445	0.0914	0.130
Sr	0.0371	0.0846	0.0954
Zr	0.0243	0.0644	0.0570

Component Loadings:

	PC 1	**PC 2**	**PC 3**
Al	0.152	0.236	0.580
Si	0.0560	-0.974	0.0457
K	0.445	0.870	0.0243
Ca	0.951	-0.149	0.106
Ti	0.652	0.0970	0.514
Mn	-0.390	-0.357	0.659
Fe	-0.837	0.162	0.278
Rb	-0.645	0.142	0.224
Sr	-0.745	0.0235	-0.232
Zr	0.928	-0.199	-0.0828

If the principle components are standardized to have unit variance, the loadings are the coefficients of the linear combination of in-model principal components used to approximate the original variables. If a correlation matrix is analyzed, then the loadings equal the correlations between the original variables and the principal components.

Fitted Correlation Matrix:

	Al	**Si**	**K**	**Ca**	**Ti**	**Mn**	**Fe**	**Rb**	**Sr**	**Zr**
Al	0.415									
Si	-0.195	0.954								
K	0.287	-0.821	0.955							
Ca	0.171	0.204	0.296	0.938						
Ti	0.421	-0.0344	0.387	0.660	0.699					
Mn	0.238	0.356	-0.468	-0.247	0.0500	0.714				
Fe	0.0718	-0.192	-0.225	-0.791	-0.388	0.452	0.805			
Rb	0.0650	-0.164	-0.158	-0.611	-0.292	0.348	0.626	0.487		
Sr	-0.243	-0.0752	-0.317	-0.737	-0.603	0.129	0.563	0.432	0.610	
Zr	0.0464	0.242	0.238	0.903	0.543	-0.345	-0.832	-0.645	-0.677	0.907

This is an estimate of the correlation matrix that results by approximating the original variables with the in-model principal components.